Using ground-based infrared spectroscopy, satellite measurements, and models to understand short-lived climate forcers and wildfire emissions over Canada

by

Victoria A. Flood

A thesis submitted in conformity with the requirements
for the degree of Doctor of Philosophy

Department of Physics
University of Toronto

Using ground-based infrared spectroscopy, satellite measurements, and models to understand short-lived climate forcers and wildfire emissions over Canada

Victoria A. Flood

Doctor of Philosophy

Department of Physics
University of Toronto

2025

Abstract

This thesis uses atmospheric measurements from ground-based Fourier transform infrared (FTIR) spectrometers to study air composition and quality, leveraged with in situ measurements, satellite data, and atmospheric models. The primary instrument, located at the University of Toronto Atmospheric Observatory (TAO), has been measuring since 2002 and is a member of the Network for the Detection of Atmospheric Composition Change (NDACC). This work added four years of data to TAO's long-term time series of 16 trace gases (C_2H_2, C_2H_6, CH_3OH, CH_4, CHF_2Cl, CO, H_2CO, HCl, HCN, HCOOH, HF, HNO_3, N_2O, NH_3, O_3 and OCS).

Simulations by models used in the 2021 Arctic Monitoring and Assessment Programme report on short-lived climate forcers are compared with column-integrated FTIR measurements from five high-latitude NDACC sites. The models exhibit an overall negative bias in tropospheric column values, with CH_4 underestimated by 9.7%, CO by 21%, and O_3 by 18%, highlighting challenges in simulating Arctic atmospheric composition.

The impacts of wildfire emissions on air quality are a concern for populations through both immediate exposure and long-range transport. Three major smoke events in Southern Ontario

resulting from the record-breaking 2023 wildfire season are examined using measurements and models. Tropospheric enhancement ratios relative to CO are reported for C_2H_6, CH_3OH, HCN, HCOOH, NH_3, and O_3. Plume transport is investigated with a back-trajectory model and space-based MOPITT CO, while plume heights are determined with FTIR CO profiles and Micro-Pulse Lidar radiative backscatter. Comparisons with the GEM-MACH-FireWork model show that large-scale plume dispersion is effectively captured, tropospheric columns are overall underestimated, and enhancements are overestimated during smoke events.

Using CO measurements from MOPITT and TAO from 2004-2019, changes to the seasonal cycle are assessed in relation to wildfire activity. A new CO peak emerges in August post-2012 in Alberta and Ontario, consistent with previous literature. Public health risks of this change are examined using a difference-in-difference analysis of monthly hospital emissions for nine cardiovascular and respiratory diseases. Using satellite XCO as an exposure metric, findings are suggestive of a link between enhanced wildfire-related CO concentrations after 2012 and worsening health outcomes, with statistically significant results for six disease-province pairings.

Acknowledgments

I would like to extend a special thank you to my supervisor, Professor Kim Strong, for your invaluable guidance, patience and encouragement throughout this journey. I am truly grateful for the many opportunities and mentorship I have received throughout this degree. I would like to recognize my doctoral committee, Professor Kaley Walker and Dr. Cyndi Whaley. Kaley, your expertise and experience has offered me essential guidance throughout this process. To Cyndi, I am grateful for your support, both academically and beyond, and the valuable insights you have provided me with as someone who has navigated a similar path.

I would like to thank Research Officer Orfeo Colebatch for his dedicated work in maintaining TAO and CARE. Without these efforts, the measurements used throughout these projects would not be possible. Further, I would like to thank the many students who have helped with the TAO operations throughout my time. I would like to acknowledge Tyler Wizenberg for all his help training me to use SFIT4, and for the continued assistance when needed.

This research would not be possible without the assistance of my many collaborators. I would like to acknowledge the NDACC IRWG members who have contributed to my projects, and provided support for SFIT4 troubleshooting, including Ivan Ortega, Corinne Vigouroux and Jim Hannigan. I would like to thank the AMAP SLCF modelling team who were readily available to assist me with model outputs and provide feedback on the manuscript. I would like to thank everyone who contributed data and guidance for Project 2, including Dr. Jack Chen for GEM-MACH FireWork, Professor James Drummond for MOPITT, and Professor Debra Wunch for the EM27/SUN and Mini Micro-Pulse Lidar. I would like to thank Dr. Rebecca Buchholz for her help creating Project 3 and connecting me with Dr. Sheryl Magzamen and Grace Kuiper, without whom I could not have completed the epidemiology analysis.

I would like to thank my family and friends who, despite having little to no idea what I do, are always there to listen to me rant and celebrate my victories. To my parents, Tom and Heather, I am thankful for your continued encouragement throughout what was likely a lot more schooling than you anticipated. To Liam, you have been by my side since day one in Grade 11 Physics, from lab partner to life partner, I am grateful for your unwavering support throughout this journey.

Table of Contents

List of Tables

List of Figures

List of Abbreviations

ACE-FTS	Atmospheric Chemistry Experiment - Fourier Transform Spectrometer
AHS	Alberta Health Service
AMAP	Arctic Monitoring and Assessment Programme
AOD	aerosol optical depth
AQHI	Air quality health index
AR6	Sixth Assessment Report (of the Intergovernmental Panel on Climate Change)
ATM	Atmosphere (line list)
AVHRR	Advanced Very High-Resolution Radiometer
AVK	averaging kernel
BL	baseline
CAD	Canadian Dollar
CAMS	Copernicus Atmospheric Monitoring System
CANDAC	Canadian Network for the Detection of Atmospheric Composition Change
CARE	Centre for Atmospheric Research Experiments
CBM-CFS3	Carbon Budget Model of the Canadian Forest Sector
CCFM	Canadian Council of Forest Ministers
CESM	Community Earth System Model
CFC	chlorofluorocarbon
CFFEPS	Canadian Forest Fire Emission Prediction System
CFS	Canadian Forest Service
CI	confidence interval
CIHI	Canadian Institute for Health Information
CLE	current legislation
CMAM	Canadian Middle Atmosphere Model
CMIP6	Coupled Model Intercomparison Project Phase 6
COCCON	COllaborative Carbon Column Observing Network
COPD	chronic obstructive pulmonary disease
CrIs	Cross-track Infrared Sounder
CSA	Canadian Space Agency
CWFIS	Canadian Wildland Fire Information System
CVD	cardiovascular disease
DEHM	Danish Eulerian Hemispheric Model
DHF	Data Host Facility
DiD	difference in difference
DOFS	degrees of freedom for signal
ECCC	Environment and Climate Change Canada

ECLIPSE	Evaluating the Climate and Air Quality Impacts of Short-Lived Pollutants
EMEP MSC-W	European Monitoring and Evaluation System-Meteorological Synthesizing Center - West
EPA	Environmental Protection Agency
FHWM	full-width at half-maximum
FINN	Fire INventory from NCAR
FIREX-AQ	Fire Influence on Regional to Global Environments and Air Quality
FTIR	Fourier transform infrared
FTS	Fourier transform spectrometer
FWI	Fire Weather Index
GDAS	Global Data Assimilation System
GEM-MACH	Global Environmental Multi-scale - Modelling air quality and Chemistry
GEM-MACH	Global Environmental Multiscale Model - Modelling Air Quality and Chemistry
GEOMS	Generic Earth Observation Metadata Standard
GEOS	Goddard Earth Observing System
GEOS-CHEM	Goddard Earth Observing System - Chemistry
GFED	Global Fire Emission Database
GHG	greenhouse gas
GISS	Goddard Institute for Space Studies
GISTEMP	GISS Surface Temperature Analysis
GM-FW	GEM-MACH FireWork
GOSAT	Greenhouse gases Observing SATellite
HDF	Hierarchical Data Format
HEGIFTOM	Harmonization and Evaluation of Ground-based Instruments for Free Tropospheric Ozone Measurements
HFC	hydrofluorocarbon
HITRAN	High-resolution Transmission Molecular Absorption Database
HWHM	half-width at half-maximum
HYSPLIT	Hybrid Single Particle Lagrangian Integrated Trajectory
IASI	Infrared Atmospheric Sounding Interferometer
ICD-10	International Classification of Diseases 10th revision
IIASA GAINS	International Institute for Applied Systems Analysis – Greenhouse gas – Air pollution Interactions and Synergies
ILC	interlayer correlation length
ILS	instrument line shape
IPCC	Intergovernmental Panel on Climate Change
IWRG	Infrared Working Group
magl	meters above ground level
masl	meters above sea level

MATCH	Multi-Scale Atmospheric Transport Chemistry
MATCH-SALSA	Multi-Scale Atmospheric Transport Chemistry – Sectional Aerosol Module for Large Scale Applications
MFR	maximum technically feasible reduction
MIRS	Multi-angle Imaging SpectroRadiometer
MMM	multi-model mean
MODIS	Moderate Resolution Imaging Spectroradiometer
MOPITT	Measurements of Pollution in The Troposphere
MOZART	Model for Ozone and Related Chemical Tracers
MPLNET	Micro-Pulse Lidar Network
MRI-ESM2	Meteorological Research Institute - Earth System Model Version 2
NAAQS	National Ambient Air Quality Standards
NACRS	National Ambulatory Care Reporting System
NASA	National Aeronautics and Space Administration
NCAR	National Center for Atmospheric Research
NCEP	National Centers for Environmental Prediction
NDACC	Network for the Detection of Atmospheric Change
NESDIS	National Environmental Satellite, Data and Information Service
NIR	near-infrared
NOAA	National Oceanic and Atmospheric Administration
NRB	normalized relative backscatter
NRC	Natural Resources Canada
NRMSE	normalized root mean square error
ODE	ozone depletion event
OEM	optimal estimation method
OMECP	Ontario Ministry of Environment, Conservation and Parks
OMI	Ozone Monitoring Instrument
OMPS LP	Ozone Mapping and Profile Suite Limb Profiler
OPD	optical path difference
PC	partial column
PDF	probability density function
PEARL	Polar Environment Atmospheric Research Laboratory
PHO	Public Health Ontario
PM	particulate matter
POLARCAT	Polar Study using Aircraft, Remote Sensing, Surface Measurements and Models, of Climate, Chemistry, Aerosols and Transport
POLMIP	POLARCAT Model Intercomparison Project
PPIC	Public Policy Institute of California

ppm	parts per million
RAQDPS	Regional Air Quality Deterministic Prediction System
RD	Rapid Delivery
READY	Real-time Environmental Applications and Display sYstem
RMS	root mean square
S5P	Sentinel-5 Precursor
SLCF	short-lived climate forcer
SNR	signal-to-noise ratio
STATS CAN	Statistics Canada
SZA	solar zenith angle
TANSO	Thermal And Near infrared Sensor for carbon Observations
TAO	University of Toronto Atmospheric Observatory
TC	total column
TCCON	Total Carbon Column Observing Network
TES	Tropospheric Emission Spectrometer
TIR	thermal infrared
TOAR	Tropospheric Ozone Assessment Report
TROPOMI	TROPOspheric Monitoring Instrument
TSP	total suspended particles
UKESM1	U.K. Earth System Model Version 1
UofT	University of Toronto
USFS	United States Forest Service
UTLS	upper-troposphere/lower-stratosphere
UV	ultraviolet
VIIRS	Visible Infrared Imaging Radiometer Suite
VMR	volume mixing ratio
VOC	volatile organic compound
WACCM	Whole Atmosphere Community Climate Model
WE-CAN	Western Wildfire Experiment for Cloud Chemistry, Aerosol Absorption, and Nitrogen
WHO	World Health Organization
WRF-CHEM	Weather Research and Forecasting Model with Chemistry

Chapter 1

1 Introduction

1.1 Motivation

Studying the composition of the Earth's atmosphere is critical for assessing environmental changes, climate dynamics, and the impact of human activities on air quality and ecosystems. Atmospheric measurements, specifically long-term datasets, play a key role in developing our understanding of atmospheric processes, trends, and changes that are occurring over time. Further, they are an essential part of model development and testing, which facilitates predictions of future climate scenarios. Such predictions inform policy and decision-making processes, contributing to international efforts like the Montreal Protocol and the Paris Agreement. The research presented in this thesis uses long-term atmospheric monitoring as a tool to investigate atmospheric composition and evaluate models, as they relate to short-lived climate forcers (SLCFs) and wildfire emissions.

The United Nations Intergovernmental Panel on Climate Change (IPCC) Sixth Assessment Report (AR6) presents a comprehensive review of global climate science. In this report, it is stated with "high confidence" that in North America anthropogenic climate-change impacts have increased in frequency and intensity in the last 20 years (Hicke, 2022). Examples of these effects are droughts, floods, and wildfires, driven by extreme temperature or precipitation, which are predicted to worsen in the future. In addition to changing the climate, atmospheric composition can impact human health; it is with "very high confidence" that these changes have led to negative effects on both physical and mental human health (Hicke, 2022). The impacts have been particularly significant in the Arctic, disproportionately affecting both communities and ecosystems in the area.

The World Health Organization (WHO) identifies air pollution as "the biggest environmental threat to human health", also stating that many common drivers of air pollution are also greenhouse gases (GHGs) (WHO, 2021). Advantageously, this means that working towards emissions reductions can have a positive impact for both the climate and human health. In Canada, from 2017-2019, air pollution is estimated to have contributed to 17,400 premature deaths and have a total economic cost of $146 billion (2020 CAD) (Health Canada, 2024). The "Path to Healthier Air" report by Toronto Public Health finds that over half of Toronto's air pollution is from local

sources, led by exhaust emissions (TPH, 2014). The most recent report released in 2014 estimates that, in the City of Toronto, air pollution accounts for 1,300 premature deaths and 3,550 hospitalizations annually; while also highlighting that there are additional widespread, harder to quantify, impacts of air pollution on the population, such as exacerbation of chronic disease symptoms and missed work or school. All three of the projects presented in this work have a connection between atmospheric composition and human well-being, whether through direct air quality impacts (such as wildfires) or through broader climate-related health risks, emphasizing the significance of the atmosphere to public health.

Figure 1.1: Roof-top views from the location of the primary three FTIR instruments used in this work, highlighting the difference between each location. Left: TAO, Toronto, Ontario, middle: CARE, Egbert, Ontario, right: PEARL, Eureka. Nunavut.

Trace gases, although making up a small fraction of the atmosphere, can have significant implications for both the climate and air quality. Fourier transform infrared (FTIR) spectroscopy is a powerful tool for atmospheric measurements of trace gases, providing valuable datasets with long time series. Utilizing data from many instruments across the globe, such as those that are part of the Network for the Detection of Atmospheric Composition Change (NDACC), allows for a comprehensive and harmonized representation of the atmosphere through time and space. The three primary FTIR instruments used in this work, located in Toronto, Ontario, Egbert, Ontario, and Eureka, Nunavut, provide measurements from urban, rural, and Arctic sites, respectively (see Figure 1.1). In the same order, the laboratory names and acronyms which will be used to identify

each location are the University of Toronto Atmospheric Observatory (TAO), the Centre for Atmospheric Research Experiments (CARE), and the Polar Environment Atmospheric Research Laboratory (PEARL). By leveraging long-term FTIR measurements, supported with models, in-situ data and satellite measurements, this research contributes to our understanding of the impacts of SLCFs and wildfires on atmospheric composition over Canada.

1.2 Background

1.2.1 Short-lived Climate Forcers

SLCFs are compounds with relatively short atmospheric lifetimes that have a direct or indirect net warming or net cooling effect on the climate. There is no fixed threshold from which a species is considered "short-lived", but the lifetimes are less than that of carbon dioxide (CO_2) and often cited as less than two decades (AMAP 2021; Szopa et al., 2021). SLCFs include methane (CH_4), ozone (O_3), black carbon, sulfate, nitrate, and organic aerosols. The IPCC reports that in addition to radiative forcing, SLCFs have been found to have negative impacts on air quality, ecosystems, and human health (Szopa et al., 2021). Understanding the impact of SLCFs on the future climate will aid in policies and mitigation strategies to stay on track with the Paris Accord and its subsequent amendments. Mitigation of both CO_2 and SLCFs are critical to reduce warming, where in addition to CO_2 reductions, methane and black carbon need to be reduced by at least 35% by 2050, to keep global temperature rise below 1.5 C° (IPCC, 2018). Due to their relatively short lifetimes, SLCFs are generally reflective of emission rates, and their abundances can have strong regional variations (Szopa et al., 2021). This means that mitigation can result in near-term impacts, but the effects will stabilize on the order of a few decades. As such, SLCF mitigation will not effectively reduce global temperature rise without reductions in long-lived climate pollutants, and should only be considered as a grace period for other adaptation strategies (Bowerman et al., 2013). Because many SLCFs are related to air quality, policies which target air quality may inadvertently have the co-benefit of reducing SLCF emissions (Szopa et al., 2021). The WHO states that reducing SLCFs can significantly benefit human health by lowering air pollution-related health issues and enhancing food security by mitigating the impacts of extreme weather (WHO, 2015). Decreasing SLCF emissions can be particularly beneficial in the Arctic because models have demonstrated a strong climate response in this region to local and remote forcing by SLCFs (Stohl et al., 2015).

The Arctic Monitoring and Assessment Programme (AMAP) is a working group of the Arctic Council, which comprises eight Arctic states (Canada, Denmark, Finland, Iceland, Norway, Russia, Sweden, and the United States). The group releases science-based reports to provide policy-relevant assessments on the Arctic region with respect to climate change, human health, and ecosystems. The 2021 Assessment Report focuses on the impacts of SLCFs in the Arctic by modelling emission scenarios with the current legislation (CLE) and with the maximum technically feasible reduction (MFR) (AMAP, 2021). CLE represents the "current emission-control legislation" and MFR represents the "best available technologies to reduce future air-pollutant emissions".

Figure 1.2 shows Figure 8.33 from Chapter 8: "Simulated impacts of SLCFs on climate and air quality" of the AMAP 2021 Report, which depicts the simulated surface temperature anomaly (relative to the mean observed temperature from 1951-1980) over time from the multi-model mean using CLE (blue) and MFR (red). The black line is the annual mean GISS Surface Temperature Analysis temperature anomaly from 1990-2019, and the shading represents the confidence intervals from the combined uncertainty of the multi-model ensemble spread and temperature variability in each individual model ensemble. The CLE and MFR both have some level of SLCF reductions relative to the model start point; despite this, the model shows that the Arctic will continue to warm until 2050 from increasing CO_2 concentrations and other GHGs. The Report states that although the MFR is not likely to produce a notable net change in Arctic temperature by 2050, the continued application of MFR through to 2050 can reduce the warming rate by 25%. The key results of SLCF reductions in the Arctic outlined in the Report are similar to those stated above, which are generally near-term results and health benefits via improved air quality. The Report cautions that neglecting to mitigate emissions will result in further SLCFs (and precursor gases) from increased temperature, and larger and more frequent fires. They emphasizes that although climate change is a global challenge, it is immediately and critically impacting the Arctic region, with implications for local communities, industry and ecosystems.

Assessing models using historical data helps provide insights into their performance. The AMAP Report evaluates the confidence in the results presented as "high" for the direction of change, although with more uncertainty in the magnitude of results as it is highly dependent on model considerations (for example the level of climate feedback), particularly for future predictions (as represented by the significant uncertainty in Figure 1.2). Some recommendations of the Report are

for timely implementation of legislation that reduces emissions and incorporates the best available technologies, and emissions reporting that is reliable and transparent to provide the necessary tools for evaluating mitigation scenarios. Chapter 4 of this thesis extends the historical surface and satellite model evaluations presented in the AMAP 2021 SLCF Report by applying a new dataset (from high-latitude NDACC FTIR measurements) to the same set of models, as applicable.

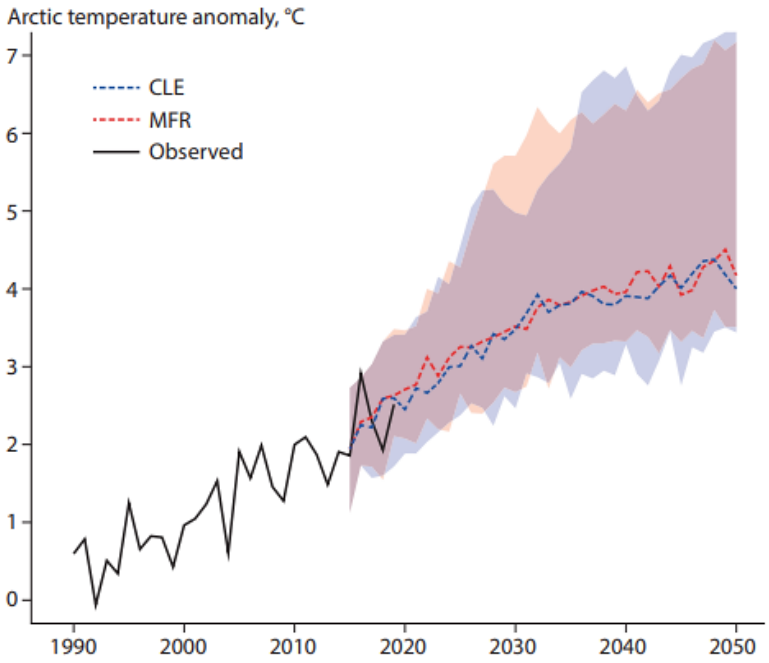

Figure 1.2: Multi-model ensemble median simulated near surface temperature anomalies, relative to mean observed temperature from 1951-1980, in the Arctic for CLE (blue) and MFR (red). The black line represents the historical observed temperature anomaly from GISTEMP v4. The shading represents combined uncertainty from the muti-model ensemble spread and temperature variability in each individual model ensemble. (Figure 8.33 - AMAP, 2021)

Canada released its own "Strategy on Short-Lived Climate Pollutants" in 2017, aiming to reduce emission sources, and achieve health and climate benefits. The approach is described as "holistic" and is to be implemented in phases, based on five main goals, which are summarized as follows (ECCC, 2017):

1. Enhancing domestic mitigation action using jurisdiction and sector-specific emission reduction strategies. Broadly, initiatives include reducing reliance on diesel in remote communities, improving appliance efficiency and building codes, improving fuel efficiency, phasing out hydrofluorocarbons (HFCs), working towards bioenergy and bioproducts, and supporting advances in sustainability technology.

2. Enhancing science and communications to broaden understanding in order to quantify emissions and assess trends. This will be used to support science-based decision making and enhance public awareness of Canada's mitigation plans.

3. Systematically engaging international partnerships to further relationships through joint action, particularly with the United States and Mexico. As part of this initiative, Canada has dedicated funding to help climate goals in developing countries, in addition to participating in projects led by the Arctic Council (such as those outlined in the AMAP Reports).

4. Coordinate Government of Canada activities to prioritize work, track progress, develop resource allocation, and work towards achieving the strategic long-term goals.

5. Collaborate with provincial and territorial governments, and other entities for work that will require a joint jurisdiction response. Partnerships could include municipal waste or transit, private sector, academia, or Indigenous communities.

1.2.2 Wildfires and Emissions

Biomass burning occurs across the world in a variety of ecosystems, driven by both human activity and natural causes. Fires may be set intentionally, e.g., for agricultural or land management purposes, or can be an unintended consequence of environmental factors. In Canada, the majority of burned area is attributed to lightning-caused fires (91% on average from 1959-2015), while they account for about 60% of the ignitions (Hanes et al., 2018). Fires are a natural and essential component of a healthy forest ecosystem; however, climate change is impacting the frequency and size of wildfires, and leading to significant environmental impacts, including the release of GHGs and loss of biodiversity. Further repercussions of fires include the economic costs of fire suppression and recovery efforts, as well as adverse effects on human health.

Canada has 347 million hectares of forested area, with 232 million hectares classified as managed (approximately 60%, encompassing regions used for timber harvest, protected areas and areas under intensive protection against natural disturbances) (NRC, 2024). The Canadian Forest Service uses the Carbon Budget Model of the Canadian Forest Sector (CBM-CFS3) to estimate the GHG sequestration and emissions of Canada's managed forests. Currently, Canada's managed forests are acting as a carbon source through disturbances such as fires, insect outbreaks, and timber practices. Figure 1.3 shows an estimate of the net GHG emissions of the managed forests from

1990 to 2023 from the CBM-CFS3, and Figure 1.4 shows a representation of the burned area in Canada from 1980-2023. The Canadian Council of Forest Ministers recently released the "Canadian Wildland Fire Prevention and Mitigation Strategy" to take action towards wildfire resiliency in Canada (CCFM, 2024). The tactic involves "a whole-of-society approach" and was made in consultation with municipal, provincial, territorial, federal, and self-governments, First Nations, Inuit, and Métis representatives, academia, and industry. It aims to incorporate Indigenous knowledge and address climate change adaptation as it relates to prevention and mitigation.

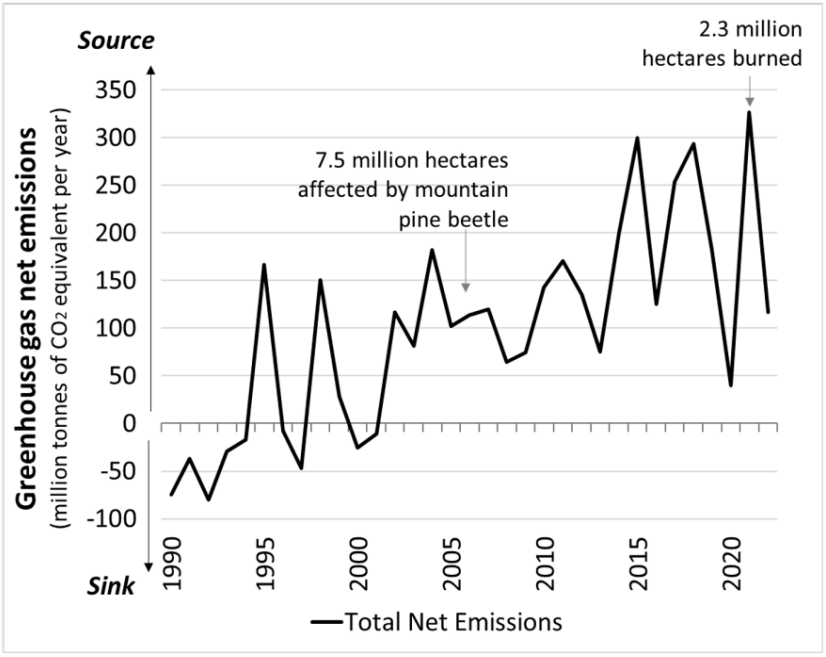

Figure 1.3: Total GHG emissions (as million tonnes of CO_2 equivalent) from Canada's managed forests by year, considering use and disposal of associated harvested wood products, and human and natural disturbances (NRC, 2024).

A study by the Great Lakes Forestry Centre, reviewing fire trends in Canada from 1959-2015, shows a significant increase in burned area over time, dominated by large fires, which were found to have doubled over the study period (Hanes et al., 2019). The Fire Weather Index (FWI) is a rating used to represent the "fire danger" of a region, encompassing temperature, humidity, wind, and precipitation (Van Wagner, 1987). Jones et al. (2022) highlight a relationship between burned area and FWI in Canada, stating that models that use FWI as an indicator for future fire activity project an increase due to anthropogenic climate change. Whitman et al. (2022) show that from 1970-2019, the province of Alberta had statistically significant increases in temperature and dryness, and a shift in fire regime characteristics whereby large fires began to dominate and reburn

frequency increased. Season-specific climate variables were shown to positively correlate with the fire activity, indicating that climate is a top-down driver for wildfires in the region. In addition to climate change causing drier, hotter conditions and a lengthening of the forest fire season, fire suppression tactics have contributed to higher instances of extreme and uncontrollable burning events (Jolly et al., 2015; Kredier et al., 2024). Such fire management policies in Canada involving fire suppression have resulted in an amplified risk of wildfires by increasing the flammability in the boreal wildland-urban interface (Parisien et al., 2020). Erni et al. (2024) used wildfire simulations to assess fire likelihood and intensity, paired with census data from Canada, finding that 283,000 people (2.2%) are in areas of high fire risk, and 30,500 (0.2%) are in areas classified as very high risk. Indigenous people who reside on a reserve are at an increased risk compared to the general population, with 14.5% of the total on-reserve population living in areas of high fire risk, and 3.7% of the total in very high risk.

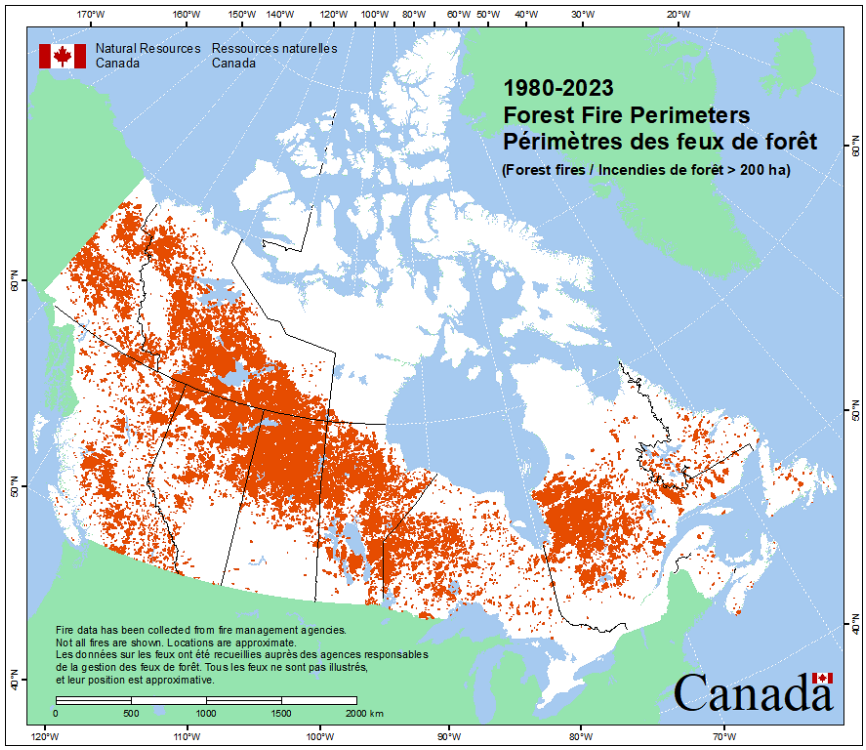

Figure 1.4: Fire perimeters from 1980-2023 in Canada as provided by fire management agencies (provinces, territories, and Parks Canada) (CWFIS, 2024).

In the summer of 2023, Canada had a record-breaking wildfire season during which approximately 4% of the forested region in the country burned (Jain et al., 2024). The carbon emissions attributed to the whole season country-wide are comparable to that of a developed country in a year (Byrne et al., 2024). Dry conditions resulting from early snowmelt and an extended period of drought, in

addition to the high-temperature anomalies, contributed to an increased FWI leading to the anomalous fire season (Jain et al., 2024). The extreme burning events that occurred in Quebec were stated to have been more than twice as likely to occur due to anthropogenic climate change (Barnes et al., 2023).

Chemical species released during biomass burning events can lead to degraded air quality and affect the climate and carbon cycle. In Canada, wildfire-$PM_{2.5}$ (particulate matter) for 2013-2015 and 2017-2018 is estimated to have caused 54-240 premature deaths due to short-term exposure, and 570-2500 premature deaths from long-term exposure, along with several other adverse health outcomes (Matz et al., 2020). The five-year (2013-2018) total economic impact of the wildfire-$PM_{2.5}$, as it relates to health, was estimated to be $49 billion (CAD) (Matz et al., 2020). Health impacts are estimated to be greatest in areas with higher exposure to wildfire $PM_{2.5}$ and a large population (i.e., Alberta and British Columbia), however they are also relevant in areas with lower exposure levels (i.e., Ontario and Quebec) (Matz et al., 2020). Areas in proximity to active fires will often have public health advisories for residents and intervention measures in place for vulnerable populations, while areas further away, which are not in the immediate disaster response area, may be less aware of their exposure (Magzamen et al., 2021).

Vegetation fires progress through several stages: ignition, flaming, glowing, smoldering and extinction, and each phase undergoes distinct processes, producing different emissions (Lombert and Warnatz, 1993). In the initial phase, with high temperature, the water and volatile extractables (such as alcohols, aldehydes and terpenes) are dried or distilled. Subsequently, heat-induced cracking of the fuel molecules causes high-molecular weight components to decompose to lower-molecular weights, eventually forming gas compounds. As the process turns from endothermic to exothermic, decomposition of hydrocellulose takes place and eventually the phase will transition from flaming to glowing combustion. The smoldering phase occurs when most of the near-surface fuel has emitted its volatile extractables and the flame ceases. Most of the emissions occur during the flaming and smoldering phases. Burn characteristics, such as burn efficiency and the transition to smoldering, are significantly influenced by the water content of the vegetation, and can alter the resulting emissions. Additional factors influencing emissions include vegetation density and structure, fuel size, and elemental composition of the vegetation.

Long-lived species are useful for tracking plumes and can provide information about the source of a biomass burning event. Yamanouchi et al. (2020) examined the long-range transport of trace gases related to fire emissions in the Toronto area using ground-based FTIR spectroscopy. Using data from 2002-2018, the study found enhancements of carbon monoxide (CO), ethane (C_2H_6), methanol (CH_3OH), hydrogen cyanide (HCN), and formic acid (HCOOH) related to boreal and temperate forest fires. Similarly, enhancements of CO, HCN, C_2H_6, ammonia (NH_3), peroxyacetyl nitrate (PAN), ethylene (C_2H_4), CH_3OH and HCOOH were detected with an FTIR in the Canadian High Arctic, and attributed to fires in British Columbia and the Northwest Territories of Canada in 2017 (Lutsch et al., 2020; Wizenberg et al., 2023). Figure 1.5 shows a photograph during the 2024 NDACC-TCCON-COCCON Annual Meeting at the National Center for Atmospheric Research (NCAR) Mesa Lab in Boulder, Colorado, where a wildfire began in a nearby forest, causing the meeting to be evacuated.

Figure 1.5: Wildfire during the July 2024 NDACC-TCCON-COCCON Annual Meeting in Boulder, Colorado.

1.3 Thesis Overview

This thesis encompasses three main projects, each aimed at addressing distinct scientific questions and research objectives through the utilization of long-term mid-infrared FTIR measurements. Chapter 2 presents the methodology and description of the FTIR instruments and retrievals used within this work. Chapter 3 provides an overview of the TAO retrieval parameters and the 2002-2024 time series of all 16 trace gases. Chapters 4, 5 and 6 report on the main three projects of this

thesis (described further in the following paragraphs), and Chapter 7 provides a summary of the work, including the significance of the scientific questions/objectives and possible future work.

Project 1 aims to address the question – ***How well do the SLCF model simulations in the AMAP 2021 Report represent historical measurements of CH_4, CO and O_3 at five Arctic FTIR sites, and what, if any, patterns arise in the discrepancies?*** This is achieved by evaluating the outputs from the 11 models matched with tropospheric column measurements in time and space. Specifically, the modelled tropospheric columns are compared with measurements from 2008-2009 and 2014-2015, from the NDACC FTIR instruments located in Eureka, Canada; Thule, Greenland; Ny Ålesund, Norway; Kiruna, Sweden; and Harestua, Norway. Biases for each model are assessed relative to the FTIR measurement uncertainty, and seasonal cycles are examined using monthly means to identify potential model shortcomings.

Project 2 aims to address the question – ***How significant were the impacts of the 2023 Canadian wildfires on the air quality and composition in Southern Ontario, and how do the GEM-MACH Firework simulations compare to ground-based and satellite measurements in the region?*** Using three distinct smoke events, air composition is assessed with measurements of biomass burning gases from the TAO and CARE FTIRs, and enhancement ratios are evaluated. Air quality during the events are reported by the provincial monitoring system and plume transport are investigated with satellite measurements of CO and a back-trajectory model. The GEM-MACH Firework model is compared to surface in-situ measurements of CO, O_3 and $PM_{2.5}$, to tropospheric columns of CO, NH_3 and O_3 from the TAO and CARE FTIRs, and to CO total columns from the Measurements Of Pollution In The Troposphere (MOPITT) satellite instrument on a broader scale.

Project 3 aims to address two questions – ***Has an increase in wildfires changed the CO seasonal cycle in Ontario and Alberta, Canada? Does health care utilization for respiratory and cardiovascular diseases present a change related to the CO seasonality and if so, can CO be used as an exposure metric?*** The work uses long-term measurements of CO from the TAO FTIR and MOPITT from 2002-2019, with a break point of pre/post 2012 to examine the seasonal cycle. Monthly emergency room counts for nine respiratory and cardiovascular diseases from health districts in Alberta and Ontario are analyzed over the same period. A difference-in-difference regression is used to evaluate if a change in health care utilization for the diseases occurs with the interaction term defined as after 2012, and the exposure metric as the MOPITT CO total column.

1.3.1 Scientific Objectives

The primary objectives of this research are derived from the scientific questions outlined above, with some elements shared between reoccurring themes, and are as follows:

(1) Maintain ongoing solar absorption FTIR measurements and trace gas retrievals at TAO, contributing to the NDACC Data Host Facility Data (DHF) and the Copernicus Atmospheric Monitoring System (CAMS) and work towards establishing a new Canadian NDACC FTIR site at CARE.

(2) Evaluate the performance of atmospheric models by leveraging FTIR datasets from the University of Toronto Atmospheric Observatory, the Centre for Atmospheric Research Experiments, the Polar Environment Atmospheric Research Laboratory, and four other Arctic NDACC stations, as well as other relevant in situ and satellite measurements.

(3) Investigate changes in atmospheric composition resulting from the long-range transport of wildfire emissions and assess the impact of this on local air quality and public health.

Objective 1 is relevant to all of the projects and is achieved through the maintenance of the TAO and CARE FTIR retrievals and the application of the data for analysis. Objective 2 is achieved within the first and second projects, wherein atmospheric models are evaluated. Objective 3 is achieved within Projects 2 and 3 wherein forest fire emissions are discussed in the context of FTIR measurements.

1.3.2 Contributions

This work builds upon the PhD thesis projects of Shoma Yamanouchi (2021) and Cynthia Whaley (2014), the publications therein, and the other predecessors who have worked with the TAO FTIR spectrometer. Throughout the course of my PhD, I helped with the regular operations of TAO and was responsible for the data processing and retrievals. Research officer Orfeo Colebatch was largely responsible for maintenance of the TAO FTIR, particularly during the COVID-19 pandemic. Other contributors to TAO operations over the duration of this work include students: Darby Bates, Gabriel Cassidy, Petra Duff, Tadgh Hearne, Beatriz Herrera, Kevin Joshy, Erin McGee, Raia Ottenheimer, and Claire Pan. The procedure for data processing included downloading National Centers for Environmental Prediction (NCEP) temperature and pressure data, preparing the various retrieval files, performing retrievals, and assessing the data quality. The CH_4, CO, H_2CO and O_3 retrievals are regularly (every 2-4 weeks) uploaded to the Copernicus

Atmospheric CAMS Rapid Delivery (RD) system. The rest of the retrieved species are uploaded annually to the public NDACC DHF. I would, at times, be requested to process data for collaborating scientists if they required data that were not yet publicly available or a new retrieval (i.e., OCS and HCFC-22). Additionally, I updated the TAO NDACC O_3 retrievals to the SFIT4 version 1.0.14, and changed the retrieval to the Tikhonov regularization parameters, as recommended by the NDACC Infrared Working Group (IRWG) O_3 Retrieval Strategy Group. C_2H_6 and HCl were set up to be run with SFIT4 version 1.0.14, and at the request of the IRWG, testing was done with high-resolution transmission molecular absorption (HITRAN) database versions 2008 and 2020 (HIT08/HIT20), and the Atmosphere (ATM) 2020 line list, with the Whole Atmosphere Community Climate Model v6 (designated IRWG ".v7"). Note the currently archived version v02 for both gases uses SFIT v0.9.4.4. When measurements at CARE began in April 2023, again Orfeo Colebatch was largely responsible for making this possible, and I was assigned regular shifts for remote operations.

Project 1 involved a collaboration with Dr. Cynthia Whaley at Environment and Climate Change Canada (ECCC) and Professor Kaley Walker. This work follows the AMAP 2021 SLCF Report, and allowed me to collaborate with many different groups, both from NDACC and the AMAP modeling teams. The models were run by the respective teams, and the output files of gridded SLCFs were supplied to me for processing. This work was presented at American Geophysical Union (AGU) 2021, Canadian Meteorological and Oceanographic Society (CMOS) 2022, ArcticNet 2022, and NDACC-IRWG meetings in 2023 and 2024, and is published in *Atmospheric Chemistry and Physics* (Flood et al., 2024).

Project 2 is a case study of the period when Southern Ontario experienced degraded air quality due to the record-breaking 2023 fire season in Canada. As a result of on-going efforts by Orfeo Colebatch, the CARE FTIR spectrometer was operational at this time, allowing for two measurement locations in the study area. Additional instruments were added such as the EM27/SUN and a mini Micro-Pulse Lidar Network (MPLNET) with help from Professor Debra Wunch, and the MOPITT satellite with input from Professor James Drummond. Further, collaborations with Dr. Cynthia Whaley and Dr. Jack Chen allowed for a comparison with ECCC's GEM MACH FireWork model. This work was presented at AGU 2023 and the NDACC-IRWG meeting 2024, and is published in *Journal of Geophysics Research – Atmospheres* (Flood et al., 2025a).

Project 3 involved a collaboration with Dr. Rebecca Buchholz from the National Center for Atmospheric Research (NCAR) using the TAO CO time series to build on the results from her biomass burning study using MOPITT data (Buchholz et al., 2022). An additional analysis of health data was included, and Dr. Sheryl Magzamen and Grace Kuiper from Colorado State University joined the project to provide expertise on the epidemiological analysis of the hospital data. The emergency room admission data were obtained from the Canadian Institute for Health Information (CIHI). This work was presented at Committee on Space Research (COSPAR) 2022, European Geosciences Union (EGU) 2023, and the NDACC-IRWG meeting 2023, and is under review in *GeoHealth* (Flood et al., 2025b).

1.3.3 Thesis Outline

The structure of this thesis is as follows:

Chapter 1, the current chapter, is the introduction, which describes the motivation, background, and scientific objectives of the thesis.

Chapter 2 outlines the primary methodology used throughout this thesis, FTIR spectroscopy, including details on the primary locations and the way in which trace gas profiles and columns are retrieved from infrared solar absorption spectra.

Chapters 3 presents the NDACC trace gas time series from TAO, the primary FTIR location used within this work.

Chapter 4 presents the work done in Project 1, with AMAP model validations of short-lived climate forcers using measurements from five Arctic NDACC FTIR stations.

Chapter 5 presents the work done in Project 2, assessing three wildfire smoke events from long-range transport to Southern Ontario in the summer of 2023, using satellite data, models, and ground-based monitoring, in addition to an evaluation of the GEM-MACH FireWork operational air quality model.

Chapter 6 presents the work done in Project 3, which evaluates a change in the seasonal cycle of CO in Alberta and Ontario attributed in previous literature to an increase in wildfires, and assesses

CO total columns with respect to healthcare utilization for nine cardiovascular and respiratory diseases over the same period.

Chapter 7 provides the conclusions to this thesis and suggestions for future work.

Chapter 2

2 Methods

The primary source of data in this work is solar-viewing mid-infrared Fourier transform infrared spectroscopy. The FTIR instruments employed in this research record solar absorption spectra optimized for different atmospheric gases by cycling through a series of optical filters covering spectral ranges between 650 and 4500 cm^{-1}. The advantages of this instrument type are that it can measure multiple species in a single scan, take many measurements in a short period of time, is available as a long time series, and provides vertical information for multiple species. Furthermore, the instruments are part of NDACC, which allows for easy access to analogous measurements from equivalent instruments in other locations, increased collaboration and knowledge sharing. The drawbacks are that it has limited spatial coverage, requires daytime and clear conditions, and only provides a limited number of measurements per day for each species. This chapter describes the origin of mid-infrared spectra, and how they are recorded and processed to retrieve trace gas profiles and columns.

2.1 Molecular Spectroscopy

Spectroscopy is a broad discipline that examines the interaction between matter and electromagnetic radiation. Molecular spectroscopy, as it relates to this work, involves the study of how molecules of trace gases interact with electromagnetic radiation from the sun. The structural properties of the molecules of each gas give rise to distinct spectral features, as the energy that is absorbed or emitted during the transition from one state to another is directly proportional to frequency, inversely proportional to wavelength, and constrained by quantum theory (Bernath, 2005). As the simplest example, one may consider a hydrogen atom that absorbs a photon with enough energy, E, to move from its ground state (n=1) to the first excited electronic state (E=10.2 eV for n=1 to n=2); when it returns to the original state, a photon of the same wavelength is emitted, releasing the absorbed energy as electromagnetic radiation. In addition to electronic energy, the structure of molecules results in additional energy signatures from their vibrational and rotational motions. The Born-Oppenheimer Approximation enables the motion of electrons and atomic

nuclei to be separated, due to the relative mass difference between the two entities; the total molecular energy can be written as independent terms, represented in Equation 2.1:

$$E_{total} = E_{electronic} + E_{rotational} + E_{vibrational} + E_{nuclear\ spin}\,. \tag{2.1}$$

When considering this equation in terms of infrared spectroscopy, it can be simplified to Equation 2.2; $E_{electronic}$ can be omitted because electronic transitions happen outside the infrared region and are generally observed in the visible and ultraviolet region, and $E_{nuclear\ spin}$ can be disregarded because it is much smaller in magnitude than the rotational and vibrational transitions in the infrared region:

$$E_{total} = E_{rotational} + E_{vibrational}\,. \tag{2.2}$$

Rotational energy is a result of the movement of the molecule about its center of gravity, and is represented in Equation 2.3 for a diatomic molecule, where *J* is the rotational quantum number (*J* = 0,1,2,…), *B* is the rotational constant, *h* is Planck's constant, *I* is the moment of inertia of the molecule, and *c* is the speed of light (Bernath, 2005). Transitions of this type have lower energy and longer wavelengths, occurring in the far-infrared or microwave region.

$$E_{rot} = BJ(J+1) = \left(\frac{h^2}{8\pi^2 Ic}\right)J(J+1)\,. \tag{2.3}$$

Equation 2.3 considers a diatomic molecule as rigid rotor, and is represented by the equally spaced lines in Figure 2.1a. To account for centrifugal distortion (*D*) that happens when the molecule rotates and the bonds distort, the rotational energy is expressed as Equation 2.4. The distortion term accounts for the change in inertia that decreases the separation between transitions at high levels of *J*, in turn decreasing the spacing between the transitions (represented in Figure 2.1b) (Liou, 2002).

$$E_{rot} = BJ(J+1) - DJ^2(J+1)^2\,. \tag{2.4}$$

Vibrational energy (E_{vib}) is due to the displacement of atoms from equilibrium. This is described for a harmonic oscillator by Equation 2.5, where v is the vibrational quantum number and ω is the frequency of vibration, which depends on the square root of the spring force constant (k) divided

by the molecule's reduced mass ($\mu = \frac{m_1 m_2}{m_1 + m_2}$) (Bernath, 2005). These transitions typically involve higher energies and occur in the mid or near-infrared regions of the electromagnetic spectrum.

$$E_{vib}(v) = h\omega\left(v + \frac{1}{2}\right) = h\left(\frac{1}{2\pi c}\sqrt{\frac{k}{\mu}}\right)\left(v + \frac{1}{2}\right). \tag{2.5}$$

When a vibrational transition occurs with a rotational transition, the process is known as vibrational-rotational spectroscopy and is the most relevant for the mid-infrared FTIR spectroscopy discussed throughout this work. The change in energy (ΔE) resulting from the absorption of an infrared photon can be grouped into three branches based on the transitions which occur. The branches occur with a vibrational change of Δv=±1, ±2, ±3… and are represented in Figure 2.1b. The P branch corresponds to a decrease in rotational quantum number by 1 (ΔJ = -1), the lines appear at lower wavenumbers than the central vibrational frequency ($\tilde{\nu}_0$). The Q branch represents no change in the rotational number (ΔJ = 0); however, this requires the molecule to have angular momentum and a dipole moment to interact with the infrared radiation. The R branch corresponds to an increase in rotational quantum number by 1 (ΔJ = +1), and the lines appear at higher wavenumbers than the $\tilde{\nu}_0$ (Bernath, 2005). When considering polyatomic molecules, the modes and interactions become more complex, however, the concept of unique spectral features which can be utilized for atmospheric trace gas analysis remains applicable.

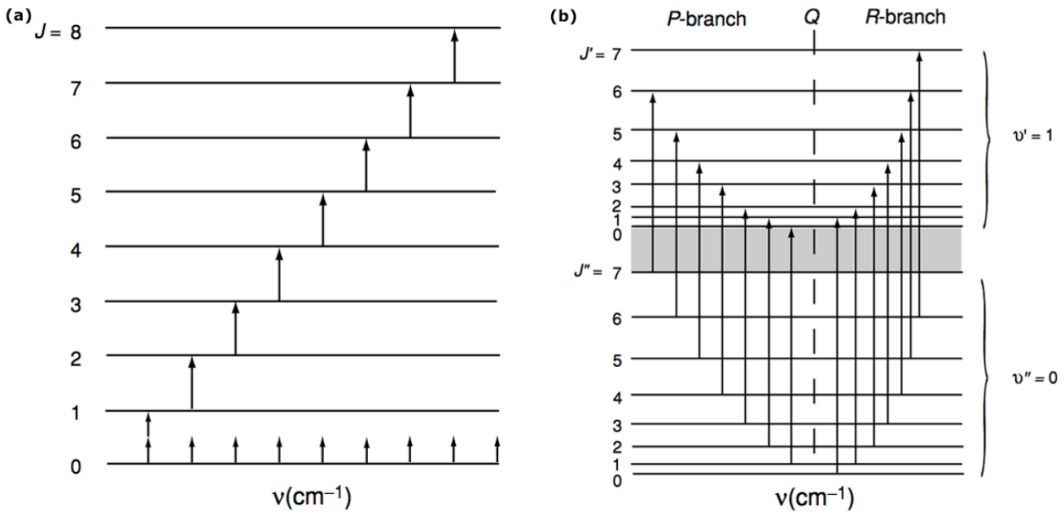

Figure 2.1: (a) Rotational transitions (ΔJ = ±1), and equally spaced spectral lines in wavenumber. (b) P, Q and R branch simultaneous vibrational and rotational transitions (figure reproduced from Liou, 2002).

2.1.1 Spectral Infrared Line Shapes

Atmospheric absorption lines will differ in shape, depth and width based on properties of the gas including temperature, pressure and concentration. The profile is influenced by the molecule's motion along the line of sight, known as Doppler broadening, and perturbations from collisions with other molecules, known as pressure/collisional broadening. Additionally, natural broadening occurs from energy fluctuations during transitions, arising from the Heisenberg uncertainty principle, however the effect is minimal compared to the other two broadening mechanisms (Liou, 2002). The strength of the spectral lines (S), described by Equation 2.6 where $\tilde{\nu}$ is the monochromatic wavenumber, is dependent on the absorption coefficient k:

$$S = \int_{-\infty}^{\infty} k \, d\tilde{\nu} \, . \tag{2.6}$$

The impact of collisional broadening on line shape is a function of pressure, and as a result is more pronounced at higher pressures, such as in the troposphere. It is the result of a shift in the frequency of the emitting molecule by hitting another molecule, which is short-lived and randomly distributed. The shape of this broadening manifests as a Lorentz profile and is represented in Equation 2.7, where k_L is the absorption coefficient, $\tilde{\nu}_0$ is the center wavenumber, α_L is the half-width at half-maximum (HWHM), and *S* is the line strength (Liou, 2002):

$$k_L = \frac{S}{\pi} \frac{\alpha_L}{(\tilde{\nu} - \tilde{\nu}_0)^2 + {\alpha_L}^2} = Sf(\tilde{\nu} - \tilde{\nu}_0) \, . \tag{2.7}$$

The Lorentzian HWHM (α_L) is dependent on temperature and pressure, as shown in Equation 2.8, where α_0 is the HWHM at standard temperature and pressure (T_0=273 K and p_0=1013 mb):

$$\alpha_L = \alpha_0 \left(\frac{p}{p_0}\right) \sqrt{\frac{T_0}{T}} \, . \tag{2.8}$$

When pressure decreases, such as in the stratosphere, Doppler broadening becomes more significant. A shift in frequency is caused by the variation in molecules' speed (u) along the line-of-sight, such that the observed wavenumber is given by $\tilde{\nu} = \tilde{\nu}_0(1 \pm \frac{u}{c})$. When considering the velocity interval u+du, the molecule's range of velocities are assumed to follow a Maxwell-

Boltzmann distribution, as a function of temperature. The line shape manifests itself as Gaussian profile function, represented as Equation 2.9; the absorption coefficient (k_D) is in terms of $\tilde{v}$, S and Doppler line width (α_D) (Liou, 2002):

$$k_D = \frac{S}{\alpha_D\sqrt{\pi}} \exp\left[-\left(\frac{\tilde{v}-\tilde{v}_0}{\alpha_D}\right)^2\right] . \tag{2.9}$$

The Doppler width of the line, α_D, is related to the temperature of the gas (T) and the mass of the molecule (m), and the HWHM is obtained by scaling α_D by the square-root of the natural log, where k_b is the Boltzmann constant:

$$\mathrm{HWHM_D} = \alpha_D\sqrt{\ln 2} = v_0\sqrt{\frac{2k_bT\ln 2}{mc^2}} . \tag{2.10}$$

At altitudes of about 20-50 km in the atmosphere, both broadening mechanisms, Lorentzian collisional-broadening and Gaussian Doppler-broadening, contribute to the shape of the spectral lines; the combination of the two is represented by a Voigt profile shape (Liou, 2002). The line shape can be expressed in terms of absorption coefficients as:

$$k_V(\tilde{v}) = k_L(\tilde{v}) * k_D(\tilde{v}) . \tag{2.11}$$

To account for all possible thermal velocities, the convolution of the two shapes is integrated from $-\infty$ to ∞ resulting in a Voigt profile ($f_{\mathrm{V}}(\tilde{v}-\tilde{v}_0)$), represented in Equation 2.12 (Liou, 2002).

$$f_{\mathrm{V}}(\tilde{v}-\tilde{v}_0) = \int_{-\infty}^{\infty} f_L(\tilde{v}'-\tilde{v}_0) * f_D(\tilde{v}-\tilde{v}')d\tilde{v}' \tag{2.12}$$

$$f_{\mathrm{V}}(\tilde{v}-\tilde{v}_0) = \frac{1}{\pi^{\frac{3}{2}}}\frac{\alpha_L}{\alpha_D}\int_{-\infty}^{\infty}\left[\frac{1}{(\tilde{v}'-\tilde{v}_0)^2+{\alpha_L}^2} exp\left(\frac{-(\tilde{v}-\tilde{v}')^2}{\alpha_D^2}\right)\right]d\tilde{v}' .$$

The HWHM of the Voigt profile can be approximated by Equation 2.13 (Griffiths and De Haseth, 2007):

$$\mathrm{HWHM_V} = \alpha_V = \frac{\alpha_L}{2} + \sqrt{\frac{{\alpha_L}^2}{4} + (\alpha_D\sqrt{\ln 2})^2} . \tag{2.13}$$

Since the FTIR instruments employed in this work sample the total atmosphere column, the Voigt line shape is the most suitable as it accounts for both Doppler and collisional broadening effects. The spectral line parameters and broadening coefficients are applied from the spectral line list databases of HITRAN (Rothman et al., 2009; 2013; Gordon et al., 2022) and ATM (Toon, 2015; 2022).

Another important aspect to consider when analyzing a spectrum is line intensity, which can be interpreted using principles of radiative transfer. As a beam of radiation passes through a medium, its energy is influenced by emission, absorption, and scattering. Equation 2.14 is used to define the change in intensity, $dI(\tilde{\nu})$, across some atmospheric distance, dL, with respect to the mass extinction cross-section (units of area per molecule for wavenumber $\tilde{\nu}$), $\sigma(\tilde{\nu})$, density of the gas (ρ), and the incoming intensity $I(\tilde{\nu})$ (Liou, 2002):

$$dI(\tilde{\nu}) = -\sigma(\tilde{\nu})\rho I(\tilde{\nu})\, dL\,. \tag{2.14}$$

This relation accounts for intensity change due to absorption and scattering by the material, where the mass extinction cross-section is the sum of mass absorption and scattering cross-sections. The beam may also undergo intensity changes in the form of increased intensity via emission or multiple scattering from all other directions. Equation 2.15 describes this change, where $j(\tilde{\nu})$ is the source function coefficient, with the same units as $\sigma(\tilde{\nu})$:

$$dI(\tilde{\nu}) = j(\tilde{\nu})\rho dL\,. \tag{2.15}$$

Equations 2.14 and 2.15 can be combined, to give the general Radiative Transfer Equation (Liou, 2002):

$$dI(\tilde{\nu}) = -\sigma(\tilde{\nu})I(\tilde{\nu})\rho dL + j(\tilde{\nu})\rho dL\,. \tag{2.16}$$

Defining a source function, $J(\tilde{\nu}) = j(\tilde{\nu})/\sigma(\tilde{\nu})$, with units of radiant intensity, Equation 2.16 can be written as Equation 2.17:

$$\frac{dI(\tilde{\nu})}{\sigma(\tilde{\nu})\rho dL} = -I(\tilde{\nu}) + J(\tilde{\nu}). \tag{2.17}$$

In the context of atmospheric ground-based solar absorption FTIR spectroscopy, when light from the sun passes through the atmosphere, the intensity is attenuated by the gases that it passes

through. In terms of the change in intensity along the path of the solar beam, $dI(\tilde{\nu})$, it is convenient to neglect the contributions from emission and multiple scattering (shown in Equation 2.15), which are relatively minimal compared to absorption, allowing for Equation 2.17 to be simplified by omitting $J(\tilde{\nu})$ (i.e., Equation 2.14). Defining the incoming intensity at L=0 as $I_0(\tilde{\nu})$, Equation 2.17 can be integrated across distance L to get the intensity at that point, $I(\tilde{\nu}, L)$:

$$I(\tilde{\nu}, L) = I_0(\tilde{\nu})\exp\left(-\int_0^L \sigma(\tilde{\nu})\rho dL\right). \tag{2.18}$$

Assuming that $\sigma(\tilde{\nu})$ is constant over distance L, Equation 2.18 can be further simplified to Equation 2.19, known as the Beer-Bouguer-Lambert Law, where u represents the mass-weighted path (Liou, 2002):

$$I(\tilde{\nu}, L) = I_0(\tilde{\nu})\exp\left(-\sigma(\tilde{\nu})\int_0^L \rho dL\right) = I_0(\tilde{\nu})\,\mathrm{e}^{-\sigma(\tilde{\nu})u}\ . \tag{2.19}$$

The transmissivity at a given wavenumber ($T(\tilde{\nu})$) is then the ratio of the transmitted to the incident intensity:

$$T(\tilde{\nu}) = \frac{I(\tilde{\nu})}{I_0(\tilde{\nu})} = \exp^{-\sigma(\tilde{\nu})u}. \tag{2.20}$$

The absorptivity is the fraction of incident radiation that has been absorbed, and is therefore the outstanding fraction removed from the incident intensity:

$$A(\tilde{\nu}) = 1 - T(\tilde{\nu}) = 1 - \exp^{-\sigma(\tilde{\nu})u}. \tag{2.21}$$

The principles and formulations outlined in this section serve as the foundation for the line-by-line radiative transfer model employed in the SFIT4 program to derive trace gas columns and profiles (Notholt et al., 2006). The algorithm divides a simulated atmosphere into several layers (48 for TAO); using a Voigt line shape the individual absorption contributions in each layer along the path are summed. Through multiple iterations the modelled spectrum is adjusted to fit the observed spectrum by adjusting the vertical profile of the trace gas of interest; further details on SFIT4 are provided in Section 2.3.

2.2 Fourier Transform Spectroscopy

Fourier transform spectroscopy uses a Fourier transform to create a spectrum from an interferogram. The FTIRs used in this work operate based on the principles of the Michelson interferometer (Michelson, 1881); a schematic of the basic Michelson interferometer is shown in Figure 2.2. The key mechanism of the device, and the subsequent mathematical procedures, relies on splitting a beam of radiation into two using a 50:50 beamsplitter, which creates a variation of optical path for each beam that results in an interference pattern upon recombination. Within the two paths travelled, the beam is reflected by either a stationary mirror or a movable (scan) mirror. The varying beam intensity that is recorded by the detector is a function of the optical path difference (OPD) (Griffiths and De Haseth, 2007).

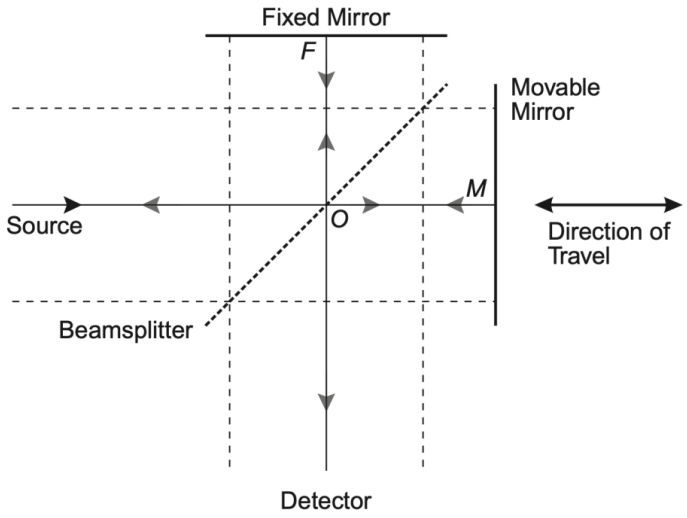

Figure 2.2: Schematic of the Michelson interferometer: the median ray is shown by the solid lines and the extremes of the collimated beam are shown by the dashed lines (Griffiths and De Haseth, 2007).

For a monochromatic beam, where $\tilde{\nu}_0 = 1/\lambda_0$, with an ideal beamsplitter and constantly moving scan mirror, the detector measures an intensity that is in and out of phase with the stationary mirror's beam, with maxima at integers of the incoming light's wavelength (λ_0) in the form of a sine wave (Griffiths and De Haseth, 2007). At zero path difference, when the two mirrors are positioned at equal distances from the beamsplitter, the beams recombine in-phase with each other, interfering constructively, such that the intensity of the beam on the detector is the sum of both beams. The same constructive interference occurs when the moveable mirror is at $\frac{1}{2}\lambda_0$, creating an OPD of λ_0. Conversely, when the scan mirror is at a distance of $\frac{1}{4}\lambda_0$, the beams recombine with

a phase shift of $\frac{1}{2}\lambda_0$, resulting in destructive interference. Equation 2.22 is used to calculate the intensity of the interference record as a function of the OPD ($I'(\delta)$), where $I(\tilde{v}_0)$ is the intensity of the source, and δ=nλ, and n is an integer:

$$I'(\delta) = \frac{1}{2} I(\tilde{v}_0)[1 + \cos(2\pi\tilde{v}_0\delta)]. \quad (2.22)$$

In practice, the constant terms are dropped and the interferogram corresponds to the varying component (the cosine term). The equation of the interferogram for a monochromatic source can then be written as Equation 2.23. B corresponds to the wavenumber-dependent spectral intensity, based on instrument characteristics it accounts for beamsplitter efficiency, detector response and amplifier characteristic (Griffiths and De Haseth, 2007):

$$I(\delta) = \frac{1}{2} B(\tilde{v}_0)\cos(2\pi\tilde{v}_0\delta)\,. \quad (2.23)$$

To account for a continuum source, such as the sun, Equation 2.23 is integrated across all wavenumbers:

$$I(\delta) = \frac{1}{2}\int_0^\infty B(\tilde{v})\cos(2\pi\tilde{v}x)\,d\tilde{v}\,. \quad (2.24)$$

A spectrum is obtained by applying a Fourier transform to the interferogram (Equation 2.24), which can then be used to derive concentrations of trace gases, as described in Section 2.3:

$$B(\tilde{v}) = 2\int_0^\infty I(x)\cos(2\pi\tilde{v}x)\,dx\,. \quad (2.25)$$

The integral in the Fourier transform ranges from x=0 to infinity, while in reality this is limited by the maximum optical path difference (x_{max}), which can be represented by a boxcar apodization function that is 1 for $x < x_{max}$, and 0 for $x \geq x_{max}$, The convolution of the interferogram and boxcar function after the Fourier transform results in a sinc function, dependent on x_{max}. The FWHM of the sinc function can be used to define the spectral resolution, such that the resolution is $0.605/x_{max}$ (Griffiths and De Haseth, 2007). However, other apodization functions can be applied to reduce the side lobes of the sinc function, with different functions offering trade-offs with the spectral

resolution. The nominal resolution is defined as $1/x_{max}$, so the 250 cm maximum OPD at TAO results in a maximum spectral resolution of 0.004 cm^{-1}, although some manufacturers may define their resolution differently (e.g., Bruker uses $0.9/x_{max}$).

FTIR spectroscopy offers several advantages over dispersive grating spectrometers, making it well-suited for atmospheric trace gas measurements; these are summarized as follows (Griffiths and De Haseth, 2007):

1. The Fellgett or multiplex advantage – the capability of measuring all wavelengths simultaneously using an interferometer (Fellgett, 1951). This allows quicker measurements as the entire range of interest can be measured in a single scan, and multiple scans can be combined to reduce random noise.
2. The Jacquinot or throughput advantage – high optical throughput of the circular aperture of the spectrometer ensures more light reaches the detector, improving the signal-to-noise ratio (Jacquinot and Dufour, 1948).
3. The Connes or wavenumber precision advantage – wavenumber calibration is determined precisely with an internal laser, of known wavelength and zero path difference as reference (Connes and Connes, 1966).

2.3 Trace Gas Retrievals

The TAO and CARE FTIR solar absorption infrared spectra used in this work are converted into trace gas profiles and columns using the SFIT4 algorithm (accessible at: https://wiki.ucar.edu/display/sfit4/), through a process called a retrieval. The program was released in 2014, building upon the SFIT2 program used by the NDACC IRWG, and continues to be updated to work towards improving retrievals and harmonizing them across the network (Pougatchev et al., 1995; IRWG, 2020). An estimate of the true state of the atmosphere, based on the measurements, is used to create a volume mixing ratio (VMR) profile of the gas of interest (note: this is the "NDACC convention" of VMR, technically it is the mole fraction, which is the moles of the gas of interest/all gases, while VMR is the volume of the gas of interest/sum of *other* gases, however, for small quantities these can be considered equivalent). The retrieval technique for most gases is based on optimal estimation, an inverse method whereby the model iteratively estimates the true state, explained further in the following section. Some of gases are retrieved using a Tikhonov regularization, which is outlined in Section 2.3.2.

2.3.1 Optimal Estimation

The optimal estimation method (OEM) is used to relate the absorption spectra measurements made by the FTIR to the most probable state of the atmosphere, and in turn derive vertical profile information of trace gases. Because the retrieval is an ill-posed problem, the model requires a priori information to solve the inverse problem. The concept of optimal estimation as it relates to solving an inverse atmospheric sounding problem is outlined in this current section; further details can be found in Rodgers (2000), and the theses of Wiacek (2006) and Taylor (2008).

The measurement vector, **y** (observed spectrum), is related to the state of the atmosphere through a forward model (**F**), encompassing the state vector, **x** (vertical profile of the gas of interest), additional model variables that the measurement is dependent on, **b** (i.e., profiles of temperature and pressure) and measurement errors (**ε**) (Equation 2.26):

$$\mathbf{y} = \mathbf{F}(\mathbf{x}, \mathbf{b}) + \boldsymbol{\varepsilon} \,. \tag{2.26}$$

The forward model simulates a spectrum using information about the physics of the measurement and the state of the atmosphere. To obtain an estimate of the atmospheric state ($\hat{\mathbf{x}}$), the forward model is inverted (**R**) to map the measurement state space into the atmospheric state space, where **c** is used to account for all retrieval method parameters that do not appear in the forward model that are needed for the inverse calculation (for example convergence criterion):

$$\hat{\mathbf{x}} = \mathbf{R}(\mathbf{y}, \mathbf{b}, \mathbf{x}, \mathbf{c}) = \mathbf{R}(\mathbf{F}(\mathbf{x}, \mathbf{b}) + \varepsilon, \mathbf{b}, \mathbf{x}, \mathbf{c}) \,. \tag{2.27}$$

The vector $\mathbf{x}_a$ represents the a priori estimate of **x**, and $\hat{\mathbf{b}}$ is the best estimate of the forward model parameters. Here, the a priori is a profile of the initial estimate of the true state. Equation 2.27 is expanded about $\mathbf{x}_a$, under the assumption that **F** and **R** are linear in the range of the a priori and true state space:

$$\hat{\mathbf{x}} = \mathbf{R}\left(\mathbf{F}\left(\mathbf{x_a}, \hat{\mathbf{b}}\right) + \mathbf{K}(\mathbf{x} - \mathbf{x_a}) + \mathbf{K}_\mathrm{b}\left(\mathbf{b} - \hat{\mathbf{b}}\right) + \varepsilon, \hat{\mathbf{b}}, \hat{\mathbf{x}}, \mathbf{c}\right) . \tag{2.28}$$

K is the weighting function matrix, which corresponds to the sensitivity of the forward model with respect to the atmospheric state (Equation 2.29), and $\mathbf{K}_\mathrm{b}$ is the parameter space weighting function, matrix which corresponds to the sensitivity of the forward model to ancillary model parameters (Equation 2.30):

$$\mathbf{K} = \frac{\partial \mathbf{F}}{\partial \mathbf{x}} \tag{2.29}$$

$$\mathbf{K}_{\mathrm{b}} = \frac{\partial \mathbf{F}}{\partial \mathbf{b}} \ . \tag{2.30}$$

An additional Taylor expansion is applied to Equation 2.28 around $\mathbf{x}_a$ to give Equation 2.31, where $\boldsymbol{\varepsilon}_{\mathbf{x}}$ is the combined error term from the model parameter error, forward model error, and retrieval noise:

$$\hat{\mathbf{x}} = \mathbf{x_a} + \mathbf{GK}(\mathbf{x} - \mathbf{x_a}) + \mathbf{GK}_{\mathrm{b}}\left(\mathbf{b} - \hat{\mathbf{b}}\right) + \mathbf{G}_{\boldsymbol{\varepsilon}} = \mathbf{x_a} + \mathbf{A}(\mathbf{x} - \mathbf{x_a}) + \boldsymbol{\varepsilon}_{\mathrm{x}} \ . \tag{2.31}$$

A gain matrix, **G**, is defined as the partial derivative of the inverse function with respect to the measurement, indicating the sensitivity of the retrieved state to the measurements:

$$\mathbf{G} = \frac{\partial \mathbf{R}}{\partial \mathbf{y}} \ . \tag{2.32}$$

The averaging kernel (AVK), **A**, is the product of the weighting function and gain matrix, which results in a partial derivative corresponding to the relationship between the retrieved state and the true atmospheric state:

$$\mathbf{A} = \mathbf{GK} = \frac{\partial \mathbf{R}}{\partial \mathbf{y}} \cdot \frac{\partial \mathbf{F}}{\partial \mathbf{x}} = \frac{\partial \hat{\mathbf{x}}}{\partial \mathbf{x}} \ . \tag{2.33}$$

The AVK is a square matrix, with dimensions equal to those of the state vector, here corresponding to the number of atmospheric layers defined at each site. The diagonal elements of **A** indicate the retrieval sensitivity at the respective atmospheric layer versus the a priori profile. The off-diagonal elements correspond to the correlation between layers, because the model is unable to resolve the true state at all layers independently. In an ideal case, the **A** matrix would be an identity matrix, where each layer is only sensitive to the atmosphere at that particular layer and is not influenced by adjacent layers or dependent on the a priori. The rows are smoothing functions, which when summed, indicate the fraction of information that is coming from the measurement itself and represents the sensitivity of the retrieval for each level (Vigouroux et al., 2009). The trace of the AVK matrix is termed the degrees of freedom for signal (DOFS) and denotes the number of independent pieces of information coming from the retrieval.

Equation 2.31 shows that the best estimate of the atmospheric state will represent a combination of information from the a priori profile and the measurement. To get to this solution, there must be an assessment of the error term $\boldsymbol{\varepsilon_x}$, which is not directly observable, but can be estimated statistically. Here, a Bayesian approach using a probability density function (PDF) for $\boldsymbol{\varepsilon_x}$ is applied. Following Bayes' Theorem, the probability of some event **x**, given the condition of **y**, is equal to the probability of **y** given **x**, multiplied by the ratio of the probability of **x** and the probability of **y**:

$$\mathrm{P}(\mathbf{x}|\mathbf{y}) = \mathrm{P}(\mathbf{y}|\mathbf{x})\frac{\mathrm{P}(\mathbf{x})}{\mathrm{P}(\mathbf{y})}. \tag{2.34}$$

Here, $\mathrm{P}(\mathbf{y}|\mathbf{x})$ is dependent on the forward model and measurement errors, $\mathrm{P}(\mathbf{x})$ is the probability of **x** based on prior knowledge, and $\mathrm{P}(\mathbf{y})$ is the probability of obtaining **y**. The theory aims to maximize the posterior probability ($\mathrm{P}(\mathbf{x}|\mathbf{y})$) with a solution for **x** that is weighted by both the a priori profile and measurement. Using this, the assumption that the relationship between **x** and **y** is linear and the error probabilities are normally distributed (Gaussian), P(**x**), P(**y**), and P(**y**|**x**) can then be written as Equation 2.35 to 2.37, respectively:

$$-2\ln\left[\mathrm{P}(\mathbf{x})\right] = (\mathbf{x}-\mathbf{x_a})^{\mathrm{T}}\mathbf{S}_{\mathrm{a}}^{-1}(\mathbf{x}-\mathbf{x_a}) + \mathrm{C_x} \tag{2.35}$$

$$-2\ln\left[\mathrm{P}(\mathbf{y})\right] = (\mathbf{y}-\overline{\mathbf{y}})^{\mathrm{T}}\mathbf{S}_{\mathrm{y}}^{-1}(\mathbf{y}-\overline{\mathbf{y}}) + \mathrm{C_y} \tag{2.36}$$

$$-2\ln[\mathrm{P}(\mathbf{y}|\mathbf{x})] = [\mathbf{y}-\mathbf{F}(\mathbf{x},\mathbf{b})]^{\mathrm{T}}\mathbf{S}_{\varepsilon}^{-1}[\mathbf{y}-\mathbf{F}(\mathbf{x},\mathbf{b})] + \mathrm{C_{yx}}\,, \tag{2.37}$$

where $\overline{\mathbf{y}}$ is the observation mean and $\mathbf{S_y}$ is the measurement error covariance matrix (in practice P(**y**) is omitted as it is deemed a normalizing factor), and the C terms represent a simplified constant term (Rodgers, 2000). Now these equations can be input into the Bayes' Equation (2.34) to create a cost function ($\mathbf{J}(\mathbf{x})_{\mathrm{cost}}$) which considers the deviations between the measurements (**y**) and forward model predictions, weighted with the uncertainties in the observations ($\mathbf{S_\varepsilon}$) and the deviations between the true state **x** and a priori $\mathbf{x_a}$, weighted by the uncertainty in the a priori estimate ($\mathbf{S_a}$):

$$\mathbf{J}(\mathbf{x})_{\mathrm{cost}} = [\mathbf{y}-\mathbf{F}(\mathbf{x},\mathbf{b})]^{\mathrm{T}}\mathbf{S}_{\varepsilon}^{-1}[\mathbf{y}-\mathbf{F}(\mathbf{x},\mathbf{b})] + (\mathbf{x}-\mathbf{x_a})^{\mathrm{T}}\mathbf{S}_{\mathrm{a}}^{-1}(\mathbf{x}-\mathbf{x_a})\,. \tag{2.38}$$

$\boldsymbol{S_\varepsilon}$ is the error covariance matrix, which comes from the observation error, and $\boldsymbol{S_a}$ is the a priori covariance matrix, representing the error associated with the a priori, and should capture the natural variability of the species. To maximize the posterior probability, the cost function should be at a minimum ($\nabla_x \mathbf{J}(x) = 0$), which is done iteratively using the Gauss-Newton method:

$$\mathbf{x_{i+1}} = \mathbf{x_i} - [\nabla_x \nabla_x \mathbf{J}(\mathbf{x}_i)]^{-1} \nabla_{x_i} \mathbf{J}(\mathbf{x}_i)\,. \tag{2.39}$$

In the form of Equation 2.31, the optimal solution will appear as:

$$\hat{\mathbf{x}}_{\mathbf{i+1}} = \mathbf{x_a} + (\mathbf{S}_a^{-1} + \mathbf{K}_i^T \mathbf{S}_\varepsilon^{-1} \mathbf{K}_i)^{-1} \mathbf{K}_i^T \mathbf{S}_\varepsilon^{-1} [(\mathbf{y} - \mathbf{y_i}) - \mathbf{K}_i(\mathbf{x_a} - \hat{\mathbf{x}}_\mathbf{i})]\,, \tag{2.40}$$

where $\mathbf{K}_i = \nabla_x \mathbf{F}(\mathbf{x}_i)$, $\mathbf{y}_i = \mathbf{F}(\mathbf{x}_i)$ from the previous iteration's estimate. In the SFIT4 program, the initial guess at i=0 will represent the a priori $\mathbf{x_a}$, and the iterations aim to reach a criterion set in the sfit.ctl files as either as "rt.convergence" (usually 0.1) achieved when the chi-squared (χ^2) is less than the predefined value, or as "rt.tolerence" (typically 0.2) which is reached when the iterative change in the spectrum is smaller than the product of the SNR and the tolerance value. If the criterion is not met within 17 iterations, the program terminates that retrieval and moves to the next measurement. Further details of the program are provided in Section 2.4.

2.3.2 Tikhonov Regularization

An alternative method to OEM for solving the inverse problem is Tikhonov regularization, that is particularly useful in cases where the a priori profile of the species is not well known (Tikhonov, 1963; Sussmann et al., 2011). This approach minimizes the difference between the measurement **y** and the forward model **F** of the true state **x** (**y**=**F(x)**=**Kx**). To estimate the true state, the distance is minimized between **F(x)** and **y** (Euclidean norm), with the addition of a regularization term (**Γ**), written as:

$$||\mathbf{Fx} - \mathbf{y}||^2 + ||\mathbf{\Gamma x}||^2\,. \tag{2.41}$$

The best estimate of the atmosphere using this method is represented as:

$$\hat{\mathbf{x}} = (\mathbf{K}^T\mathbf{K} + \mathbf{\Gamma}^T\mathbf{\Gamma})^{-1}\mathbf{\Gamma}^T\mathbf{y}\,. \tag{2.42}$$

The regularization matrix reduces oscillating profiles by giving preference to a particular solution,

based on a DOFS scaling factor α, and a discrete first derivative operator ($\mathbf{L_1}$) which constrains the retrievals to a constant profile for the difference ($\mathbf{x}$–$\mathbf{x_a}$):

$$\mathbf{\Gamma} = \alpha \mathbf{L}_1^{\mathrm{T}} \mathbf{L}_1 \, . \tag{2.43}$$

The choice of the regularization parameter (α or sometimes λ) is a fine balance between spectral noise and information content. If the value is too high, the retrieval will have low DOFS and be constrained to the a priori, while if the value is too low, the retrieval will have higher DOFS but be under-constrained and fit the noise. The regularization matrix can be equated to the inverse model (with *n* layers) as $\mathbf{R} = \in \boldsymbol{\mathcal{R}^{nxn}}$, allowing for an equivalent expression to Equation 2.40 for Tikhonov regularization to be written as (Sussman et al., 2011):

$$\hat{\mathbf{x}}_{\mathbf{i+1}} = \mathbf{x_i} + (\mathbf{K}_\mathbf{i}^{\mathrm{T}} \mathbf{S}_\varepsilon^{-1} \mathbf{K_i} + \mathbf{\Gamma})^{-1} \mathbf{K}_\mathbf{i}^{\mathrm{T}} \mathbf{S}_\varepsilon^{-1} [(\mathbf{y} - \mathbf{y_i}) - \mathbf{\Gamma}(\mathbf{x_i} - \mathbf{x_a})] \, . \tag{2.44}$$

2.4 NDACC – IRWG

NDACC is composed of more than 80 stations across the globe, 25 of which have a mid-infrared FTIR instrument (see Figure 2.3). NDACC aims to provide a long-term database of high-quality atmospheric composition measurements to assess the links between climate, air quality, and composition, and as a resource for other atmospheric investigations such as satellite validation and model development (De Mazière et al., 2018). There are both instrument working groups and theory and analysis working groups to oversee instrument and algorithm quality and promote the use of the data. The TAO and PEARL FTIR instruments are members of the IRWG and follow specific guidelines as such. The CARE FTIR instrument is not (yet) a member but is set up similarly to TAO and therefore follows the same procedures.

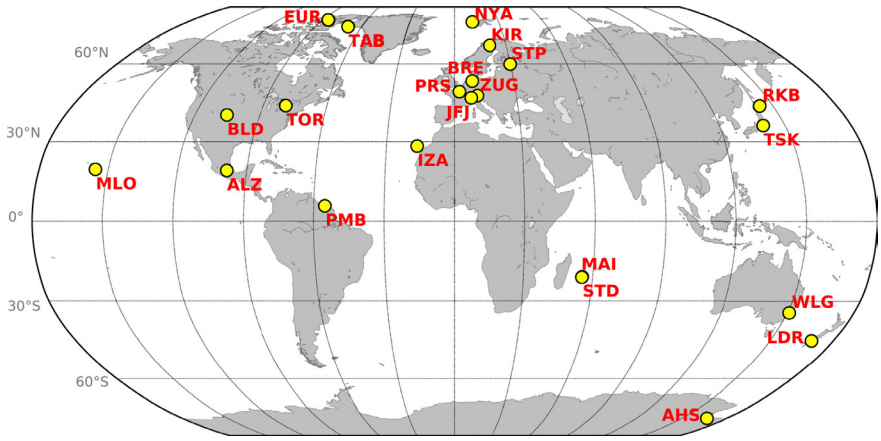

Figure 2.3: Map of NDACC-IRWG FTIR stations from Hannigan et al. (2022).

The instruments record high-resolution solar absorption spectra under day-light clear-sky conditions. These FTIR spectrometers use a series of optical filters mounted in a filter wheel to limit the spectral range of sunlight which enters the instrument; this helps reduce photon shot noise from fluctuations in the number of detected photons (Bell, 1972). The IRWG has standard filters that each instrument iteratively rotates through during the day; these are listed for TAO (and CARE) and PEARL in Table 2.1.

Table 2.1: NDACC IRWG filter numbers and spectral ranges for TAO/CARE and PEARL.

NDACC Filter Number	Approximate Range [cm^{-1}]	
	TAO / CARE	PEARL
1	4000 - 4300	3950 - 4300
2	2900 - 3500	2700 - 3600
3	2400 - 3100	2400 - 3100
4	2000 - 2700	1900 - 2700
5	1500 - 2200	1800 - 2200
6	750 - 1300	650 - 1400
7	-	600 - 1050

2.4.1 SFIT4

As part of the SFIT4 program set-up, several inputs are needed to run the forward model used in the retrieval process. In SFIT4 v0.9.4.4, a priori profiles are calculated based on the 1980-2020 mean profile from the Whole Atmosphere Community Climate Model (WACCM) v4 (Marsh et al., 2013), and temperature and pressure profiles are from the U.S. National Centers for Environmental Prediction (NCEP) (Kalnay et al., 1996). The retrieval of each gas uses small portions of the spectrum called microwindows that contain spectral lines of interest, as well as lines of interfering species that must be considered. The spectroscopic absorption parameters used are from HIT08 (Rothman et al., 2009). A transition to SFIT4 version 1.0+ is underway; WACCM has been updated to include years from 1980-2040 (v6), and line lists are being upgraded with HIT16 (Rothman et al., 2013), HIT20 (Gordon et al., 2022), and ATM2020 (Toon, 2022), depending on the species. Specialized working groups are testing the best combination of the line lists for optimized harmonization across the network, and the update for the ozone retrieval is outlined in Section 3.3.

The SFIT4 program creates a model atmosphere using the forward model for the defined microwindows with the input of the a priori profile, meteorological information, and spectroscopic line parameters. SFIT4 uses a Voigt line shape and assumes each atmospheric layer is homogenous

and in a state of local thermodynamic equilibrium. The VMR profile of the target gas is adjusted iteratively to reduce the difference between the observed and calculated spectrum. When the value between iterations meets the convergence criterion, the retrieval is complete; if this is not achieved within 17 iterations, the retrieval has not reached convergence and is incomplete. The measurement error covariance matrix ($\mathbf{S_\varepsilon}$) is derived from the SNR of the spectrum as:

$$\mathbf{S_\varepsilon} = \frac{\mathbf{I}}{\mathrm{SNR}^2} \,. \tag{2.45}$$

The a priori covariance matrix, $\mathbf{S_a}$, is input in the user files for each species, and can be used as a tuning parameter to reduce oscillations in the retrieved profiles. It should represent the variability of the species, and is usually a diagonal matrix:

$$\mathbf{S_a} = \mathbf{I}\sigma^2 \,, \tag{2.46}$$

where σ is the expected deviation from the a priori profile, as a percentage. This is often the standard deviation of the mean WACCM profiles. In the Tikhonov approach, the $\mathbf{S_a}$ matrix is replaced by the $\mathbf{L_1}$ regularization matrix. An inter-layer correlation (ILC) may be set to reduce oscillations in retrieved profiles by defining a length at which adjacent layers are correlated. This defines the corresponding off-diagonal elements of the $\mathbf{S_a}$ matrix, where W is the correlation width and z_i is the altitude:

$$\mathbf{S_{a,ij}} = \mathbf{S_{a,ii}} e^{-\frac{|z_i - z_j|}{W}} \,. \tag{2.47}$$

The $\mathbf{S_a}$ and ILC for all of the TAO species are listed in Table 3.1 in Chapter 3.

Once trace gas profiles and columns are calculated, essential considerations for the data utilization and publication process are quality control and uncertainty analysis. Quality control involves manually identifying and removing measurements that, despite completing the retrieval process, exhibit poor statistical reliability. Uncertainty values, on the other hand, provide a means to weigh confidence in the results, enabling a quantitative evaluation of their accuracy and reliability. These steps ensure that the final dataset uploaded to the NDACC DHF is a high-quality, transparent product, providing confidence in its use for scientific research and atmospheric monitoring.

The following paragraph will briefly detail the SFIT4 uncertainty variables; refer to Wiacek (2006) for a comprehensive overview of the retrieval error analysis for the TAO FTIR spectrometer. SFIT4 performs error analysis calculations based on the methodology of Rodgers (2000), and is partitioned into two categories, systematic ($\mathbf{S}_{sys}$) and random ($\mathbf{S}_{ran}$). The systematic uncertainty includes errors from spectral line parameters (intensity, broadening), $\mathbf{S}_{line}$, and temperature, $\mathbf{S}_{temp\_sys}$. The random uncertainty includes errors from the measurement, $\mathbf{S}_{meas}$, solar zenith angle (SZA), $\mathbf{S}_{SZA}$, interference, $\mathbf{S}_{intspect}$, retrieval parameters (wavelength shift, instrument line shape, background slope, phase error), $\mathbf{S}_{retparam}$, and temperature, $\mathbf{S}_{temp\_rand}$. Temperature errors are derived from comparisons of radiosonde data from the Buffalo Niagara International Airport (42.56°N, 78.44°W, 215 masl), approximately 145 km away (closest available), and the Toronto NCEP daily temperature profiles for 2010. Up to 30 km $\mathbf{S}_{temp\_sys}$ is the average difference and $\mathbf{S}_{temp\_rand}$ is the standard deviation, and above that, the mean value of $\mathbf{S}_{temp\_sys}$ is used, and the mean NCEP error is used for $\mathbf{S}_{temp\_rand}$. If available, $\mathbf{S}_{line}$ are taken from the HITRAN database, and if not, they are set at 20%. For TAO, the average change in SZA over a 10-minute scan period is taken as 0.43° and used for $\mathbf{S}_{SZA}$. The total error is obtained by taking the square root of the sum of squares of the terms outline above, written as "$\mathbf{S}_{sys}$" and "$\mathbf{S}_{ran}$" in Equation 2.47; the time-series average, $\mathbf{S}_{total}$, for each TAO species is shown in Table 3.2 in Chapter 3:

$$S_{total} = \sqrt{S_{sys}^2 + S_{rand}^2}\,. \tag{2.47}$$

In SFIT4 v.0.9.4.4, each species has an RMS/DOFS ratio, which filters out measurements with high root-mean-square (RMS) fitting residual, usually meaning a poor fit likely with low SNR, and/or lower than normal DOFS, indicating poor data quality. In the updated SFIT v1.0+, there is a setting to input a range of acceptable RMS and DOFS, which acts to replace the RMS/DOFS filter. Further outliers that make it through the filtering are assessed based on their individual spectral fits.

2.4.2 TAO

The FTIR spectrometer at the University of Toronto Atmospheric Observatory in downtown Toronto (43.66°N, 79.4°W, 174 masl) has been operating since 2002, and is one of the early urban sites in the NDACC IRWG. The instrument is located on the 16th floor of the Burton Tower in the McLennan Physical Laboratories Building (left panel of Figure 2.4), where the sun is directed with

an altitude-azimuth sun-tracker on the roof (middle panel of Figure 2.4.), and through a series of mirrors reaches the instrument (right panel of Figure 2.4). For a comprehensive description of the TAO installation, calibration, and initial development, refer to Wiacek (2006), and subsequent TAO overviews can be found in Taylor (2008), Whaley (2014), and Yamanouchi (2021). The data are submitted to both the NDACC DHF and the CAMS RD system. The standard IRWG gases that are archived on the NDACC DHF are C_2H_6, CH_4, CO, HCl, HCN, HF, HNO_3, N_2O, and O_3, along with research products C_2H_2, CH_3OH, CHF_2Cl, HCOOH, H_2CO, NH_3, and OCS. Chapter 3 provides further details of the TAO retrievals, including plots of the a priori profiles, AVKS, mean retrieved profiles, and column time series.

Figure 2.4: Images of the TAO set-up. Left: Burton Tower of the McLennan Physical Laboratories Building where TAO is located, Middle: Roof of the Burton Tower, with the sun-tracker cover open and the fixed heliostat mirror visible. Right: Inside the TAO laboratory where the solar beam is coming through the roof entry and being directed into the DA8.

The instrument is an ABB Bomem DA8 spectrometer, which uses a dynamic alignment on the moving mirror, and is the last of its type in NDACC. A schematic of the instrument is depicted in Figure 2.5. The solar beam that is directed from outside into the lab is passes through one of the six filters in the filter wheel (ranges listed in Table 2.1) and passes through an external aperture ("Emission Port / Iris" in Figure 2.5). The light is directed by a folding mirror (first mirror after input) through a potassium bromide (KBr) beamsplitter, which allows for a range of approximately 650 to 6600 cm^{-1} to be observed. The partitioned beam then travels either to the fixed mirror or the scan mirror with a maximum OPD of 250 cm, which, as discussed in Section 2.2, gives a

spectral resolution of 0.004 cm^{-1}. The DA8 scan mirror moves at 1.0 cm/s and completes four scans per measurement, lasting approximately 15 minutes total. There are two detectors that cover the spectral range of the six filters; the Indium Antimonide (InSb) detector covers approximately 1500-5000 cm^{-1} and the Mercury Cadmium Telluride (MCT or HgCdTe) detector covers 700-4500 cm^{-1}.

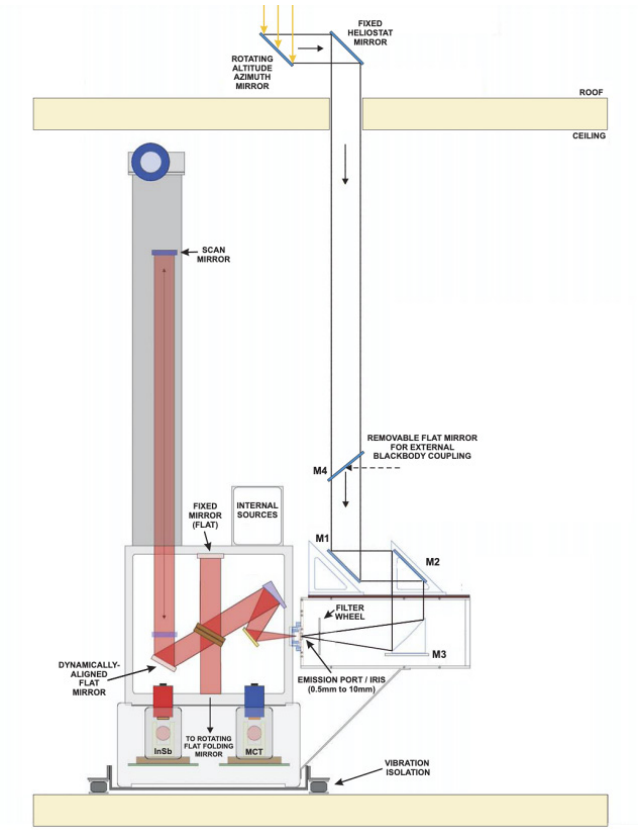

Figure 2.5: Schematic of TAO DA8 FTIR spectrometer from Wiacek (2006).

Operations are semi-automated: they require personnel to start up and shut down each day, but run continuously between with an automated sun-tracker in a housing that closes upon the detection of precipitation. The sun-tracker and housing were manufactured by AIM Controls Inc., California, USA, with tracking provided by two stepper motors on elevation and azimuth axes. The system originally used four photo-diodes for active tracking; this was upgraded to a camera and solar-disk-fitting system in September 2014 similar to that described by Franklin (2015), which provides a pointing accuracy of around 30 arcseconds (Yamanouchi, 2021). Improvements to the measurement automation were made when the cover was wired to a relay board (March 2015) and Norhof LN_2 autofill dewars were installed (June 2021); these changes allowed for remote operations and increased the number of measurement days per year (see Figure 2.6 for a bar chart

of the number of measurement days across the entire time series). Personnel are required on site to fill the liquid nitrogen dewars (approximately every two weeks), and on occasion for troubleshooting.

Recent TAO maintenance adjustments that were implemented during the last four years include:

- August 2021: KBr beamsplitter rotated in its housing to maximize signal.
- November 2021: DA8 folding mirror adjusted to improve instrument line shape (ILS).
- November 2022: Scan motor replaced due to DA8 alignment scan motor intermittent fault in March 2022.
- September 2022: Z10 resistor on MCT preamplifier gain circuitry adjusted from 10 kOhm to 30 kOhm to increase gain.
- September 2022: TAO filter wheel replaced, as the old filter wheel started to rotate to the wrong filter.
- November 2024: Folding mirror realigned using laser retroreflector to improve ILS.

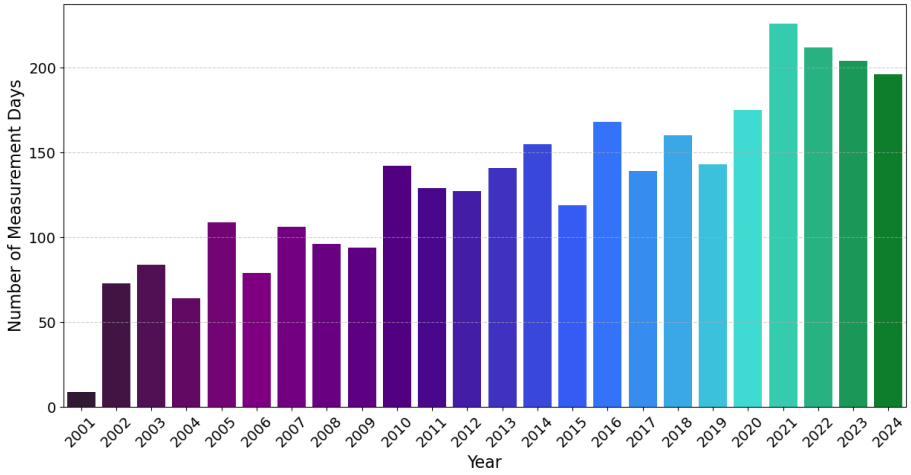

Figure 2.6: Measurement days for the TAO FTIR spectrometer by year from 2001-2024.

The ILS is monitored to assess the alignment and performance of the FTIR. This is done at TAO using an external mid-infrared globar as a source to measure an HBr or N_2O gas cell of a known quantity, analyzed with the LINEFIT v14.5 software package (Hase, 2012). This program retrieves a theoretical ILS, modulation efficiency, phase error, and HBr (or N_2O) column concentration from the cell spectra. As described in Section 2.2, the TAO line shape is a sinc function; if the instrument is properly aligned, this will be symmetric. The modulation efficiency shows the signal intensity as a function of OPD and should ideally be close to 1 along the entire optical path; if it is varying substantially the instrument needs to be realigned. The phase error depicts the asymmetry of the line shape, and if it is not close to 0, the interferometer mirrors are not aligned. A LINEFIT analysis

output for December 18, 2024, is shown in Figure 2.5; the ILS is on the left, the modulation efficiency for several runs from 2019-2024 is in the top right, and the phase error for the same runs is on the bottom right.

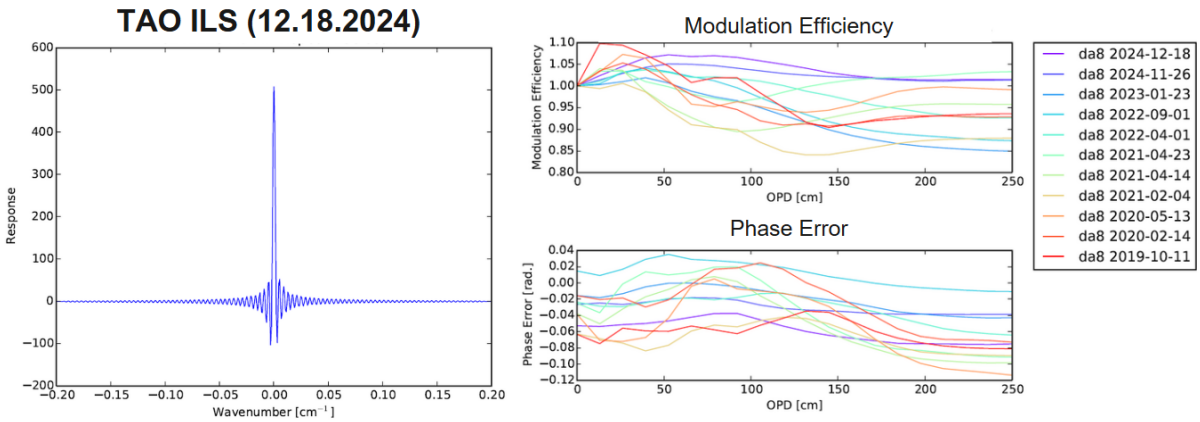

Figure 2.7: LINEFIT output for the TAO FTIR spectrometer. Left panel shows the ILS results from an HBr spectrum recorded on December 18, 2024. Right top panel shows the modulation efficiency and bottom right panel shows phase error, both as a function of OPD for runs with HBr cell #48 from 2019-2024.

2.4.3 CARE

The FTIR located at ECCC's Centre for Atmospheric Research Experiments in Egbert (44.23°N, 79.78°W, 251 masl) is an ABB Bomem DA8 similar to that at TAO, however it is an older model that uses the fixed mirror for dynamic alignment. The instrument has the same maximum OPD, spectral resolution, and filters as TAO. ECCC installed the instrument and began operations in 1996, measuring intermittently until 2010. After a period of downtime, followed by upgrades (including a new Bruker sun-tracker and SIL cover) and maintenance by the Strong Group, particularly by Research Officer Orfeo Colebatch, routine operation began in April 2023. CARE is located in a rural area approximately 70 km north-west of TAO, and while it undergoes similar long-range transport to TAO, it has differing localized emissions (Whaley et al., 2013). Whaley et al. (2013) estimated that with an average wind speed above 3 km altitude of 12.6 m/s, an air parcel would travel between the two sites in under 2 hours, and as such they can be treated as complementary measurement sites. Similar to TAO, operations can be run remotely with occasional on-site visits. Figure 2.8 shows photographs from the CARE facility; the left panel shows the sun-tracker cover open on the roof of the building, the middle panel shows the lab with

the DA8 and LN_2 dewars, and the right panel shows the inside of the DA8 with the panel off. The CARE FTIR has yet to be certified as an NDACC instrument, although its operation and retrievals are following standard NDACC-IRWG protocols, and the long-term plan is to pursue formal certification for membership.

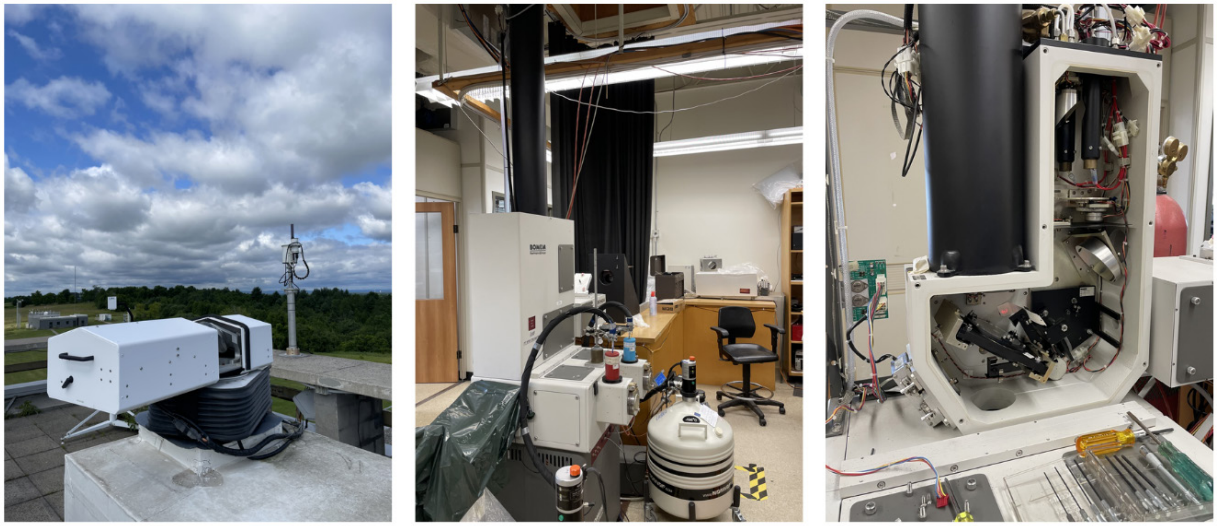

Figure 2.8: Images from the CARE facility. Left: Bruker sun-tracker and SIL housing open on the roof. Middle: FTIR laboratory with DA8 and Norhof LN_2 dewar visible. Right: DA8 cover open to show the interferometer and source compartments.

The timeline for major upgrades and maintenance of the CARE FTIR spectrometer includes:

- July 2019: DA8 emission input optics aligned.
- January 2019: Bruker A547N sun-tracker aligned and SIL sun-tracker cover installed.
- January 2020: Norhof LN_2 autofill dewars installed on the InSb and MCT detectors.
- April 2023: Regular measurements began.
- December 2023: Vacuum pump replaced with an Agilent IDP-15.

The ILS is monitored with the same procedure as described for TAO, using LINEFIT on HBr cell measurements with an external mid-infrared globar. The output for an ILS measurement taken on August 18, 2023 is shown in the left panel of Figure 2.9, the modulation efficiency for several runs from 2022-2023 is in the top right, and the corresponding phase errors are on the bottom right.

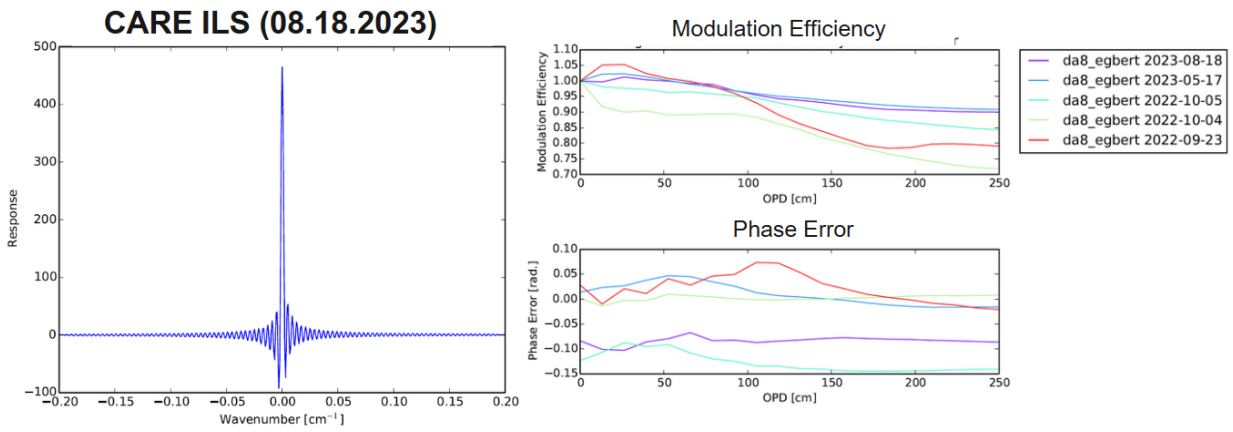

Figure 2.9: LINEFIT output for the CARE FTIR spectrometer. Left panel shows the ILS result from August 18, 2023. Right top panel shows the modulation efficiency and bottom right panel shows phase error, both as a function of OPD for runs with HBr cell #49 from 2022-2023.

2.4.4 PEARL

The FTIR at PEARL in Eureka, Nunavut (80.05° N, 86.42°W, 610 masl) is part of the Canadian Network for the Detection of Atmospheric Composition Change (CANDAC). The instrument is a Bruker IFS 125HR, which is operated at a maximum OPD of 257 cm and a spectral resolution of 0.0035 cm^{-1} for NDACC mid-infrared measurements with a KBr beamsplitter (resolution defined by Bruker as 0.9/MOPD). By switching the KBr for a CaF_2 beamsplitter and using an InGaAs detector, the FTIR operates as part of the Total Carbon Column Observing Network (TCCON), recording near-infrared (NIR) measurements. On-site personnel are needed to swap the beamsplitters to share measurement time between both spectral regions and to cool the detectors with liquid nitrogen. Measurements are made during the sunlit portion of the year, from late February to mid-October, and began in August 2006. Measurements have been sparse since the end of March 2020 due to the pandemic, when access to Eureka was limited for an extended period, as well as further complications with the condition of the road to the Ridge Lab and funding availability. When in regular operation, the data from the PEARL FTIR are submitted to NDACC DHF, CAMS RD, and TCCON. The ten standard IRWG gases archived are C_2H_6, CH_4, $ClONO_2$, CO, HCl, HCN, HF, HNO_3, N_2O, and O_3, along with research products C_2H_2, C_2H_4, CH_3OH, HCOOH, H_2CO, NH_3, NO_2, OCS and PAN. For a description of the PEARL FTIR installation, calibration and initial development, refer to Batchelor et al. (2009) and Lindenmaier (2012), and for a detailed overview of the instrument and retrievals, refer to Wizenberg (2023).

Chapter 3

3 TAO Retrievals and Time Series

This chapter presents the retrievals of trace gases from the TAO mid-infrared FTIR, located on the roof of the McLennan Physical Laboratories Building at the University of Toronto. There are currently 16 species uploaded annually to the NDACC DHF, and four that are uploaded monthly to the CAMS RD database. The newest species to be added are OCS and CHF_2Cl (HCFC-22), with the TAO data included in Hannigan et al. (2022) and Zhou et al. (2024) respectively, while the O_3 retrieval has been updated as described in Section 3.3. The other species archived to the NDACC DHF are C_2H_2, C_2H_6, CH_3OH, CH_4, CO, H_2CO, HCl, HCN, HCOOH, HF, HNO_3, N_2O, and NH_3. The CAMS RD gases are CH_4, CO, H_2CO and O_3. As the most recently updated species, CHF_2Cl, and O_3 were retrieved using SFIT4 version 1.0.18, while all the other species were retrieved using version 0.9.4.4.

3.1 Retrieval Parameters

As discussed in Chapter 2, microwindows with atmospheric absorption lines are used to retrieve vertical profiles and columns of the trace gases. Table 3.1 lists the gas formula and name, the spectral microwindows which are used for the retrievals at TAO, the interfering species included in the retrieval, the $\mathbf{S}_a$ (value or range) used, and the interlayer correlation length. The species marked with an asterisk (*) are the standard NDACC-IRWG species ($ClONO_2$ is also a standard species but is not an archived gas at TAO due to its small mid-latitude abundance). Of the standard gases, NDACC labels O_3, HCl, HF and HNO_3 as stratospheric gases, CH_4, C_2H_6, CO, HCN, and N_2O as tropospheric gases, and the remaining are considered research products (Yamanouchi et al., 2023). If a gas is retrieved with Tikhonov regularization, it is indicated in the $\mathbf{S}_a$ column, otherwise the standard OEM is used.

Table 3.1: Gases retrieved from TAO FTIR spectra (NDACC standard species marked with ''), fitted microwindows, interfering species, $\boldsymbol{S}_a$ range (or marked as Tikhonov regularization), and interlayer correlation length.*

Gas	Microwindow(s)	Interfering Species	$\mathbf{S}_a$ (%)	ILC (km)
C_2H_2 Acetylene	1. 3250.40 – 3250.80 2. 3268.25 – 3268.75 3. 3304.70 – 3305.40	H_2O, HCN, $H_2{}^{17}O$, $H_2{}^{18}O$, HDO, O_3	21-131	4

C_2H_6 Ethane*	1. 2976.66 – 2976.95 2. 2983.20 – 2983.55 3. 2986.50 – 2986.95	H_2O, O_3	30	4
CH_3OH Methanol	1. 992.00 – 998.70 2. 1029.00 1037.00	CO_2, H_2O, O_3, O_3^{667}, O_3^{668}, O_3^{676}, O_3^{686}	100	4
CH_4 Methane*	1. 2613.70 – 2615.40 2. 2835.50 – 2835.80 3. 2921.00 – 2921.60	CO_2, H_2O, HDO, NO_2	Tik.	n/a
CHF_2Cl Chlorodifluoromethane or HCFC-22	1. 828.75 – 829.40 2. 1115.50 – 1116.10	CO_2, H_2O, O_3	Tik.	n/a
CO Carbon Monoxide*	1. 2057.70 – 2058.00 2. 2069.56 – 2069.76 3. 2157.50 – 2159.15	CO_2, H_2O, N_2O, O_3, OCS	1-8	2
H_2CO Formaldehyde	1. 2763.425 – 2763.60 2. 2765.725 – 2765.975 3. 2778.15 – 2779.10 4. 2780.65 – 2782.00	CH_4, HDO, N_2O, O_3	Tik.	n/a
HCl Hydrochloric Acid*	1. 2727.73 – 2727.83 2. 2775.70 – 2775.80 3. 2925.88 – 2926.00	CH_4, HDO, N_2O, NO_2, O_3	10	none
HCN Hydrogen Cyanide*	1. 3268.05 – 3268.40 2. 3287.10 – 3287.35 3. 3299.30 – 3299.60 4. 3331.40 – 3331.80	C_2H_2, CO_2, H_2O, $H_2{}^{17}O$, $H_2{}^{18}O$, N_2O	20	4
HCOOH Formic Acid	1. 1102.00 – 1109.00 2. 1178.40 – 1178.80	CCl_2F_2, CH_4, CHF_2Cl, H_2O, HDO, N_2O, NH_3	Tik.	n/a
HF Hydrogen Fluoride*	1. 4038.86 – 4039.05	H_2O, CH_4	50	none
HNO_3 Nitric Acid*	1. 867.50 – 870.00	H_2O, NH_3, OCS	20	4
N_2O Nitrous Oxide*	1. 2481.30 – 2482.60 2. 2526.40 – 2528.20 3. 2537.85 – 2538.80 4. 2540.10 – 2540.70	CH_4,CO_2, H_2O, HDO, O_3	1	4
NH_3 Ammonia	1. 930.32 – 931.32 2. 966.97 – 967.675	$CO_2{}^1$, $CO_2{}^2$, $CO_2{}^3$, H_2O, HNO_3, O_3	50	4
O_3 Ozone*	Original v0.9.4.4: 1. 782.56 – 782.86 2. 788.85 – 789.37 3. 993.30 – 993.80 4. 1000.00 – 1004.50	C_2H_4, CO_2, H_2O, O_3^{668}, O_3^{686}	8.3-10	2
	Updated v1.0+ : 1. 991.25 – 993.80 2. 1001.47 – 1003.04 3. 1005.00 – 1006.90 4. 1007.348 – 1009.00	C_2H_4, CO_2, O_3^{668}, O_3^{686}	Tik.	n/a
OCS Carbonyl Sulfide	1. 2047.85 – 2048.24 2. 2049.77 – 2050.18 3. 2051.18 – 2051.46 4. 2054.33 – 2054.67	CO, H_2O, $H_2{}^{18}O$, O_3	7-53	4

Table 3.2 shows the mean DOFS and percent uncertainty from the entire 2002-2024 time series for the total columns and tropospheric (0-12 km) and stratospheric (12-50 km) partial columns, in addition to the ranges for which the mean sensitivity is greater than 0.5. The tropospheric height is taken from the average reported for TAO in Hannigan et al. (2022), derived from NCEP temperature profiles. The random and systematic FTIR partial column uncertainties are calculated using the error covariance matrices, following the method outlined in Vigouroux et al. (2009). The square root of the associated error is taken, and this is scaled to a percent uncertainty using the corresponding column. The mean systematic and random percent errors are calculated using all the measurements for each year, then the mean of these annual average systematic and random percent errors is taken, and those two values are added in quadrature to get the overall mean percent uncertainty for the species. The sensitivity corresponds to the sum of the AVKS rows at each altitude; when this is greater than 0.5 this means more than half of the retrieved profile information comes from the measurement (Vigouroux et al., 2009). Together the metrics in Table 3.2 highlight the differences between different vertical regions of the retrieval in terms of the information content, uncertainties, and sensitivity to the atmosphere.

Figure 3.1 shows the mean AVK profile for each species, partitioned into the tropospheric partial column (0-12 km, green dot-dash line), the stratospheric partial column (12-50 km, light blue dashed line), and the total column (blue dotted line), with a grey line marking an AVK of 1. An ideal AVK would be 1 for the total column, which would represent a total column retrieval which is sensitive to the true state of the atmosphere at all levels and the 0-12 km and 12-50 km AVKS would only peak within those bounds, meaning the retrievals of those partial columns would only include information from the respective altitude.

Table 3.2: The mean total column (TC) and 0-12 km and 12-50 km partial column DOFS (±1σ), percent uncertainty, and altitude range with sensitivity >0.5, for the entire TAO FTIR time series (2002-2024).

Gas	DOFS			Total Uncertainty (%)			Sensitivity >0.5
	TC	0-12 km	12-50 km	TC	0-12 km	12-50 km	(km)
C_2H_2	1.45±0.26	1.39±0.24	0.05±0.02	29.51	28.56	15.70	0.36-16.54
C_2H_6	1.87±0.29	1.59±0.22	0.29±0.07	4.86	4.85	12.68	0.36-15.40
CH_3OH	1.53±0.16	1.48±0.14	0.04±0.01	15.68	15.74	43.49	0.75-15.40
CH_4	2.11±0.21	1.12±0.11	0.97±0.11	4.40	4.16	8.06	0.36-37.56
CHF_2Cl	1.02±0.3	0.74±0.02	0.27±0.02	13.60	13.96	13.09	0.36-22.77
CO	2.19±0.24	1.84±0.14	0.31±0.11	2.96	3.14	6.91	0.36-37.56
H_2CO	1.23±0.15	1.03±0.07	0.14±0.08	15.83	15.92	30.71	0.36-28.40
HCl	1.79±0.31	0.001±0.002	1.79±0.21	2.63	0.16	2.80	14.30-40.17
HCN	2.09±0.39	0.97±0.16	1.11±0.23	6.45	7.44	7.20	2.17-29.92
HCOOH	1.06±0.04	0.96±0.02	0.09±0.02	13.48	12.96	14.83	0.36-18.92
HF	1.87±0.29	0.02±0.01	1.86±0.28	3.06	3.10	3.16	18.92-40.17
HNO_3	1.36±0.26	0.23±0.14	1.08±0.21	3.64	6.14	4.16	1.66-28.40
N_2O	2.88±0.24	1.79±0.13	1.10±0.13	3.94	3.88	7.13	0.36-26.94
NH_3	1.12±0.10	1.09±0.10	0.0005±0.0005	17.07	17.09	2.36	0.36-21.45
O_3 (v1.0+)	3.67±0.21	1.00±0.12	2.65±0.12	3.94	6.07	4.15	3.93-46.68
OCS	2.60±0.44	1.06±0.19	1.55±0.24	2.63	2.51	5.33	0.75-33.30

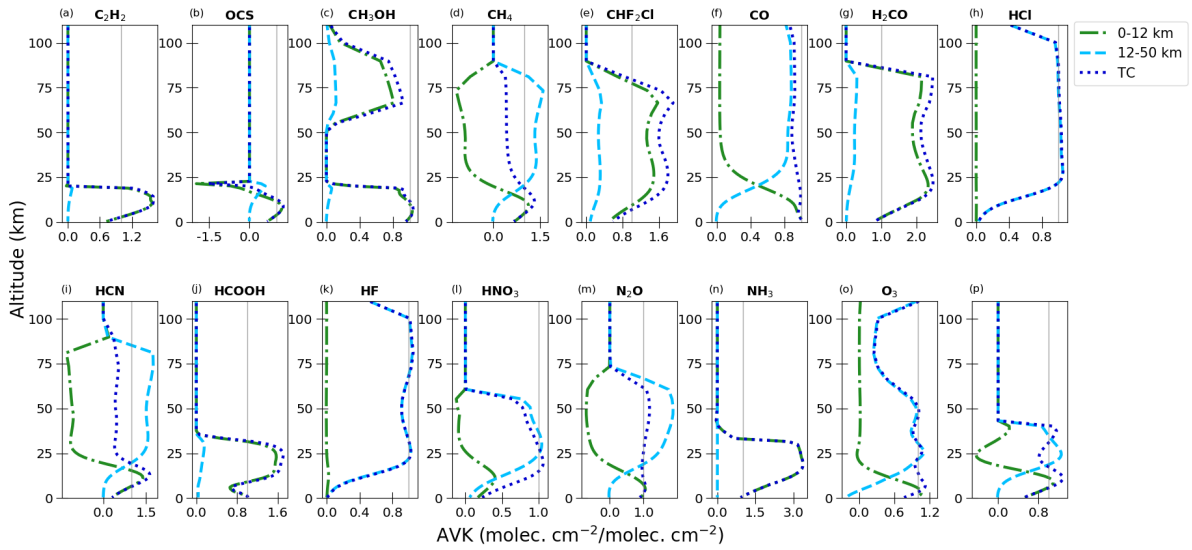

Figure 3.1: Mean AVK for 0-12 km partial column (green dot-dash line), 12-50 km partial column (light blue dashed line) and total column (blue dotted line) for all the NDACC archived TAO FTIR species (2002-2024). The vertical grey line marks the AVK of 1.

Figure 3.2 shows the 2002-2024 mean VMR profiles (green), where the shaded areas represent ±1σ of the mean, and the a priori VMR profile (blue). Figure 3.3 shows the same plot, zoomed into the 0-12 partial column.

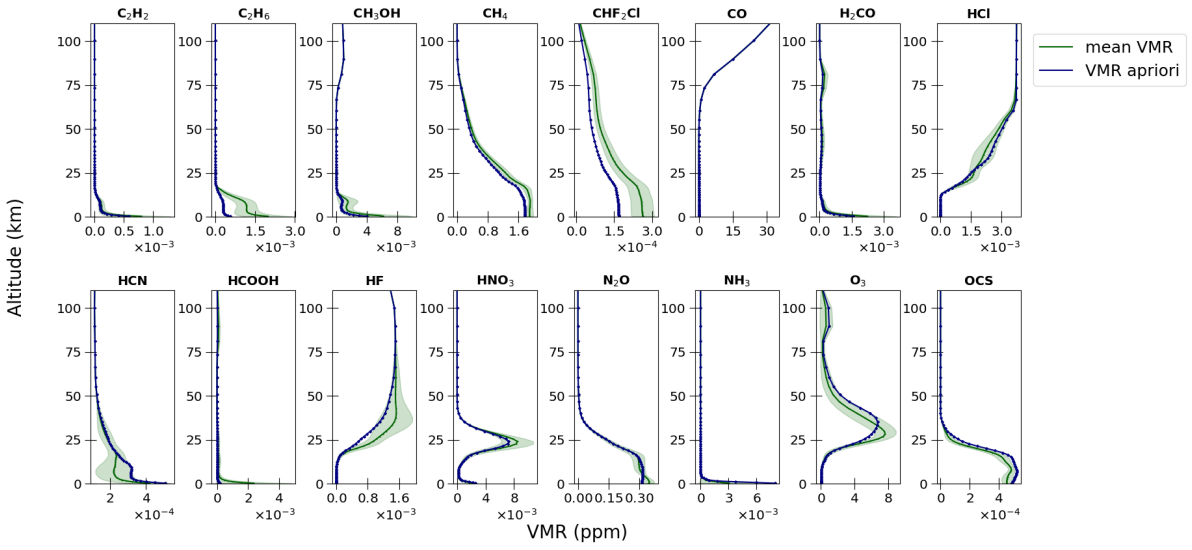

Figure 3.2: Mean VMR profile (green) and a priori (blue) in ppm, for all the NDACC archived TAO species (2002-2024). The green shaded area corresponds to ±1σ of the mean.

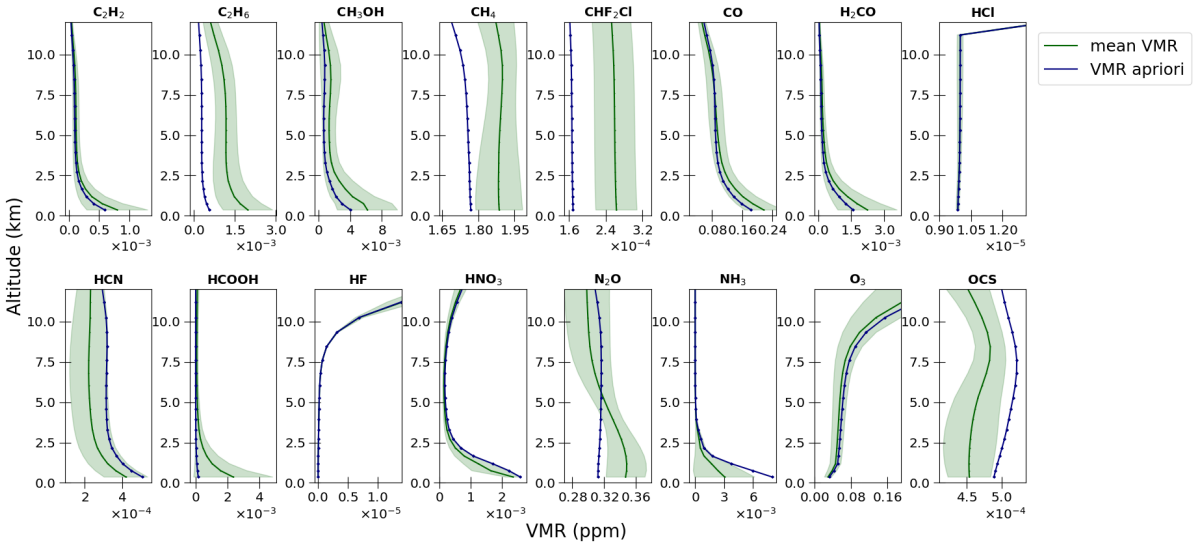

Figure 3.3: Same as Fig 3.2, zoomed into the 0-12 km region.

3.2 2002-2024 TAO Time Series

Figures 3.4 to 3.19 show the total column time series for each of the NDACC archived species. The upper panel in each figure shows the total column by date from 2002-2024, with a horizontal line representing each year's mean value. The lower panel shows all the total columns by day of year, with the overall monthly mean marked with a black dot. The marker color changes from a dark purple, to blue, through to green with the progression of the years, following the same colour scheme as in Figure 2.6. A brief description is provided for each gas, discussing properties such as lifetime and sources and referencing back to the relevant figures and tables.

3.2.1 Acetylene

Acetylene (C_2H_2) is primarily found in the troposphere, as seen in the VMR profile (Figure 3.2) with a maximum near the surface, and the similar DOFS between the TC and 0-12 km partial column (Table 3.2). It has both natural and anthropogenic sources, although is primarily from the use of fossil and bio fuels, and biomass burning (Xiao et al., 2007, and references therein). The atmospheric lifetime is approximately two weeks, making wildfire-related enhancements at TAO sometimes difficult to detect relative to the background levels (Yamanouchi et al., 2023). The total column time series and monthly means of C_2H_2 are shown in Figure 3.4. The seasonal cycle shows a minimum in the summer due to oxidation by hydroxyl radicals (OH), and a maximum in the winter when OH is reduced due to decreased photochemical activity.

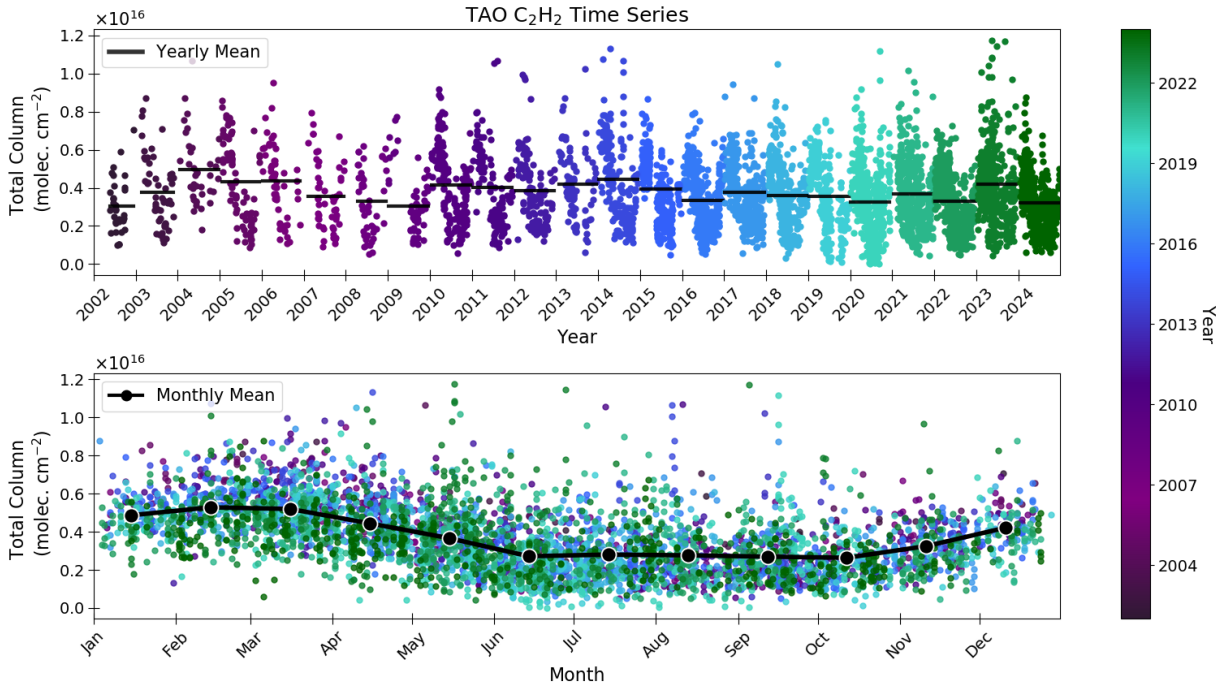

Figure 3.4: TAO total column time series of acetylene, by date with the yearly means marked by the horizontal line (upper panel), and by day of year with the monthly mean marked with black dots (lower panel). Year and month marked at the beginning of the period.

3.2.2 Ethane

Ethane (C_2H_6) is a tropospheric species, as demonstrated by the peak values in the average VMR profile shown in Figure 3.2. C_2H_6 has a lifetime of approximately two months, it is emitted primary via oil and gas production, with a small portion from biogenic emissions and biomass burning (Maddanu & Proietti, 2023). Examining the total columns measured at TAO from 2002-2008 and 2009-2018, Yamanouchi et al. (2021a) found a reversal in the trends from decrease in -0.74 % per year to an increase of 1.19%, when partitioning between the two time periods. Enhancements from wildfire events measured at TAO are examined in Chapter 5 and have also been discussed in Griffin et al. (2013), Lutsch et al. (2016), and Yamanouchi et al. (2020). Similar to C_2H_2, the seasonal cycle has a summer minimum, as seen in Figure 3.5, driven by OH oxidation, since OH is most abundant during the summer months.

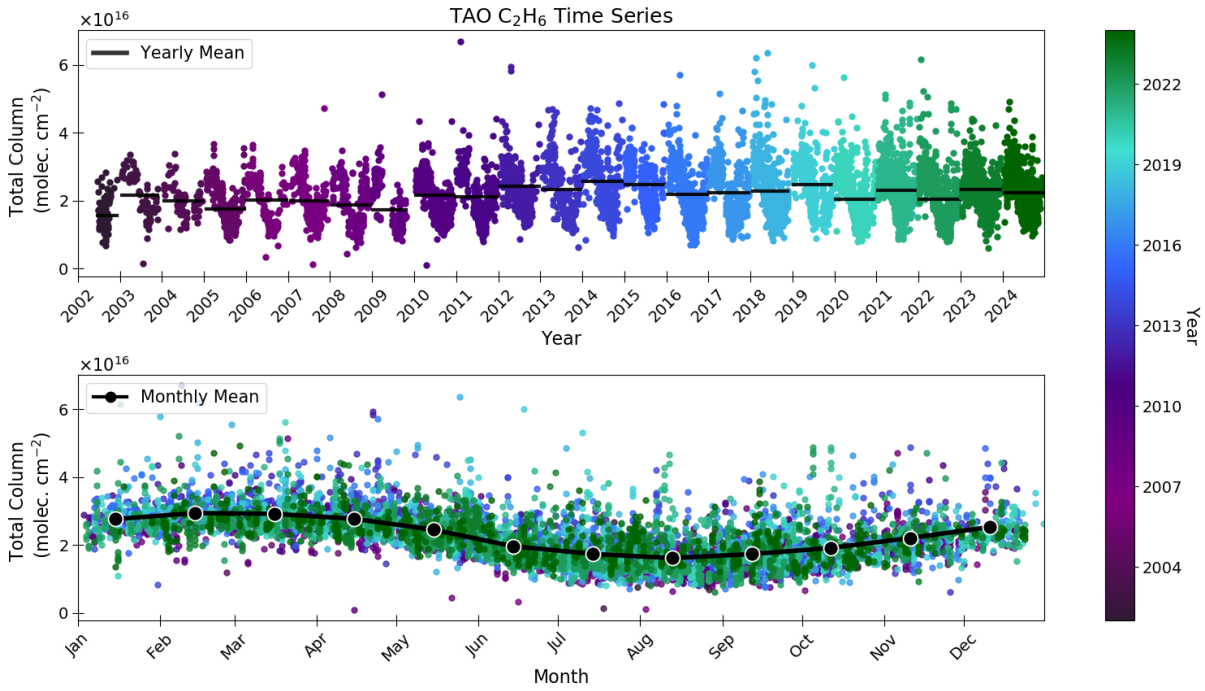

Figure 3.5: Same as Figure 3.4 for ethane.

3.2.3 Methanol

Methanol (CH_3OH) is a tropospheric species, with the VMR profile peaking in the lower levels of the troposphere (Figure 3.2) and most of the DOFS (1.48 compared to 1.53 for the TC) within the 0-12 km partial column. CH_3OH is a volatile organic compound (VOC) with a short global atmospheric lifetime, on the order of five days (Bates et al., 2021). The seasonal cycle peaks in the summer months driven by increased natural sources such as vegetation and biomass burning, despite a primary sink from OH oxidation. There is a winter minimum from a reduction in sources and sometimes low detection, with many retrievals not reaching convergence. Figure 3.6 shows the time series by date and month, where enhancements from biomass burning events are visible. These enhancements are discussed in relation to the 2023 Canadian forest fires in Chapter 6, and for observations between 2002 and 2018 in Yamanouchi et al. (2021).

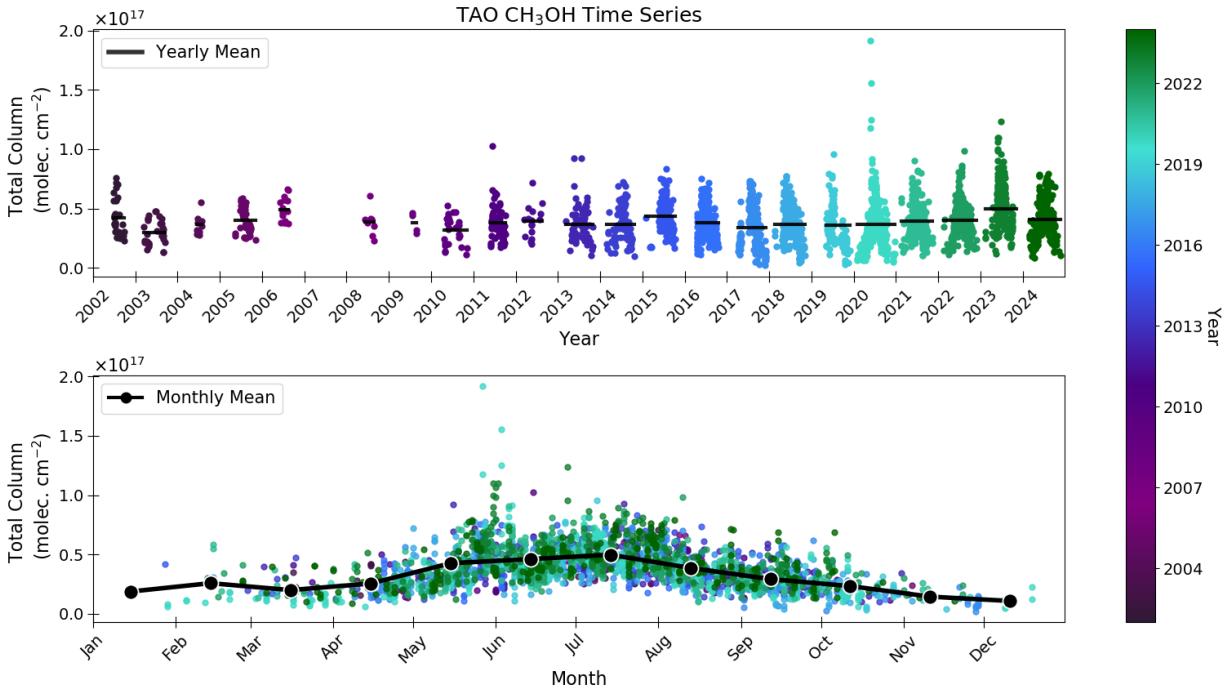

Figure 3.6: Same as Figure 3.4 for methanol (note: 2007 had no retrievals pass the quality check).

3.2.4 Methane

Methane (CH_4) is primarily a tropospheric species, although its profile extends into the stratosphere (Figure 3.2), and the retrieval is sensitive to both regions with a sensitivity >0.5 from the lowest layer up to approximately 40 km, and a DOFS of roughly 1 in both the troposphere and stratosphere (Table 3.2). It is long-lived, on the order of a decade, and is the most abundant hydrocarbon in the atmosphere (Saunois et al., 2020). There are several sources, both anthropogenic and natural, such as fossil fuel production, waste, agriculture, wetlands and biomass burning, and a primary sink from OH. Due to the number of different sources and long lifetime, the seasonal cycle observed at TAO is relatively flat, as seen in the lower panel of Figure 3.7. Biomass burning is estimated to account for approximately 5% of the global methane emissions in a year (from 2008-2017) (Saunois et al., 2020), although enhancements have not been observed within the TAO dataset. The upper panel of Figure 3.7 shows the time series by date, where one may note a slight increasing trend, which was reported in Yamanouchi et al. (2021a) as 0.41% per year. This dataset has been used to validate CH_4 data products including those from the Thermal And Near infrared Sensor for carbon Observations (TANSO) Fourier transform spectrometer (FTS) on the Greenhouse gases Observing SATellite (GOSAT) (Olsen et al., 2017), and the

TROPOspheric Monitoring Instrument (TROPOMI) on the Sentinel-5 Precursor (S5P) mission (Sha et al., 2021). Despite the relatively long lifetime, it is considered an SLCF and is discussed with respect to Arctic modelling in Chapter 4.

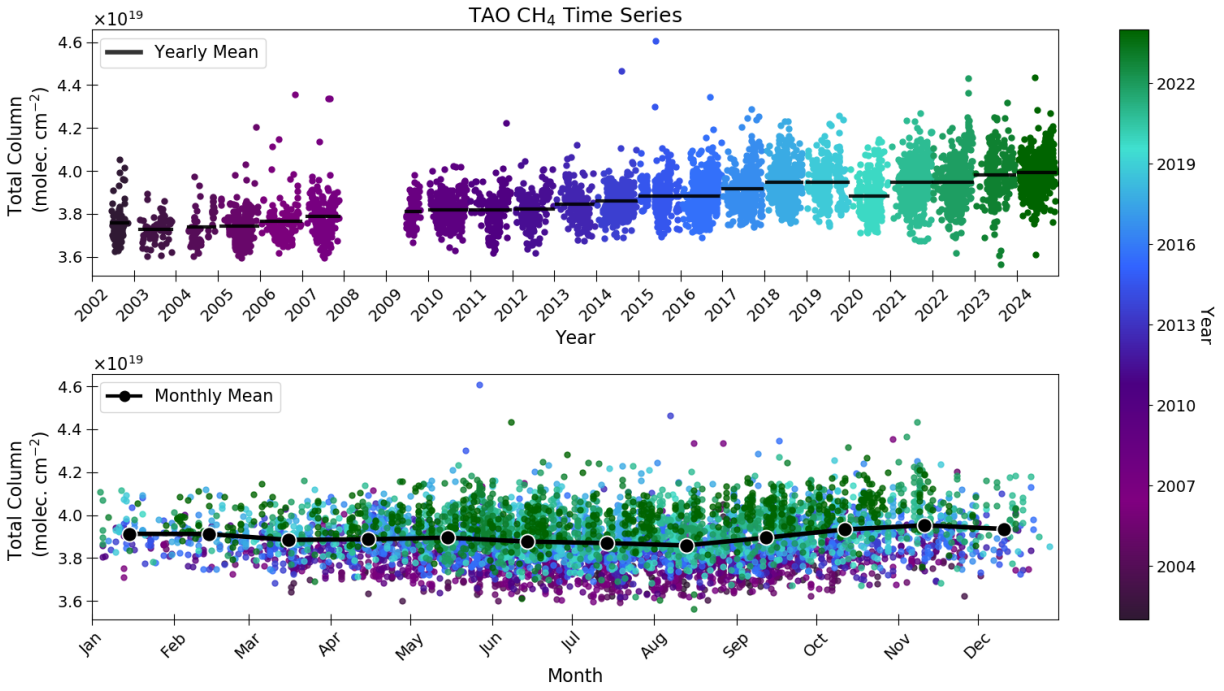

Figure 3.7: Same as Figure 3.4 for methane (note: 2008 is omitted due to instrument issues causing poor data).

3.2.5 HCFC-22

Chlorodifluoromethane (CHF_2Cl), or HCFC-22, is the most recent research product added to the TAO database following the implementation of an NDACC-IRWG harmonized retrieval (Zhou et al., 2024). The species is an anthropogenic ozone-depleting substance, which was introduced as a replacement to chlorofluorocarbons (CFCs) with a lifetime of approximately 12 years (Zhou et al., 2024 and references therein). An agreement was made in the 1987 Montreal Protocol to phase out ozone-depleting substances; reductions of the consumption and production of HCFCs began later, and is still underway. The total column trends from 16 NDACC-IWRG FTIR sites show that the growth rate of HCFC-22 has been decreasing since 2009, which agrees with satellite and surface samples (Zhou et al., 2024). Note that TAO was included in this study, although not included in the growth rate calculation as the time period provided was too short (2002-2013 was omitted from the study due to inconsistencies in the retrievals, possibly resulting from issues with the MCT detector).

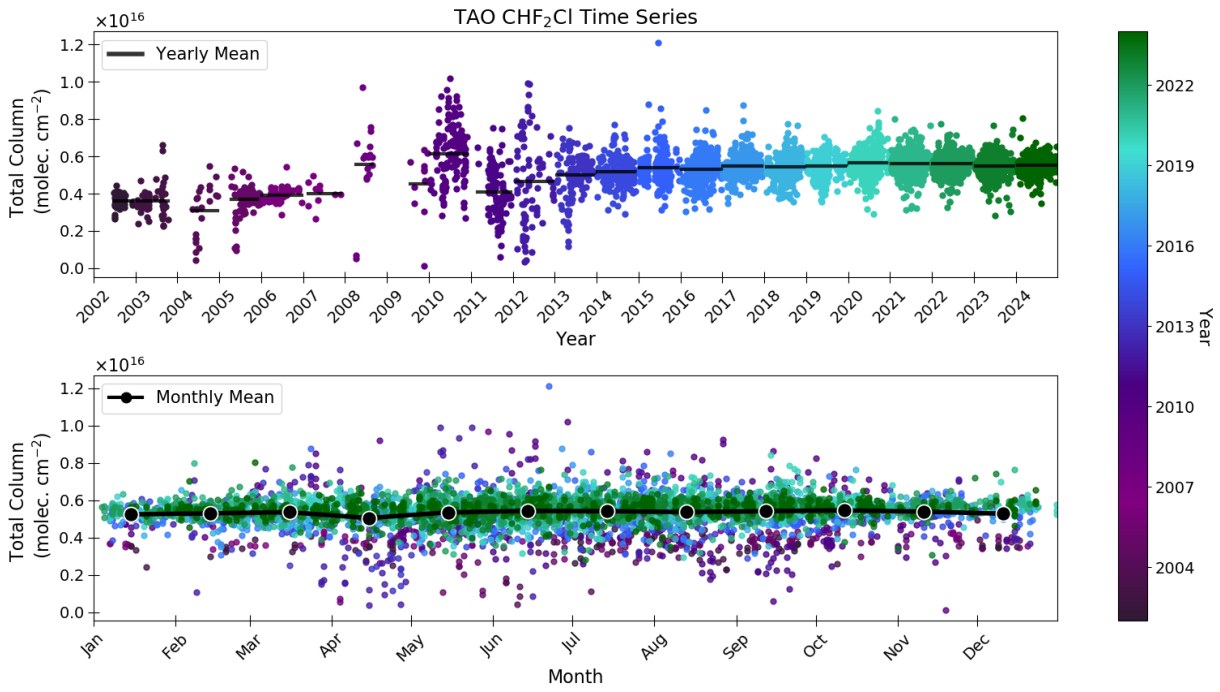

Figure 3.8: Same as Figure 3.4 for chlorodifluoromethane.

3.2.6 Carbon Monoxide

Carbon monoxide (CO) is a tropospheric species, however it is also present in the upper atmosphere, as seen in the VMR profile (Figure 3.2). It has a total column AVK close to unity for the whole column, and sensitivity >0.5 from the surface to approximately 40 km. The lifetime of CO is on the order of 1-2 months, with the main sink being OH oxidation. The seasonal cycle follows a similar pattern to other species with OH sinks, however the scale on the monthly mean plot (bottom panel of Figure 3.9) is elongated due to enhancements from biomass burning events, reducing the visibility of the underlying seasonal cycle. Other relevant sources of CO include fossil fuel combustion and as a byproduct of hydrocarbon oxidation. This dataset has been used to validate several satellite CO data products, including MOPITT (Buchholz et al., 2017), and TROPOMI on S5P (Sha et al., 2021). CO is studied in Chapters 4, 5, and 6, with respect to Arctic modelling as an SLCF precursor, enhancements from the 2023 Canadian wildfires, and the impacts of biomass burning on the seasonal cycle and health care utilization.

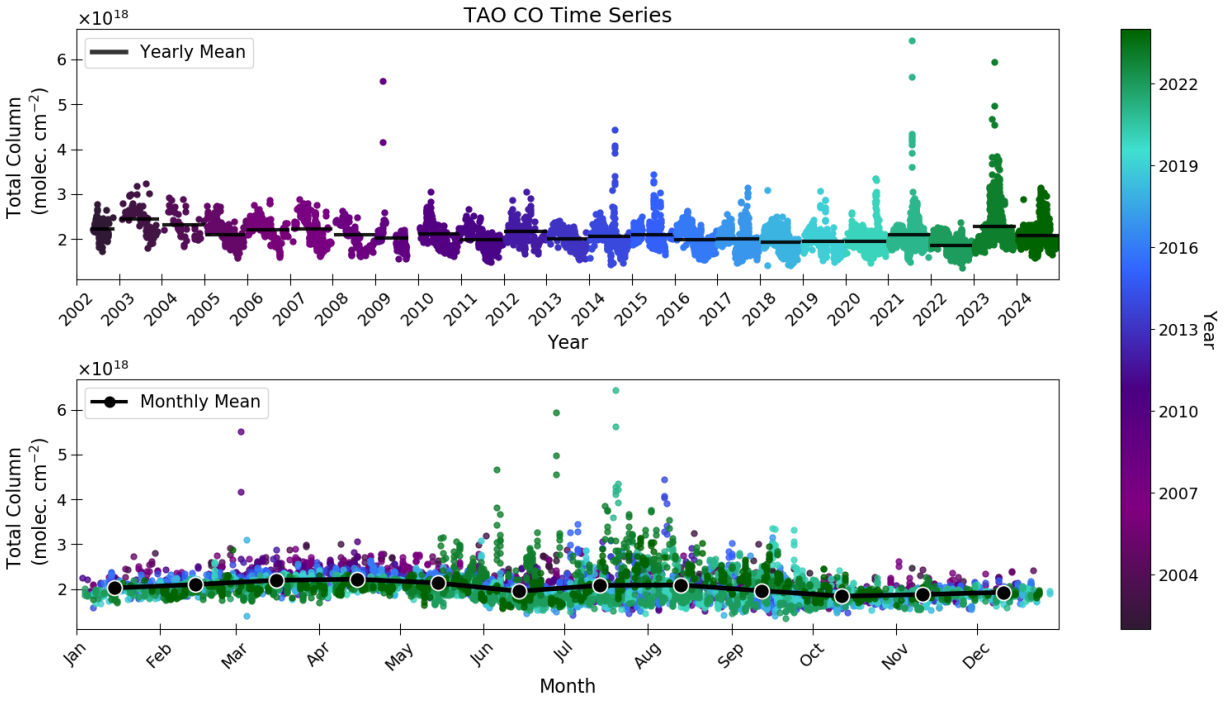

Figure 3.9: Same as Figure 3.4 for carbon monoxide.

3.2.7 Formaldehyde

Formaldehyde (H_2CO) is predominantly present in the troposphere, as shown by the VMR profile, and this is also where majority of the DOFS are accounted for (1.03 in the 0-12 km partial column, compared to 1.23 for the total column). As seen in Figure 3.10, there is a pronounced seasonal cycle with a maximum in the summer, largely influenced by its production via the oxidation of CH_4 and VOCs and biomass burning, which also reach their peak levels during this period. H_2CO readily reacts with OH and therefore has a short lifetime, on the order of hours. The rapid reactivity makes H_2CO an important intermediary in the formation of secondary pollutants in the atmosphere. This retrieval was harmonized with 20 other sites in the network (Vigouroux et al., 2018), and the dataset was later used to validate satellite H_2CO data products such as those from TROPOMI on S5P (Vigouroux et al., 2020) and the Ozone Monitoring Instrument (OMI) (Müller, et al., 2024 and Ayazpour et al., 2025).

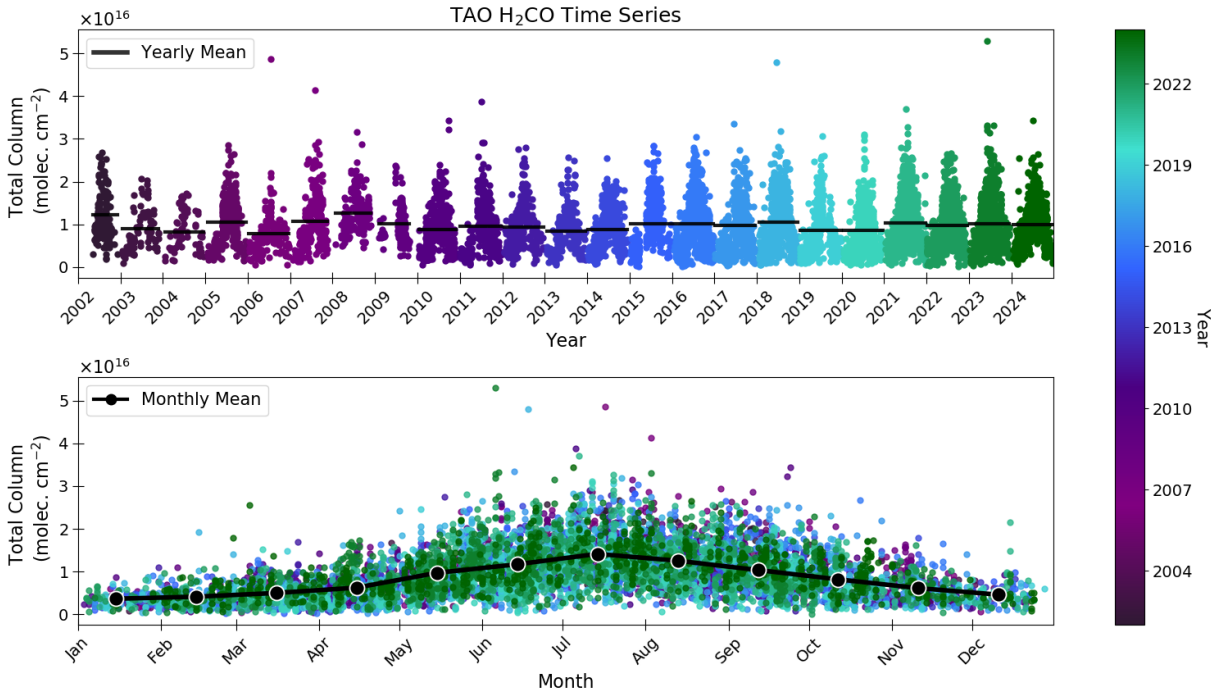

Figure 3.10: Same as Figure 3.4 for formaldehyde.

3.2.8 Hydrochloric Acid

Hydrochloric acid (HCl) is a stratospheric species, with next to no contributions from the troposphere, as seen in the VMR profile, and further reflected in the >0.5 sensitivity range from approximately 14-40 km. The primary source of HCl is from the photodissociation of CFCs and HCFCs in the stratosphere. As a chlorine reservoir, HCl plays a key role in catalytic ozone destruction. The seasonal cycle has a maximum in the spring, and a minimum in the summer, driven by tropopause height (Kohlhepp et al., 2012); enhancements in the total column are sometimes observed as a result of polar vortex intrusions (Whaley et al., 2013).

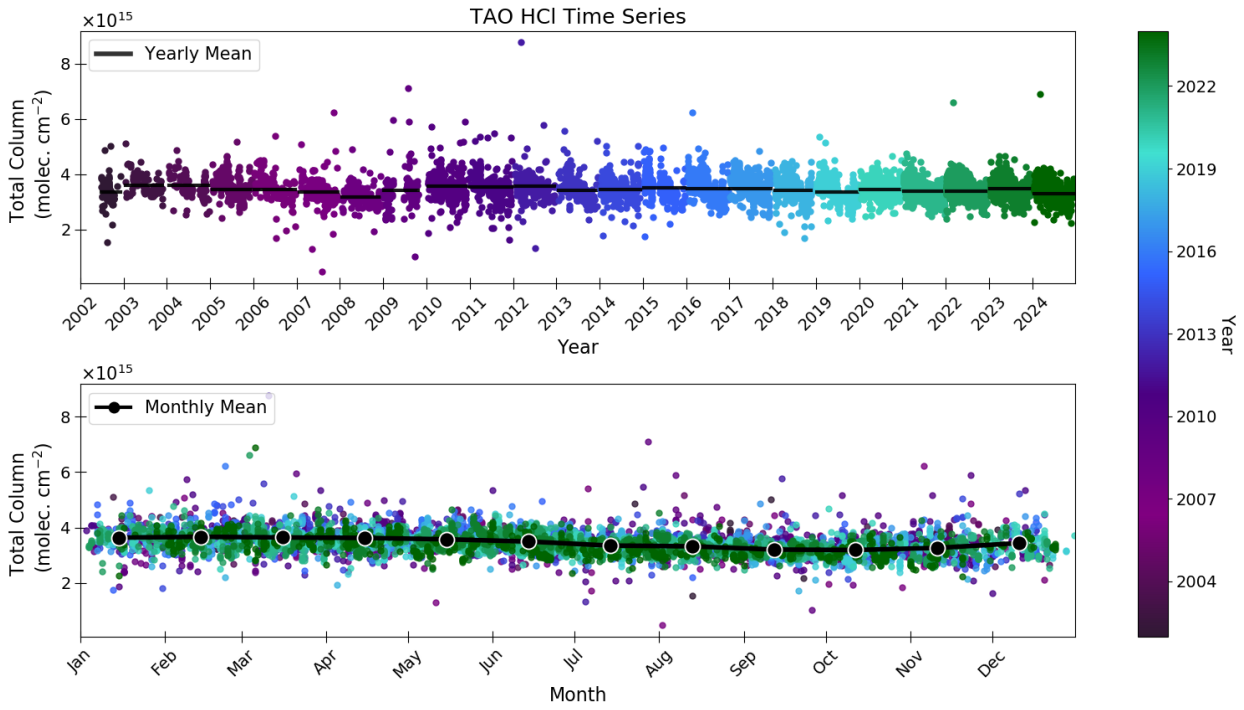

Figure 3.11: Same as Figure 3.4 for hydrochloric acid.

3.2.9 Hydrogen Cyanide

Hydrogen cyanide (HCN) is a predominantly tropospheric species, with the VMR profile peaking in the lower levels, however there is a distribution into the stratosphere as well (Figure 3.2). The retrieval has about 1 DOFS for both areas of the atmosphere and has a sensitivity >0.5 from about 2-30 km. HCN has a tropospheric lifetime of approximately five months, with its primary source being biomass burning, and to a lesser extent industrial activities. Atmospheric removal of HCN occurs mainly through reactions with OH, in addition to ocean uptake (Bruno et al., 2023). The seasonal cycle, as seen in Figure 3.12, peaks in the summer and is at a minimum in the winter. Wildfire-related enhancement of HCN measured at TAO are observable in Figure 3.12, particularly in the summers of 2014 and 2023, which are examined in Lutsch et al. (2016) and Chapter 5, respectively.

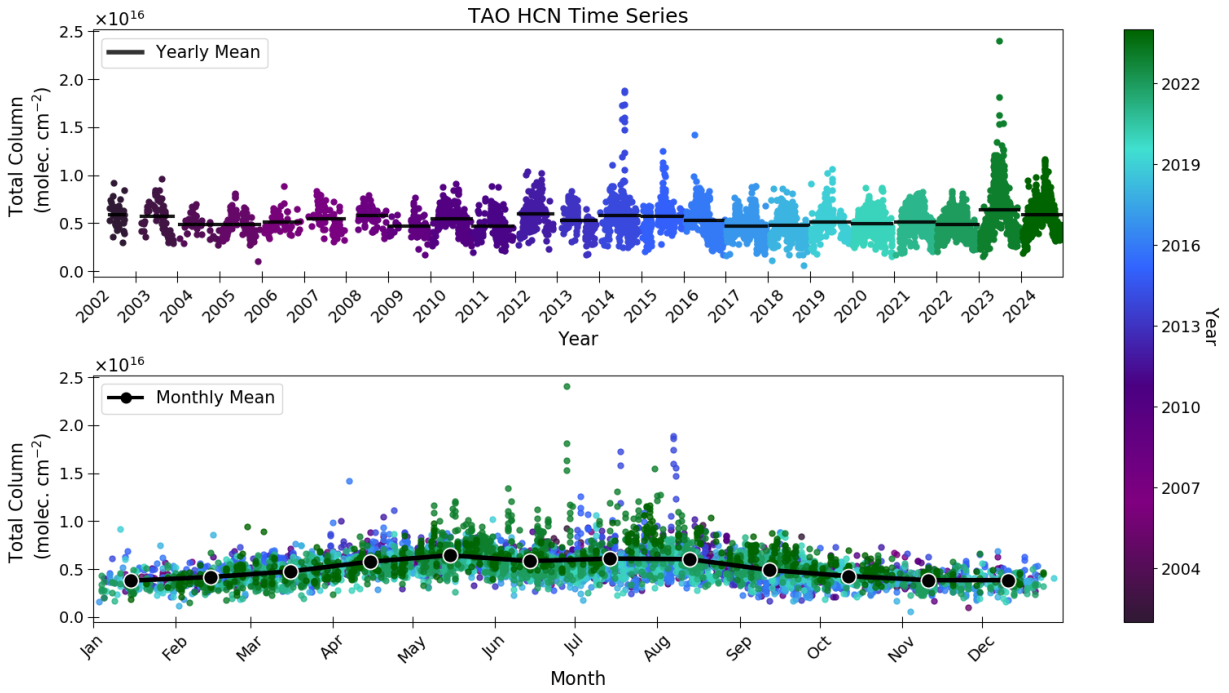

Figure 3.12: Same as Figure 3.4 for hydrogen cyanide.

3.2.10 Formic Acid

Formic acid (HCOOH) is a troposphere species, as seen in the VMR profile (Figure 3.2), with very little information coming from the stratospheric portion of the retrieval (12-50 km DOFS=0.09). The seasonal cycle (as seen in the lower panel of Figure 3.13) has a summer peak driven by biogenic emissions, and sometimes biomass burning enhancements. It is a VOC with an atmospheric lifetime of 2-4 days; the main sink is OH oxidation, in addition to both wet and dry deposition (Millet et al., 2015, and references therein). This dataset has been used to validate HCOOH data products from the Infrared Atmospheric Sounding Interferometer (IASI) (Franco et al., 2020). Biomass burning enhancements can be observed in the time series, these are discussed in Yamanouchi et al. (2020) for measurements from 2002-2018 and in Chapter 5 for the summer of 2023.

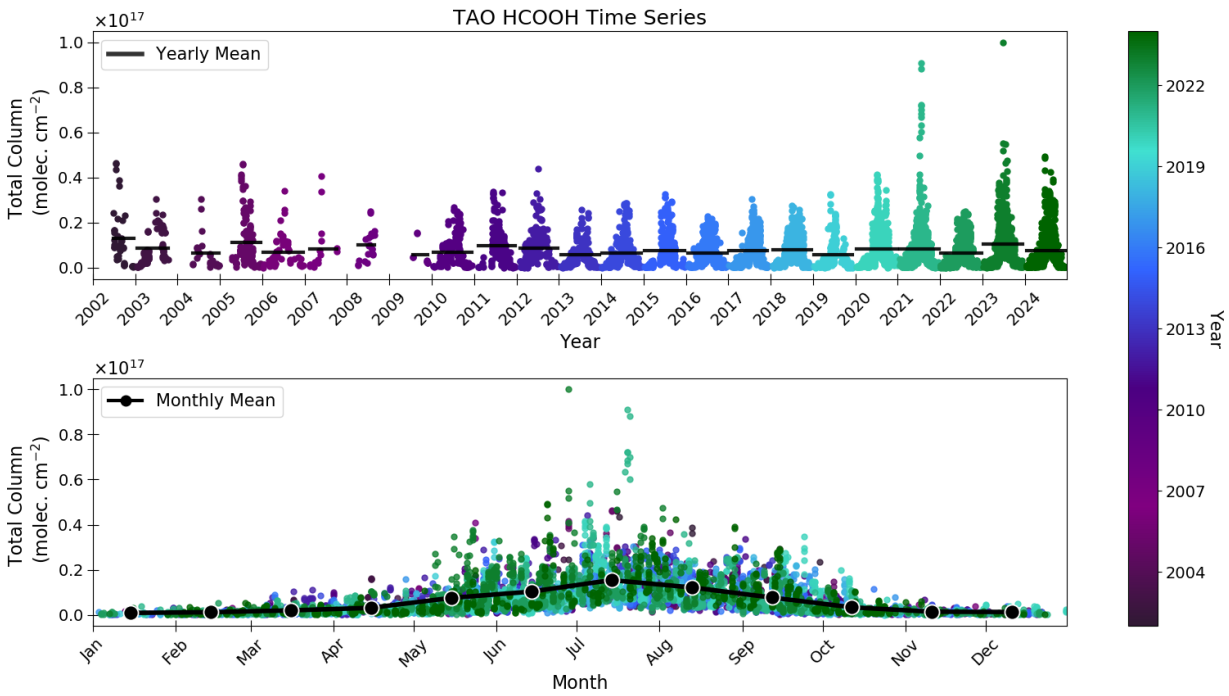

Figure 3.13: Same as Figure 3.4 for formic acid.

3.2.11 Hydrogen Fluoride

Hydrogen fluoride (HF) is a stratospheric species, with a VMR profile that increases above 10 km (Figure 3.2), a sensitivity >0.5 from 19-40 km, and negligible DOFS in the tropospheric column (Table 3.2). It has many similarities to HCl; it is formed by photodissociation of CFCs and HCFCs, has a summer minimum, and is used as a tracer for polar vortex intrusions (Kohlhepp et al., 2012; Whaley et al., 2013). HF is long lived, with a lifetime over a decade; Yamanouchi et al. (2021a) report a small increasing trend of 0.59% per year (top panel of Figure 3.14).

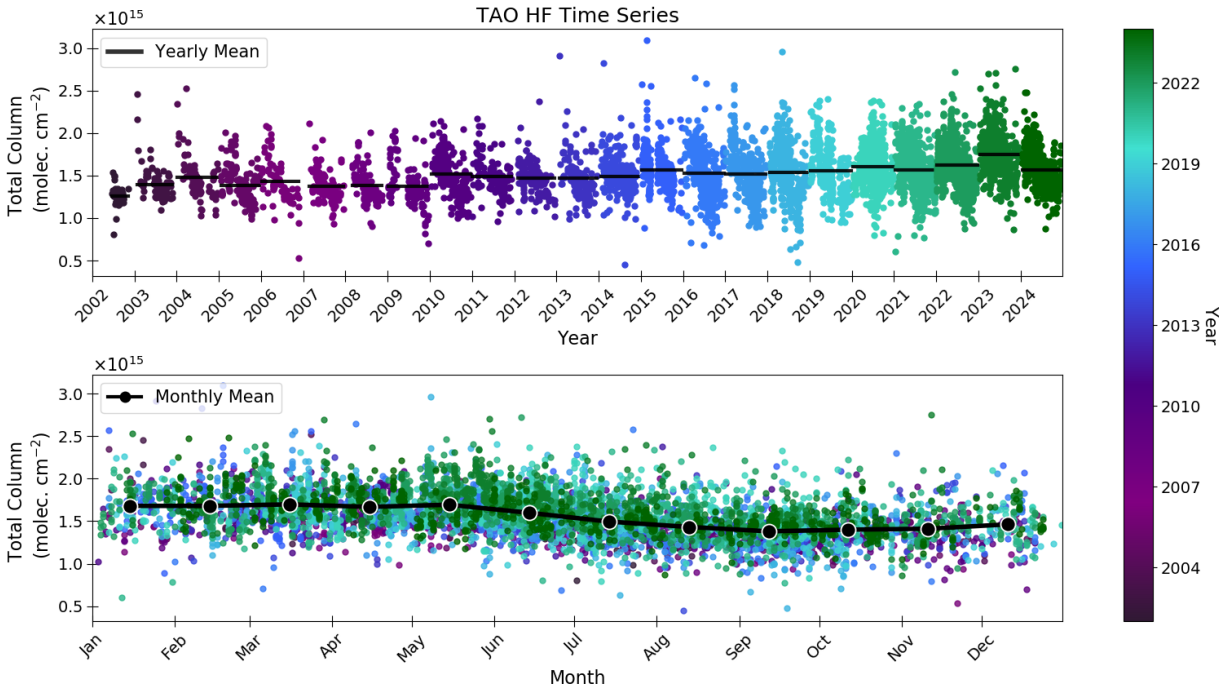

Figure 3.14: Same as Figure 3.4 for hydrogen fluoride.

3.2.12 Nitric Acid

Nitric acid (HNO_3) is a stratospheric species, with minor contributions from the troposphere, as seen in the VMR profile (Figure 3.2). In the stratosphere, where HNO_3 has a lifetime from weeks to months, it acts as a reservoir species for reactive nitrogen, serving as a temporary sink for NOx, before it converts back via OH or photolysis. In the troposphere, it is also a sink for NOx, although it has a shorter lifetime on the order of days (Jacob, 1999). It is released through wet and dry deposition, playing a role in Earth's surface nitrogen cycle. The seasonal cycle, as seen in Figure 3.15, has a maximum in the winter and a minimum in the summer, driven by the increase in sunlight and OH availability which enhances the conversion back to reactive nitrogen. This dataset was used as part of the HNO_3 validation of the Atmospheric Chemistry Experiment - Fourier Transform Spectrometer) (ACE–FTS) (Wolff et al., 2008).

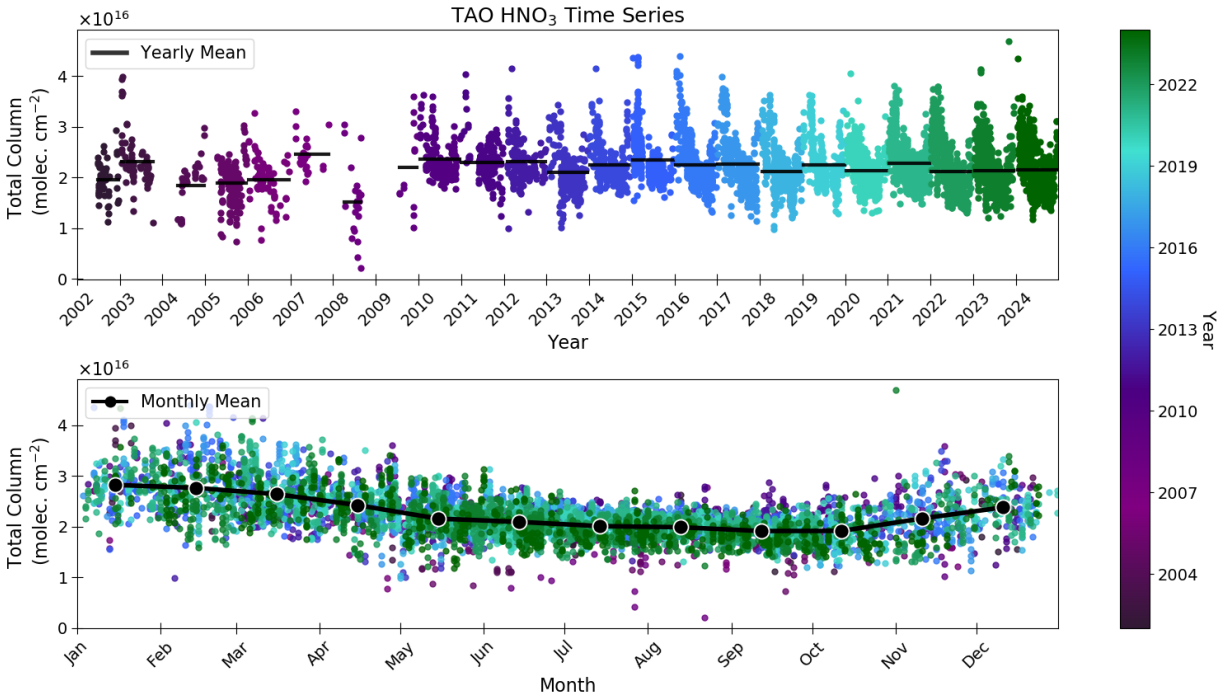

Figure 3.15: Same as Figure 3.4 for nitric acid.

3.2.13 Nitrous Oxide

Nitrous oxide (N_2O) is a tropospheric species, although it has contributions (see VMR profile in Figure 3.2) and retrieval sensitivity in the stratosphere as well (sensitivity>0.5 from the surface to approximately 27 km). With a lifetime of over a century, N_2O is transported into the stratosphere where it can act as an ozone-depleting substance (Ravishankara et al., 2009). There are several sources, both natural and anthropogenic, such as soils, wildfires, wetlands, industrial and agricultural activities (Jacob, 1999). There is no seasonal cycle observed in the total columns at TAO (see Figure 3.16), although total column depletion has been used to identify polar vortex intrusions (Whaley et al., 2013). This dataset was used as part of the N_2O validation for the ACE–FTS (Strong et al., 2008).

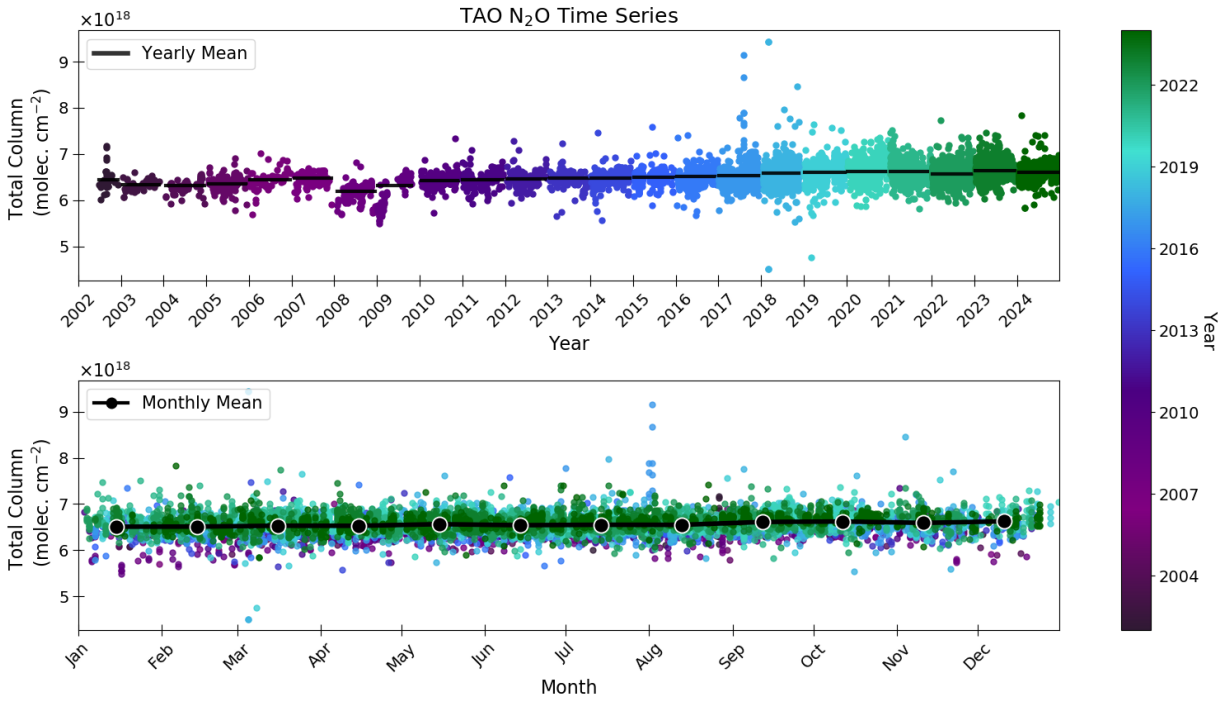

Figure 3.16: Same as Figure 3.4 for nitrous oxide.

3.2.14 Ammonia

Ammonia (NH_3) is a tropospheric species, which is represented by the VMR profile in Figures 3.2 and 3.3. The retrieval has a sensitivity >0.5 up to 21 km, however the total column AVK is nearly identical to the 0-12 km AVK and this region accounts for essentially all of the DOFS. NH_3 plays a role in aerosol formation, with an atmospheric lifetime ranging from a few hours to a few days, leading to numerous episodic features (Van Damme et al., 2018; Yamanouchi et al., 2023). The time series and seasonal cycle at TAO (Figure 3.17) shows several enhancements in the spring, largely attributed to agricultural emissions, a primary source in the region. NH_3 over Toronto has been reported to be increasing at a rate of 3.34 % per year (from 2002-2018) based on the TAO FTIR column; surface and satellite measurements also showed an increasing trend over this period (Yamanouchi et al., 2021b). Local levels are further influenced by industrial activities and fossil fuel combustion, of which the highest concentrations have been attributed to long-range transport from the United States (predominantly south/southwest of Toronto) (Viatte et al., 2022). This dataset has been used to validate satellite NH_3 data products from IASI (Dammers et al., 2016) and the Cross-track Infrared Sounder (CrIs) (Dammers et al., 2019). Additional peak enhancements correspond to biomass burning events, some of which are discussed in Chapter 6 for the 2023 Canadian wildfires.

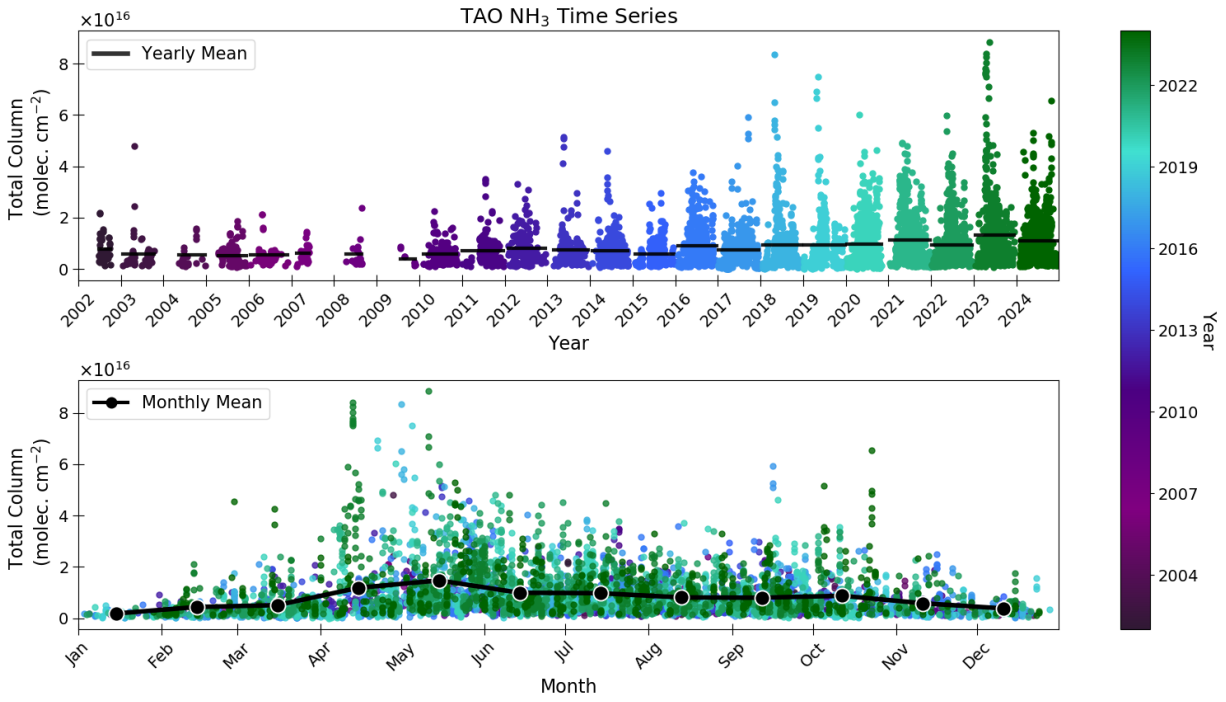

Figure 3.17: Same as Figure 3.4 for ammonia.

3.2.15 Ozone

Ozone (O_3) is primarily a stratospheric species, with the profile dominated by the ozone layer (at approximately 25 km). The retrieval has sensitivity>0.5 from about 4-40 km, with a mean DOFS in the troposphere of 1 and a mean DOFS in the stratosphere of 2.65, allowing it to be used for studies in both regions. In the stratosphere, the lifetime of ozone is on the order of hours to months, governed by altitude, and the photochemical processes of the Chapman mechanism and loss by reactions with hydrogen oxides (HOx), NO_X, and ozone-depleting substances (i.e., HCFCs, CFCs, halons…) (Jacobs, 1999). The total column time series (Figure 3.18) has a seasonal cycle with a maximum in the spring related to the poleward and downward transport into the region via Brewer-Dobson circulation, and a minimum in late summer/fall when photochemical reactions dominate.

In the troposphere, O_3 is an oxidant and precursor for OH, which controls the oxidizing power in the troposphere, while also negatively impacting air quality and acting as a GHG. Tropospheric O_3 can be transported from the stratosphere (Hocking et al., 2007), although it is primarily produced as a secondary pollutant from precursor gases such as NO_x and VOCs. As a result, lifetimes are variable, ranging from hours to weeks (based on location and season), classifying it as an SLCF (Monks et al., 2015). Whaley et al. (2015) used tropospheric O_3 measurements from

TAO collected between 2004 and 2007, along with a tagged GEOS-Chem transport model, to investigate O_3 pollution events in the Toronto area. The findings indicate that events are most sensitive to fossil fuel NOx, which can be transported from southern Ontario and the United States and are correlated with high temperature and pressure systems. Tropospheric O_3 measurements in the Northern Hemisphere during the COVID-19 pandemic (April-August 2020) showed an average decrease of 7% compared to the 2000-2020 mean; within this period the TAO measurements were reported to have an average anomaly of -4.9% (Steinbrecht et al., 2021). This dataset has also been used as part of the Tropospheric Ozone Assessment Report (TOAR) Harmonization and Evaluation of Ground-based Instruments for Free Tropospheric Ozone Measurements (HEGIFTOM) Project (Van Malderen et al., 2025a; 2025b). The study reported that from 2002-2022 total tropospheric ozone ("TrOC" = surface to 300 hPa partial column) in Toronto had a negative trend between -1.15 to -1.77 ppbv/decade, depending on the regression used (quantile by observation or monthly mean or multiple linear regression by monthly mean). Tropospheric O_3 is discussed in Chapter 4 in relation to Arctic modelling, and in Chapter 6 with respect to the 2023 Canadian wildfires.

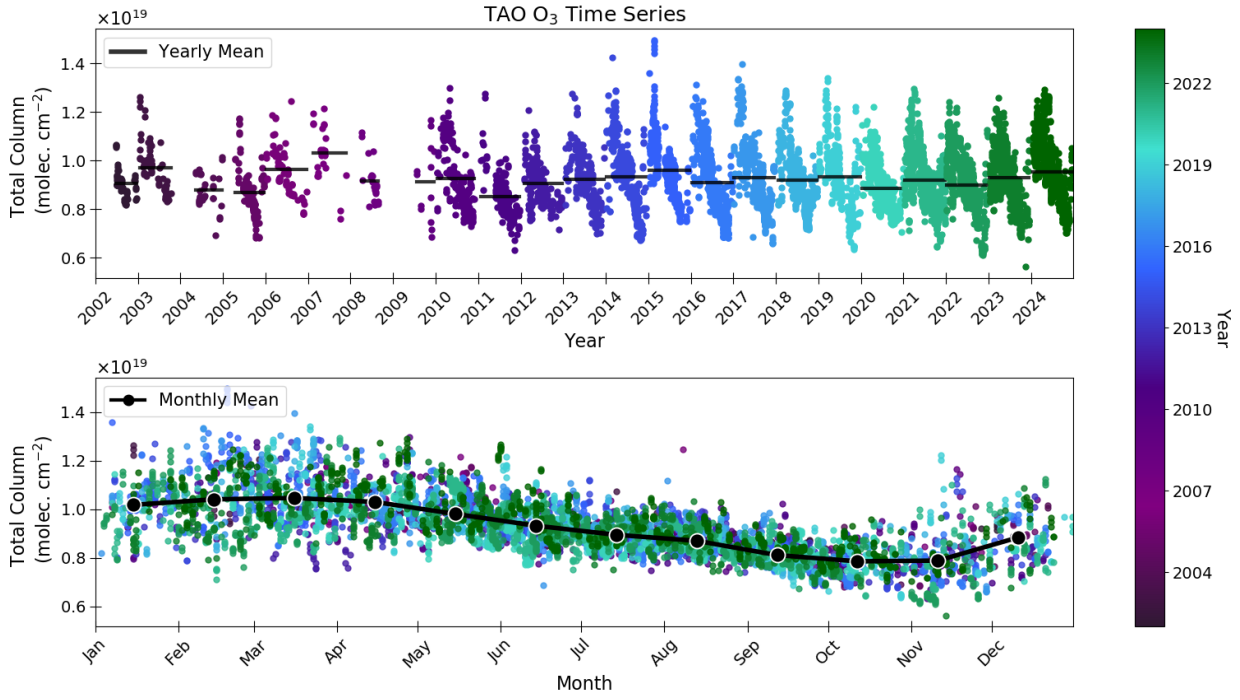

Figure 3.18: Same as Figure 3.4 for ozone.

3.2.16 Carbonyl Sulfide

Carbonyl sulfide (OCS) is the penultimate research product added to the TAO NDACC-IRWG archives as part of a network-wide trend study presented in Hannigan et al. (2022). It is the most prevalent sulfur compound in the troposphere and source to the stratosphere. It has natural and anthropogenic sources with a lifetime of approximately 2-3 years (Hannigan et al., 2022, and references therein). The seasonal cycle at TAO (Figure 3.19) peaks in the summer as a result of increased vegetation at that time. Long-term trends from 22 NDACC-IRWG FTIR stations across globe showed an overall positive trend from 2008-2016 in the troposphere, changing to a negative trend until 2020, driven by anthropogenic emissions. Following the same trend, from 2008 to 2016 OCS at TAO increased by 0.76 ± 0.11% per year in the troposphere, after which it began to decrease, although this latter period is too short to quantify a trend (Hannigan et al., 2022).

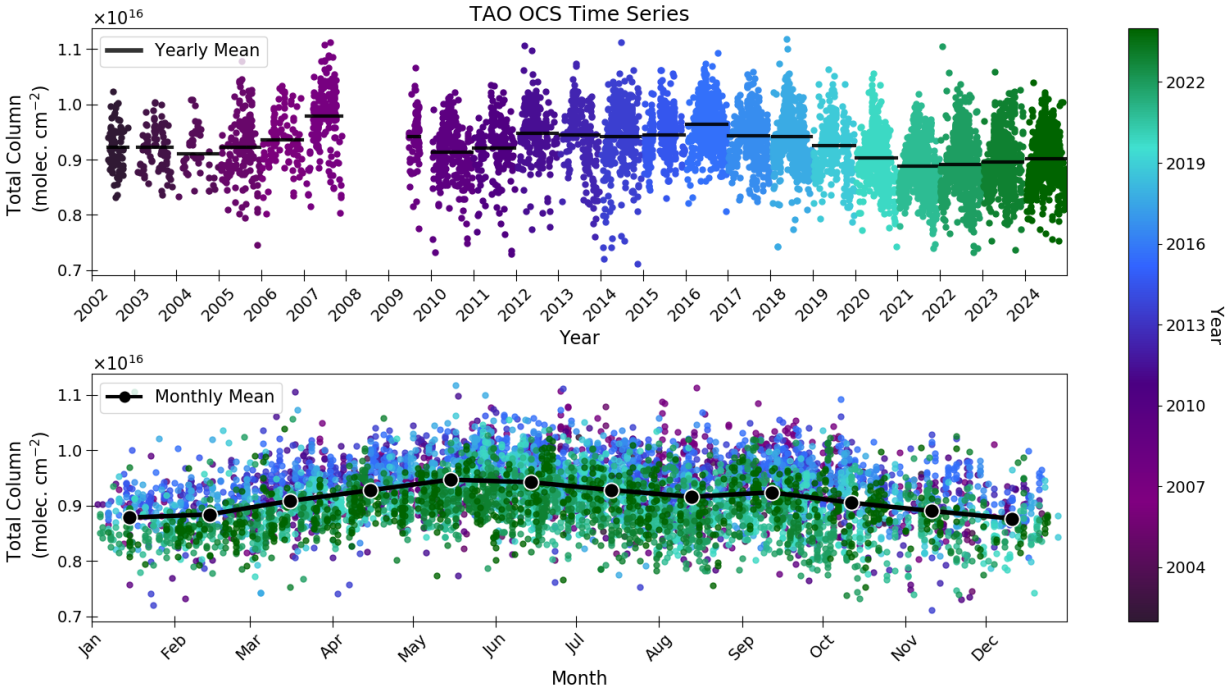

Figure 3.19: Same as Figure 3.4 for carbonyl sulfide (note: 2008 is omitted due to instrument issues causing poor data).

3.3 Ozone Retrieval Update

The NDACC IRWG O_3 Retrieval Strategy Group was assembled to work towards a harmonized FTIR retrieval strategy across the network. In this, they tested primary retrieval parameters one at a time (i.e., spectroscopy, spectral range, a priori profile, regularization…), assessing the impact on RMS fitting residuals, DOFS, uncertainty, profiles, and total columns, and comparing to other co-located instruments. They found that changing from HIT08 to HIT20, with H_2O from ATM20, decreased total column values by ~2-3%, improving comparisons with Dobson and Brewer and ozonesonde measurements. They updated the microwindows (listed in Table 3.1) to reduce interference from water vapor absorption lines, resulting in improved RMS and vertical sensitivity. The change in a priori from WACCM version 6 to version 7 did not result in better statistics for O_3, but was chosen to be updated for consistency with other target molecules that did have improvements with the updated version (note this corresponds to the WACCM v6 model output, the averaged and interpolated profiles for IRWG are denoted as ".v7"). Regularization was tested by comparing Tikhonov and OEM retrievals; there was no effect on the total column, however, the Tikhonov approach resulted in improved agreement with ozonesondes in the troposphere, but not in the lower/middle stratosphere (compared to OEM), and improved the long-term trend comparison with ozonesondes.

After the strategy group determined the most optimal parameters, they were sent out to the wider NDACC-IRWG group to be implement into their retrieval, as version "irwg2023". The key changes for TAO with this update involved updating the SFIT4 version from v0.9.4.4 to v1.0.18, modifying the microwindows, and changing the retrieval from OEM to Tikhonov, which required selecting a correlation alpha value (α). Described in Chapter 2, α acts as a scale factor that constrains the retrieved profile to the a priori profile. An α that is too small will give larger DOFS as the profile is less constrained and may fit variations attributed to noise, an α that is too large will give small DOFS and over-constrain the retrieval to the a priori profile. It is important to balance a realistic DOFS with allowing the retrieval to vary. The O_3 correlation α was chosen by testing several different options and reviewing the retrieved profile shape, DOFS, RMS fitting residual, chi-squared, and microwindow spectral fits.

Figure 3.20 shows an example of the testing output for a TAO measurement taken on July 20, 2021 (at 19:57:52 UTC); this was used to assess the impact of different α values on the total column

value, RMS fitting residual, DOFS, χ^2, and profile shapes. Ultimately, α=8000 was chosen through trial and error to best balance a reasonable average DOFS and profile shape. Table 3.3 shows the mean DOFS and percent uncertainty for the 2002-2023 time series with the previous method and the new method. Figure 3.21 shows a comparison of the previous (v0.9.4.4, navy dots) and the updated (v1.0+, green x markers) O_3 time series; the slightly smaller total column is expected (average -2.67%) with HIT20.

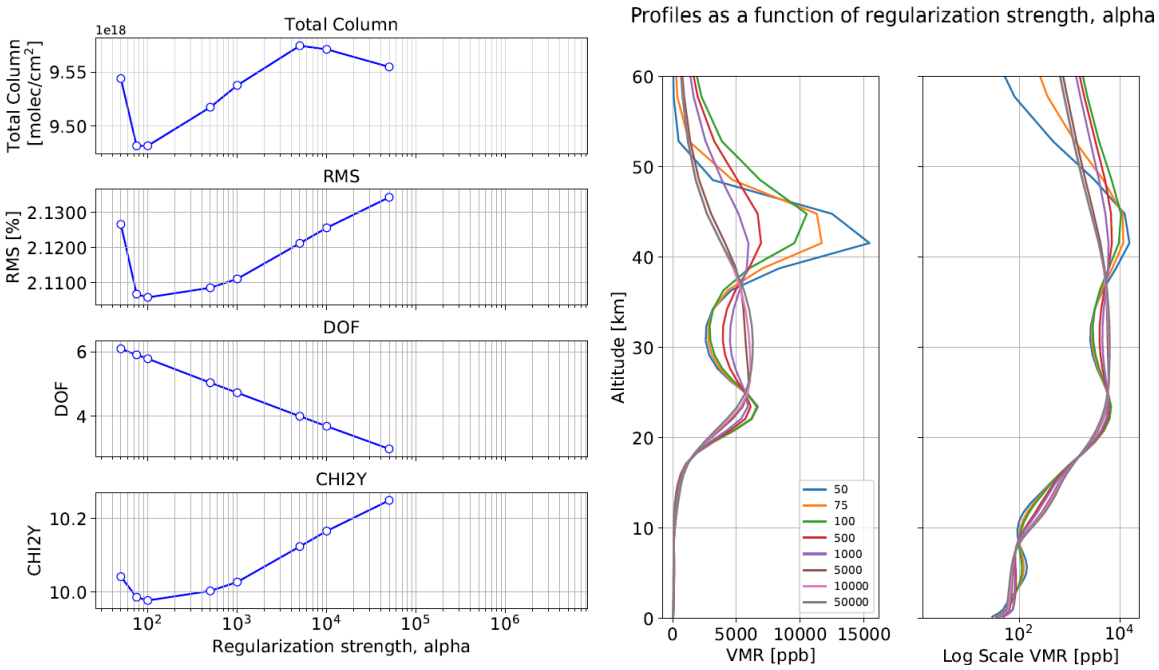

Figure 3.20: Example of the Tikhonov α testing outputs for ozone retrieval "20210720.195752".

Table 3.3: Comparison between the mean DOFS ± one standard deviation and mean overall percent uncertainty for TAO ozone retrievals from 2002-2023 SFIT4 v0.9.4.4 with OEM and v1.0+ with Tikhonov regularization (α=8000).

	Original v0.9.4.4	**Updated v1.0+**
Retrieval	Optimal estimation	Tikhonov regularization
Mean DOFS	4.41±0.52	3.67±0.21
Mean Overall Uncertainty (%)	5.52	3.94

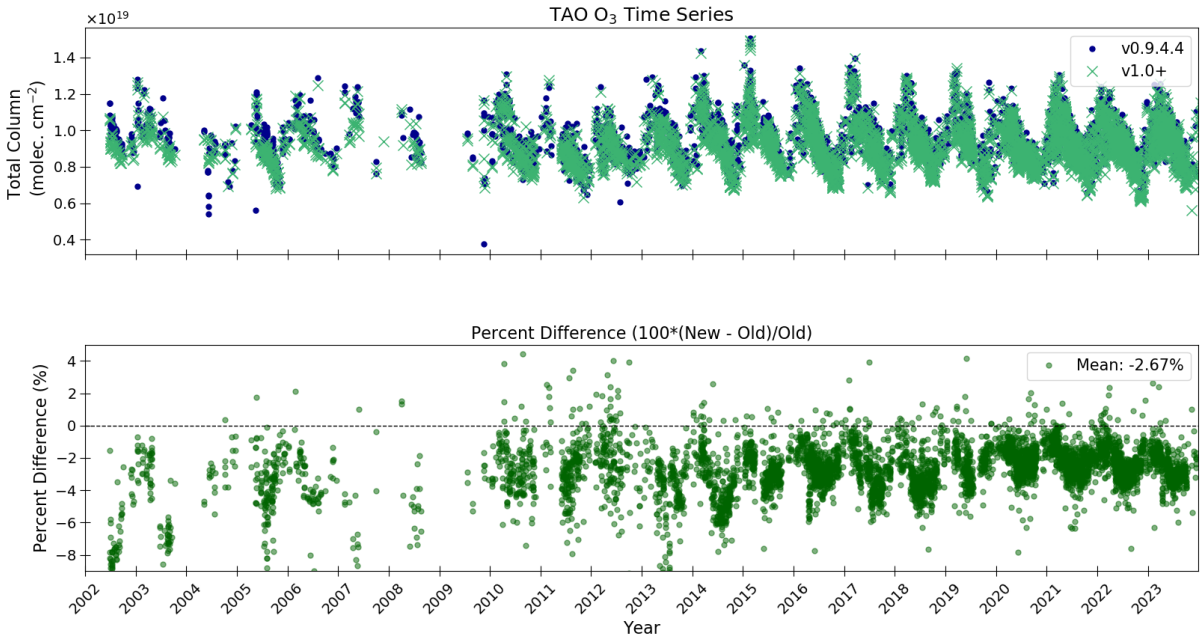

Figure 3.21: Upper panel: Comparison between the previous (navy dots) and the updated (green x) O_3 total column. Lower panel: Percent difference between the two retrievals (100[new-old]/old).*

Chapter 4

4 Evaluating Modelled Tropospheric Columns of CH_4, CO and O_3 in the Arctic Using FTIR Measurements

This chapter evaluates tropospheric columns of CH_4, CO and O_3in the Arctic simulated by 11 models, using data from five high-latitude ground-based FTIR spectrometers in NDACC. The models were selected as part of the 2021 AMAP Report on short-lived climate forcers. This work augments the model–measurement comparisons presented in that report by including a new data source: column-integrated FTIR measurements, whose spatial and temporal footprint is more representative of the free troposphere than in situ and satellite measurements. This work is published in *Atmospheric Chemistry and Physics*, as "Evaluating modelled tropospheric columns of CH_4, CO and O_3 in the Arctic using ground-based Fourier transform infrared (FTIR) measurements" (Flood et al., 2024).

4.1 Introduction

Five of the 28 NDACC FTIR stations are located at latitudes north of 60˚ N; for the purpose of this study, these will all be referred to as Arctic sites. The five sites are Eureka, Canada; Ny Ålesund, Norway; Thule, Greenland; Kiruna, Sweden; and Harestua, Norway. These high-latitude NDACC FTIR instruments provide a valuable set of long-term, measurements of multiple species of interest in the Arctic. Performing model–measurement comparisons with partial column data supports and thus complements the assessments presented in the 2021 AMAP Report. Previous studies have used FTIR data to examine model biases in the Arctic (e.g., Wespes et al., 2012; Zhou et al., 2019; Mahieu et al., 2021).

AMAP has provided reports on SLCF impacts on the Arctic dating back to 2008. The 2021 AMAP SLCF Assessment Report assesses the impacts of black carbon, CH_4, O_3, and sulfate aerosols on the air quality, climate, and human health in the Arctic region (AMAP, 2021). A key difference from previous AMAP reports is the emphasis on air quality and human health. In addition to these SLCFs, the analysis includes the SLCF precursor gases CO, nitric oxide (NO), and nitrogen dioxide (NO_2). The report compares the output from 18 models with various historical measurements, including satellite, aircraft, ship, and in situ datasets. These observations are used

to assess what processes need to be revised in the models and how these shortcomings impact the further application of the models, such as for climate and health predictions. Other chapters explore emissions, measurement advances, trends, climate and air quality impacts, health ecosystem impacts, and next steps. A prominent theme in this report is the severity of change happening in the Arctic. This includes the amplification of the pace of change in physical drivers, such as temperature and snow cover, and the frequency of extreme events, such as wildfires and incidents of rapid sea-ice loss. These factors contribute to ecosystem disruption, directly affecting local Arctic communities, in addition to having global repercussions. SLCF reductions are motivated by the near-term (20-30 years) benefits and by the goal of slowing the warming of the Arctic climate, which results in more wildfires and permafrost melt and, in turn, an increase in emissions of SLCFs and precursor gases (AMAP, 2021). The projections in this report provide guidance, objectives, and cautions for potential reduction implementation scenarios (AMAP, 2021).

Measurements in the Arctic are difficult due to the harsh environment, remote locations, and high operating costs, resulting in a scarcity of monitoring stations and a limited representation of atmospheric vertical information. Using measurements to evaluate model simulations of the Arctic is important because the latter are used to project future changes in the Arctic, a region that is sensitive to climate change, warming at a rate 3 to 4 times the global average (Bush and Lemmen, 2019; Ballinger et al., 2020; AMAP, 2021; IPCC, 2021; Rantanen et al., 2022). These factors have led to initiatives like the AMAP SLCF assessment and the POLARCAT (Polar Study using Aircraft, Remote Sensing, Surface Measurements and Models, of Climate, Chemistry, Aerosols and Transport) Model Intercomparison Project (POLMIP), which, in part, aim to assess model performance in the Arctic region. POLMIP examined 11 atmospheric models in relation to a variety of Arctic observations taken as part of the International Polar Year in 2008 (Emmons et al., 2015). AMAP and POLMIP, in addition to the subsequent complementary publications (i.e., Wespes et al., 2012; Emmons et al., 2015; Monks et al., 2015; Whaley et al., 2022, 2023, Law et al., 2023), provide a valuable point of reference for the modelling of CH_4, CO, and O_3 in the Arctic, which is explored in this chapter. This allows for the findings presented here to be appraised relative to results from the same models compared to other instruments, with differing temporal frequency and altitude ranges (i.e., Whaley et al., 2022, 2023), with different simulations and Arctic FTIR measurements (i.e., Wespes et al., 2015), and to generally assess the similarities and differences that arise within Arctic SLCF modelling.

This project examines simulations from 11 models that were run for the 2021 AMAP SLCF Assessment Report, to assess the agreement between modelled trace gas concentrations and ground-based retrievals from high-latitude FTIR spectrometers. Specifically, this chapter presents comparisons of CH_4, CO and O_3 partial columns (from 0-7 km) for the years 2008, 2009, 2014, and 2015. The models examined are chemical transport and climate models: CESM, CMAM, DEHM, EMEP MSC-W, GEM-MACH, GEOS-Chem, MATCH, MATCH-SALSA, MRI-ESM2, UKESM1 and WRF-CHEM (see Table 4.3). The objective is to utilize the high-quality, long-term Arctic FTIR datasets to assess how well the models perform. The remainder of this chapter is organized as follows: Section 4.2 provides a description of the datasets used, Section 4.3 describes the analysis methodology, Section 4.4 examines the results and compares them with similar studies, and Section 4.5 presents the summary and conclusions. The appendix for this chapter is Appendix A, and follows after Chapter 7.

4.2 Datasets

4.2.1 FTIR Spectroscopy

The primary references and details of the NDACC FTIR sites used in this study are presented in Table 4.1. As these instruments require sunlight and a clear line-of-sight to the sun to make measurements, the high-latitude datasets are limited to the sunlit portion of the year at each location. Refer back to Chapter 2 for details of FTIR spectroscopy. All sites included in this study use SFIT4, except Kiruna, which uses a comparable retrieval code called PROFFIT, which has been shown to agree well with SFIT2 (which preceded SFIT4) (Hase et al., 2004).

The number of measurements, mean DOFS, and mean percent uncertainty in the 0-7 km partial columns of CH_4, CO, and O_3 for 2008, 2009, 2014, and 2015, for each station, are listed in Table 4.2. The mean systematic and random percent errors are added in quadrature to get the overall mean percent uncertainty for the species. The mean partial column (0-7 and 7-20 km) and total column AVKs for CH_4, CO, and O_3 for 2008, 2009, 2014, and 2015, are shown in Figure 4.1. The lowest-level difference between Kiruna and the other locations results from the use of a stronger constraint for the lowest level with the PROFFIT retrieval; however, retrieval error and noise indicate that the agreement between the AVKs is reasonable (Hase et al., 2004).

Table 4.1: Summary of NDACC FTIR sites used in this study.

Site	Location	Key References	Operations
Eureka, Canada	80.05°N, 86.42°W 610 masl	Batchelor et. al. (2009)	Late February to Mid-October
			Since 2006
Ny Ålesund, Norway	78.92°N, 11.93°E 15 masl	Notholt et al. (1997a,b); Notholt et al. (2000)	Mid-March to September
			Since 1992
Thule, Greenland	76.53°N, 68.74°W 225 masl	Hannigan et al. (2009)	March to October
			Since 1999
Kiruna, Sweden	67.84°N, 20.41°E 419 masl	Blumenstock et al. (1997, 2009)	Mid-January to November
			Since 1996
Harestua, Norway	60.2°N, 10.8°E 596 masl	Galle et al. (1999)	All Year
			Since 1994

Table 4.2: Summary of FTIR measurement statistics for the five NDACC stations used in this study.

Site	Number of Measurements (2008, 2009, 2014, 2015)			Mean DOFS (0-7 km)			Mean Percent Uncertainty (0-7 km)		
	CH_4	CO	O_3	CH_4	CO	O_3	CH_4	CO	O_3
Eureka	754	736	684	0.84	1.1	0.80	4.6	3.9	8.2
Ny Ålesund	205	128	121	0.81	1.3	0.79	11.5	7.7	4.9
Thule	406	459	474	0.78	1.6	1.2	5.7	5.4	3.9
Kiruna	397	299	322	0.96	1.6	0.86	3.6	6.4	7.2
Harestua	151 (no 2008)	No CO	169 (no 2008)	0.78	N/A	1.12	5.2	N/A	4.1

As described in Chapter 2, the DOFS and AVKs are indicators of the vertical information within a retrieval. Figure 4.1 shows that the mean partial column AVKs for 0-7 and 7-20 km are distinguishable, with maxima at different altitudes. The mean total column AVKs for all three species appear smooth around 1.0, which indicates that contributions from all altitudes have similar weights in the total column. By altitude, the sensitivity of each species is >0.5 in the 0-7 km partial column range examined (not shown), meaning that more than half of the retrieved profile information comes from the measurement (Vigouroux et al., 2009). The average DOFS vary by

species and station, given the reduced column height of 0-7 km; some of the values are less than 1, meaning the retrieval is somewhat constrained by the a priori profile. However, it should be noted that the comparisons presented in this chapter account for the vertical sensitivity of the FTIR measurements by smoothing the model data with the AVKs.

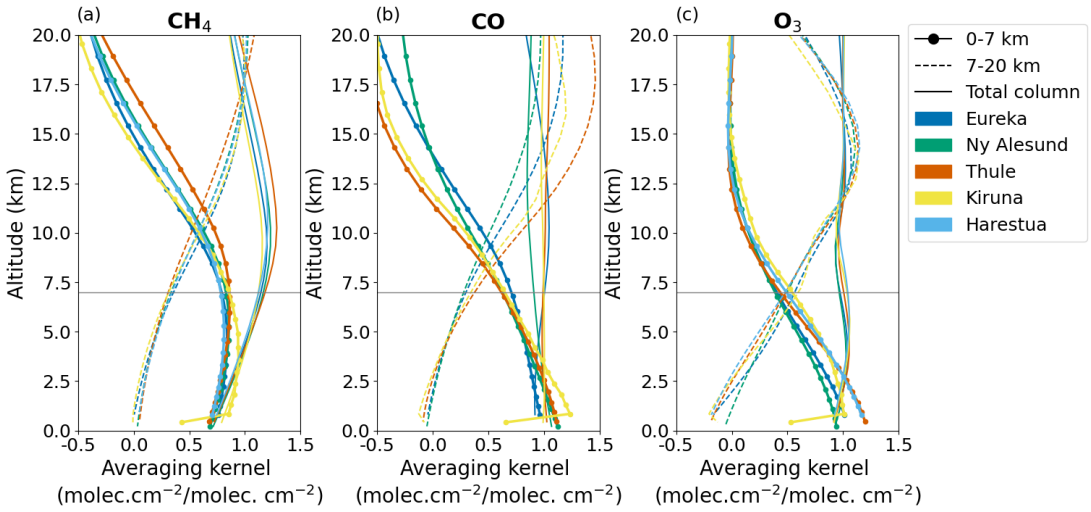

Figure 4.1: Mean 0-7 km partial column averaging kernels (lines with circle markers), mean 7-20 km partial column averaging kernels (dashed lines), and mean total column averaging kernels (solid lines), all in units of (molec/cm^2) / (molec/cm^2), by altitude, for (a) CH_4, (b) CO, and (c) O_3. Means are for 2008, 2009, 2014, and 2015 for all five FTIR sites except Harestua (no 2008 data).

4.2.2 Atmospheric Models

The models used in this study provide three-dimensional VMR fields for 2008, 2009, 2014, and 2015. These four years were selected for the 2021 AMAP SLCF Assessment; 2008 and 2009 were previously evaluated in the 2015 AMAP Report and 2014 and 2015 were added to include more recent results from years for which Arctic measurements were available at the time (AMAP, 2021). Note that not every model has provided all three gases; there are three which have CH_4, nine with CO, and 11 with O_3 (see Table 4.3). The model simulations are the same as those discussed in Whaley et al. (2022, 2023), and in the 2021 AMAP SLCF Report, however, the analyses there were performed with the monthly-mean output, while the analysis here is with the 3-hourly output, all of which is available at http://crd-data-donnees-rdc.ec.gc.ca/CCCMA/products/AMAP/. While more models participated in the AMAP SLCF Assessment (18 total) and other species were simulated, these were not included in the current study because either the models did not have 3-hourly outputs or the FTIR retrievals had insufficient tropospheric sensitivity (e.g., NO_2).

This set of models is a mix of Earth system models, chemical transport models, global transport models, and chemistry climate models. The models all used the same set of anthropogenic emissions from ECLIPSE v6b (Evaluating the Climate and Air Quality Impacts of Short-Lived Pollutants) by the IIASA GAINS (International Institute for Applied Systems Analysis – Greenhouse gas – Air pollution Interactions and Synergies) model (Amann et al., 2011; Klimont et al., 2017; Höglund-Isaksson et al., 2020). However, the models differ in their use of biogenic and volcanic emissions, tropospheric gas-phase chemistry complexity, and pressure/spatial grids. Four of the 11 models simulate the stratosphere fully, one (GEOS-Chem) uses a simplified linearized stratospheric chemistry, one (GEM-MACH) only simulates the troposphere and the rest use prescribed climatologies at the stratospheric boundary (Whaley et al., 2022). Nine of the 11 models examined use the Global Fire Emissions Database (GFED, van der Werf et al., 2017) or GFED-based (Coupled Model Intercomparison Project Phase 6 - CMIP6) forest fire emissions, and nine of the 11 exclusively use ECLIPSEv6b for agricultural waste burning. A summary of the models is presented in Table 4.3, including which gases are included in this study, their resolution, and to what degree stratospheric chemistry is considered. It should be noted that the CH_4 concentrations in these models have been prescribed (Whaley et al., 2022). The prescribed concentrations are input at the bottom model layer, and all come from the same dataset (Prather et al., 2012; Olivié et al., 2021), but the resulting CH_4 partial columns differ based on the processes within each model. For a full description of the models, see Appendix A of Whaley et al. (2022) and the references in Table 4.3.

Table 4.3: Summary of models used in this study.

Model	3-Hourly Outputs	Primary Reference	Horizontal Resolution / Scale	Stratospheric Chemistry
CESM *Community Earth System Model*	CO, O_3	Liu et al. (2016); Danabasoglu et al. (2020)	1.9° × 2.5° global	comprehensive
CMAM *Canadian Middle Atmosphere Model*	CH_4, CO, O_3	Jonsson et al. (2004); Scinocca et al. (2008)	3.75° × 3.75° global	comprehensive
DEHM *Danish Eulerian Hemispheric Model*	O_3	Christensen (1997); Brandt et al. (2012); Massling et al. (2015)	50 km polar stereographic	none
EMEP MSC-W *European Monitoring and Evaluation System-Meteorological Synthesizing Center - West*	CO, O_3	Simpson et al. (2012, 2019)	0.5° × 0.5° global	prescribed
GEM-MACH *Global Environmental Multiscale Model - Modelling Air Quality and Chemistry*	CO, O_3 (only 2015)	Gong et al. (2015); Makar et al. (2015a,b); Moran et al. (2018)	15 km Arctic regional	none
GEOS-Chem *Goddard Earth Observing System - Chemistry*	CH_4, CO, O_3	Bey et al. (2001)	2° × 2.5° global	simplified
MATCH *Multi-Scale Atmospheric Transport Chemistry*	CO, O_3	Robertson et al. (1999)	0.75° rotated lat-lon regional	prescribed
MATCH-SALSA *Multi-Scale Atmospheric Transport Chemistry - Sectional Aerosol Module for Large Scale Applications*	CO, O_3	Robertson et al. (1999); Andersson et al. (2007); Kokkola et al. (2008)	0.75° rotated lat-lon regional	prescribed
MRI-ESM2 *Meteorological Research Institute - Earth System Model Version 2*	CH_4, CO, O_3	Kawai et al. (2019); Yukimoto et al. (2019); Oshima et al. (2020)	chemistry: 280 km general: 120 km global	comprehensive
UKESM1 *U.K. Earth System Model Version 1*	O_3	Kuhlbrodt et al. (2018); Williams et al. (2018); Sellar et al. (2019)	140 km global	comprehensive
WRF-CHEM *Weather Research and Forecasting Model with Chemistry*	CO, O_3 (only 2014 / 2015)	Marelle et al. (2017, 2018)	100 km regional-Arctic	prescribed

4.3 Methods

As mentioned, the models provided 3-hourly VMRs on model-specific pressure levels and latitude/longitude grids. The process of aligning the model output to FTIR data is described by the flowchart in Figure 4.2.

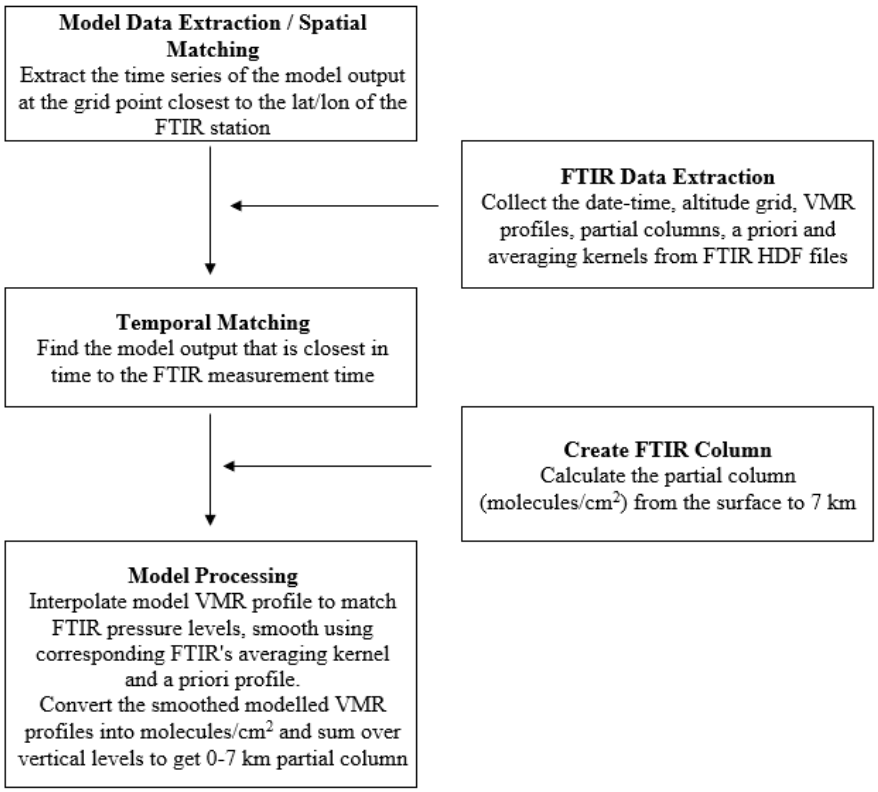

Figure 4.2: Flow chart depicting the process of matching model output to FTIR data.

This procedure modifies the model output to correspond to an FTIR measurement, making the resulting partial columns equivalent for further comparison. The date/time and VMR profiles from the model output are extracted from the grid point that is closest to the FTIR location. The FTIR measurements are matched with the 3-hourly model measurement closest in time (within $\pm<1.5$ hours), this is done to minimize the time difference between the two points, such that no measurement is greater than 1.5 hours from a modelled output. If more than one FTIR measurement coincides with a model output (i.e., multiple measurements are within 1.5 hours of the same model time), the FTIR measurements are averaged. After the model outputs are matched to the FTIR measurements, they are interpolated onto the pressure grid of the FTIR profile. Then, the model VMR profile is smoothed using the respective FTIR measurement's AVK and a priori

profile. The purpose of smoothing the model data with the FTIR AVK is to adjust the model to the vertical sensitivity of the FTIR measurement (Rodgers and Connor, 2003; Wunch et al., 2010). The calculation for the smoothing is shown in Equation 4.1, where $\mathbf{x_a}$ is the FTIR a priori VMR vertical profile, **A** is the VMR AVK matrix from the corresponding FTIR measurement, and $\mathbf{x}_{model}$ is the modelled VMR vertical profile:

$$\boldsymbol{x}_{smooth} = \mathbf{x}_\mathrm{a} + \mathbf{A} \times [\mathbf{x}_{model} - \mathbf{x}_\mathrm{a}] \ . \tag{4.1}$$

The model VMR profile is then transformed to a layer profile in units of molecules per centimeter squared using the ratio between the VMR and layer partial column (in molecules per centimeter squared) in the retrieved FTIR profile as the conversion factor. At this point, the model output has the same altitude grid and units as the FTIR retrieval, which allows for partial columns to be summed. Partial columns from 0-7 km were calculated given AMAP's focus on SLCFs in the troposphere, with the cap at 7 km chosen to limit any stratospheric influence. Note that "0 km" is used as a proxy for the minimum altitude, but this varies, based on location, with the altitude of each instrument listed in Table 4.1. The partial column examined here (0-7 km) encompasses 11 vertical layers for all sites, except Ny Ålesund, which has an additional (12^{th}) layer given the lower altitude of its location (see Table 4.1).

To compare the model and FTIR partial columns, a model-measurement percent difference (Δ_i) is calculated, as defined by Equation 4.2 for a single model-measurement pair (i), where $PC_{M,i}$ and $PC_{F,i}$ are the 0-7 km partial columns for the model and FTIR, respectively:

$$\Delta_i = \left(\frac{PC_{M,i} - PC_{F,i}}{PC_{F,i}} \right) \times 100 \ . \tag{4.2}$$

A regression line is fit to the raw scatter-plot data of the model output versus FTIR measurements using all the available data points, where each plot includes the equation of this line and the correlation coefficient, R^2. The normalized root mean square error (NRMSE), given by Equation 4.3, is presented for each model and location, where *N* is the total number of model-measurement pairs (Kärnä and Baptista, 2016). The root mean square error is normalized to the standard deviation of the FTIR data (σ_F) used in the respective analysis:

$$NRMSE = \frac{1}{\sigma_F}\sqrt{\left[\sum_{i=1}^{N}\frac{(PC_{M,i} - PC_{F,i})^2}{N}\right]}. \quad (4.3)$$

In addition to evaluating the models using every available FTIR data point in the analysis years, the monthly mean annual cycles are also presented. The monthly mean partial columns ($PC_{F,monthly,j}$) are calculated by taking the mean of every measurement in a given month (j), where N_j is the number of points included in the month for all years considered. The monthly model mean partial columns ($PC_{M,monthly,j}$) are made in the same manner, using only the smoothed partial columns that have a corresponding matching FTIR measurement, as defined above. Equation 4.4 outlines the calculation of a monthly mean partial column for month j for (a): the FTIRs ($PC_{F,monthly,j}$), and (b): the models ($PC_{M,monthly,j}$):

$$PC_{M,monthly,j} = \frac{1}{N_j}\sum_{i=1}^{Nj} PC_{M,i}\,, \quad (4.4a)$$

$$PC_{F,monthly,j} = \frac{1}{N_j}\sum_{i=1}^{Nj} PC_{F,i}\,. \quad (4.4b)$$

The model-measurement monthly mean percent difference ($\Delta_{monthly,j}$), shown by Equation 4.5, follows the same process as the monthly-mean partial column, and is the mean value from Equation 4.2 for each month (j) across the years, where the error bars on the monthly mean plots represent the standard deviation of this mean:

$$\Delta_{monthly,j} = \frac{1}{N_j}\sum_{i=1}^{Nj} \Delta_i\,. \quad (4.5)$$

The mean of these monthly mean differences is used to calculate the overall mean percent difference (Δ_O) for each model, sometimes referred to as model bias, where N_{months} is the number of measurement months in a calendar year at that location (see Table 4.1), and the uncertainty given is the standard deviation of this mean:

$$\Delta_O = \frac{1}{N_{months}} \sum_{j=1}^{N_{months}} \Delta_{monthly,j}. \quad (4.6)$$

Finally, the monthly multi-model mean (MMM) partial column for month j ($PC_{MMM,monthly,j}$) is calculated by taking the mean $PC_{M,monthly,j}$ for all models, at a given location, calculated with Equation 4.4a, and the MMM monthly mean difference ($\Delta_{MMM,monthly,j}$) is the mean of $\Delta_{monthly,j}$ for all models, at a given location calculated with Equation 4.5. The overall percent difference of the MMM-measurement ($\Delta_{O,MMM}$) is given by Equation 4.7:

$$\Delta_{O,MMM} = \frac{1}{N_{months}} \sum_{j=1}^{N_{months}} \Delta_{MMM,monthly,j}. \quad (4.7)$$

These steps are taken to establish the modelled seasonal cycles, and quantify the differences between the models and measurements, by month and season. Further, assessing the MMM by month allows for a general overview of when and where models diverge from measurements and can help suggest shortcomings in the models. There are not enough measurements per day to evaluate a diurnal cycle, although it is expected to be small in the Arctic, and there are not enough years available in the 3-hourly dataset used here to examine long-term trends.

When discussing FTIR uncertainty, this refers to the mean uncertainty per gas and station, as listed in Table 4.2. When discussing the mean difference between the model and measurements, this refers to the overall mean difference (Δ_O) as described by Equation 4.6. These two parameters are used to assess model performance: if Δ_O is within measurement (FTIR) uncertainty, the model can be considered in general agreement with the FTIR; if $\Delta_O \pm$ the standard deviation of the mean is within the measurement uncertainty, then the model is sometimes in agreement with the measurements; and if the uncertainty and Δ_O do not overlap then the model and measurements do not agree.

4.4 Results and Discussion

This section presents the analyses described above, for CH_4, CO and O_3, and discusses the findings in the context of the 2021 AMAP SLCF Assessment Report, and other related literature. Given the volume of data (three species, five locations, and 11 models), only selected plots are shown in the

main text, with the remaining figures provided in Appendix A. This appendix includes plots for each location, showing the time series of the 0-7 km partial column for each measurement / model pair and the associated model minus measurement percent difference, the equivalent plot reduced to monthly mean data (an individualized version of Figures 4.3, 4.5 and 4.9), and the 0-7 km column of FTIR vs smoothed model for the remaining locations (analogous to Figures 4.4, 4.8 and 4.10). Figure 4.15 provides a summary of the overall differences for each model and location by species, as described by Equation 4.6. Table 4.4 summarizes the overall MMM difference for each species at each location, and the overall average for each species. All the comparisons shown are for a 0-7 km partial column, where the model output is smoothed as described by Equation 4.1.

4.4.1 CH_4

CH_4 is a powerful GHG, and its emissions are expected to increase in the Arctic due to melting permafrost (IPCC, 2021). CH_4 is also involved in the formation of tropospheric O_3, which is the third strongest anthropogenic GHG and an air pollutant at the surface. Therefore, it is important for both air quality and climate models to represent CH_4 accurately. The CH_4 plots for Ny Ålesund, Thule, Kiruna, and Harestua are provided in Appendix A.I, following the same order discussed here for Eureka.

Figure 4.3 shows the monthly mean 0-7 km partial column time series for the FTIR and models at each location (a-e), with the percent difference between the monthly mean model and monthly mean measurement for all locations shown in panel f. This shows that apart from a few outliers, the pattern of the seasonal cycle of CH_4 is consistent, although the amplitude is underestimated. The uniformity between the years (see Figures A.1-A.5 for full data time series plots) and consistency of the model biases between sites is likely a consequence of CH_4 being prescribed in the models, in addition to the longer lifetime of CH_4, relative to the other SLCFs. This is also seen in Figure 4.4 (and Figures A.11-A.14), where the model and FTIR columns are compared, with the line of best fit and R^2 as indicated in the legend.

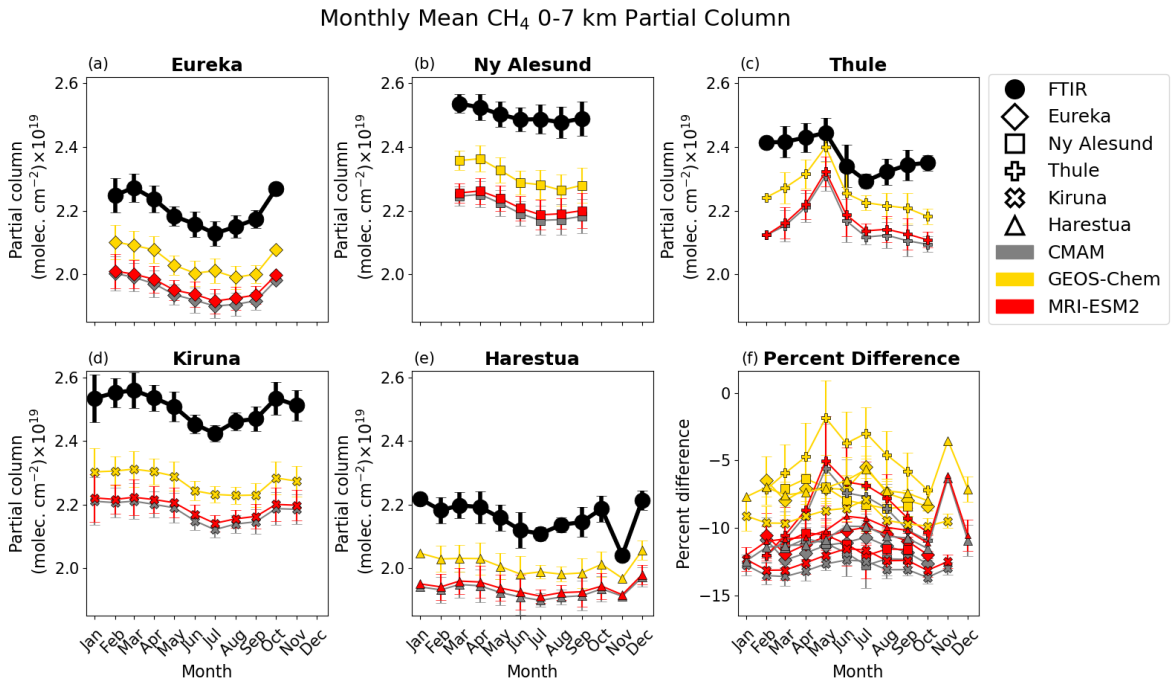

Figure 4.3: (a-e) Monthly mean FTIR (black) and smoothed model (colour) 0-7 km partial columns of CH_4 ($PC_{F,monthly,j}$ and $PC_{M,monthly,j}$, respectively), for each location, shown with the same y-axis. Error bars represent the standard deviation of the monthly mean. (f) Mean model-measurement percent difference by month ($\Delta_{monthly,j}$) for each model (by colour) and location (by marker). Error bars represent the standard deviation of the monthly mean percent difference.

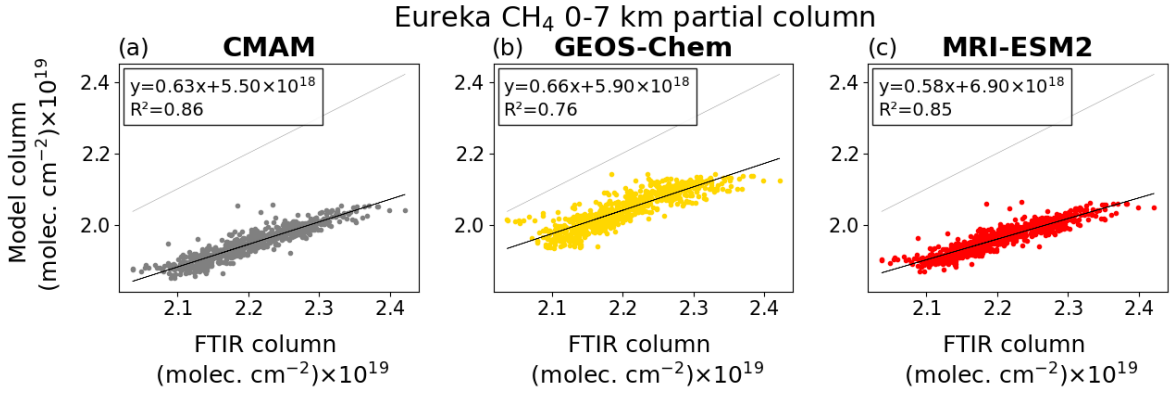

Figure 4.4: Smoothed model vs. FTIR 0-7 km partial columns of CH_4 for Eureka, showing all available model-FTIR corresponding data. The black line is the line of best fit, where the equation and R^2 are noted in the legend. The 1:1 line is shown in light grey.

A summary of the overall mean difference, R^2, and the normalized root-mean-square error for each location is shown in Figure 4.5. Across all three models, Arctic CH_4 is underestimated compared to the FTIR measurements. The surface in situ CH_4 comparison in Whaley et al. (2022) showed

that measured surface CH_4 VMRs are much more variable than the modelled VMRs. However, in the 0-7 km partial columns in this study, CH_4 is well-mixed and more homogenous, resulting in better agreement between the models and the FTIR measurements. The low bias we find in this study for the Arctic sites is consistent with the global comparisons of these models to satellite measurements in Whaley et al. (2022), which found that some models did not distribute CH_4 with an accurate north-south gradient; this resulted in low biases in the Arctic and high biases in lower latitudes due to higher CH_4 concentrations in the northern hemisphere from increased sources (both natural and anthropogenic). GEOS-Chem implemented a north-south gradient in the prescribed CH_4 (compared with the simplified global average interpolated in time that the other models prescribe at the surface), which is reflected in the smaller overall model-measurement percent difference, compared to other models, in all locations (note Figure 6 in Whaley et al., 2022). However, the R^2 of GEOS-Chem vs. FTIR is smaller than that for the other models at some locations (Eureka and Kiruna), which can be attributed to the increase in variability the gradient introduces – including some instances of overestimation. The mean differences for each model across sites are relatively consistent, while the results vary more when comparing R^2 and NRMSE. Particularly, when comparing between the same model, the R^2 for Ny Ålesund is the lowest and the NRMSE is the highest. The data from Ny Ålesund show less of a seasonal cycle than the other locations, and the FTIR uncertainty for CH_4 at Ny Ålesund is more than twice that of the other sites (see Figure 4.15). The larger uncertainty may lead to reduced sensitivity to small changes, and increased variability masking seasonal changes, which can contribute to the discrepancy between the models and observations. The mean difference for GEOS-Chem is within the uncertainty of the FTIR measurements for Ny Ålesund, and Thule, as is the mean difference for MRI-ESM2 at Ny Ålesund, none of the other models are within the FTIR uncertainty at the given location (see Figure 4.15).

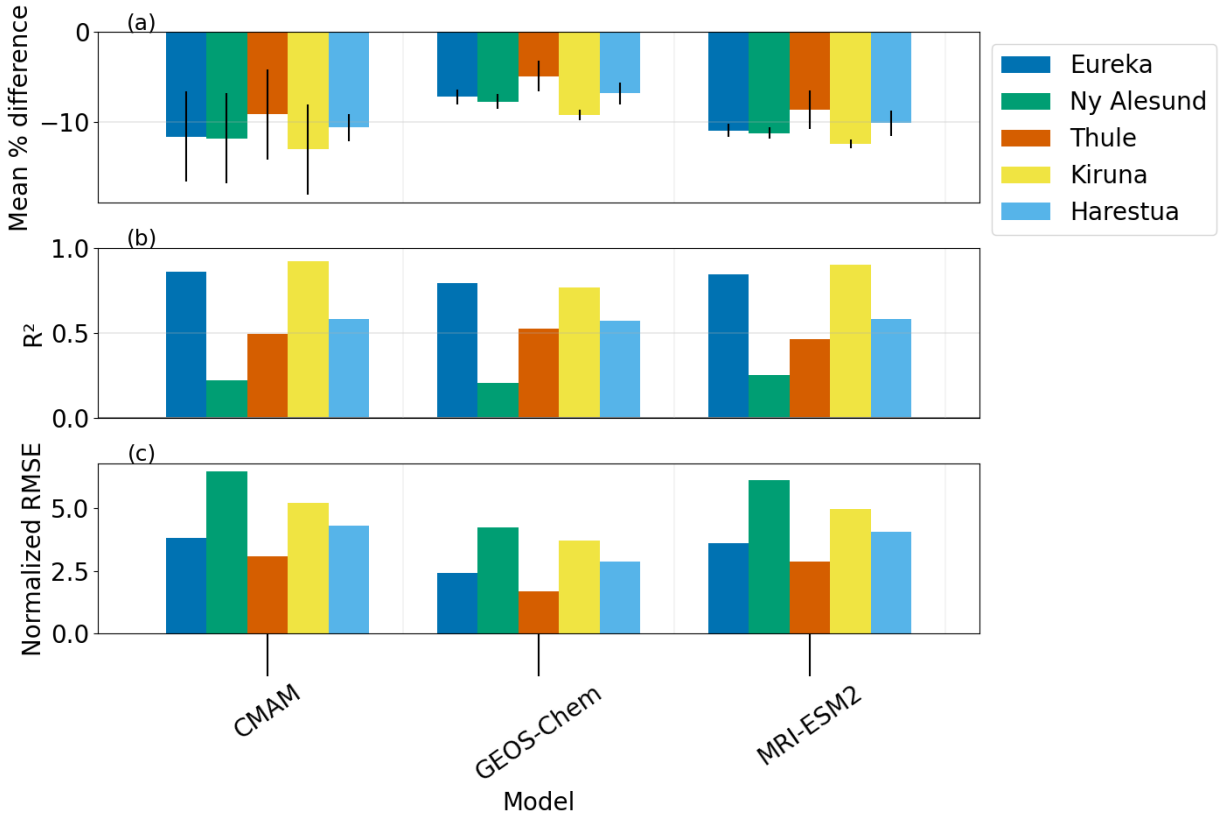

Figure 4.5: By model and location: (a) Overall model-measurement mean percent difference for CH_4 0-7 km partial columns (Δ_O), with error bars that represent the standard deviation of the mean, as shown in the legend of Figures A.6-A.10. (b) R^2 as shown in Figures 4.4 and A.11-A.14. (c) Normalized root-mean-square error.

Figure 4.6 shows the multi-model mean (MMM) for each location, and the percent difference compared to the monthly mean FTIR. The error bars and shading represent the standard deviation of the mean. The AMAP SLCF Assessment Report compares the models with surface CH_4 measurements and finds that the MMM bias for Arctic CH_4 is +1.3% (AMAP, 2021). When comparing with 0-7 km FTIR partial columns, the MMM bias ranges from -5 to -15% (Figure 4.6(f)) and unlike the results in the AMAP Report, the comparisons are not improved by choosing a multi-model mean because all three models have a negative bias. The FTIR retrievals show good sensitivity to tropospheric CH_4 (sensitivity >0.5), however, as these column measurements average out CH_4 biases over the tropospheric column, they are not expected to exactly match the surface measurement comparisons. Furthermore, due to the sharp decrease in CH_4 above the tropopause (Whaley et al., 2022), a poor representation of the tropopause height may contribute to the low bias in the modelled 0-7 km partial columns, as shown from O_3 data in Whaley et al., 2023. The AMAP Report also includes a comparison with upper-troposphere/lower-stratosphere (UTLS) CH_4 VMRs as measured by the ACE-FTS satellite instrument and finds that the models are biased

low by ~100 ppbv in the vicinity of the tropopause (300 hPa; around~8-9 km), indicating that the modelled tropopause may be too low (Whaley et al., 2022). The results found here are consistent with Whaley et al. (2022), in that that the model simulations of both the lower troposphere (0-7 km partial columns) and the UTLS are biased low, and models with north-south CH_4 gradients (here, only GEOS-Chem) have smaller biases than those that do not. Generally, the models can represent the temporal variability in the tropospheric column well, although are biased low in magnitude, outside of the range of the FTIR uncertainty.

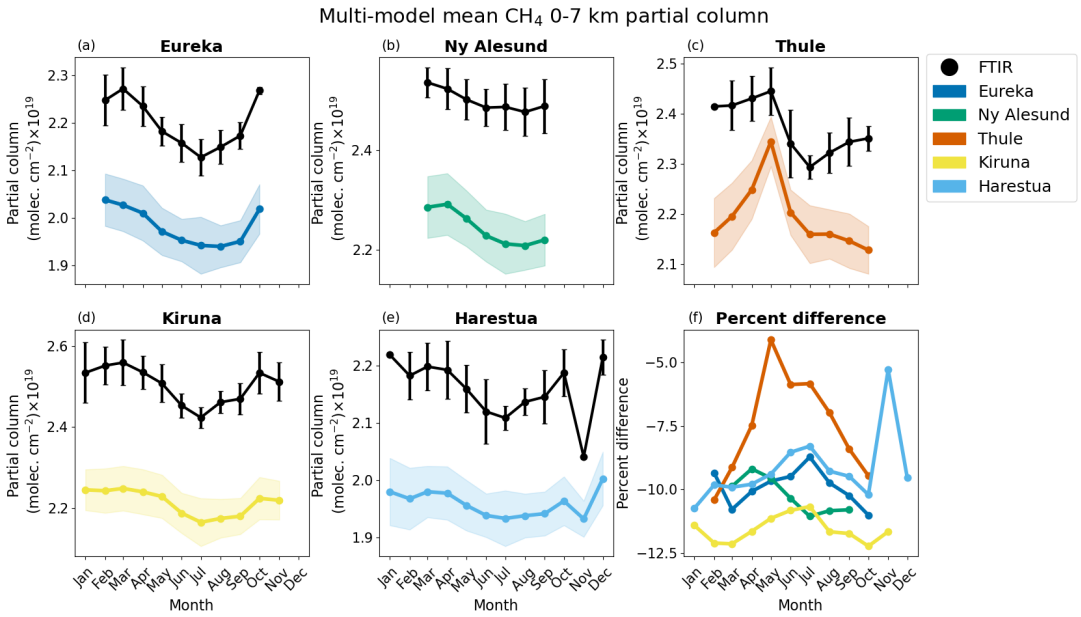

Figure 4.6: (a-e) Monthly mean FTIR (black) and multi-model mean (colour) 0-7 km partial columns of CH_4 ($PC_{F,monthly,j}$ and $PC_{MMM,monthly,j}$, respectively), with error bars and shaded areas, respectively, representing the standard deviation of the mean. (f) Monthly mean percent difference of the MMM ($\Delta_{O,MMM}$) for all locations.

4.4.2 CO

Like CH_4, CO is involved in tropospheric O_3 formation in the presence of NO_x. Thus, in order to properly simulate tropospheric O_3, it is important for models to accurately simulate CO. In the Arctic, CO is used as a tracer for identifying and quantifying influences from biomass burning and lower latitude anthropogenic emissions (e.g., Fisher et al., 2010; Monks et al., 2015; Viatte et al., 2015; Lutsch et al., 2020)

Nine of the 11 models examined in this study provided 3-hourly outputs for CO; WRF-Chem only has outputs for 2014 and 2015, and GEM-MACH only has data for 2015 (Table 4.3). Seven of the nine CO models examined use GFED-based fire emissions. The remaining models are EMEP MSC-W which uses FINN (Fire INventory from NCAR) fire emissions, and GEM-MACH, which uses CFFEPS (Canadian Forest Fire Emission Prediction System) fire emissions (Whaley et al., 2022). Evidence of biomass burning events can be observed in the summer months when examining the CO seasonal cycle with all available measurement points, where there are sporadic increases in the measured CO (Figures A.15-A.18). The CO time series data (i.e. Figures A.15-A.22) indicates that the GFED-based models may overestimate CO from biomass burning as their bias shifts positive in the summertime relative to the rest of the time series. This feature is absent for GEM-MACH, which does not have a consistent trend between sites during the summer (although results are only available for one year), and for EMEP MSC-W, which shifts more negatively in the summertime. It is well known that the fire emissions inventories vary greatly from each other (AMAP, 2021), causing these differences in model results.

Figure 4.7 (and Figures A.19-A.22) shows the monthly mean partial columns and percent differences between the models and the FTIR measurements. This allows for an overview of the mean percent difference and how the model biases change over the year. For example, MATCH exhibits a positive shift in bias from the end of summer to the fall in all locations. WRF-Chem is biased low in the spring and summer, but agrees better with the observations from August onwards, in contrast to EMEP-MSC-W, which tends to diverge from the measurements in the mid- to late summer. GEM-MACH is the only model that has a positive mean difference in all locations. The year-round difference is likely due to the fact that this model used anthropogenic emissions produced locally for most of its regional domain, instead of the ECLIPSEv6B anthropogenic emissions that all of the other models used, and lateral regional boundary conditions provided from MOZART4 (Model for Ozone and Related Chemical Tracers, version 4) global simulations (Emmons et al., 2010; Gong et al., 2018; AMAP, 2021). Further, Figure 4.8 (and Figures A.23-A.25) shows the correlations between the modelled and FTIR partial columns, with the line of best fit and R^2 indicated in the legend. For many models, the 1:1 correlation (and Figure 4.8 and Figures A.23-A.25) shows that models have better agreement with the FTIR for low CO values and the disparity increases as CO increases, i.e. the line of best fit and 1:1 line diverge. The points with

the maximum CO VMRs correspond to the FTIR springtime peak in the CO cycle (since wintertime CO measurements are not possible during polar night).

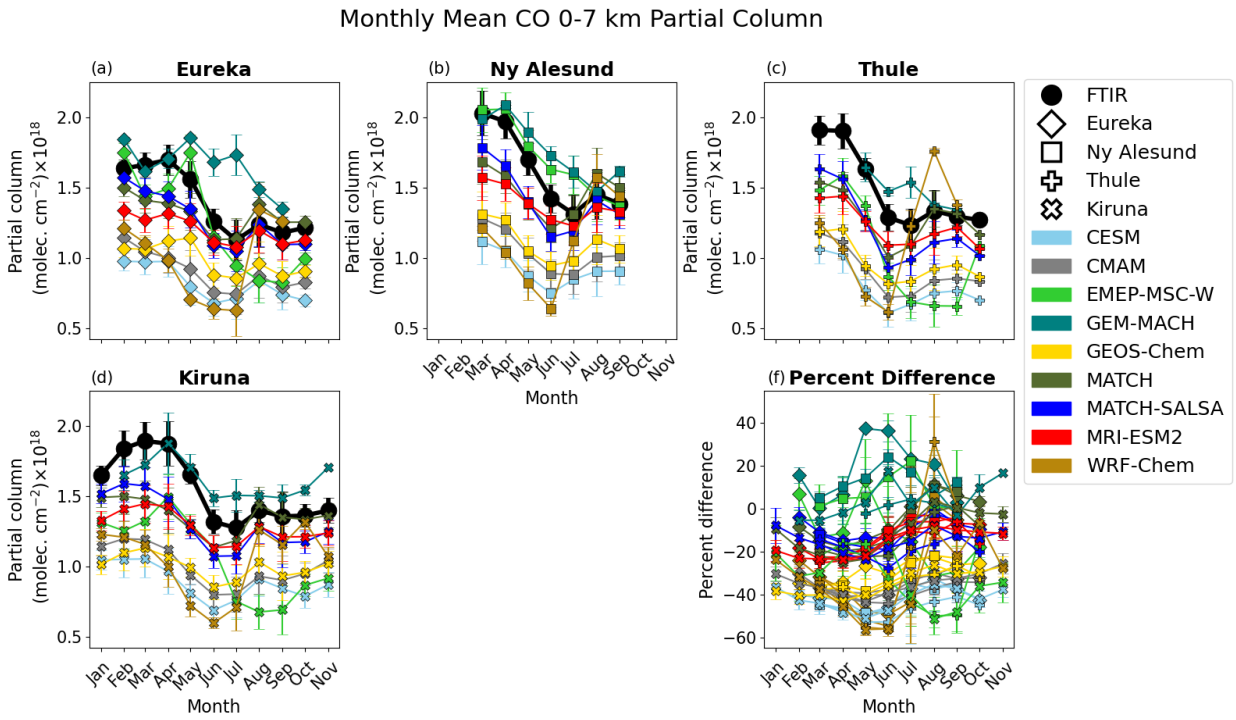

Figure 4.7: (a-e) Monthly mean FTIR (black) and smoothed model (colour) 0-7 km partial columns of CO ($PC_{F,monthly,j}$ and $PC_{M,monthly,j}$, respectively), for each location, shown with the same y-axis. Error bars represent the standard deviation of the monthly mean. (f) Model-measurement mean percent difference by month ($\Delta_{monthly,j}$) for each model (by colour) and location (by marker). Error bars represent standard deviation of the monthly mean percent difference.

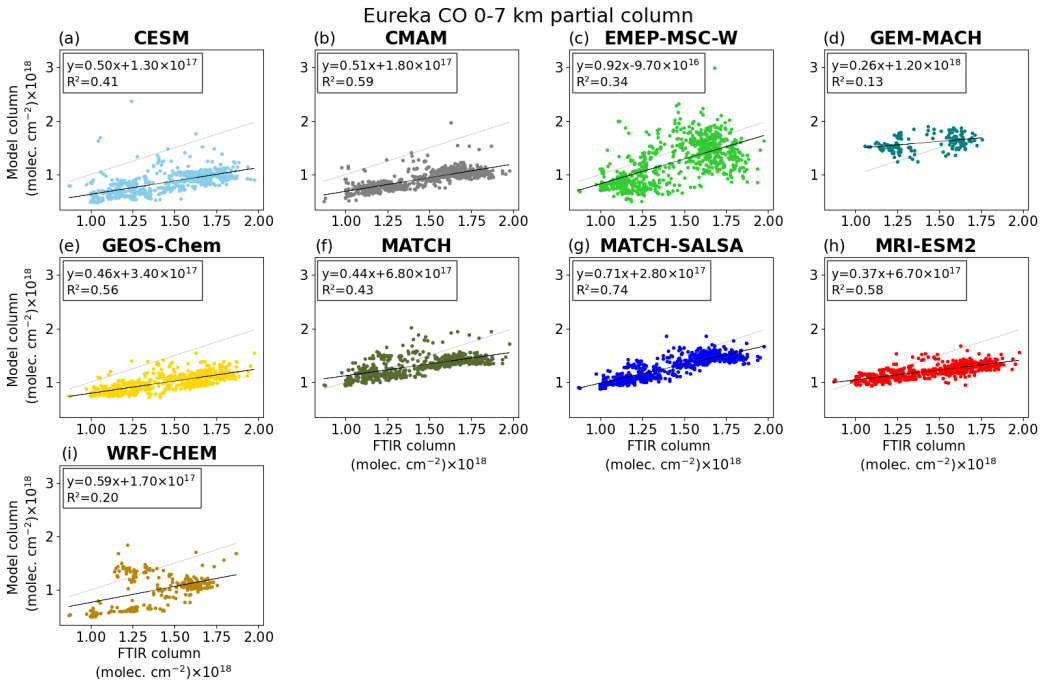

Figure 4.8: Smoothed model vs. FTIR 0-7 km partial column of CO for Eureka, showing all available model-FTIR corresponding data. The black line is the line of best fit, where the equation and R^2 are noted in the legend. The 1:1 line is shown in light grey.

Figure 4.9 summarizes the overall model-measurement mean percent difference R^2, and normalized root-mean-square error for all locations. GEM-MACH has a mean percent difference that is within the FTIR uncertainty for Thule and Kiruna, EMEP MSC-W and MATCH are simulated within the mean FTIR uncertainty for Ny Ålesund (see Figure 4.15). MATCH-SALSA and MRI-ESM2 exhibit high R^2 and low percent difference across all locations, relative to the other models' values, although their columns do not fall within the FTIR uncertainties. GEM-MACH and MATCH have NRMSE comparable to MATCH-SALSA and MRI-ESM2, despite generally lower R^2. WRF-Chem shows better agreement with the FTIR measurements from Eureka, where the NRMSE is comparable to CESM, CMAM and GEOS-Chem. This is likely a result of the increased density of measurement points in August and September, when WRF-Chem exhibits a minimum bias compared to the FTIR data, and because the comparison only includes data points from 2014 and 2015. The large negative biases earlier in the year lead to low R^2 and high NRMSE at all sites. This appears to be linked to negative biases in modelled surface CO over mid-latitude source regions, and in the free troposphere compared to MOPITT data, as reported by Whaley et al. (2022). Overall, four model-location pairs have a mean difference within the average

FTIR 0-7 km partial column uncertainty (see Table 4.2), and when including the standard deviation of the mean difference, an additional eight pairs out of 36 meet this criterion.

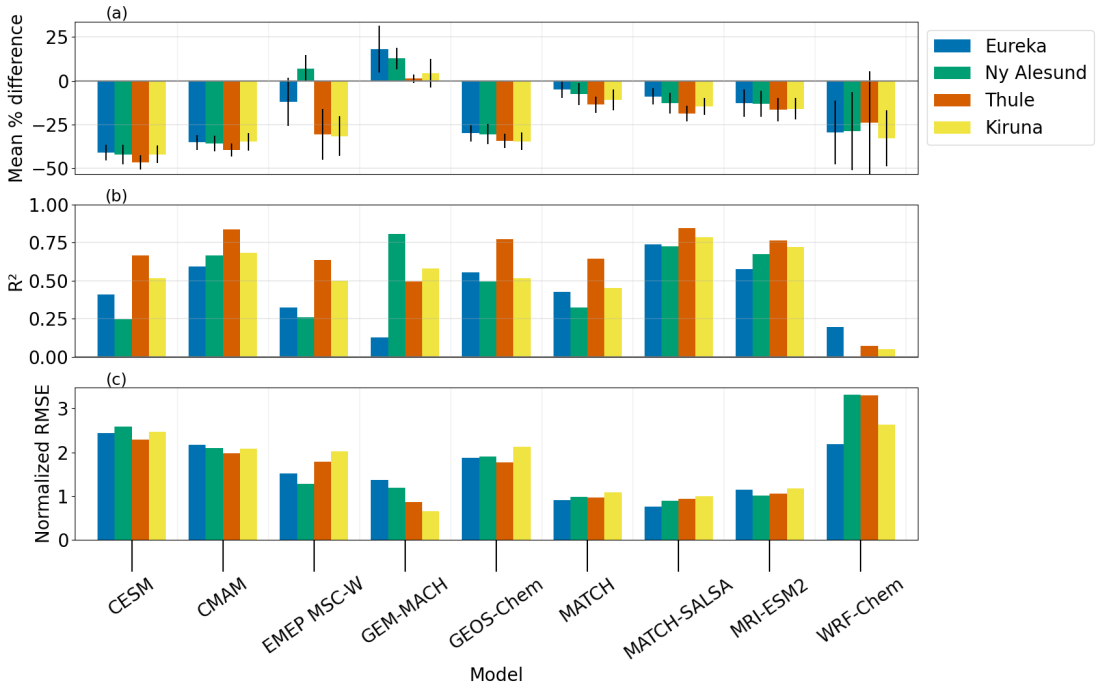

Figure 4.9: By model and location: (a) Overall model-measurement mean percent difference for CO 0-7 km partial columns (Δ_O), with error bars that represent the standard deviation of the mean, as shown in the legend of Figures A.19-A.22. (b) R^2 as shown in Figures 4.8 and Figures A.23-A.25. (c) Normalized root-mean-square error.

Figure 4.10 shows the monthly MMM for CO at each location, with the percent difference in the last panel (f). This highlights the general tendency of the models to underestimate tropospheric CO more in the spring than in the summer, which has been observed by other Arctic model-measurement comparison studies (e.g., Monks et al., 2015; Whaley et al., 2022), and globally (e.g., Kopacz et al., 2010) . The AMAP SLCF Assessment Report found that compared to CO from various surface networks, the models had a greater bias than for the other SLFCs examined, underestimating CO in the spring and overestimating CO in the summer (AMAP 2021). The same pattern was observed when comparing with MOPITT satellite CO in the free troposphere, at the 600 hPa level (Whaley et al., 2022). The change from a negative winter-spring bias to a positive summer bias was observed in model comparisons to surface CO measurements at two additional Arctic sites, Zeppelin, Norway and Utqiagvik/Barrow, USA, with a -20-30% bias in the first six months of the year (Whaley et al., 2023), which is compatible with results shown in Figure 4.10(e).

In POLMIP, models were run for 2008 with a standardized emissions inventory; there is some overlap of models examined here, although a different emissions input was used (see Emmons et al., 2015 for full project description). Similar to the results presented here, the POLMIP study found that relative to surface, airborne, and satellite Arctic tropospheric measurements, CO was underestimated by the models (MMM gross error 9-12%), with a more negative bias in the winter/spring compared to the summer, although the models still broadly captured the seasonal cycle (Monks et al., 2015). Using an idealized tracer, POLMIP examined anthropogenic and biomass burning influences in Arctic regions, demonstrating a seasonal dependence of transport efficiency. It was shown that for anthropogenic emissions, Europe influences the surface CO, while Asia and North America have more influence higher in the troposphere (Monks et al., 2015). Furthermore, the tracer investigation in that study showed that OH differences account for more variability between the models than the transport mechanisms within the individual models. However, it can be noted that although models may reduce negative biases through better OH chemistry, this alone will not resolve the differences between the model and measurements (Monks et al., 2015).

The current study, the POLMIP study, and the AMAP Report exhibit similarities in the model-measurement comparisons of CO. Most notably, all three studies show negative biases early in the year, which shift positively in the summer: the model-FTIR comparisons become less negative, while the AMAP-surface measurement comparisons change to a positive bias. Lutsch et al. (2020) also reported a low bias in GEOS-Chem lower tropospheric CO columns compared with measurements from ten FTIR stations, including four sites in this study, although they found a greater underestimation for Eureka and Thule in July and August due to transported boreal wildfire emissions not fully captured by the model, particularly for years after 2015 not included in the present study. Previously published studies point to underestimated anthropogenic emissions as a source of the discrepancies (Monks et al., 2015, Whaley et al., 2022; 2023). The results of the model-FTIR comparisons presented here support this reasoning, as the only model with a positive bias (GEM-MACH) has additional local Arctic emissions (Gong et al, 2018). The models may be improved with more refined OH chemistry, although it is unlikely to completely resolve the inconsistencies (Monks et al., 2015); improvements to long-range transport and biomass burning inventories could also reduce the differences between model results and measurements.

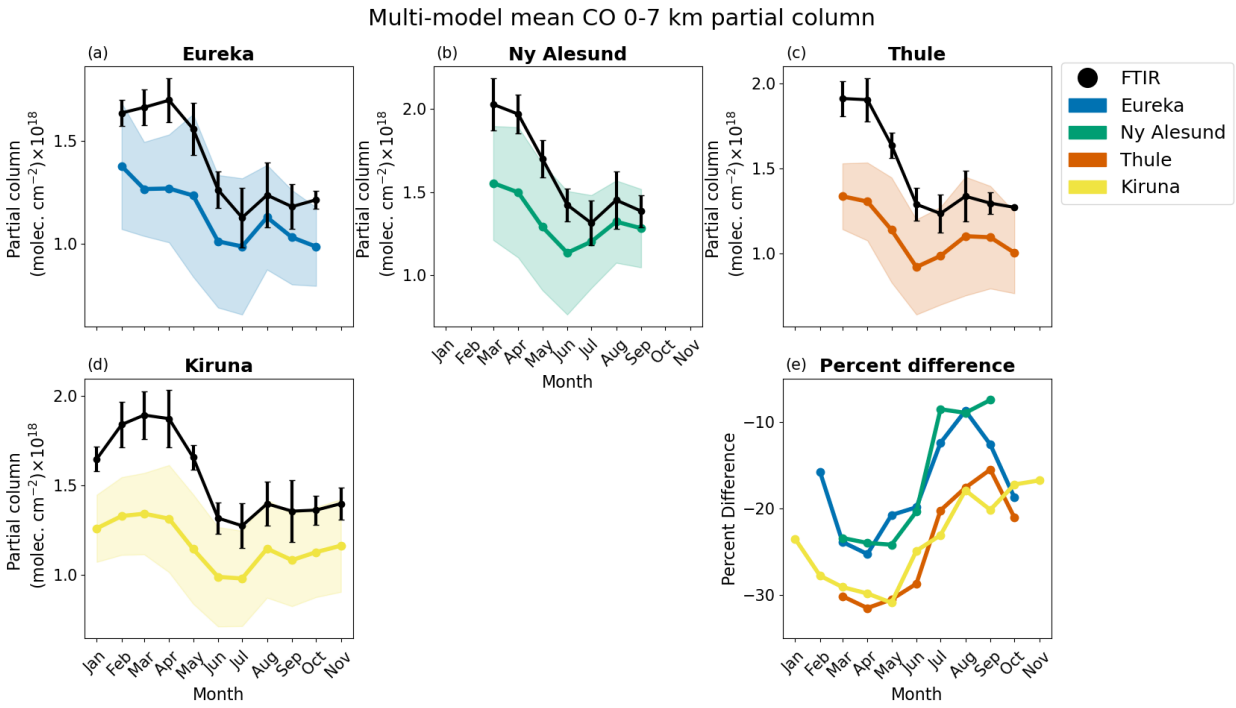

Figure 4.10: (a-d) Monthly mean FTIR (black) and multi-model mean (colour) 0-7 km partial columns of CO ($PC_{F,monthly,j}$ and $PC_{MMM,monthly,j}$, respectively), with error bars and shaded areas representing the standard deviation of the mean. (e) Monthly mean percent difference of the MMM ($\Delta_{O,MMM}$) for all locations.

4.4.3 O_3

Tropospheric O_3 is both a significant anthropogenic GHG and an air pollutant that has impacts on human health and ecosystems. In the troposphere, O_3 is a secondary pollutant, produced by photochemical oxidation of volatile organic compounds in the presence of NO_x. In addition to atmospheric photochemistry, its production is highly sensitive to meteorological conditions. Diurnal impacts on O_3 production are minimal in the Arctic, relative to lower latitudes, due to the gradual and prolonged change in solar altitude/zenith angle throughout the year. While O_3 processes are complex, O_3 is often quite well reproduced by models, possibly due to compensating biases in its precursors (Whaley et al., 2022). Although progress has been made, sparse observations, Arctic amplification, and a changing global climate hinder the understanding and modelling of O_3 in Arctic regions (Whaley et al., 2023). For a summary of the current understanding of Arctic tropospheric O_3, see Whaley et al. (2023).

All 11 of the models examined in this study provide 3-hourly O_3 concentrations. The full data time series plots (Figures A.26-A.30) demonstrate the variation between the models and throughout the

year, which is likely a by-product of the complexity in modelling tropospheric O_3. Figure 4.11 (and Figures A.31-A.35) shows the monthly mean partial columns (a-e) and percent differences (f) to highlight the parts of the year which are overestimated or underestimated. For example, "springtime" (referred to here as when the sun rises, in approximately late February at the highest latitude sites, until May) O_3 is of interest in the Arctic due to the springtime maximum in its seasonal cycle, and the potential for both stratospheric ozone intrusions into the upper (mid) troposphere and surface O_3 depletion events (ODEs) due to bromine explosions and halogen chemistry. However, the 0-7 km partial column FTIR O_3 seasonal cycle, shown here, is dominated by the free troposphere and stratospheric processes, and does not have a springtime minimum from surface ODEs, as one might expect from surface measurements (Solberg et al., 1996; Berg et al., 2003; Skov et al., 2006; Eneroth et al., 2007; Whaley et al, 2023). The Arctic surface ODE features are primarily limited to the near surface/lower boundary layer (<2 km), whereas the 0-7 km partial column is dominated by the free troposphere (Zhao et al., 2016). It can be noted that all of the models in this study lack the necessary halogen chemistry needed to simulate ODEs in the high Arctic (Whaley et al., 2023).

Figure 4.11 shows that across all locations, MATCH-SALSA overpredicts O_3 by 35-75% in winter, which gradually declines until May, after which the bias becomes negative. GEM-MACH, GEOS-Chem, UKESM1 and WRF-Chem underestimate springtime O_3 most substantially across all sites. The discrepancies may arise from inaccuracies in model water vapor leading to an increase in O_3 destruction and/or a lack of O_3 transported from mid-latitudes, which is a substantial source of tropospheric O_3 in the Arctic (Hirdman et al., 2010; Whaley et al., 2023). In the case of the regional GEM-MACH model, low biases in O_3 or precursor species at the lateral boundary conditions may also be contributing. CESM, CMAM, DEHM and MRI-ESM2 demonstrate reasonable agreement with measured springtime O_3 across locations, in addition to a smaller overall mean percent difference, relative to other models. EMEP MSC-W and WRF-Chem simulate springtime O_3 comparable to the aforementioned models, although negative biases later in the year lead to a larger overall mean percent difference. This may indicate that these models have too much photochemical O_3 loss in the summer months.

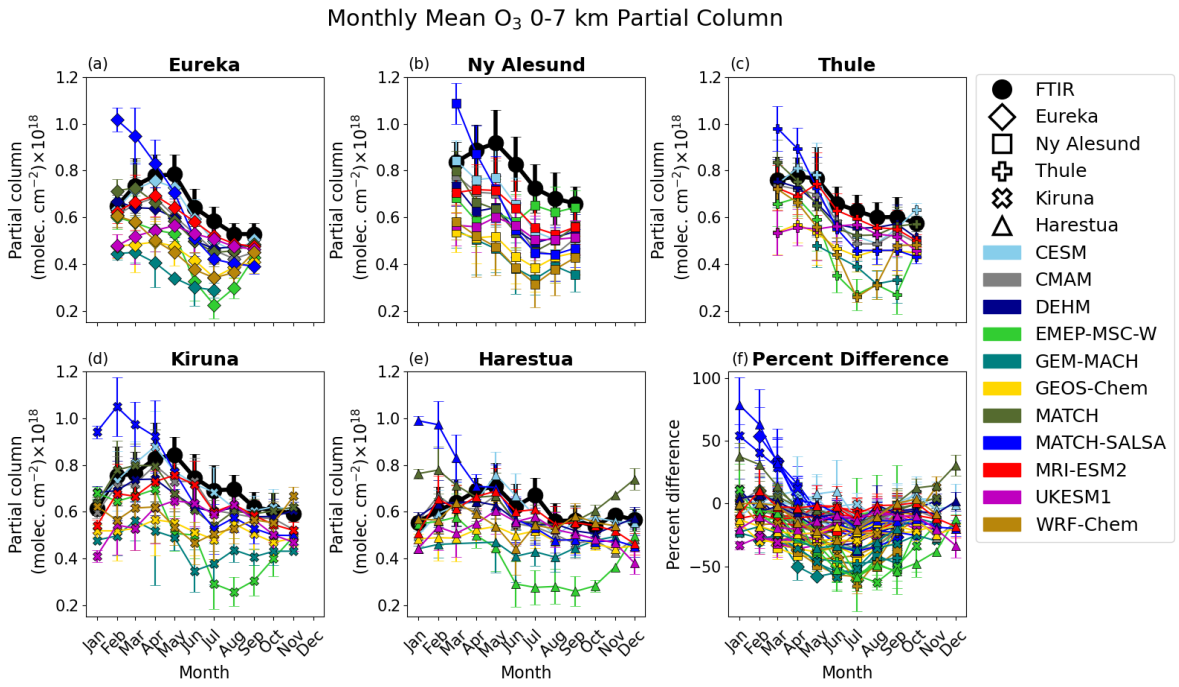

Figure 4.11: (a-e) Monthly mean FTIR (black) and smoothed model (colour) 0-7 km partial columns of O_3 ($PC_{F,monthly,j}$ and $PC_{M,monthly,j}$, respectively), for each location, shown with the same y-axis. Error bars represent the standard deviation of the monthly mean. (f) Model-measurement mean percent difference by month ($\Delta_{monthly,j}$) for each model (by colour) and location (by marker). Error bars represent standard deviation of the monthly mean percent difference.

Figure 4.12 (and Figures A.36-A.39) shows the model versus FTIR O_3 0-7 km partial columns, with the line of best fit and R^2 shown in the legend, along with the 1:1 line. The general underestimation towards the largest values could be related to the underestimation in precursor species (such as CO or NO_x), a lack of long-range transport, an underestimation of ozone production in air masses during long-range transport to the Arctic, or a combination thereof. Using a MOZART-4 tagged tracer simulation of O_3, Wespes et al. (2012) examined source attributions of the tropospheric O_3 columns measured by the FTIR instruments at Thule and Eureka. Their analysis shows that the retrievals have minimal contribution from the a priori (~1%), resulting in high vertical sensitivity throughout the troposphere. The tropospheric column source contributions were estimated, where over half was attributed to anthropogenic sources, followed by stratospheric influence and lastly lightning and biomass burning emissions (Wespes et al., 2012). The seasonal cycle of Arctic O_3 has been shown to vary based on geographical conditions, such as if the site is coastal, inland or at a high elevation (Whaley et al., 2023). Moreover, O_3 partial columns can be variable because they depend on the vertical distribution of O_3, which is determined by a

combination of emissions, chemistry, dynamics, and radiation, all of which vary with altitude (Rap et al., 2015). Notably, Arctic O_3 columns have strong gradients in the influences on the vertical profile from mid-latitude regions (Europe, North America and Asia), which also vary with season (Monks et al., 2015). The combination of these factors leads to an increasingly complex series of model processes, which can also result in compounding errors. Without sensitivity simulations, like those carried out in Monks et al. (2015) and Rap et al. (2015), it is difficult to definitively say which of these processes are responsible for the underestimations found in this study.

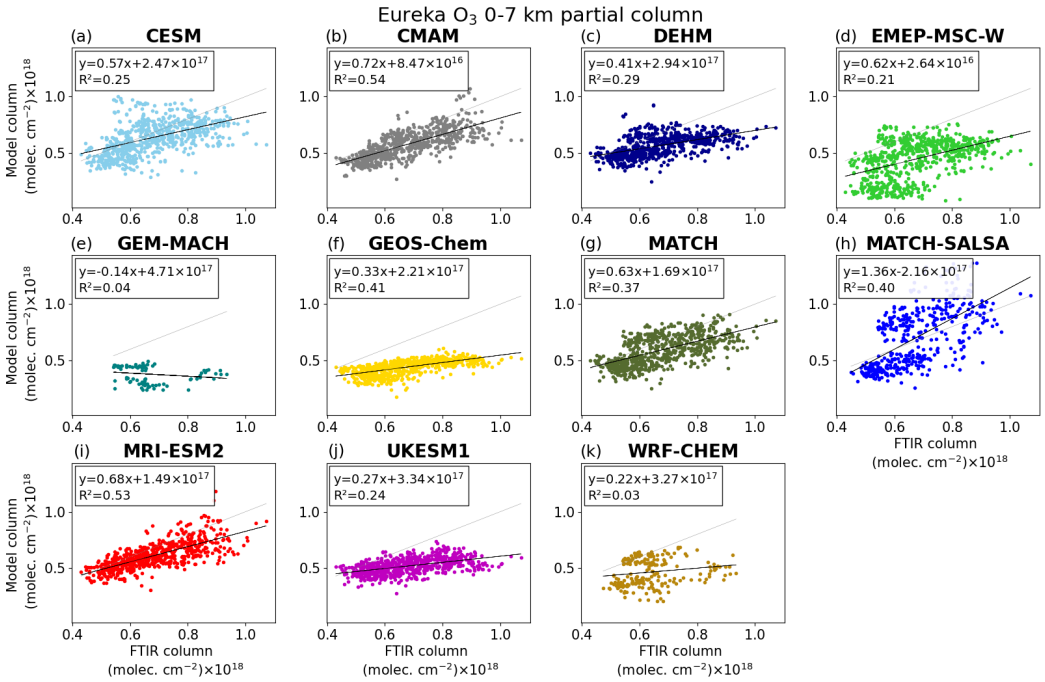

Figure 4.12: Smoothed model vs. FTIR 0-7 km partial columns of O_3 for Eureka, showing all available model-FTIR corresponding data. The black line is the line of best fit, where the equation and R^2 are noted in the legend. The 1:1 line is shown in light grey.

Figure 4.13 shows the summary of O_3 mean percent differences, R^2, and normalized root-mean-square error. The model-FTIR comparisons reveal that the spatial resolution, and inclusion of stratospheric chemistry in the models does not necessarily improve results (refer to Table 4.3 for horizontal resolution and stratospheric chemistry). For example, WRF-Chem, EMEP MSC-W, and GEM-MACH show a low R^2 and higher NRMSE (varying between sites and models), although contributing to this for WRF-Chem and GEM-MACH could be the limited number of analysis years (two and one, respectively). These air-quality focused models have detailed chemistry and were run at higher spatial resolutions, whereas for example CMAM, a climate-focused model, has a coarser resolution with simplified tropospheric chemistry and demonstrates larger R^2 and smaller

mean percent differences (Figure 4.13). However, when considering the stratosphere, CMAM, which includes comprehensive stratospheric chemistry, has comparable metrics in Figure 4.13 to DEHM, which uses prescribed climatologies for the stratosphere, although resolution differences may contribute to compensating errors. Similarly, Whaley et al. (2022) stated that the degree of stratospheric chemistry in the models did not reveal a consistent benefit or disadvantage when comparing the models with surface measurements. Here, the O_3 partial column comparisons show significant variation, although again models largely underestimate FTIR measurements. The R^2, mean percent difference, and NRMSE are relatively consistent, where models with a larger percent difference also have weaker correlations and higher NRMSEs. An exception to this is CESM, which has one of the smallest overall differences across the models and locations. However, in the model vs. FTIR plots (Figures 12 and A.36-A.39), CESM has considerable scatter above and below the line of best fit, resulting in a decreased mean difference, while also reducing R^2, unlike MRI-ESM2, which has a similar mean percent difference and NRMSE, but a stronger linear correlation.

To supplement the aircraft and satellite campaigns undertaken for the POLARCAT study, daily mean O_3 measurements from the FTIR instruments at Eureka and Thule were compared to MOZART-4 simulations in Wespes et al. (2012). When examining a partial column from the ground to 300 hPa (approximately 9 km), the smoothed model showed a bias of -15% relative to the FTIR. This is consistent with their analysis of aircraft observations, which revealed that the model underestimated O_3 by 5-15%. Results here are similar to those presented in Wespes et al. (2012), where across all the locations and models, 24 of the 55 model-measurement mean percent differences were within ±15% (see Figure 4.15). The FTIR uncertainty for O_3 partial columns ranges from 3.9% to 8.2%; the overall mean percent difference for MATCH-SALSA falls within these uncertainty bounds for all locations, and CESM, DEHM, MATCH and MRI-ESM2 are within FTIR uncertainty for all locations but Ny Ålesund.

The AMAP SLCF Assessment Report finds that the multi-model mean of Arctic O_3 has a bias of +11 ± 3% relative to surface measurements (AMAP, 2021). When partitioning results by region, all the models had positive biases when compared to the surface measurements in Alaska and negative biases in Northern Europe, resulting in a relatively small mean bias across the Arctic as a whole (Whaley et al., 2022). Inaccuracies in long-range transport of O_3 and its precursors, such as PAN, may have contributed to the increased discrepancy seen in the model-FTIR comparisons

of the current study, particularly in partial columns with larger values. For example, the underestimation of CO (see Figures 4.9-4.10) or underestimations related to PAN (e.g., Walker et al., 2012; Wizenberg et al., 2024) may contribute to the negative bias in O_3. Most models in AMAP (2021) show negative biases for Greenland and Northern European locations, which would correspond closer geographically with the FTIR sites examined here. When comparing the AMAP models to TES (Tropospheric Emission Spectrometer) and ACE-FTS satellite O_3 measurements, the biases are negative at lower altitudes, and become positive at higher altitudes (Whaley et al., 2022). AMAP model vs. ozonesonde comparisons showed similar elevated positive biases around 6-8 km of up to ±50%, again indicating that the models may produce too much O_3 from mid-latitude anthropogenic emissions or that there may be too much downward transport of O_3 from the stratosphere (Whaley et al., 2023). The best performance in that study came from the multi-model mean, which simulated O_3 within ± 8% throughout the troposphere.

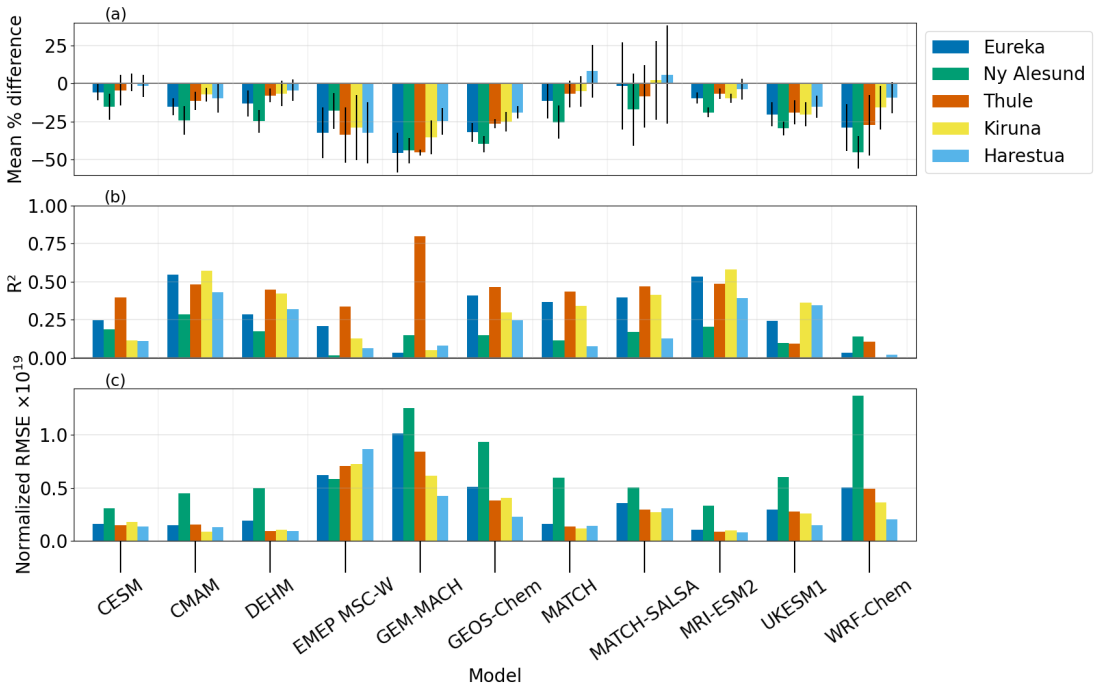

Figure 4.13: By model and location: (a) Overall model-measurement mean percent difference for O_3 0-7 km partial columns (Δ_O), with error bars that represent the standard deviation of the mean, as shown in the legend of Figures A.31-A.35. (b) R^2 as shown in Figures 4.12 and A.36-A.39. (c) Normalized root-mean-square error.

Figure 4.14 shows the monthly MMM for O_3 at all locations, along with the monthly mean FTIR and the associated percent difference. This shows that the models, as a whole, have an increased negative bias in the middle of the year relative to the winter, while still exhibiting a negative bias

overall. The longitudinal range of sites examined here may limit biases to be negative, not capturing the positive-negative gradient from west-east in O_3 found in the AMAP Report (AMAP, 2021; Whaley et al., 2022). Nonetheless, the model-FTIR O_3 comparisons reflect the proclivity of the models to underestimate Arctic O_3 in the lower troposphere, as also found in the aforementioned studies. The results of this study agree with results from previous studies and suggest that improvements are still needed for accurate modelling of O_3 and CO in the Arctic (Whaley et al., 2023). Models still require improvements in their treatment of stratospheric-tropospheric exchange and Arctic boundary layer processes to better simulate Arctic O_3, as well as further improvements and understanding about processes influencing O_3 removal through dry deposition and O_3 photochemical production from anthropogenic, biomass burning and natural sources in the lower and mid troposphere.

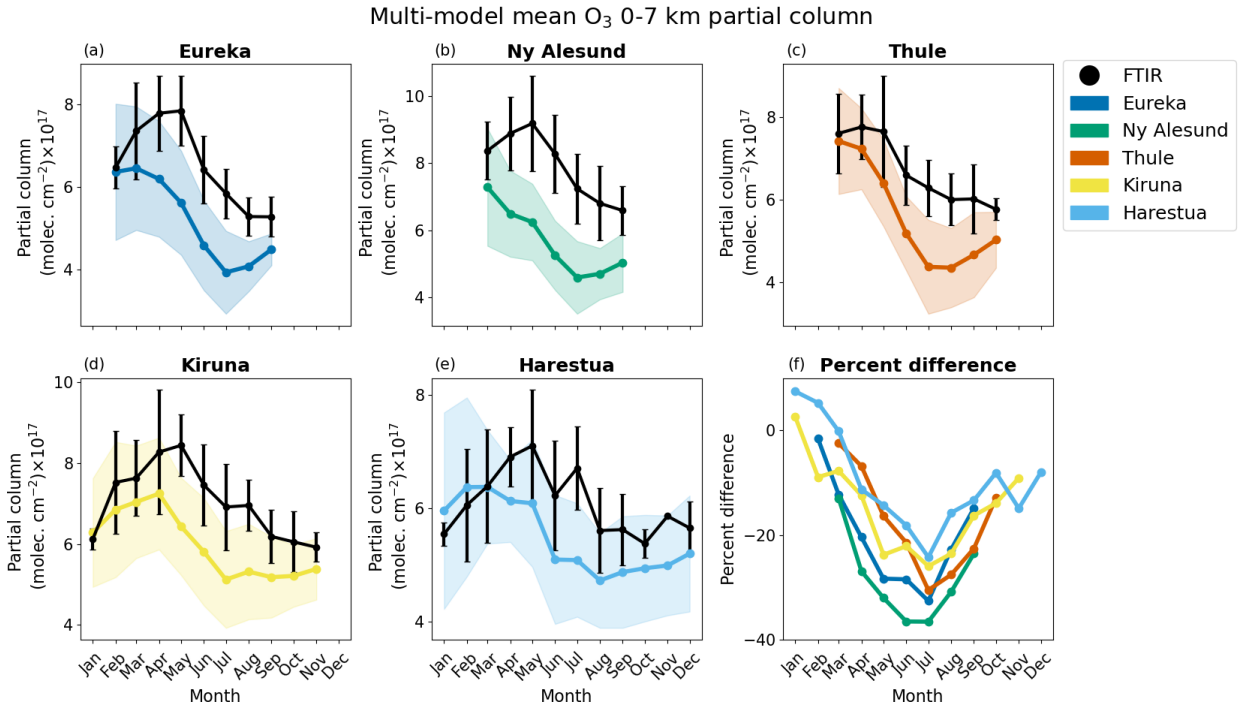

Figure 4.14: (a-e) Monthly mean FTIR (black) and multi-model mean (colour) 0-7 km partial columns of O_3 ($PC_{F,monthly,j}$ and $PC_{MMM,monthly,j}$, respectively), with error bars and shaded areas representing the standard deviation of the mean. (f) Monthly mean percent difference of the MMM ($\Delta_{O,MMM}$) for all locations.

4.5 Conclusions

This study compares atmospheric models with data from five Arctic NDACC ground-based FTIR spectrometers. The models simulate SLCFs and precursor gases with 3-hourly outputs for the years

2008, 2009, 2014, and 2015. Here, a total of three models are evaluated for CH_4, nine for CO, and 11 for O_3. The model simulations are compared with FTIR tropospheric partial column measurements to assess performance throughout the year and across locations.

Generally, across the five locations, the model simulations of 0-7 km partial columns of CH_4, CO and O_3 are underestimated. There were no significant patterns in the biases identified between the sites, species, or models examined. Modelled CH_4 partial columns are relatively consistent across the year, broadly capturing seasonal cycles, with the exception of a few outliers. CO simulations are inconsistent in reproducing the seasonal cycle, underestimating springtime partial columns compared to the rest of the year, and skewing differences to be more positive when there are enhancements due to biomass burning events. Similarly, the models underestimated O_3 maxima more than O_3 minima in the troposphere. The multi-model means are reflective of these trends, for which (ignoring outliers), the CH_4 mean percent difference is relatively consistent across the year, CO has a maximum difference in the spring and a minimum in the summer, and O_3 has maximum difference centered around the summer. The AMAP SLCF Assessment Report found the best results using a multi-model mean for all species when comparing with surface measurements (AMAP 2021; Whaley et al., 2022). However, here, the multi-model means of the tropospheric column for all species are biased low. The average MMM mean difference is approximately -10% for CH_4, -21% for CO and -18% for O_3 (see Table 4.4), where the uncertainty of the FTIR 0-7 km partial column is on the order of 6% on average. When examining the models and location pairs individually, the mean difference (inclusive of standard deviation) is within the respective FTIR uncertainty, for six of 15 model-FTIR comparisons for CH_4, 12 of 34 for CO, and 25 of 55 for O_3 (see Figure 4.15).

These evaluations show that models are lacking some degree of transport and/or emissions to accurately reproduce tropospheric columns and seasonal variability in the Arctic. Model evaluation can provide a valuable checkpoint to help improve the representation of the Arctic in atmospheric models. NDACC FTIR spectrometers were selected for this project because of the wide range of species measured, high spectral resolution, multiple high-latitude sites, and publicly available data; in addition, the column-integrated FTIR measurements used in this study have a spatial and temporal footprint that is more representative of the free troposphere than in situ and satellite measurements. Future work would benefit from the inclusion of sensitivity studies, furthering the model-measurement comparisons with mid-latitude NDACC FTIR sites, and

extending comparisons to a longer timeframe, with some models and locations having data from as early as 1990.

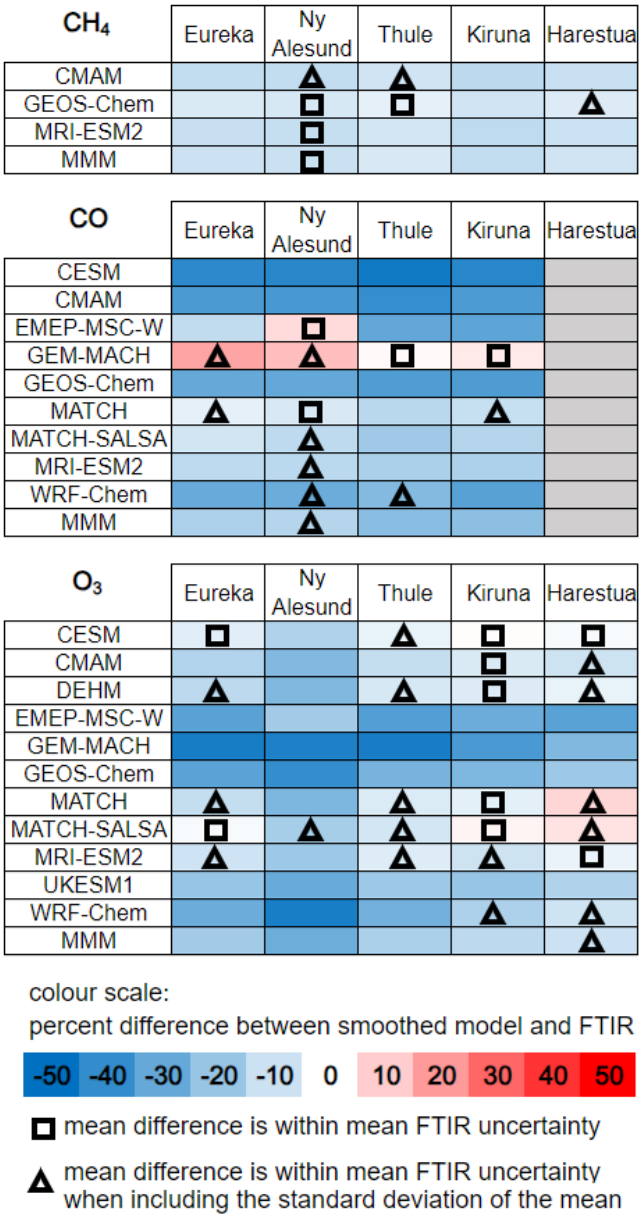

Figure 4.15: Summary of model-measurement mean percent difference (Δ_O) for each model and location by species. MMM is the multi-model mean ($\Delta_{O,MMM}$). The colour scale indicates the mean percent difference relative to the FTIR measurements, from blue (-50%) to red (+50%). A square marker indicates that the mean percent difference is within the FTIR uncertainty. A triangle marker indicates that the mean difference is within the FTIR uncertainty combined with the standard deviation of the monthly mean percent difference.

Table 4.4: The multi-model mean percent difference ($\Delta_{O,MMM}$) for each species at each location, including the overall average percent difference for each species and the standard deviation of the mean.

Gas	Location	MMM Percent Difference
CH_4	Eureka	-9.9 ± 0.7
	Ny Ålesund	-10.2 ± 0.7
	Thule	-7.5 ± 2.0
	Kiruna	-11.6 ± 0.5
	Harestua	-9.2 ± 1.4
	Average	-9.7
CO	Eureka	-17.6 ± 5.6
	Ny Ålesund	-16.7 ± 7.9
	Thule	-24.4 ± 6.5
	Kiruna	-23.7 ± 5.2
	Average	-20.6
O_3	Eureka	-20.1 ± 10.2
	Ny Ålesund	-28.5 ± 8.3
	Thule	-17.6 ± 9.8
	Kiruna	-14.6 ± 8.7
	Harestua	-9.6 ± 9.5
	Average	-18.1

Chapter 5

5 The Impact of the 2023 Canadian Forest Fires on Air Quality in Southern Ontario

This chapter examines the impacts of the record-breaking 2023 Canadian wildfire season on air quality and composition in Southern Ontario. The analysis focuses on three main events (May 16-23, June 3-9, and June 17-30, 2023) when the composition of smoke was measured over Toronto and Egbert, Ontario. Tropospheric columns (0-10 km) of multiple trace gases were measured using TAO and CARE FTIRs to assess enhancement ratios during events. Plume transport was analyzed using HYSPLIT, GEM-MACH-FireWork (GM-FW), and MOPITT CO satellite data. Additional measurements included surface CO, O_3, and $PM_{2.5}$, plume height from MiniMPL, and EM27/SUN XCO columns. The GEM-MACH FireWork model was evaluated using tropospheric column measurements, surface and satellite measurements. This work is published in the *Journal of Geophysical Research - Atmospheres*, as "The Impact of the 2023 Canadian Forest Fires on Air Quality in Southern Ontario" (Flood et al., 2025a).

5.1 Introduction

The summer of 2023 marked an unprecedented year for wildfires in Canada. The burned area surpassed 16 million hectares, which is more than the cumulative total burned area from the previous eight years (2015-2022) (CWFIS, 2024). The National Oceanic and Atmospheric Administration 2023 Annual Climate Report indicates that 2023 was the hottest year on record, both globally and for North America (NOAA, 2024). The 2023 fire season was unique for Canada: it started in late April, which is earlier than normal, and persisted into October (Jain et al., 2024). Sizable wildfire events, such as those occurring in 2023, can have significant implications for local ecosystems, human health, and the economy.

Over 5000 air quality alert bulletins were issued by ECCC in 2023, compared to the national annual average of 1,300 from 2017-2022 (Jain et al., 2024). During the summer of 2023, some of the worst-affected areas of Canada had more than 60 days with poor air quality due to wildfire-related pollution (Jain et al., 2024). Negative health impacts are more significant to communities closer to the fire-affected areas; however, as fires continue to increase in frequency and size, exposure rates both locally and via long-range transport will rise. Although Southern Ontario does not generally

experience wildfires, the area is densely populated, with ~7 million people, or 18% of Canada's population, living in the Greater Toronto and Hamilton Area (Stats. Can., 2023) and is susceptible to long-range transport of emissions from sizeable wildfire events, as observed in the summer of 2023.

Generally speaking, estimates of fire emissions and transport dispersion models have key areas for improvement, including plume height parameterizations, vegetation type, fire type representations, plume chemistry and atmospheric transport (e.g., wind, precipitation, temperature), all of which may be confounded when fire plumes from several events are reaching one location at the same time. Chemical transport models which include fire emissions and simulate atmospheric processes, including chemistry, are applied operationally for emergency response and public health purposes, and as such it is important to work towards improvements of the models. A key step in this process is to evaluate models with observational data. The prolonged, large-spread smoke events that occurred in the summer of 2023 across Canada, and the subsequent atmospheric measurements, provide an opportunity to test the performance of the models.

This study aims to evaluate the impact of the 2023 Canadian wildfires on the atmospheric composition and air quality in Southern Ontario through the amalgamation of data from several ground-based and satellite atmospheric monitoring instruments, a chemical transport model, and a back-trajectory model. The transport of wildfire smoke is evaluated through its related trace gases using measurements from high-resolution, ground-based FTIR spectrometers, located in Toronto and Egbert, Ontario. This method is capable of simultaneously measuring several atmospheric trace gases, to provide information about the composition of the smoke plume. Additionally, CO measurements are supplemented with total column CO from a lower-resolution FTIR instrument at the University of Toronto and from the MOPITT satellite instrument. Smoke plume heights are assessed with a MiniMPL instrument, and trajectories are estimated using the HYSPLIT dispersion model. Surface concentrations of CO, O_3 and $PM_{2.5}$ from the Ontario Ministry of Environment, Conservation and Parks (OMECP) are discussed in relation to air quality during these events. The GM-FW air quality forecast model outputs are evaluated against tropospheric partial columns of CO, NH_3 and O_3, local surface measurements of CO, O_3 and $PM_{2.5}$, and mapped satellite total column CO. The rest of this chapter is structured as follows: Section 5.2 describes the datasets used, Section 5.3 outlines the methodology, Section 5.4 presents results and discussion, and

Section 5.5 provides a summary and conclusions. Supplementary material is included in Appendix B.

5.2 Datasets

5.2.1 FTIR Measurements

Solar-viewing FTIR spectrometers are used to record solar absorption spectra from which trace gas profiles and columns are retrieved. The method requires sunny days with relatively low cloud/haze to operate, which leads to intermittent gaps in the measurements. Unless otherwise stated, the use of "FTIR" (data/measurements) refers to the high-resolution FTIR instruments described in Sect. 5.2.1.1, while data from the lower-resolution EM27/SUN FTIR will be specified as such.

5.2.1.1 High-Resolution FTIR

For a description of FTIR spectroscopy and the instruments at TAO and CARE, see Chapter 2. The instrument locations are shown in Figure 5.1, where the yellow 'x' marks CARE and orange '+' marks TAO. The FTIR measurements examined in this chapter are CO, C_2H_6, CH_3OH, HCN, HCOOH, NH_3 and O_3 (Yamanouchi et al., 2023). The daily mean CO tropospheric columns are well-correlated (R=0.85) between the TAO and CARE sites. The TAO 2002-2023 0-10 km partial column, 10-20 km partial column, and total column VMR AVKs for each of these species are shown in Figure 5.2, providing information about the contributions of the different altitudes to the retrieved columns. Table 5.1 lists the mean percent uncertainty, and mean DOFS of the 0-10 km partial column, and total column DOFS for the gases of interest, using the entire TAO time series.

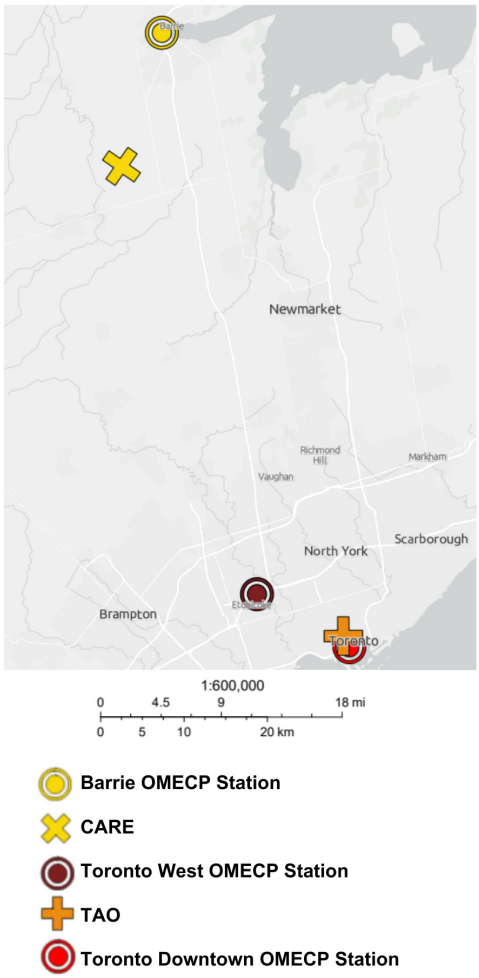

Figure 5.1: Map showing the locations of the ground-based instruments used in this study (Esri, 2024).

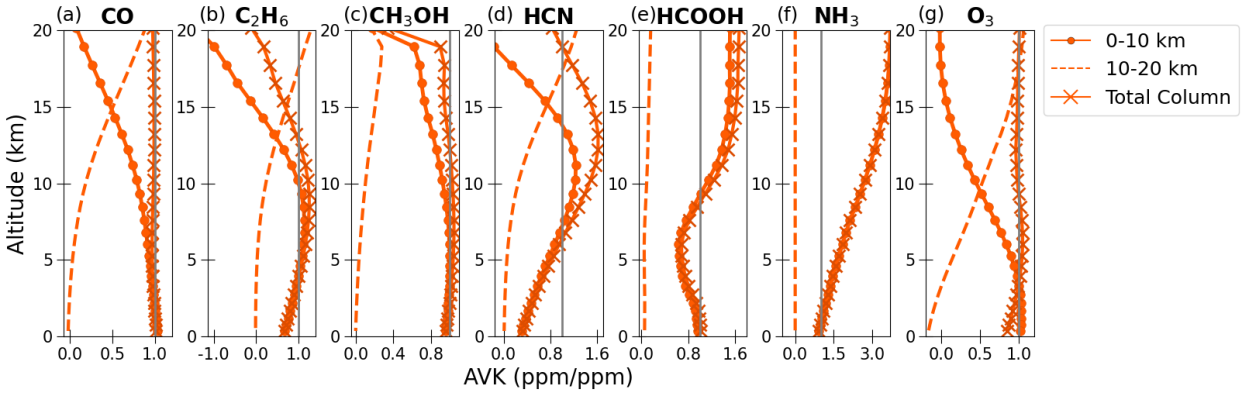

Figure 5.2: Mean 2002-2023 averaging kernels from TAO for 0-10 km (round markers) and 10-20 km (dashed line) partial columns, and for total columns shown for 0-20 km ('X' markers), with a grey line marking 1.

Table 5.1: Mean 2002-2023 TAO 0-10 km partial column percent uncertainty and DOFS, and total column DOFS for species of interest.

Gas	0-10 km Partial Column Percent Uncertainty	Mean Total Column DOFS ±1σ	Mean 0-10 km Partial Column DOFS ±1σ
CO	3.52	2.20 ± 0.25	1.69 ± 0.12
C_2H_6	4.90	1.88 ± 0.29	1.36 ± 0.19
CH_3OH	16.5	1.51 ± 0.15	1.37 ± 0.12
HCN	7.99	2.11 ± 0.40	0.82 ± 0.14
HCOOH	13.1	1.06 ± 0.04	0.93 ± 0.2
NH_3	15.4	1.11 ± 0.09	1.11 ± 0.09
O_3 (*v0.9.4.4*)	6.28	4.38 ± 0.52	1.11 ± 0.18

5.2.1.2 EM27/SUN FTIR

The EM27/SUN FTIR used in this study is located at the University of Toronto (UofT), co-located with the TAO FTIR (TAO "+" marker in Figure 5.1). This instrument uses a retrieval software called "GGG" to obtain column-averaged dry-air mole fractions (X_{gas}) of several species, including CO, CO_2, and CH_4 (Hedelius & Wennberg, 2023). The instrument is designed to be a portable solar-viewing Fourier transform spectrometer with a 1.8 cm optical path difference and a spectral resolution of 0.5 cm^{-1} (as defined by Bruker's 0.9/max OPD), with a spectral range of 6000-9000 cm^{-1} (Gisi et al., 2012). One scan takes approximately 6 seconds, allowing for a more frequent product compared to the DA8 FTIR, which takes about 12 minutes. The dry-air mole fraction of CO (XCO) total column measurements are used here to supplement the CO measurements made by the higher-spectral-resolution FTIR data described above.

5.2.2 Air Quality Data

The OMECP partners with ECCC to provide hourly concentrations of pollutants and an Air Quality Health Index (AQHI) at 38 ambient air monitoring stations across the province to inform the public of the impact of local air quality on their health (OMECP, 2024). Surface measurements for CO, O_3, and $PM_{2.5}$, and the AQHI are acquired for May through September 2023 for locations in Toronto and Barrie (closest OMECP station to Egbert). The manufacturer's instrument detection limits are 0.04 ppm for CO, 0.5 ppbv for O_3, and 0.5 $\mu g/m^3$ for $PM_{2.5}$ at the Toronto Downtown location, and 0.1 $\mu g/m^3$ for $PM_{2.5}$ at the Barrie location (Teledyne Advanced Pollution Instrumentation 2016; Thermo Fisher Scientific 2013, 2017a, 2017b). Note that only the "Toronto

West" location provides CO measurements. The circles in Figure 5.1 show the OMECP station locations, where Barrie is in yellow (~18 km from CARE), Toronto West (~13 km from TAO) is in maroon, and Toronto Downtown is in red (~2 km from TAO). The daily mean values for $PM_{2.5}$ between the Toronto Downtown and Barrie locations are well correlated (R=0.90).

5.2.3 MOPITT

The MOPITT instrument is on NASA's Terra satellite, launched in 1999, and is operated by the Canadian Space Agency. It measures CO, focusing on the lower atmosphere, via a nadir-viewing infrared radiometer, covering 82°S to 82°N (Drummond et al., 1995). Following a sun-synchronous polar orbit (98.5° inclination angle) at an altitude of approximately 705 km. The spatial resolution is 22 km at nadir with a swath of 640 km wide, and global coverage is achieved approximately every three days. The satellite has an overpass time of 10:30 / 22:30 local time, and provides CO as a total column average in ppbv. Validation using aircraft profiles shows that retrieval biases are on the order of ±5% (Deeter et al., 2022). The thermal-infrared (TIR) and NIR V9 mean total column over the event periods of interest are mapped to provide large-scale context of the extent of the CO enhancements and used to assess the GM-FW CO long-range transport (NASA/LARC/SD/ASDC, 2024).

5.2.4 Mini Micro-Pulse Lidar

MPLNET is a global network of ground-based lidar instruments that measures aerosol and cloud vertical profiles in support of the NASA Earth Observation System program (Campbell et al., 2002). The MiniMPL instrument located at the University of Toronto contributes measurements to MPLNET (TAO "+" marker in Figure 5.1). It samples the atmosphere every 60 seconds up to 30 km and operates during daylight hours from sunrise to sunset. The data product used here is the Normalized Relative Backscatter (NRB), which is a relative lidar signal strength, in MHz km^2 μJ^{-1} this is used to represent the approximate height of transported smoke layers (NASA, 2024).

5.2.5 HYSPLIT

The HYSPLIT model is used to compute air parcel trajectories, dispersion, transport, deposition and transformation (Draxler and Hess, 1998; Stien et al., 2015). A primary feature of the program is the ability to simulate back-trajectories used for source-receptor relationship studies. In the context of smoke plumes, the program can be used to calculate source dispersion from the point

of the fire (e.g., Li et al., 2020) or to calculate back-trajectories to investigate the sources contributing to air concentrations at a particular receptor location (e.g., Selimovic et al., 2019). Furthermore, HYSPLIT is used for the operational smoke forecasting system at the National Oceanic and Atmospheric Administration (NOAA) to produce 48-hour smoke transport and concentration predictions (Stein et al., 2009), and for the United States Forest Service ensemble trajectories (USFS, 2024).

HYSPLIT offers a user-friendly online version called READY (Real-time Environmental Applications and Display sYstem) (Rolph et al., 2017). This allows a user to choose a location, height, meteorology, and timeframe to run trajectory dispersion simulations forwards or backwards in time. The air parcel trajectories move a single Lagrangian particle with the mean wind from the user-defined meteorological scheme, in this case the Global Data Assimilation System (GDAS) meteorology on 1° latitude-longitude grid with 23 pressure levels, and at 3-hour intervals. Errors in the trajectory arise from uncertainties in the input data such as the forecast meteorology and representation of the atmosphere through space and time, in addition to computational errors, which in total are estimated to account for 15-30% of the distance travelled (Draxler & Rolph, 2007).

There are four options for the trajectory simulations: standard, matrix, ensemble or frequency. In the current application, the ensemble type was used, which starts 27 individual trajectories from the same location, with the initial calculation of the meteorological grid offset by ±1 grid point in the horizontal direction and 0.01 sigma units in the vertical. Using an ensemble of trajectories in the area of interest allows for a better approximation of the true state. Because uncertainties accumulate as a result of initial conditions in the trajectory calculation, running the ensemble simulation gives more confidence in the trajectory of air into a region in comparison to a single trajectory (Draxler, 2003). Running this program with back-trajectories allows for an assessment of air mass source areas for plumes that reached the location on a given date.

5.2.6 GEM-MACH FireWork

ECCC produces a near-term operational regional air quality forecast called the Regional Air Quality Deterministic Prediction System (RAQDPS). This is used to generate local AQHI forecasts based on model-predicted surface concentrations of O_3, $PM_{2.5}$ and NO_2 pollutants (Chen & GEM-MACH development team, 2019). Underlying this system is the chemical transport model

GEM-MACH. FireWork is an extension of the RAQDPS with the same anthropogenic emissions, grid, meteorology, and boundary conditions, but with the addition of near-real-time biomass-burning emissions (Pavlovic et al., 2016; Chen et al., 2019). The chemical lateral boundary conditions are from the MOZART seasonal chemical climatology that does not vary with time, and the meteorological lateral boundary conditions are from nested GEM simulations. The wildfire locations from the previous 24-hour are obtained from the Canadian Forest Services (CFS) operational Canadian Wildland Fire Information System (CWFIS), using satellite hotspot data. Fire emissions are estimated using the CFFEPS accounting for fire behaviour and regional meteorology (Chen et al., 2019). This allows for model simulations over the North American domain on a 10x10 km grid, with and without fire emissions. Fire plume height is determined by the thermodynamic plume rise scheme in CFFEPS. When compared with satellite observations from the Multi-angle Imaging SpectroRadiometer (MISR) and TROPOMI, on average, the GM-FW fire plume heights were above the observation by approximately 60-320 m and 270-580 m, respectively (Griffin et al., 2020), although this is within the uncertainty range of these measurements. GM-FW fire emissions were compared to well-established global fire emissions inventories regionally and globally for the years 2015-2020, and were found to be within the range of these datasets, indicating that the modelled fire emissions should be realistic (Anderson et al., 2024).

The output includes three-dimensional fields of VMRs for several chemical species. Here, vertical profiles of CO, NH_3 and O_3 over downtown Toronto and Egbert are extracted from the simulations with and without fire emissions and used to derive columns as described in Section 4.3. Surface values for CO, O_3, and $PM_{2.5}$ are extracted from the area corresponding to the OMECP locations of Toronto Downtown, Barrie, and Toronto West (for CO). The mean total column CO over the period of the three events is mapped over the area of Canada, and compared to MOPITT CO over the same time. Hereafter, these model results will be referred to as GM-FW (all emissions) or GM (without fire emissions). The data version used in these comparisons corresponds to “024”, where GM is “RAQDPS024” and GM-FW is “RAQDPSFW024” (ECCC, 2024).

5.2.7 Fire Perimeters

The fire perimeters used here are provided by the CWFIS Datamart (CWFIS, 2024). The hotspot locations are identified with satellite imagery from multiple sources, including the Advanced Very

High-Resolution Radiometer (AVHRR) from the NOAA National Environmental Satellite, Data and Information Service (NESDIS), and NASA's Moderate Resolution Imaging Spectroradiometer (MODIS) and Visible Infrared Imaging Radiometer Suite (VIIRS). These are processed into mapped areas with inputs from fire management, fire weather/fire danger rating systems.

5.3 Methods

5.3.1 Defining Enhancements and Events

Trace gas enhancements in the 0-10 km TAO FTIR partial columns are identified relative to the historical monthly means. These monthly means are derived from the TAO time series for 2002-2022, labelled in Figure 5.3 as the baseline ("BL"). Given the extended gap in the FTIR operations at CARE, the TAO baseline is used for both locations. Enhancement events are defined as a period for which CO is (generally) above the 1σ standard deviation of the monthly mean. The baseline is used to calculate the relative percent enhancements during different events in Section 5.4. Figure 5.3a shows the 0-10 km partial column time series of the TAO (orange markers) and CARE (yellow markers) FTIR measurements, and the baseline (black line) with ±1σ (grey shading). These are supplemented with measurements from the EM27/SUN FTIR (Figure 5.3b) co-located with TAO. Figure 5.3c shows the OMECP surface hourly $PM_{2.5}$ measurements from Toronto and Barrie, along with the 2020 Canadian Ambient Air Quality Standard (CAAQS) for $PM_{2.5}$ marked in red (27 $\mu g/m^3$ over 24-hour mean) (Health Canada, 2023). Several enhancements of CO can be seen throughout the summer, and three events of interest (May 16-23, June 3-9, and June 17-30) are highlighted in the figure with light blue shading; these events are discussed in detail in Section 5.4. Similar to Figure 5.3a and Figures B.1-B.6 show the time series for 2023 of the other species discussed.

To compute enhancement ratios between the fire-related species (as listed in Table 5.1) and CO, a linear regression is applied to the "partial column enhancement" using all measurements within the defined events which occur within ±3 hours of a CO measurement (Lutsch et al., 2016; Yamanouchi et al., 2020). The partial column enhancement is expressed as the difference between the 0-10 km partial column measurement, and the monthly baseline (e.g., Paton-Walsh et al., 2005). As not every measurement within the events is enhanced, there are instances of negative values in these plots. The uncertainty of the enhancement ratio (slope) accounts for the errors in

retrievals of both species (x and y axes) following the unified least squares approach in York et al. (2004).

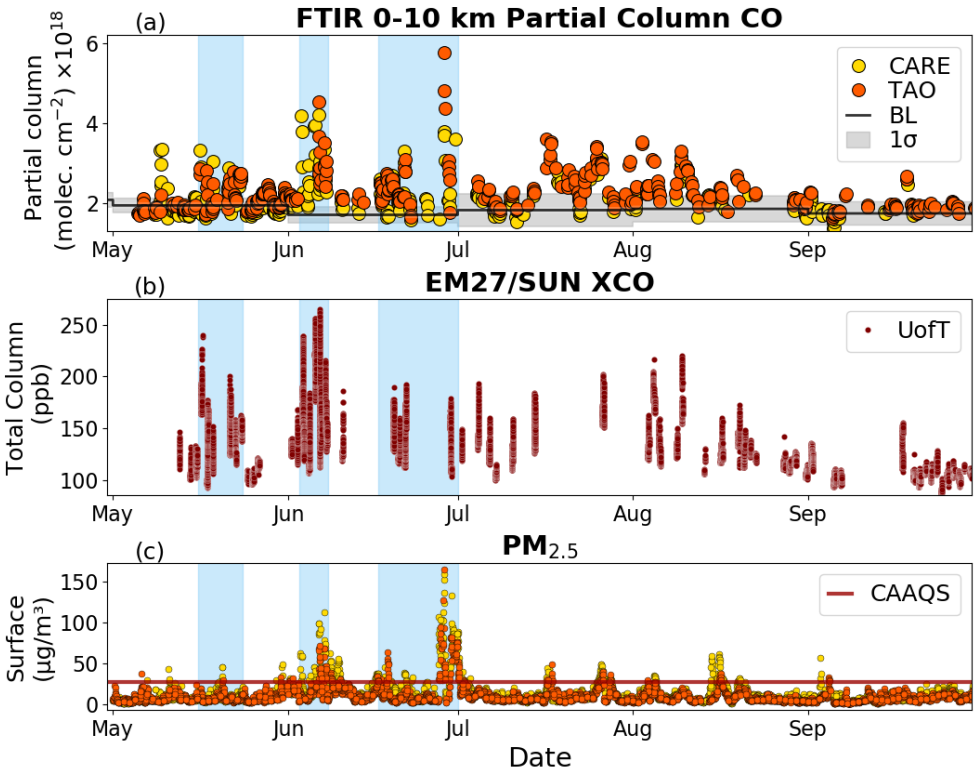

Figure 5.3: (a) CO 0-10 km partial columns from the TAO FTIR (orange) and CARE FTIR (yellow) with the TAO monthly mean baseline (BL) ±1σ marked with a black line and grey shading, (b) UofT EM27/SUN XCO. (c) OMECP $PM_{2.5}$ from Toronto (orange) and Barrie (yellow) with the CAAQS marked in red. The three events of interest are within the blue shaded regions.

5.3.2 Back-Trajectories

To determine the source of the air parcels transported over the TAO and CARE sites during the three events, the HYSPLIT ensemble trajectory model was used in the back-trajectory simulation analysis. The times and dates of back-trajectories for each event were chosen based on when the CO enhancements, as measured by the high-resolution and EM27/SUN FTIRs (as shown in Figure 5.3), and OMECP hourly air quality reports were at their peak values (similar to Selimovic et al., 2019). The dates/times chosen were 20:00 UTC May 16 for Event 1, 19:00 UTC June 6 for Event 2, and 21:00 UTC June 28 for Event 3. The trajectories were calculated for 72 hours back from these air parcel arrival times.

To choose the heights for which the back-trajectories are released, the TAO FTIR and MiniMPL data were used to determine the presence of the smoke layer during each event. Figure 5.4 shows the percent difference between the measured profiles during the day selected for the back-trajectory and the baseline profile to locate the altitudes of the peak relative enhancements. To supplement this, the MiniMPL NRB values corresponding to the same measurement time (within ±1 hour) were plotted as a function of altitude. In the FTIR profiles, there are maxima in the differences profile (Figure 5.4a-c) at approximately 5 km for Event 1, and 1 km for Events 2 and 3. These correspond well with the peak NRBs observed by the MiniMPL (Figure 5.4d-f) for those events, which are at higher vertical resolution than the FTIR data. (Note that the MiniMPL points above the fire enhancements are a result of noise from signal attenuation from above the smoke layer). Based on these profiles, the HYSPLIT ensemble back-trajectories were released from 1000 m and 5000 m, which corresponds to the peak CO and NRB profiles for the three events.

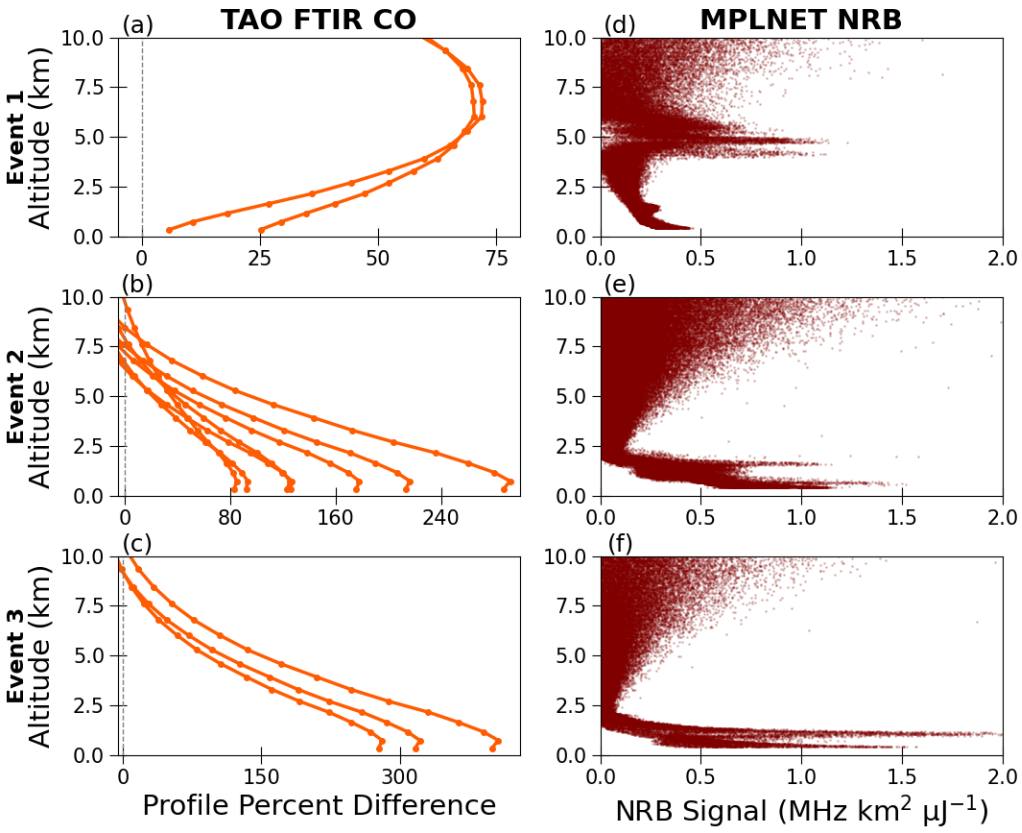

Figure 5.4: (a-c) TAO FTIR CO profile percent difference between the measurements on the peak day and the TAO baseline (100×[meas. - mean]/mean), (d-f) UofT MPLNET Normalized Relative Backscatter (NRB) for the times corresponding to FTIR measurements. Event 1 (a/d) shows May 16, Event 2 (b/e) shows June 6, and Event 3 (c/f) shows June 28.

5.3.3 GEM-MACH FireWork Comparisons

Model simulation results are available at one-hour intervals, so the FTIR measurements are matched with the output at the nearest hour. The FTIR and model data are aligned using the process outlined in Section 4.3 (and Flood et al., 2024). Briefly, the modelled atmospheric profile is extracted corresponding to the geographic location closest to the FTIR instruments, interpolated onto the FTIR pressure grid, and smoothed with the corresponding AVK and a priori profile. The smoothed model output is converted from a VMR profile (in ppmv) to a vertical profile in molecules/cm^2, and summed from 0 to 10 km to get partial columns.

These are used to evaluate how the GM-FW model simulates the tropospheric columns of CO, NH_3 and O_3, as compared to the high-resolution FTIR instruments at TAO and CARE. Using the GEM-MACH outputs with fire emissions ("GM-FW") versus without fire emissions ("GM") allows for the direct attribution and assessment of the impact of wildfires on atmospheric composition in the downwind receptor areas. The differences are assessed as a time series with the percent difference between GM-FW and the time-matched FTIR measurement, and overall percent difference (the mean of the percent differences) and the NRMSE error (as described in Section 4.3). In addition, the comparisons are presented in scatter plots, with a linear regression showing the slope and R value for both locations.

To assess the GM-FW vertical profiles, the mean profiles for each event are compared to the mean TAO FTIR profiles for each event. Additionally, the mean percent enhancement is calculated, similar to Figure 5.4a-c, with the FTIR compared to the baseline profile, and GM-FW compared to GM to show where in the profile the enhancements are the most significant.

In addition to the partial columns and profiles, the GM-FW surface VMR of CO, O_3 and $PM_{2.5}$ are compared with the OMECP surface measurements from the Barrie and Toronto stations. As mentioned, CO is only available from Toronto West, and the closest OMECP location to Egbert is Barrie; for these, the model output is extracted for the closest possible grid point. As both the model and OMECP give hourly concentrations, the comparisons are made using daily averages to reduce the impact of outliers and diurnal cycles. Similarly these are shown as a time series with percent difference, overall mean percent difference, NRMSE, and as a scatter plot with a linear regression.

To evaluate plume location during the events, the event-averaged CO VMR from GM-FW is plotted on a map of Canada, and on a zoomed-in map of Southern Ontario for each event. Comparing these maps with the similar maps of event-averaged CO columns measured by MOPITT allows for an assessment of the CO spatial distribution during each event.

5.4 Results and Discussion

5.4.1 Long-Range Transport of Events

Three events were defined based on the enhancements as discussed above. The time marked as "Event 1" is from May 16-23, "Event 2" is from June 3-9, and "Event 3" is from June 17-30. Each event resulted in progressively worse air quality in Southern Ontario (see the AQHI from Toronto Downtown for each event in Table B.1 and AQHI map in Figure B.7). Toronto experienced a total of 14 "poor air quality" days during the summer of 2023, where the maximum single-day mean $PM_{2.5}$ reached 129 μg m^{-3} (during Event 3), almost five times the CAAQS (Health Canada, 2023; Jain et al., 2024). Mendez-Espinosa et al. (2019) found both a temporal and spatial coincidence between pollution levels (including CO and $PM_{2.5}$), fire location/frequency and air mass origin when using HYSPLIT back-trajectories to examine urban air quality with fires within a buffer zone. Here, the difference between events can be observed in both the size/number of active fires and the long-range transport that is incident on the region, as depicted by the HYSPLIT back-trajectories.

Figure 5.5 shows the HYSPLIT 72-hour ensemble back-trajectory initiated at 5000 meters above ground level (magl) (a, c, e) and 1000 magl (b, d, f) from TAO for Event 1 (a, b), Event 2 (c, d) and Event 3 (e, f). The colour bar (blue to yellow) indicates the frequency at which air parcels from the ensemble passed over a given area, where a brighter yellow represents a higher occurrence. The red polygons represent the active fire hotspots at that time of the event with data from the CWFIS Datamart. The distance between TAO and CARE (70 km) is minimal compared to the distanced travelled by the air parcels as depicted in the back-trajectories; the CARE back-trajectories are comparable to these for TAO and are available in Appendix B (Figure B.8).

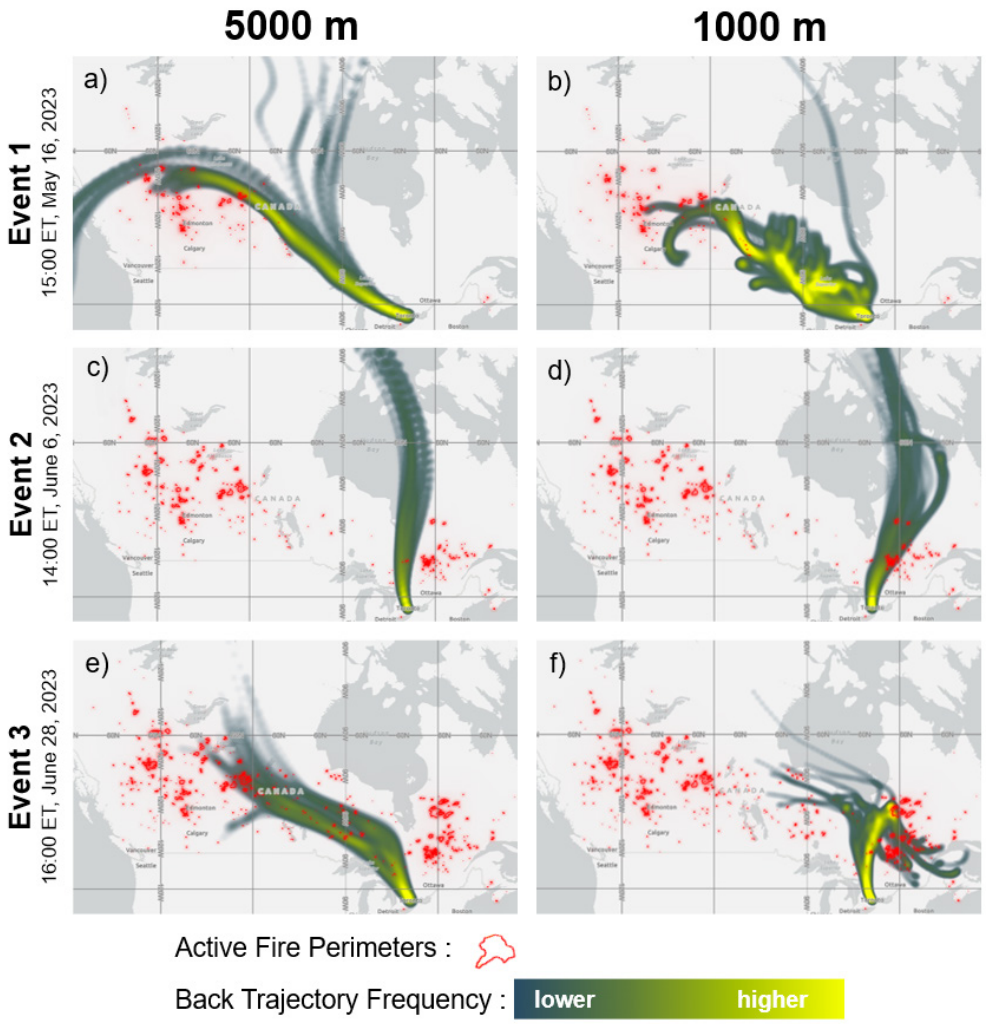

Figure 5.5: HYSPLIT 72-hour ensemble back-trajectories, initiated from TAO at the times listed, from 5000 m (a,c,e) and 1000 m (b,d,f). Red polygons represent the active fires at the time (CWFIS, 2024; Esri, 2020).

Event 1 was an early season event, where fires were concentrated in Western Canada. Figure 5a (and Figure B.8a) shows that the trajectories around 5 km in altitude during this time had passed over the fires in Alberta and Saskatchewan. The 1 km trajectories (Figures 5.5b and B.8b) did not extend as far, but show some overpass of fires in the Prairies. During Event 1, the AQHI remained predominately at "low risk" in both Toronto and Barrie, but with enhanced tropospheric columns, indicating that smoke plumes were aloft in the area. According to the CWFIS hotspot report, approximately 9506 km^2 were burned in Canada during Event 1 (CWFIS, 2024).

Event 2 happened as fire activity across Canada began to increase, particularly in Quebec. Figure 5.5c/d (and Figure B.8c-d) shows that at this time both the 1 km and 5 km trajectories had travelled

a similar path, crossing over fires in northwest Quebec. During this event, the AQHI in Southern Ontario was generally rated as “moderate risk”, with surface VMRs above the CAAQS threshold, and partial columns greatly enhanced. According to the CWFIS hotspot report, approximately 13,153 km^2 were burned in Canada during Event 2 (CWFIS, 2024).

Event 3 exhibited the most severe air quality degradation in Southern Ontario region, with active fires in many areas across the country. Figure 5.5e (and Figure B.8e) shows that the 5 km trajectories reached the region after passing over fires in Northern Alberta, Saskatchewan, Manitoba, and Northern Ontario. The 1 km trajectories (Figures 5.5f and B.8f) can be seen passing over the large active fires in Quebec. At the peak of the smoke event, the AQHI in Barrie and Toronto was labelled as “high risk”, smoke haze was visible to the eye and both surface and partial column measurements reached their local maximum for the year. According to the CWFIS hotspot report, approximately 24,659 km^2 were burned in Canada during Event 3 (CWFIS, 2024).

5.4.2 Enhancement Ratios

Enhancement ratios indicate the downwind relationship between a target species and a long-lived reference species (here CO) and provide insight into the composition of a plume. These relationships can be a useful reference point for developments in chemical transport models. As described in Section 5.3.1, the enhancement ratios are represented by the error-weighted linear regression of the partial column enhancements, during the events. Figure 5.6 shows the 0-10 km partial column enhancements between each gas and CO for May to September 2023 measured within 3 hours of each other for both TAO and CARE (grey), the times which correspond to measurements within the fire events are coloured. The number of measurements for any given time is dependent on the operations of the FTIR, which may be restricted due to reduced solar intensity (e.g., weather, cloud, haze thick smoke) or operational downtimes. Due to the similarities shown in the long-range trajectories examined in Section 5.4.1 (Figures 5.5 and B.8), the line of best fit and the consequent regression analysis is applied to the combination of CARE and TAO data, to maximize the number of data points used. To examine the differences between the fire events and their transport to Southern Ontario, the enhancement ratios for each event are plotted separately (Figure 5.6). Assuming that the major contributions throughout each event are represented by the HYSPLIT back-trajectories (Figure 5.5 and B.8), Event 1 was due to transport from Western Canada, Event 2 from Quebec, and Event 3 a mix of both. Figure B.9 shows the same information

as Figure 5.6, but with data from the three events combined, and a single enhancement ratio calculated for each species. Table B.3 summarizes the different slopes and R values between the two methods and indicates if the slope/R value increased (green shading), decreased (red shading) or remained the same (yellow shading) relative to the combined value.

Considering the slope and R values of the enhancement ratios for all the events, a positive relationship is observed between enhancements in CO with C_2H_6 (R=0.36-0.52), CH_3OH (R=0.64-0.82), HCN (R=0.51-0.77), and HCOOH (R=0.66-0.87) during the events. The correlation between CO and NH_3 (R=0.32-0.47) is lower, and even less so for O_3 (R=0.06-0.49). There are fewer enhancements present in the time series for NH_3 and O_3 (as seen in Figure B.5 and B.6), which result in more partial column enhancements on or near the negative axes, and less correlation with the fire-enhanced CO values. This may be linked to NH_3's short lifetime with primarily agricultural sources in Southern Ontario, and O_3's non-linear photochemistry that may be suppressed during some fire events. The regression only considers points during the events, similar to other studies which examine enhancement ratios with FTIR measurements (e.g., Lustch et al., 2016, 2020; Yamanouchi et al., 2020), where all observations within an event are used. However, the ratios presented here consider the partial column enhancements relative to the background level, rather than a total column measurement, as the previously mentioned studies do.

Comparing the 2023 enhancement ratios to those discussed in the long-term TAO analysis (Yamanouchi et al., 2020), C_2H_6 is within the broad range previously reported (0.003-0.009 vs. 0.0012-0.019), CH_3OH is generally lower (0.016-0.028 vs. 0.029-0.045), HCN is within the previously reported range (0.003-0.006 vs. 0.0037-0.0057), and HCOOH is also lower (0.012-0.030 vs. 0.033-0.041). When comparing with the combined values, with the exception of O_3, all of the enhancement ratios are increased with Event 1 (smoke from western Canada), decreased with Event 2 (smoke from Quebec), and are mixed for Event 3 (increased, decreased, and unchanged). The Event 1 values are closer to those reported in Yamanouchi et al. (2020), consistent with less intense, long-range transport more commonly experienced by the Toronto area. The differences in enhancement ratios between the three events may be due to differences in vegetation, burn phase, meteorology along the plume path, and/or chemistry and plume aging. All are particularly relevant for CH_3OH and HCOOH, which have a more significant difference in slopes and improved R-values when split, and are shorter-lived species (Jacob et al., 2005; Paulot et al., 2011). Species like C_2H_6 and HCN have somewhat higher R values when combined, and less

significant slope changes, which is consistent with their longer chemical lifetimes and less dependence on plume aging over these distances and time scales (Viatte et al., 2015; Xiao et al., 2008). The higher R values and broad range in ratios between events for NH_3 and O_3 highlight the reactivity and variability of these species, which will be discussed further in the following paragraphs.

NH_3 was not discussed in respect to biomass burning enhancements with the TAO FTIR in Yamanouchi et al. (2020), however it was considered in Lutsch et al. (2020) in relation to the long-range transport of emissions from the 2017 fires in Northwest Territories, Canada. They report an enhancement ratio of 0.00465 with an R value of 0.45; here, the R value and slope are lower (R=0.34 and 0.003). Additionally, the NH_3/CO correlation coefficient derived from the same 2017 fires are higher at the High Arctic site at Eureka (80°N) than at Toronto (R=0.70 vs. R=0.45), in part because of fewer local NH_3 sources (e.g., agricultural, urban, industrial) contributing to the signal in the Arctic. During the 2019 Fire Influence on Regional to Global Environments and Air Quality (FIREX-AQ) campaign, NH_3 and submicron particulate ammonium (NH_4^+) were measured with aircraft in smoke plumes. This showed that in wildfire plumes, NH_3 was converted to NH_4^+ within 2 hours of emission (Tomsche et al., 2023). Using aircraft measurements from the Western Wildfire Experiment for Cloud Chemistry, Aerosol Absorption, and Nitrogen (WE-CAN), Lindaas et al. (2021) studied NH_3 and NH_4^+ in fresh (<1 day) to old plumes (>3 day). They found that conversion to NH_4 increases NH_3 loss in fresh plumes; although background errors become larger as a plume dilutes and enhancements approach background levels. Adams et al. (2019) discuss the broad range of NH_3/CO emission factors, referencing a short (and method-dependent) lifetime (3-48 hours) and the association of NH_3 release during smoldering combustion. The combination of a short lifetime, reactivity, and variable local sources in Southern Ontario can all contribute to the lower correlation seen here.

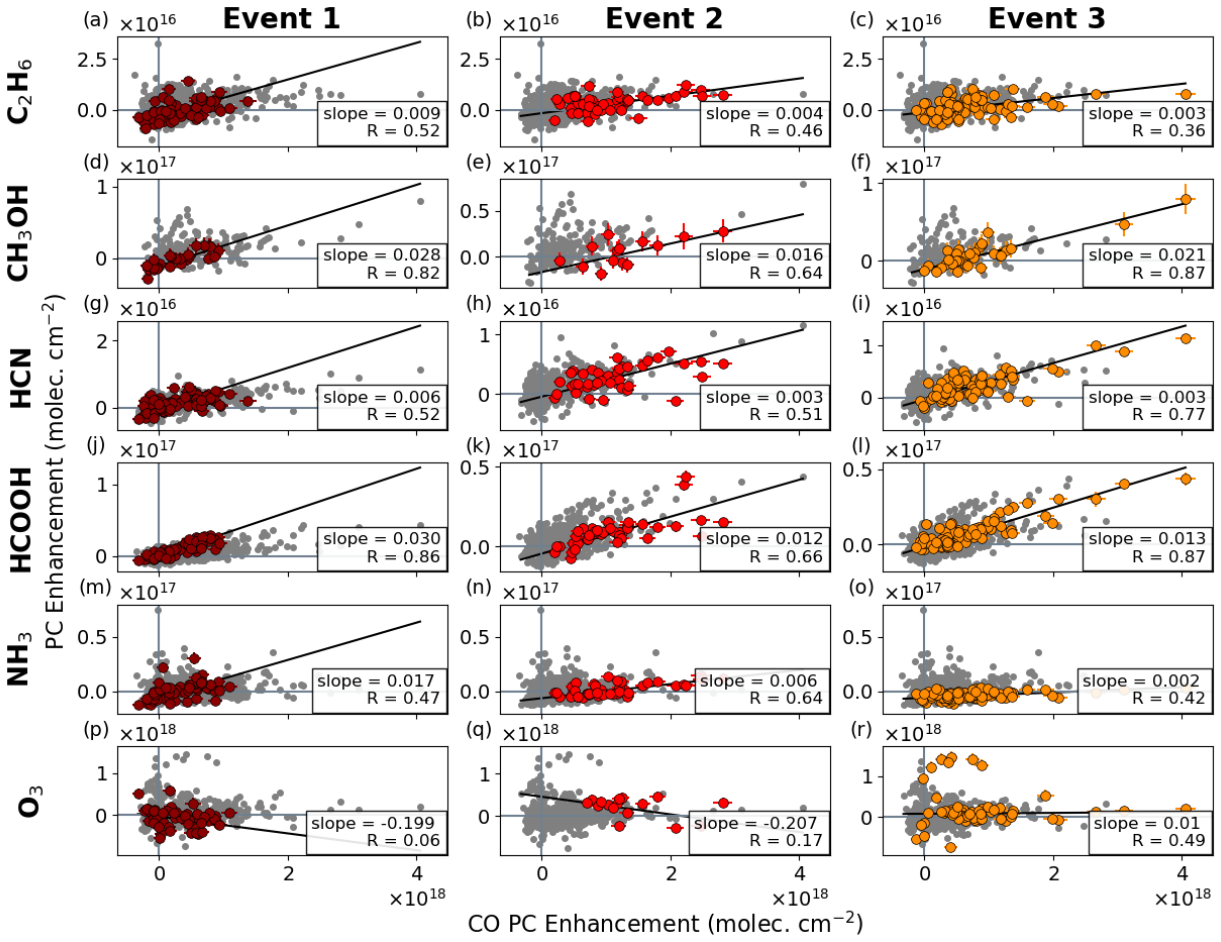

Figure 5.6: 0-10 km partial column enhancement of biomass-burning-related species vs. CO (measured within ±3 hours) for TAO and CARE FTIR May - September 2023 (grey), events are marked with colour, and separated by column. Error-weighted slopes are shown for the combined TAO and CARE datasets.

The concentration of O_3 resulting from wildfires also varies with properties such as plume height, burn characteristics, plume age, and meteorology (Jaffe & Widger, 2012). The ratio of O_3/CO above a background value can indicate the O_3 production within a smoke plume, and has been found to have a wide range of values, including negative values (Jaffe & Widger, 2012, and references therewithin). Ratios have been found to be higher in tropical/equatorial areas and increase with plume age, both of which are influenced by NOx availability (Jaffe & Widger, 2012). Schneider et al. (2021) found that surface O_3 in Western Canada was both enhanced and reduced during wildfire events, remarking that pollutants present in urban areas can confound the ratios. A study of the intense 2016 Alberta boreal forest fires found no substantial increase in surface O_3 with downwind plumes aged approximately 0.5-2.5 days, citing unfavourable meteorological conditions for O_3 formation (Wentworth et al., 2018). All of these factors may contribute to the

poor correlation observed between O_3 and CO in the TAO and CARE datasets with respect to the 2023 Canadian wildfires. Furthermore, the previous long-term analysis of wildfire emissions present in the TAO FTIR dataset did not discuss O_3 enhancements related to biomass burning (Yamanouchi et al., 2020). The surface O_3 measurements collected in Toronto and Barrie by OMECP during the summer of 2023 are quite variable, there are some instances where the values surpass the CAAQS standard (62 ppbv, based on the 3-year average of the fourth-highest daily maximum), however these do not align with the events discussed in this chapter (see Figure B.10).

Zhang et al. (2024) used two satellite instruments, ACE-FTS and OMPS LP (Ozone Mapping and Profile Suite Limb Profiler), to assess trace gas enhancements related to the 2023 wildfires. Examining the monthly mean profiles from 40°N to 70°N, an increase at altitudes between about 8-11 km for CO, C_2H_6, CH_3OH, HCN, and HCOOH in 2023, relative to the 2004-2022 mean, was observed. However, the profiles were not significantly enhanced in the stratosphere, indicating that the plumes were transported within the troposphere. This is consistent with the MPLNET and FTIR profiles plotted in Figure 5.4, in addition to the correlations observed in Figure 5.6 and the enhancements in the time series (Figures 5.3 and B.1-B.6).

5.4.3 GEM-MACH FireWork Model-Measurement Comparisons

This section evaluates the GM-FW outputs around Toronto and Egbert with FTIR partial column and OMECP surface measurements, and more broadly across Canada with time-averaged total columns from MOPITT. This allows for an assessment of the location-specific model performance at the surface and through the troposphere, and a broader perspective of long-range transport. GM (without fire emissions) is shown in the column FTIR and surface comparisons (Figures 5.7-5.9 and 5.11) to highlight and quantify the difference caused by the fire emissions, specifically when GM-FW values are above those of GM. Table 5.2 outlines the mean percent difference and NRMSE spanning May through September, by gas and location for the FTIR and surface comparisons.

5.4.3.1 Tropospheric Column Comparisons

Figures 5.7-5.9 show the time series of the 0-10 km partial columns of CO, NH_3 and O_3 from the FTIRs and corresponding model simulated column densities (both GM and GM-FW) for TAO (panel a) and CARE (panel b), where the points are time-matched, as described in Section 5.3.3.

Similar to Figure 5.3, the baseline is indicated with a black line, and ±1σ is represented with grey shading. Panel c of Figures 5.7-5.9 shows the percent difference between the GM-FW and FTIR partial columns for both locations. As the model values are aligned with the FTIR using information from the retrieval, as outlined in Section 5.3.3, model results are only applicable when there is a corresponding FTIR measurement. Figure B.11 shows the time-matched GM-FW partial columns versus the FTIR partial columns of CO, NH_3, and O_3 with a line representing the linear relationship for each location, and a black line representing a 1:1 ratio. Generally, in the 0-10 km partial column the model underestimates background concentrations of CO, NH_3, and O_3 with the overall percent difference across the May – September period for the combination of TAO and CARE being -12.97%, and -44.32%, and -21.73%, respectively. These negative biases (Table 5.2) are greater than the FTIR measurement uncertainties (Table 5.1) and may indicate that the anthropogenic emissions (or subsequent chemistry) of these species is underestimated.

As seen in Figure 5.7c, the GM-FW model underestimated the enhancements in the tropospheric partial columns of CO for Event 1, relative to the FTIR in both locations. Although there are a few points with a positive bias, these do not correspond to the enhanced FTIR measurements. For Event 2, the magnitude of enhancements in GM-FW CO are low in comparison to those measured in the earlier days of the event by the FTIRs, appearing minimally enhanced compared to GM (as seen in Figure 5.7a and 5.7b), until towards the end of the event (June 6-7). Throughout Event 2, the CO at CARE is generally underestimated, however the maximum column is overestimated at TAO, showing some instances with larger partial columns than in Event 3. Similar to Event 2, the GM-FW values for Event 3 have minimal increases between GM and GM-FW until later in the event when the maximum enhancements are reached, though these are well represented by GM-FW relative to the FTIRs. The assorted CO enhancements seen in the FTIR time series throughout the rest of the season are also underestimated by GM-FW, with an overall mean difference of -12.97%. Despite some differences between locations during the events, the overall biases and NRMSE for GM-FW relative to the FTIR tropospheric CO partial columns are comparable (-15.37% / 1.25 for TAO and -10.26% / 1.11 for CARE, respectively).

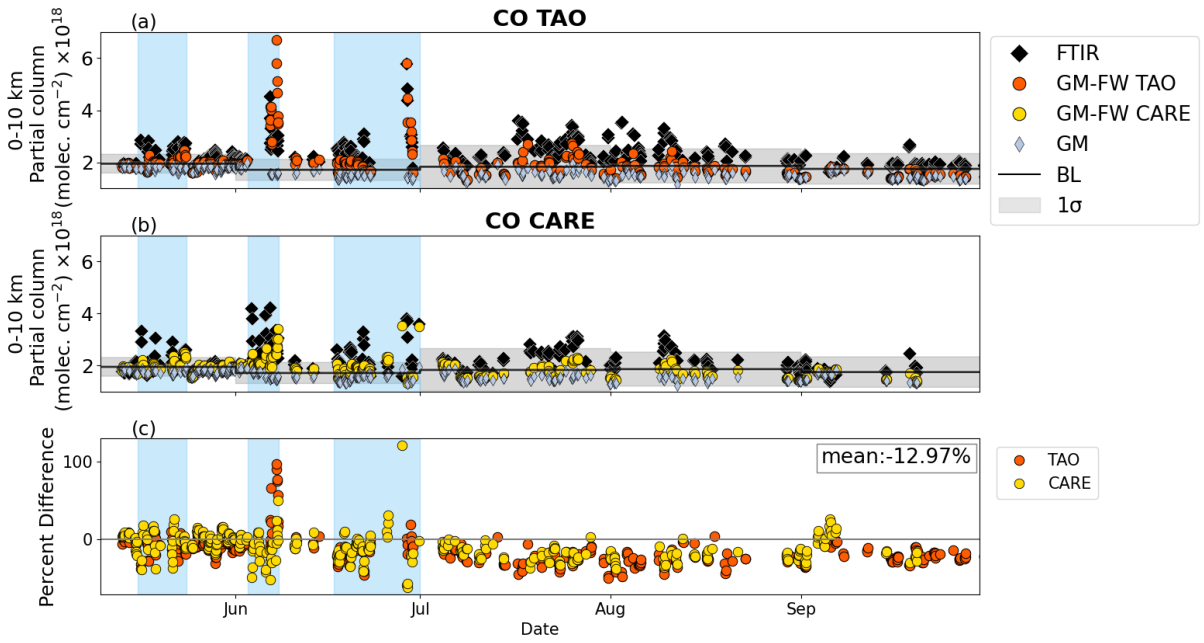

Figure 5.7: 0-10 km partial column CO from (a) TAO and (b) CARE for the FTIR (black diamonds), GM (grey diamonds) and GM-FW (orange/yellow points). (c) percent difference between GM-FW and FTIR for both TAO (orange) and CARE (yellow) (100×(GM-FW – FTIR)/FTIR). Events 1-3 are marked with blue shading, the black line is the baseline (monthly mean), and the grey shading is ±1σ of the monthly baseline.

NH_3 was enhanced above the baseline +1σ for Event 1 (Figure 5.8), though GM-FW simulated enhanced NH_3 for all three events. The NH_3 is better represented at CARE compared to TAO with approximately 25% difference in the mean bias and a NRMSE of 0.82 vs. 1.34 (see Table 5.2). The difference between the rural and urban locations may indicate that a local emission source(s) is underrepresented in the model. Comparing satellite-derived emission ratios to the GM-FW modelled values from the Alberta Horse River fires, Adams et al. (2019) reported that the NH_3/CO ratio was in good agreement (approximately 1.5 times lower in the model). Comparing this finding with the overestimation of NH_3 during the events seen in Figure 5.8, suggests the model assigns a reasonable NH_3 emission at the source, but has a lifetime that is too long. In addition, background NH_3 may be underestimated by the model due to a lack of the bidirectional flux process (Farquar et al., 1980). The re-emission of deposited NH_3 was added in a research version of GM and shown to reduce its negative bias in background conditions (Whaley et al, 2018), but is not included in the operational version of the model used in this work.

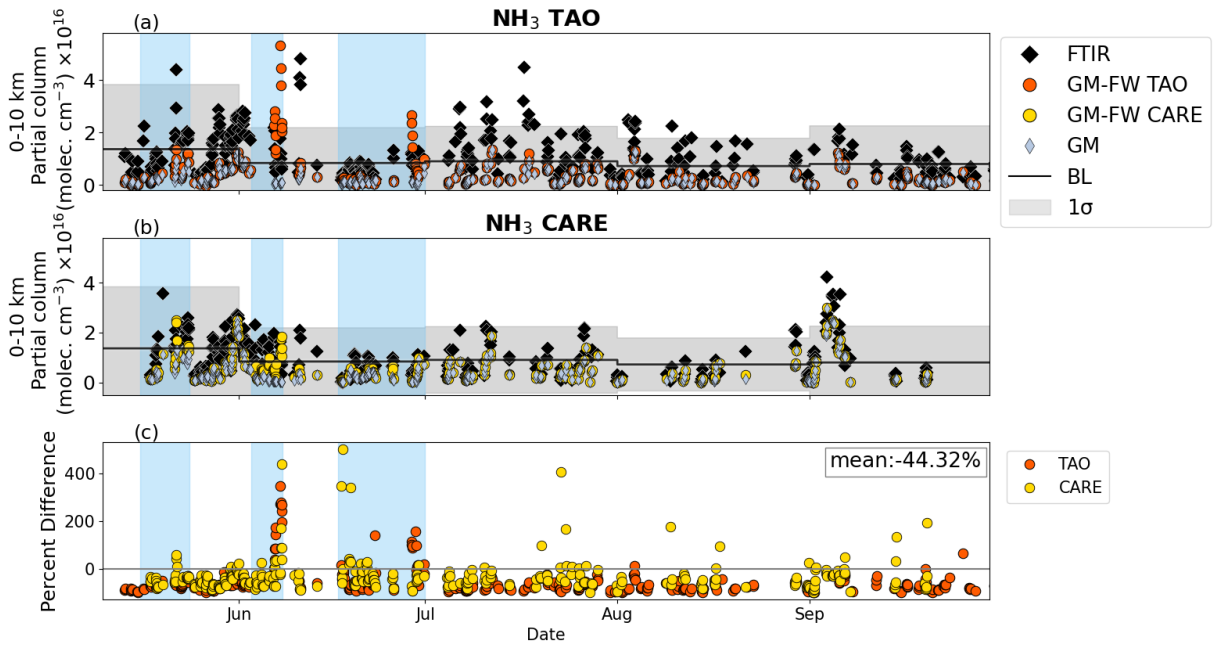

Figure 5.8: 0-10 km partial column NH_3 from (a) TAO and (b) CARE for the FTIR (black diamonds), GM (grey diamonds) and GM-FW (orange/yellow points). (c) percent difference between GM-FW and FTIR for both TAO (orange) and CARE (yellow) (100×(GM-FW – FTIR)/FTIR). Events 1-3 are marked with blue shading, the black line is the baseline (monthly mean), and the grey shading is ±1σ of the baseline.

O_3 enhancements were measured during Events 1 and 3 at CARE, but not for any events at TAO. GM-FW simulated only very small increases in O_3 during Event 3 at TAO. The overall O_3 percent difference for both TAO and CARE are on the order of -21%, while the NRMSE is somewhat better for CARE at 1.34 vs. 1.64 at TAO.

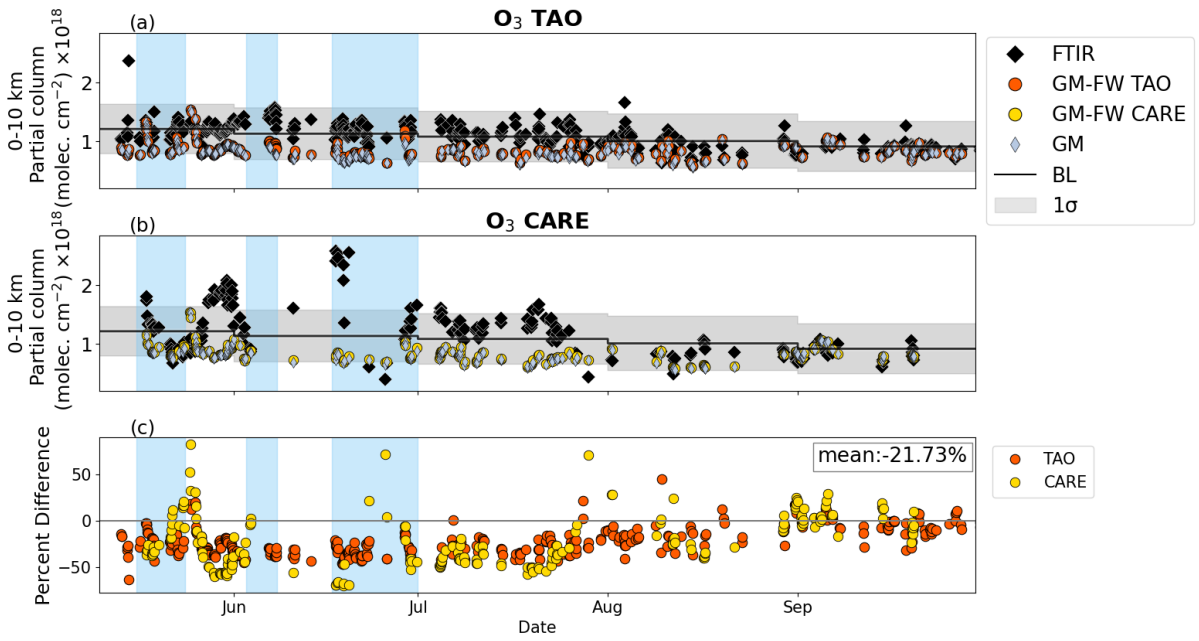

Figure 5.9: 0-10 km partial column O_3 from (a) TAO and (b) CARE for the FTIR (black diamonds), GM (grey diamonds) and GM-FW (orange/yellow points). (c) percent difference between GM-FW and FTIR for both TAO (orange) and CARE (yellow) (100×(GM-FW – FTIR)/FTIR). Events 1-3 are marked with blue shading, the black line is the baseline (monthly mean), and the grey shading is ±1σ of the baseline.

Table 5.2: Mean percent difference (100×(GM-FW – FTIR)/FTIR) and NRMSE for the comparisons of GM-FW to measurements of tropospheric columns and the surface concentrations for CO, NH_3, O_3 and $PM_{2.5}$ from May-September 2023.

		Tropospheric Column		Surface	
		TAO	**CARE**	**Toronto**	**Barrie**
CO	Mean % Difference	-15.37	-10.26	28.98	/
	NRMSE	1.25	1.11	1.73	/
NH_3	Mean % Difference	-55.92	-30.49	/	/
	NRMSE	1.34	0.82	/	/
O_3	Mean % Difference	-21.61	-21.95	-24.07	-5.43
	NRMSE	1.64	1.34	1.37	0.85
$PM_{2.5}$	Mean % Difference	/	/	52.24	-52.02
	NRMSE	/	/	1.34	0.87

The vertical profiles retrieved with the FTIR were compared with those from GM-FW (unsmoothed), Figure 5.10a-c shows the mean VMR profile for each event, and the monthly mean baseline profiles for May and June. To assess the altitude and magnitude of enhancements, Figure 5.10e-f shows the mean "percent enhancement" profiles for GM-FW and the TAO FTIR over each event (similar to Figure 5.4a-c). The mean FTIR profiles are made using all of the available measurements during each of the three events, while the percent enhancement is the percent difference between the event-averaged profile and the relevant monthly mean baseline profile. The

mean profile for GM-FW uses all of the days during each of the three events, limited to 7 AM to 7 PM local time to reflect the daytime constraint of the FTIRs, while the enhancement profile is defined relative to the corresponding mean GM profile. These differences aim to represent the percent contribution from the wildfire emissions at the time of the events, relative to the background VMRs.

GM-FW and the FTIR both show the CO maximum in the lowest layers near the surface for Events 2 and 3. But for Event 1, the model shows a vertical profile where CO was at a maximum around 4 km aloft (Figure 5.10a). The FTIR profile does not quite match that, however, its vertical resolution is lower, and it is influenced by the a priori profile shape. The CO attributed to the smoke plumes (Figure 5.10d) is generally overestimated at their peaks relative to the FTIR, but this could be due to the FTIR's lower vertical resolution. The GM-FW CO VMR for Event 2 at TAO is overestimated by about 50% in the lowest 3 km, which is consistent with the results seen in Figure 5.7.

The smaller NH_3 and O_3 enhancements in the FTIR measurements during the events, as seen in Figure 5.6 (5.8 and 5.9), is reflected by overlap of the FTIR event profiles with the May and June monthly means (grey lines in Figures 5.10b and 5.10c), and consequently the FTIR profiles show less distinct patterns between events. It is clear from Figure 5.10e that the GM-FW NH_3 is significantly overestimated in all three events relative to the GM, at altitudes ranging from ~1-3 km for Event 3, to 3.5-5.5 km for Events 1 and 2. This may be less obvious in the time series plots as some of the extreme NH_3 outliers by GM-FW that are creating the high bias may be missed by gaps in the FTIR measurements and/or reduced by the smoothing routine; nonetheless, there are still instances where the GM-FW minus FTIR difference is over 400% (Figure 5.8c). O_3 enhancements in GM-FW are primarily seen in the lower 2.5 km for Events 2 and 3, while the FTIR enhancement profiles oscillate around the monthly mean baselines. The variability in O_3 enhancements may be a result of competing processes; O_3 enhancements from fire can occur from the emitted VOCs interacting with urban NO_x pollution, however reduced photolysis in smoke plumes may cause a reduction in O_3.

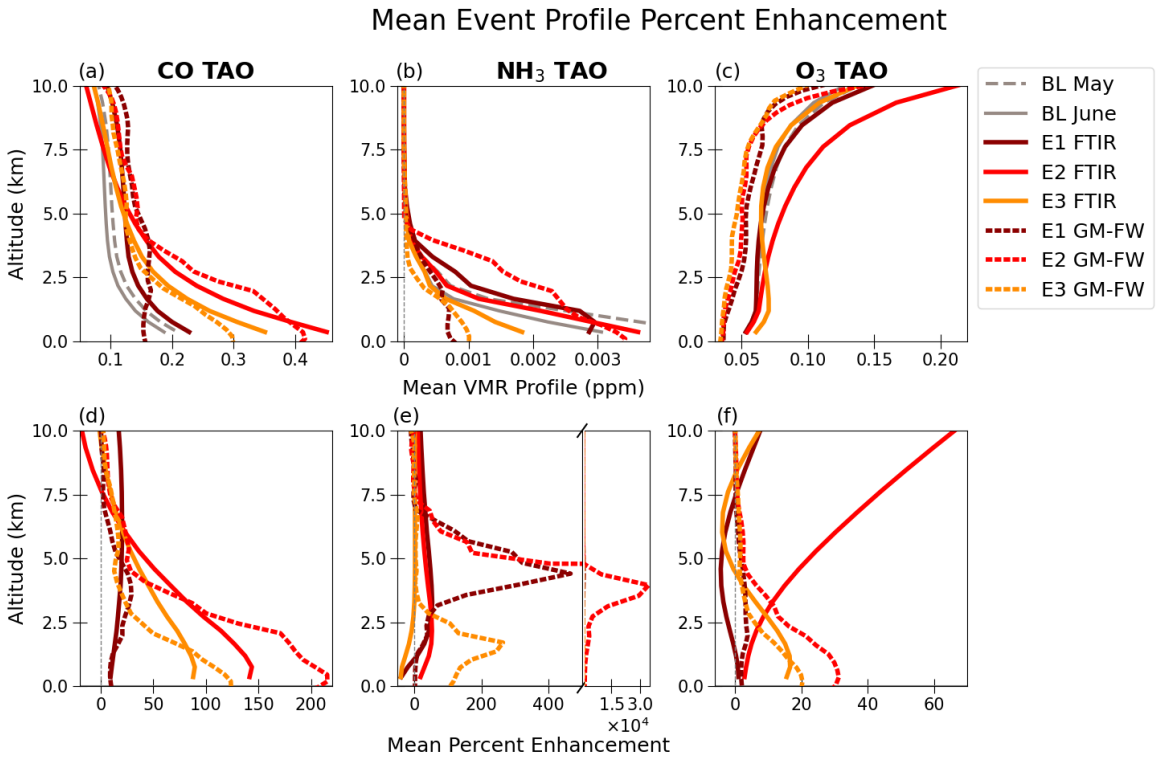

Figure 5.10: (a-c) The mean VMR profile by event from the TAO FTIR (solid lines) and GM-FW (dashed lines), and the monthly mean May and June baseline profiles (grey). (d-f) The mean percent enhancement profiles for each event; solid lines are 100×(TAO FTIR event-averaged profile – the relevant monthly mean baseline profile) and dashed lines are 100×(GM-FW event-averaged profile – GM event-averaged profile).

5.4.3.2 Surface Comparisons

Figure 5.11 shows the GM (grey diamonds) and GM-FW (Toronto in orange and Barrie in yellow) daily surface means compared to the OMECP daily mean surface concentrations for CO, O_3 and $PM_{2.5}$ (black diamonds). The model results are extracted at the closest location to each OMECP station. The bottom row (panels f-h) shows the percent differences between the daily surface GM-FW and surface measurement, with the mean percent difference representative of all the points on each panel. Figure B.12 shows the comparison of daily mean GM-FW vs. the OMECP for CO, O_3 and $PM_{2.5}$, and Table 5.2 shows the mean percent difference and NRMSE by location. Using the summer mean values from Table B.2 and the instrument detection limits from Section 5.2.2, the approximate percent uncertainty is 10% for surface CO, <2% for surface O_3, and approximately

5% for surface $PM_{2.5}$ at Toronto, and <1% for surface $PM_{2.5}$ at Barrie. Comparing these to the mean percent differences in Table 5.2, the model bias outweighs the uncertainty in each case.

The OMECP surface CO shows a few enhancements throughout the summer (see Figure B.10c). As seen in Figure 5.11a, both GM and GM-FW often overestimate the surface CO. GM-FW shows more surface enhancements (in frequency and value) than the OMECP measurements. Furthermore, there are points from GM that are enhanced relative to an average day, implying a direct anthropogenic source, even at times when the CO is likely related to fire emissions (e.g., following Event 3), suggesting that the fire emissions only contributed a small amount to the enhanced CO at that time. Both observations and GM-FW showed greater fire enhancements in the CO column compared to the surface, indicating the model roughly captures CO enhancements aloft from the fire emissions. However, the positive surface bias, compared to the negative tropospheric column bias, may indicate that the model overestimates CO at the surface and poorly characterizes the vertical distribution of background CO.

Surface O_3 is generally underestimated by GM and has only a few points from GM-FW that are enhanced due to fire emissions during Events 2 and 3. The mean percent difference for both tropospheric column comparisons and Toronto surface comparisons are all similar (-21% to -24%). The Barrie station has a smaller bias of -5.43% and NRMSE of 0.85, however this may be impacted by the upward trend seen in September (see Table 5.2 and Figure 5.11g).

GM-FW $PM_{2.5}$ shows a mean overestimation of 52% at Toronto, and a mean underestimation of 52% in Barrie, which results in a near 0 mean difference when the results from the two locations are combined (see Table 5.2 and Figure 5.11h). The GM points in Figure 5.11 also show this difference, which suggests there is an overestimation of urban emissions, and underrepresentation of rural emissions within the model. However, the timing in $PM_{2.5}$ enhancements from smoke is captured within the model, though with inconsistent magnitudes. The $PM_{2.5}$ biases may be influenced by the above-mentioned differences in NH_3 (see Table 5.2 and Figure B.11c).

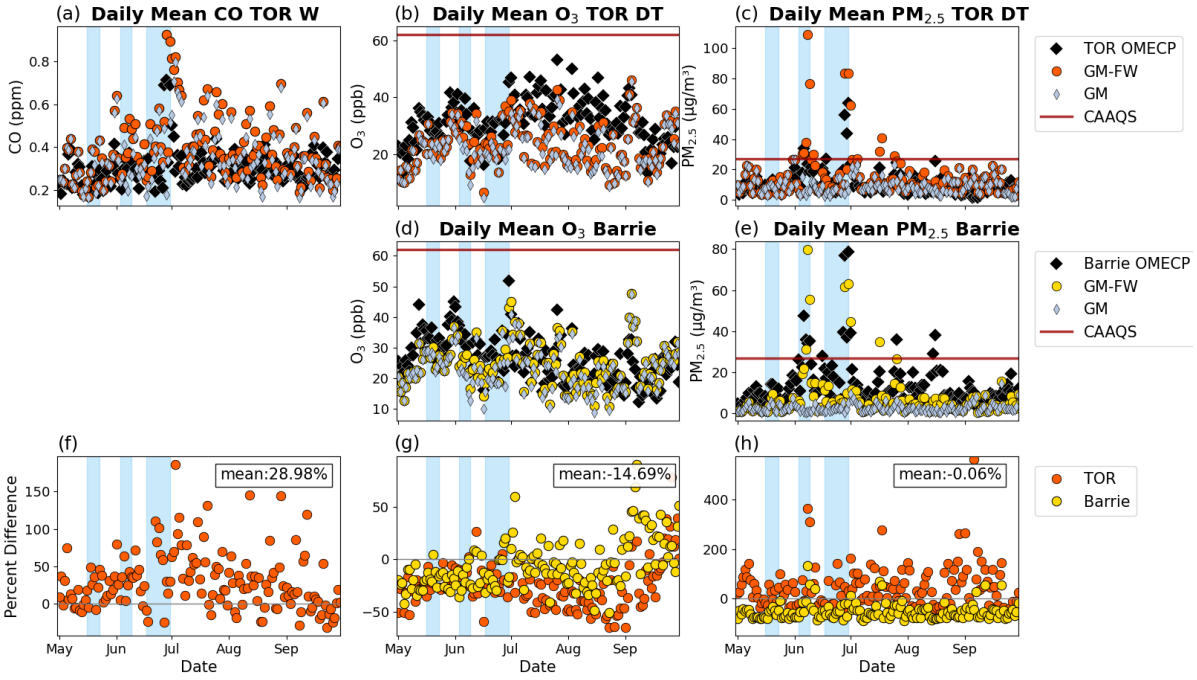

Figure 5.11: Daily mean surface values from OMECP, GM, and GM-FW for (a) CO (Toronto West), (b,d) O_3 (Toronto Downtown and Barrie) and (c,e) $PM_{2.5}$ (Toronto Downtown and Barrie), with the CAAQS marked by a red line. (f-h). The percent difference between GM-FW and OMECP (100×(GM-FW – OMECP)/OMECP). The mean differences in panels f-h is for all the points combined.

5.4.3.3 Satellite Comparisons

Figure 5.12 shows the GM-FW and MOPITT mean total column XCO over Canada for each event period, where the location of TAO and CARE is marked with a cyan circle. Although the model has a higher spatial resolution than the satellite (22 km × 22 km for MOPITT vs. 10 km × 10 km for GM-FW) potentially leading to larger peak values, overall, the regions with notable enhancements are comparable. This indicates that the model effectively represents the long-range transport of CO during the smoke events, which indirectly indicates that the fire plume height of the emissions is probably accurate.

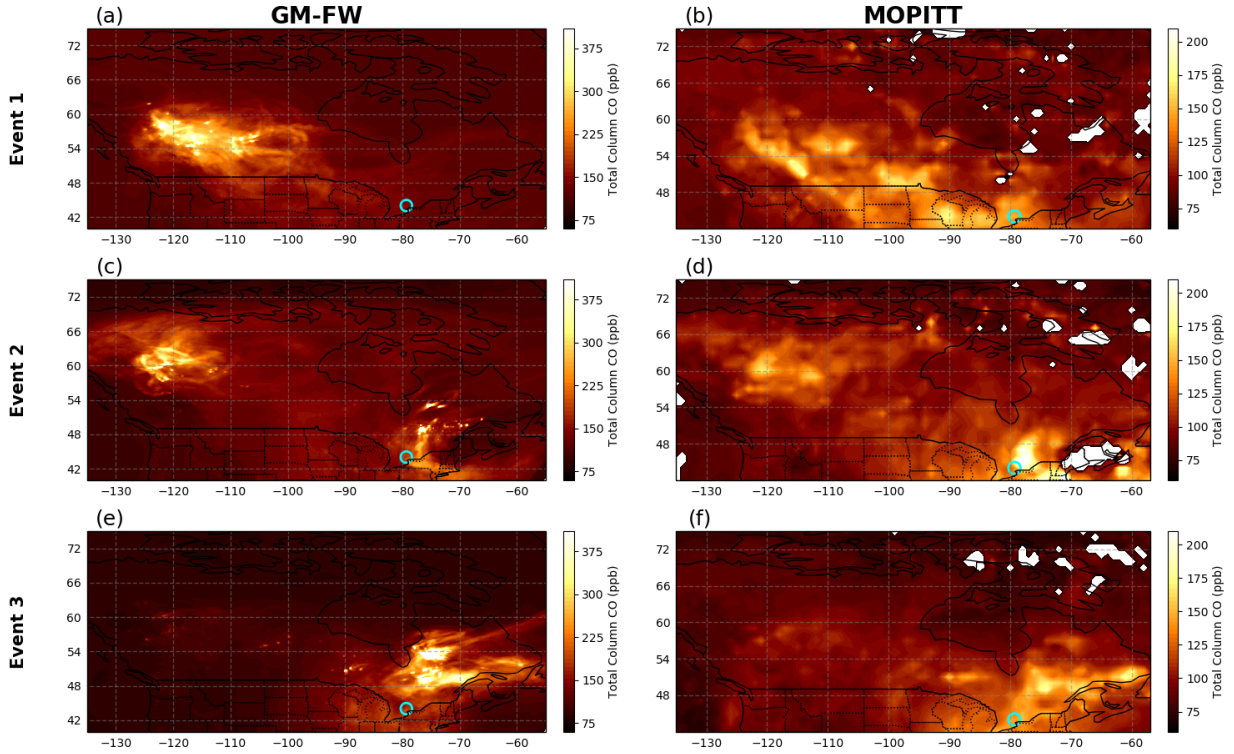

Figure 5.12: Mean total column CO (ppbv) during each of the three events (May 16-23, June 3-9, and June 17-30, 2023), from GM-FW (a, c, e) and MOPITT (b, d, f). The general area of TAO and CARE is marked with a cyan circle. Note scales differ between GM-FW and MOPITT.

Figure 5.13 shows the same information as Figure 5.12, but zoomed into Southern Ontario, including Toronto and Egbert. Panels a and b show that for Event 1, when both TAO and CARE CO were underestimated by the model (as seen in Figure 5.7), the model vs. MOPITT results are spatially consistent. This implies that the model's event-averaged plume was in the correct location, however, overall, the model is underestimating the mean CO over Event 1. Panel a and b in Figure 5.13 may indicate that this is related to resolution, where MOPITT measurements are coarser. For Event 2, Figure 5.7 showed that the model overestimated CO at TAO, but underestimated CO at CARE. From Figure 5.13c-d, it looks like the event-averaged plume was not actually over either site during Event 2 – according to MOPITT, it was to the east of both sites – but GM-FW located it further to the south, thus causing the overestimation at TAO, but not at CARE. Finally, for Event 3, Figure 5.7 implied that the model CO matched well for TAO, but was a little underestimated for CARE. Figure 5.13e-f is again consistent with Figure 5.7, and shows that this underestimation was because the area of reduced CO in GM-FW was closer to CARE than to TAO, while that reduced CO area was located even further west in the MOPITT measurements.

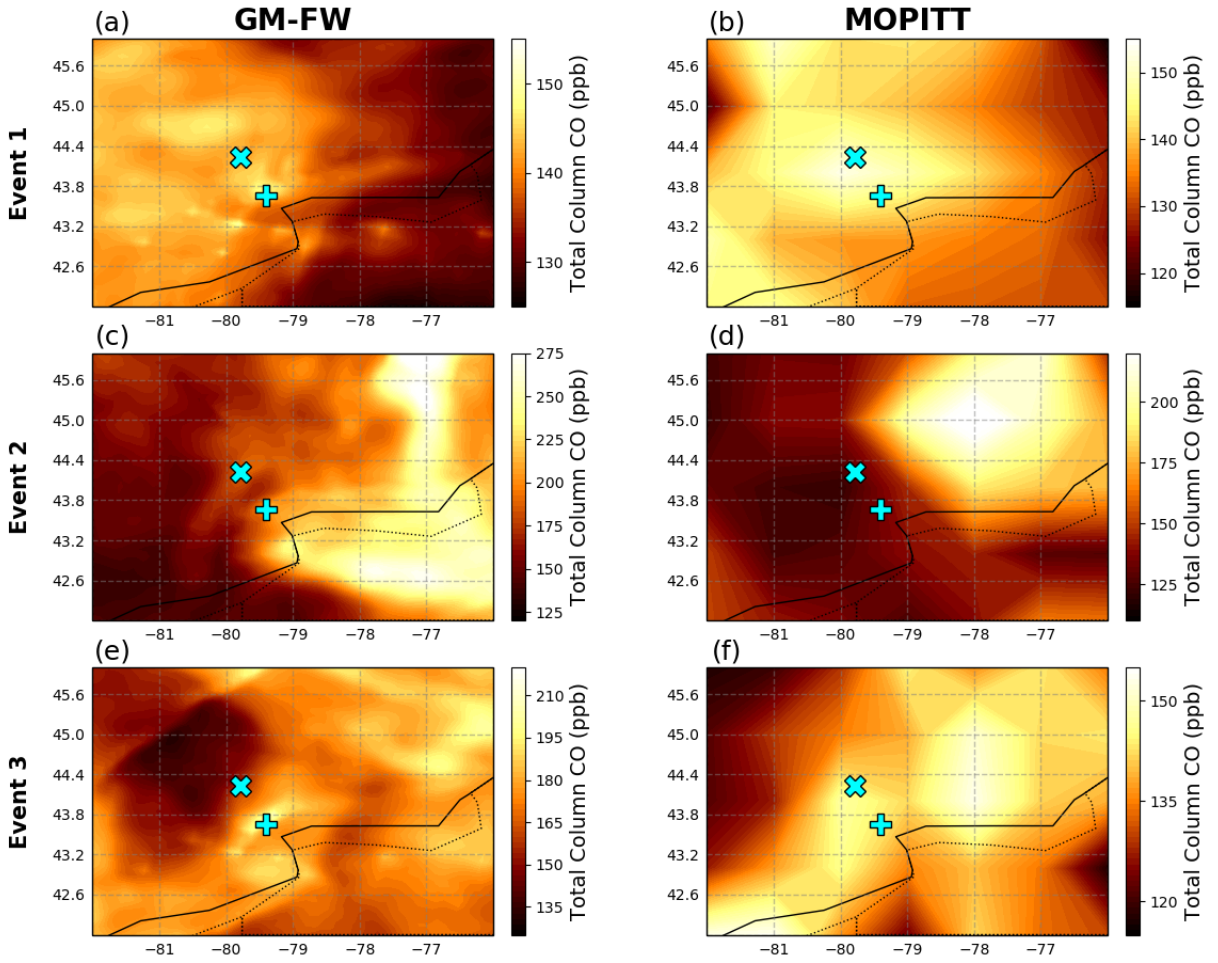

Figure 5.13: Same as Figure 5.12, zoomed into the area of Southern Ontario (CARE marked with the cyan 'X', TAO marked with the cyan '+'). Note that the scales have changed from Figure 5.12 and differ between panels.

5.5 Conclusions

The unprecedented intense wildfire season of 2023 in Canada burned approximately 4% of Canada's forested area, resulting in widespread evacuations and air quality warnings (Jain et al., 2024). Above-average heat anomalies and prolonged dry conditions contributed to what is the largest burn season in Canadian history. Understanding how long-range transport of wildfire plumes affects atmospheric composition and air quality is crucial, particularly in a changing climate. Despite the distance from the fires, Southern Ontario experienced several smoke plume events, some of which led to degraded air quality (see Table B.2 for comparisons of CO, O_3 and $PM_{2.5}$ with 5-year means). The trace gases CO, C_2H_6, CH_3OH, HCN, and HCOOH were found to be enhanced in the troposphere in relation to long-range transport from fires in Western Canada

and Quebec. Profile analysis using the relative enhancement of CO measured by the TAO FTIR and the NRB from a MiniMPL shows that the smoke layer in Toronto was at an altitude of approximately 5 km for early season events, and reached altitudes below 1 km at the peak of severity. Back-trajectories indicate that enhancements came from both Western Canada and Quebec, with similar patterns of long-range transport for the areas of Toronto and Egbert. Three events were examined in detail, where Event 1 (May 16-23) primarily came from fires in the Prairie region, with smoke residing at about 5 km and having little impact on air quality. Event 2 (June 3-9) shows air coming from Quebec in both the 1 km and 5 km layers, resulting in moderate air quality degradation. Event 3 (June 17-30) shows 1 km air coming from Quebec and 5 km air traveling from the west, resulting in the most significant poor air quality event for the Toronto region, during the summer of 2023.

The comparisons presented in this chapter provide information that can be used to improve the GM-FW model, which ultimately supports operational air quality monitoring in Canada. When compared to the tropospheric column measurements of CO, NH_3 and O_3, GM-FW has an overall negative bias, indicating that anthropogenic emissions may be underestimated. During the smoke events examined, GM-FW shows instances of both overestimating and underestimating the magnitude of the tropospheric column. This study provides a novel vertical profile comparison between GM-FW and CO, NH_3 and O_3 with ground-based FTIR, which showed that GM-FW simulated the peak altitudes well, confirmed on large spatial scales with MOPITT data, although small differences in high-resolution downwind plume locations can impact site-specific results. NH_3 was highly overestimated during fire events, indicating that the NH_3 lifetime is likely too high, and chemical loss/conversion needs to be improved. The model was unable to capture the O_3 profile variability. When compared to OMECP surface values, GM-FW has a high bias for CO and a low bias for O_3, with a high bias for $PM_{2.5}$ in the urban area of Toronto and a low bias in the more rural area of Barrie. The biases for both surface and tropospheric comparisons were greater than the respective measurement uncertainties. Compared with MOPITT total column satellite measurements, GM-FW effectively captures the distribution of CO during smoke events, the small differences shown in the location of the plumes help explain the FTIR-model comparison results. Overall, the model-measurement comparisons show that the GEM-MACH FireWork model is able to represent tropospheric, ground-level, and wide-spread enhancements from wildfire emissions, although the magnitude of these enhancements has room for improvement.

Uncertainties in several parameters, such as emission estimates, plume chemistry, and plume dynamics, are still present and impact modelling capabilities. This evaluation of the operational air quality model used for the AQHI and air quality alerts in Canada presented in this study offers insights for modelers to identify areas of improvement, specifically addressing extreme events, long-range transport, and altitude-dependent enhancement distribution. Further assessment of the sensitivity of the model simulations to variations in emissions and atmospheric lifetimes can help resolve inconsistencies between source and downwind atmospheric composition. Future research could expand on this study by incorporating more years of data and conducting a model sensitivity analysis to assess specific shortcomings in the GM-FW model.

Chapter 6

6 Assessing the Impact of Wildfire Emissions on the Seasonal Cycle of CO and Emergency Room Visits in Alberta and Ontario, Canada

This study uses a decade and a half (2004-2019) of satellite and ground-based carbon monoxide measurements to evaluate a change in its seasonal cycle due to wildfire emissions. To determine whether the observed increase in CO has implications for public health, emergency room admissions for nine cardiovascular and respiratory diseases were examined over the same time period. Monthly emergency room admissions from Alberta and Ontario for the diseases were assessed with a difference in difference analysis, using MOPITT XCO as the exposure metric. The findings are suggestive of a link between enhanced wildfire-related CO concentrations after 2012 and worsening health outcomes, with statistically significant results for six of the eighteen disease-province pairings. This work has been submitted to *GeoHealth (Flood et al., 2025b)* and is under review.

6.1 Introduction

Long-term monitoring of both environmental and health impacts of wildfires is increasingly important as both the frequency and severity are anticipated to rise in Canada (Hanes et al., 2018). This study is motivated by the work of Buchholz et al. (2022), who found a change in the CO seasonal cycle in the Pacific Northwest using MOPITT data. This trend was also reported in Central USA and Northeast North America. The change was observed when comparing the monthly average CO column from MOPITT from 2002-2011 with that from 2012-2018, revealing a new emerging peak in August that was attributed to an increase in wildfires in the area. A similar pattern was with aerosol optical depth (AOD) from MODIS using the same time period. The split of the time periods was selected by a consistent change between the time period in the regions examined for both CO and AOD. The work here builds on these findings to assess CO trends over the provinces of Alberta and Ontario, Canada and for the highly populated area of Toronto, Ontario, which occasionally experiences long-range transport of air pollution from wildfires.

Over the decade from 2009 to 2019, the average burn area by province and territory is led by the Northwest Territories, then Saskatchewan, followed by Alberta, with Ontario ranking 8th out of 13 in this list (CWFIS, 2024). Although Ontario, specifically the densely populated area of Southern Ontario, is less proximate to wildfire-prone regions, it can still experience degraded air quality from long-range transport of smoke plumes (Flood et al., 2025a). Alberta has an active wildfire season locally, and also experiences long-range transport from the surrounding provinces and territories.

In Canada from 2013-2015 and 2017-2018, acute health impacts from wildfire smoke exposure have been estimated to cost up to CDN $1.8 billion, while the cost of chronic health impacts may be as much as CDN $19 billion (Matz et al., 2020). In the same study, the continued exposure to wildfire $PM_{2.5}$ was estimated to reduce life expectancy in Canada (depending on the location) by 0.05 to 0.42 years. During the summer of 2015, the city of Calgary, Alberta experienced an episode of poor air quality resulting from the long-range transport of wildfire smoke from wildfires in the Pacific Northwest. Outpatient data showed an elevated risk of respiratory disease morbidity of 33% during and after the event, related to increased $PM_{2.5}$ (Mahsin et al., 2022). Children (ages 0-9) were found to have an increased risk particularly for asthma, acute bronchitis and acute respiratory infection, while seniors were at a higher risk of congestive heart failure and ischemic heart disease (Mahsin et al., 2022). A study focused on an area of southeast British Columbia during the wildfire season of 2003, found an increase in respiratory-related physician and hospital visits linked to wildfire smoke exposure using ground-based PM_{10} monitoring, a dispersion model, and satellite imagery (Henderson et al., 2011). The authors note the agreement between the results using PM_{10} and using satellite monitoring, suggest that it can be effective exposure metric alternative to surface monitoring.

Studies commonly use $PM_{2.5}$ as a gauge for smoke exposure related to health effects, although Wettstein et al. (2018) identified the need for studies to incorporate other fire-related emissions as exposure metrics. CO has been well established as a useful tracer for the transport of wildfire plumes using both space-based measurements (e.g., Edwards et al., 2004; Pope et al., 2021) and ground-based measurements (e.g., Viatte et al., 2013; Franklin et al., 2014; Lutsch et al., 2020; Flood et al., 2025a). Henderson et al. (2011) highlight the value of assessing acute and chronic exposure from wildfires using remote-sensing data, particularly for rural and isolated areas where surface air quality monitoring may not exist. While correlations have been sought for long-term

exposure in proximate populations, it is important to also consider the impacts of the long-range transport of pollutants from wildfires, which can be tracked using remote-sensing data and has the advantage of providing both long-term data sets and widespread coverage.

Based on the wildfire health impact studies in Canada discussed above, there is a deficiency in research that incorporates long-term monitoring and long-range effects, along with assessments that do not rely on the use of particulate matter (PM_{10} or $PM_{2.5}$). This study aims to address this gap and contribute to a framework that may support similar studies in the future. To evaluate if the reported increase of wildfire-related CO emissions has an impact on the health care system in Canada, emergency room admissions for cardiovascular and respiratory diseases are assessed using the same portioning (pre/post 2012) discussed in Buchholz et al. (2022), as records are available. The objective is to assess whether emergency care utilization for respiratory and cardiovascular diseases in Ontario and Alberta, Canada is correlated with atmospheric CO from wildfires, and in turn, whether CO can be a useful exposure metric for health effects. The structure of this chapter is as follows: Section 6.2 describes the datasets and the methods used to analyze them, Section 6.3 presents the results and discussion, and Section 6.4 provides conclusions.

6.2 Data Sets and Methods

6.2.1 CO Measurements

6.2.1.1 MOPITT

The MOPITT instrument was introduced in Section 5.2.3; the data used here are the TIR/NIR v9 L3 product (Deeter et al., 2022). The joint TIR-NIR product provides larger DOFS, better vertical resolution, and higher sensitivity to CO in the lower troposphere, compared to TIR or NIR alone (Deeter et al., 2013). Retrieval biases for the V9 TIR-NIR product range from 1.90% at the surface with a peak bias of -5.82% around 500 hPa (Deeter et al., 2022). MOPITT validation using NDACC data found that at Toronto the TIR-NIR DOFS were 1.63 (over land), with a column AVK that peaks in the mid-troposphere and can be considered similar for other mid-latitude areas (i.e., Ontario as a whole, and Alberta) (Buchholz et al., 2017).

MOPITT data are extracted for the areas which encompass the provinces of Alberta and Ontario. To obtain a column-averaged dry-air mole fraction (XCO in ppbv), the daytime retrieved total column CO is divided by the daytime dry-air column, provided in the MOPITT data files. To

account for the change in background atmospheric CO over the study period, CO is detrended using the North American average change of -0.57±0.3% per year (derived from 2002-2018) (Buchholz et al., 2021), prior to seasonal cycle analysis. To coincide with the available health data, MOPITT data from 2004 to 2019 are used in this study.

6.2.1.2 FTIR Spectroscopy

The TAO CO total column 2002-2020 average DOFS is 2.16 ± 0.29 and percent uncertainty is 2.97% (Yamanouchi et al., 2023). The column measurements are dominated by the troposphere, in both column density and retrieval sensitivity. This allows for CO enhancements measured at TAO to provide an indicator for the presence of wildfire smoke (e.g., Lutsch et al., 2016; Yamanouchi et al., 2020; Flood et al., 2025a). For consistency with the MOPITT data, the TAO FTIR columns from 2004 to 2019 are made into monthly averages and detrended with the same North American average trend of -0.57±0.3% per year (Buchholz et al., 2021).

6.2.2 Health Data

The hospital emergency room data used in this work were provided by the Canadian Institute for Health Information (CIHI) National Ambulatory Care Reporting System (CIHI, 2024). The data were aggregated such that one count for each month in each health district was provided for each of the ICD-10 (International Classification of Diseases 10th revision) code groupings, as listed in Table 6.1. The ICD-10 codes are of relevant cardiovascular and respiratory diseases, selected following Hahn et al. (2021) and Magzamen et al. (2021). The data contain no identifying information such as age or gender, and cell values less than 5 were suppressed by CIHI (a placeholder value of 4 was set, with only two instances of this). The hospital records were obtained for Alberta and Ontario based on CIHI data holding availability, records were not accessible for other provinces or territories prior to 2012, and as such were not reviewed in this work.

There are five zones in the Alberta Health Service (AHS) network (North, Edmonton, Central, Calgary and South), and emergency room admission data were provided from 2010 to 2020 (as shown in Figure 6.1). There are 14 zones in the Ontario Public Health (PHO) network (Erie St. Clair, South West, Waterloo Wellington, Hamilton-Niagara Haldiman Brent, Central West, Mississauga-Halton, Toronto-Central, Central, Central-East, South-East, Champlain, North-Simcoe-Muskoka, North-East, North-West), and the data were provided for 2004 to 2020 (as

shown in Figure 6.2). The emergency room counts were normalized by population (admissions per 100,000), to account for population changes over the time period studied (AHS & PHO, last access: 30 August 2024). Data from 2020 were obtained but not included in the analysis due to anomalies in emergency care usage as a result of the COVID-19 pandemic. The emergency room admissions are used as a point of reference for the health care utilization over time. Figure 6.3 shows the time series data for all nine diseases in each province to provide context for the admission rates (per 100,000 people) in each province.

Table 6.1: Name and ICD-10 codes for the diseases examined.

Disease	**ICD-10 Codes**
Hypertension	I10-I13, I15
Ischemic Heart Disease	I20-I25
Arrhythmia	I46-I49
Heart Failure	I50
Cerebrovascular Disease	I61-I69, G45
Pneumonia	J12-J18
Acute Lower Respiratory Infections	J20-J22
Chronic Obstructive Pulmonary Disease (COPD)	J40-J44, J47
Asthma	J45

Figure 6.1: Map of Alberta provincial health districts from which emergency room admission data were obtained (STATS CAN, 2018a).

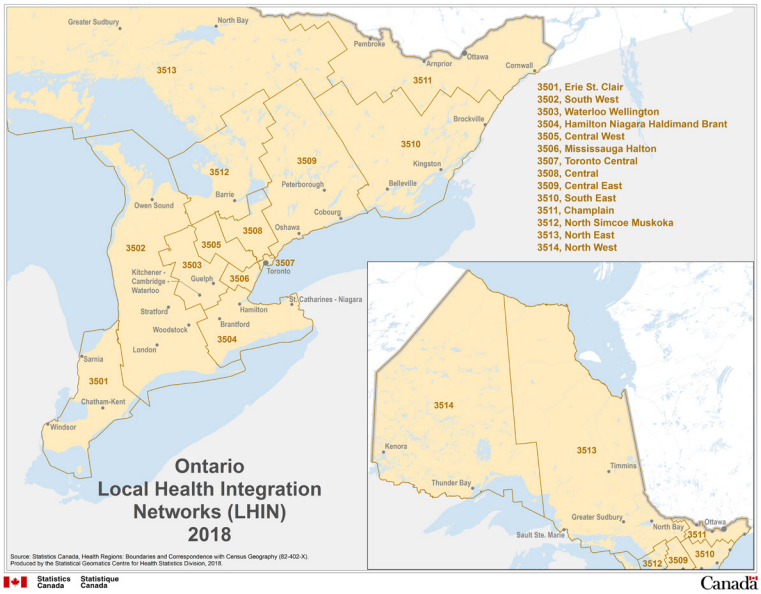

Figure 6.2: Map of Ontario provincial health districts from which emergency room admission data were obtained (STATS CAN, 2018b).

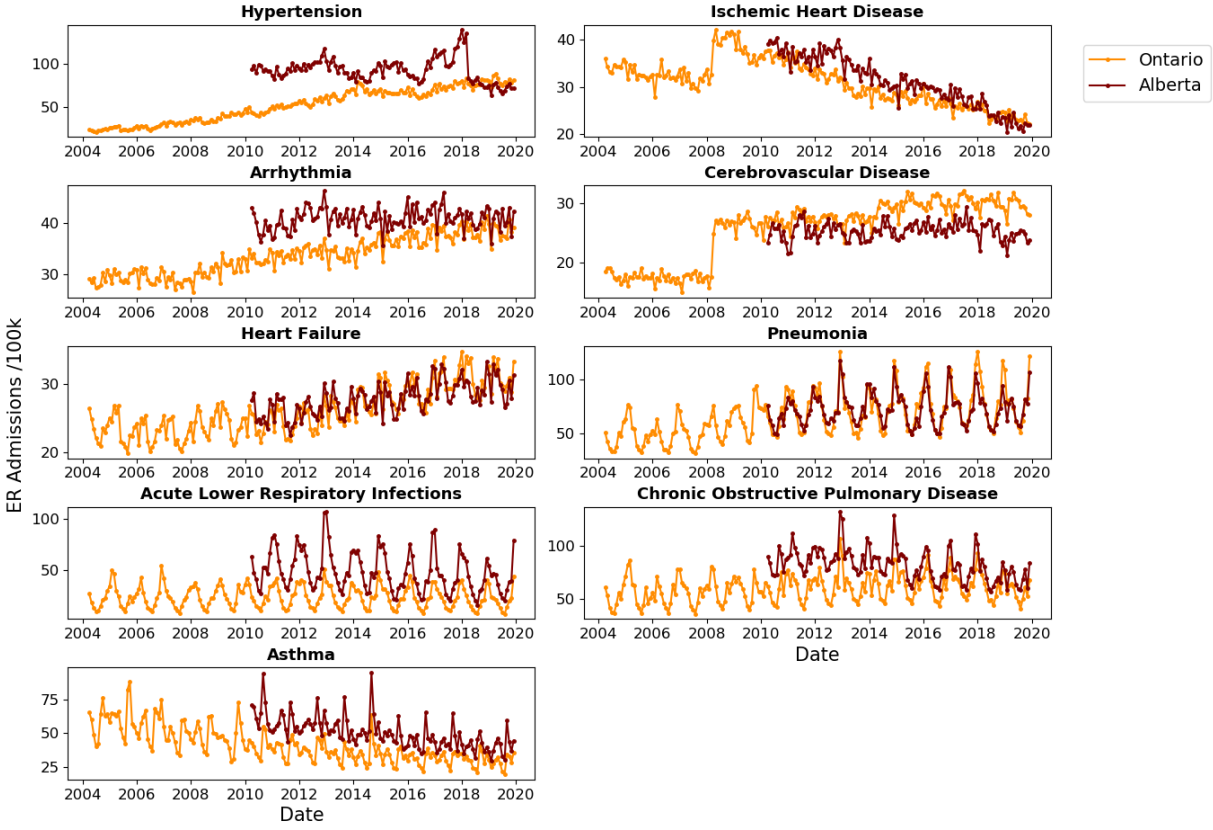

Figure 6.3: Time series of monthly hospital emergency room (ER) admissions per 100,000 for each province (Ontario in orange, Alberta in maroon), for the nine diseases studied.

6.2.3 Difference in Difference Analysis

A difference in difference (DiD) analysis was applied to the hospital admissions data and MOPITT measurements. This approach compares a "pre-treatment" (2004-2011 for Ontario, 2010-2011 for Alberta) and "post-treatment" (2012-2019) period, where the change in trends between the two periods is the "difference-in-differences." In the absence of a change, the two regressions would remain the same. Unlike other DiD applications, the exposure metric and outcome metrics used in this work are not binary; although there are "before" and "after" periods, there is no available control group that did not experience the change in CO. The equation and parameters, presented in Table 6.2, are adapted from the DiD analysis in Card and Krueger (1993) and Zahran et al. (2014). The model assesses the monthly hospital admissions per 100,000 residents in each health district (N_{mR}), where exposure is the XCO (ppbv) in a given month, with an interaction term (i_{co}) of before (0) and after (1) January 1, 2012 (corresponding to the timeframes discussed in Buchholz et al., 2022), and covariant controls for month (m) and health region (R). The coefficients are determined by using an ordinary least squares approach to minimize the sum of squared residuals with the change in N_{mR}, when only the respective variable is changed. The DiD was performed for each province individually. In short, we consider the pre-2012 population by health region and province as the appropriate counterfactual for the post-2012 (inclusive) population.

The resultant is measured as hospitalizations (per 100,000), and the interaction term is dictated by before vs. after 2012, to identify the difference in the hospitalization rate-XCO relationship between the two time periods. The month and region are included to control for potential differences in XCO and hospitalizations that may occur regionally or temporally. Within the DiD, the β_4 and β_5 coefficients represent the change in hospital admissions compared to the month and region, respectively, when holding everything else constant. Since month and region do not interact with the other covariates, β_4 and β_5 can be interpreted independently of other variables in the model and are not relevant to the discussion of the relationship between XCO, hospital admissions, and period. Coefficient β_1 is related to the variable XCO and represents the change in hospital admissions per 1 ppbv increase in XCO when the period is pre-2012, and β_3 is related to the interaction term (i_{co}) and represents the change in the effect of 1 ppbv increase in XCO on hospitalizations before 2012 vs. after 2012 (inclusive). Therefore, the combined sum of $\beta_1 + \beta_3$ is the change in hospitalizations, per 1 ppbv increase in XCO, in the post 2012 period.

The β_1 and β_3 terms resulting from the DiD analysis are evaluated with two statistical parameters, the 95% confidence interval (CI) and the p-value. The 0.025 to 0.975 range of the confidence interval indicates the range over which 95% of the data is normally distributed, where a significant result will not contain a null value. The p-value signifies the probability of the variable having no influence on the dependent variable (N_{mR}), and that the observed correlation happens by chance, where a lower value (<0.05) is indicative of a better relationship. A further breakdown of the equation is provided in Appendix C.

Table 6.2: Summary of DiD equation and variables.

$N_{mR} = \beta_0 + \beta_1 X_{CO} + \beta_2 t + \beta_3 i_{co} + \beta_4 m + \beta_5 R$			
Variable	**Definition**	**Coefficient**	**Relevance**
N_{mR}	Total admissions in a month for each health district (per 100,000 population)	-	-
-	-	β_0	Intercept
X_{CO}	"Exposure", detrended monthly mean from MOPITT in ppbv	β_1	The change in hospitalizations per 1 ppbv increase in XCO when the period is pre-2012
t	Period: 0 for pre-2012, 1 for post-2012	β_2	Change in hospitalizations post-2012 vs. pre-2012 when XCO is held constant
i_{co}	CO interaction term $(= t * X_{CO})$	β_3	The change in the effect of a 1 ppbv increase in XCO on hospitalizations post-2012 vs. pre-2012
m	Month indicator (only July, August, September)	β_4	Change in hospitalizations per month, when the rest of the variables are held constant
R	Health region indicator	β_5	Change in hospitalizations per health region, when the rest of the variables are held constant

6.3 Results and Discussion

Following the findings in Buchholz et al. (2022), the analysis is performed for two periods, defined as "pre-2012" (start to December 31, 2011) and "post-2012" (January 1, 2012 to end). All the datasets end with 2019 for consistency with the health data, and are analyzed from 2004 to match the available Ontario health data, with the exception of the Alberta hospitalization data, which are only available from 2010 onwards.

6.3.1 CO Seasonal Cycle

To assess if a change in the CO seasonal cycle is detected in the study regions, MOPITT and TAO FTIR CO data are examined pre-2012 and post-2012. Figure 6.4 shows the mean XCO measured

by MOPITT in August over Canada, for the two corresponding time periods, 2004-2011 and 2012-2019. The post-2012 period in Figure 6.4b shows large areas across the country with a higher monthly mean XCO than the pre-2012 period displayed in Figure 6.4a. Figure 6.4c shows the difference between the two periods (2012-2019 minus 2004-2011), where yellow and orange represents a decrease in XCO, white is no change (0 difference), and red to black is an increase in XCO from the earlier period to the later period.

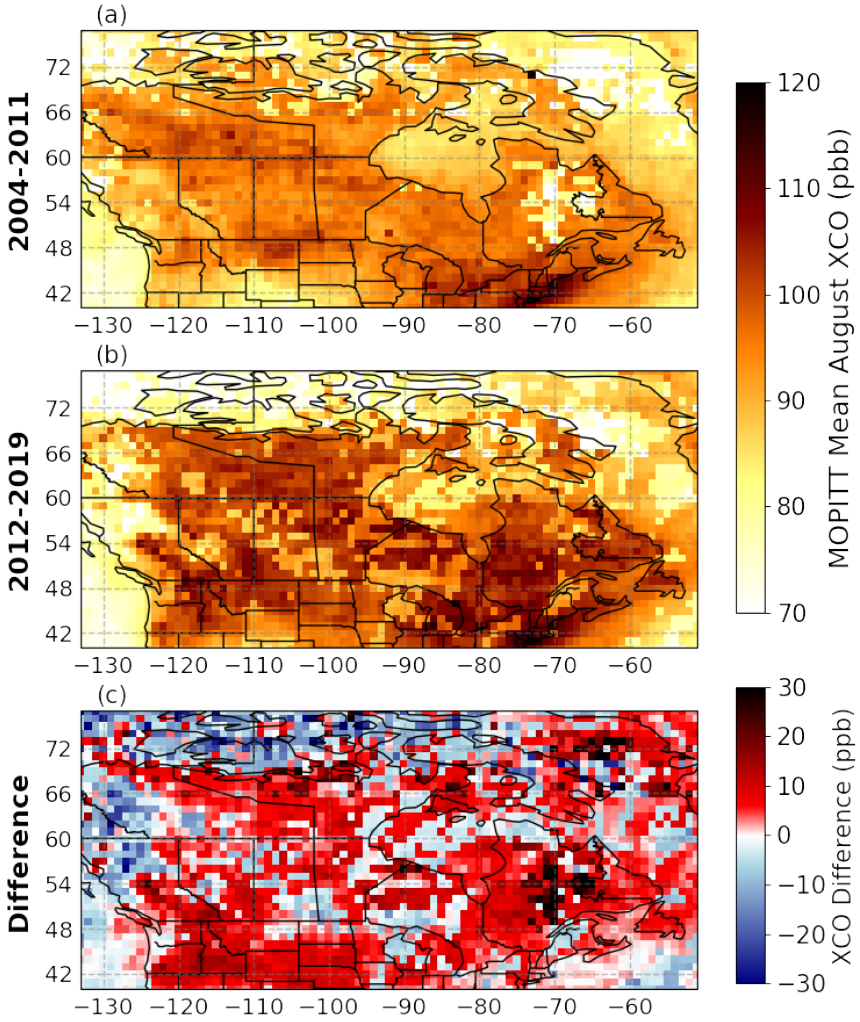

Figure 6.4: MOPITT monthly mean August XCO for (a) 2004-2011 and (b) 2012-2019, and (c) the difference (2012-2019 mean minus 2004-2011 mean).

To examine the differences for Alberta and Ontario, the detrended monthly mean XCO is plotted in Figure 6.5 by month, for 2004-2011 and 2012-2019, with ±1 standard deviation of the mean shaded. For both provinces, a larger value is seen in August (and a somewhat larger value in July and September) for the post-2012 period, compared to pre-2012, although with some overlap when

considering the standard deviation of the mean. Similarly, the detrended monthly mean total column CO from the TAO FTIR is plotted in Figure 6.6 to determine whether a change is detected from a ground-based instrument in downtown Toronto. Here, the mean CO total column in August (and less-so in July and September) is seen to be larger for 2012-2019, however the year-to-year variability represented by the standard deviation shows significantly more overlap with the mean total column for 2004-2011.

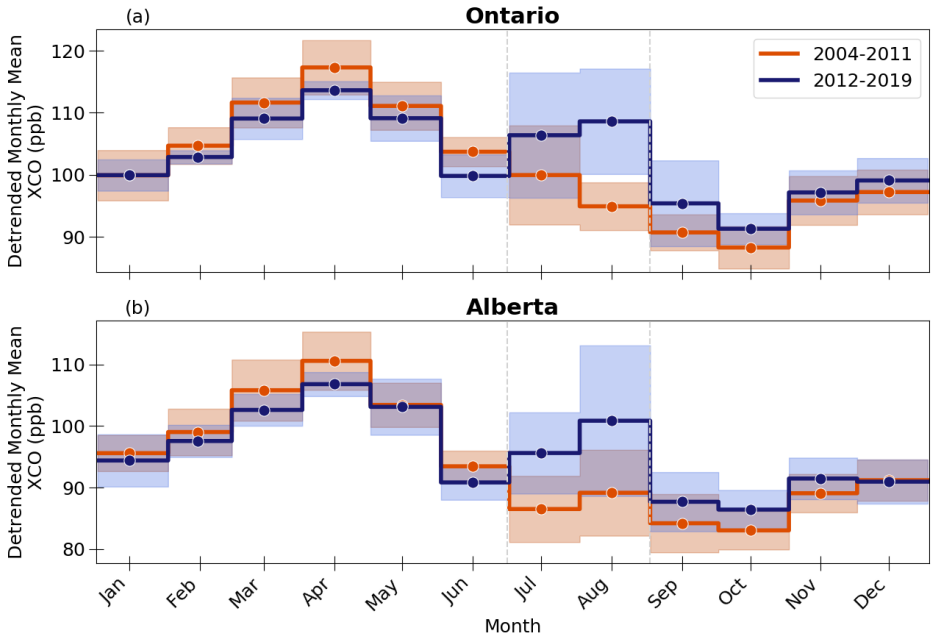

Figure 6.5: Detrended monthly mean XCO from MOPITT for (a) Ontario and (b) Alberta, for 2004-2011 (orange) and 2012-2019 (blue), with ±1σ indicated by the shading.

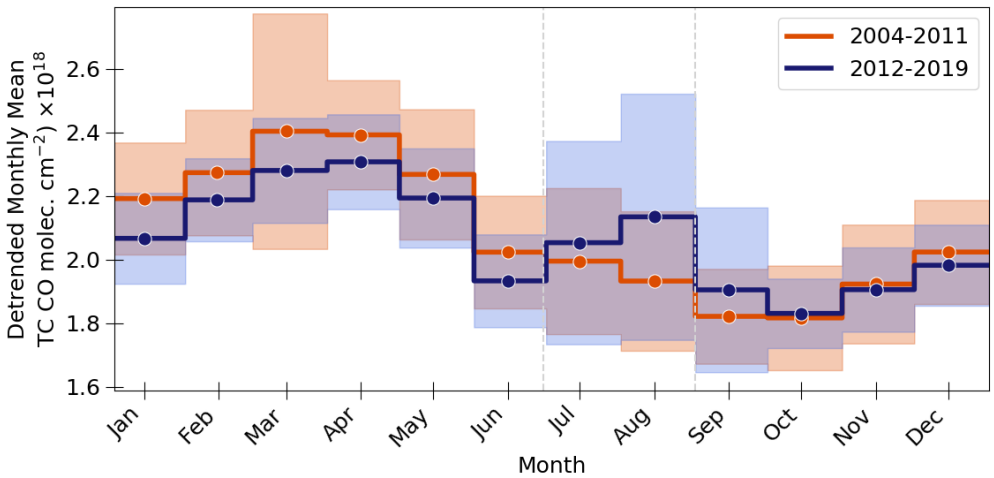

Figure 6.6: Detrended monthly mean total column (TC) CO from the TAO FTIR for 2004-2011 (orange) and 2012-2019 (blue), with ±1σ indicated by the shading.

6.3.2 DiD Results

Table 6.3 summarizes the DiD regression statistics for each disease in each province, using the equation and definitions provided in Table 6.2, and Figure 6.7 shows the results in the form of a bar chart for Alberta (cool colours) and Ontario (warm colours), the top panel is β_1 and β_3 , where the error bars represent the confidence interval, and the lower panel is $\beta_1 + \beta_3$. The XCO β_1 term represents the change in monthly hospitalizations per 100,000 associated with a 1 ppbv increase in XCO, in the pre-2012 period. The i_{co} β_3 term represents the change in the effect of a 1 ppbv increase in XCO on monthly hospitalizations per 100,000 between pre-2012 and post-2012. The significance column is determined by the confidence interval and p-value: "no" means that both the confidence interval and the p-value suggest that the coefficient is insignificant; "possibly" indicates that the coefficient may be significant (confidence interval contains the null but only minimally, and the p-value<0.10); and "yes" signifies that the coefficient is significant based on both the confidence interval and the p-value. If the β term is shaded red, the relationship is negative; if it is green, the relationship is positive. When the i_{co} β_3 is marked with an asterisk (*), this indicates that β_3 is positive and larger in magnitude than the absolute value of β_1, which means that the relationship between XCO and hospitalizations has gone from negative in the pre-2012 period to positive in the post-2012 period, and that the interaction between XCO and time period is significant.

Twelve out of the eighteen disease-province pairs have a negative XCO β_1 term and a positive i_{co} β_3 term, meaning that the negative effect of 1 ppbv increase in XCO on hospitalizations is attenuated (a positive shift) in the post-2012 period, compared to the pre-2012 period. Of those, half (six) are considered significant (hypertension-ON, ischemic heart disease-ON, arrhythmia-AB, arrhythmia-ON, cerebrovascular disease-ON and asthma-ON). In both Ontario and Alberta, XCO has a negative effect with arrhythmia hospitalizations in the pre-2012 period that is greatly attenuated in the post-2012 period, by a significantly positive interaction term. The interpretation of the i_{co} β_3 and XCO i_1 terms is that the effect on monthly arrhythmia hospitalizations from a 1 ppbv increase in XCO after 2012 is -0.002 ($\beta_1 + \beta_3$ = -0.127 + 0.125) admissions per 100,000 in ON and -0.036 ($\beta_1 + \beta_3$ = -0.521 + 0.485) admissions per 100,000 in AB. For hypertension in Ontario, the β_3 coefficient is significant and greater than the absolute value of β_1, which represents an inversion of the relationship between hospitalizations and XCO pre-2012 (β_1 = -1.716) to post-

2012 ($\beta_3 = 1.876$), when a 1 ppbv increase in XCO is associated with 0.16 ($\beta_1 + \beta_3 = -1.716 + 1.876$) additional monthly hospitalizations per 100,000 people.

*Table 6.3: Summary of DiD Regression Statistics: the β term corresponds to β_1 for XCO and β_3 for i_{co}, shaded red if it is negative and green if it is positive, and marked with * if β_3 is positive and $\beta_3 > |\beta_1|$, and significant; the 95% confidence interval and p-value are used to determine significance, indicated with yes (bold font), no, or possibly.*

Disease	Province	Variable	β_1 for XCO, β_3 for i_{CO}	95% Confidence Interval [0.025/0.975]	P-Value	Significant
Hypertension	ON	XCO	**-1.716**	-2.333 / -1.097	<0.001	**yes**
		i_{co}	**1.876***	1.181 / 2.57	<0.001	**yes**
	AB	XCO	-0.856	-3.50 / 1.79	0.523	no
		i_{co}	0.961	-1.66 / 3.58	0.469	no
Ischemic Heart Disease	ON	XCO	**-0.303**	-0.458 / -0.148	<0.001	**yes**
		i_{co}	**0.387***	0.212 / 0.561	<0.001	**yes**
	AB	XCO	0.417	-0.055 / 0.888	0.083	possibly
		i_{co}	-0.439	-0.906 / 0.028	0.065	possibly
Arrhythmia	ON	XCO	**-0.127**	-0.21 / -0.045	0.003	**yes**
		i_{co}	**0.125**	0.032 / 0.218	0.009	**yes**
	AB	XCO	**-0.521**	-0.889 / -0.153	0.006	**yes**
		i_{co}	**0.485**	0.121 / 0.85	0.009	**yes**
Heart Failure	ON	XCO	0.065	-0.017 / 0.148	0.121	no
		i_{co}	**-0.094**	-0.186 / -0.001	0.048	**yes**
	AB	XCO	-0.198	-0.49 / 0.094	0.182	no
		i_{co}	0.220	-0.069 / 0.509	0.134	no
Cerebrovascular Disease	ON	XCO	**-0.228**	-0.33 / -0.126	<0.001	**yes**
		i_{co}	**0.189**	0.075 / 0.304	0.001	**yes**
	AB	XCO	-0.147	-0.394 / 0.100	0.241	no
		i_{co}	0.139	-0.105 / 0.385	0.260	no
Pneumonia	ON	XCO	0.119	-0.127 / 0.365	0.341	no
		i_{co}	-0.218	-0.495 / 0.059	0.122	no
	AB	XCO	-0.477	-1.089 / 0.136	0.126	no
		i_{co}	0.482	-0.124 / 1.088	0.118	no
Acute Lower Respiratory Infections	ON	XCO	-0.008	-0.1 / 0.083	0.860	no
		i_{co}	-0.001	-0.104 / 0.102	0.982	no
	AB	XCO	-0.193	-0.595 / 0.209	0.344	no
		i_{co}	0.141	-0.257 / 0.538	0.486	no
Chronic Obstructive Pulmonary Disease (COPD)	ON	XCO	-0.004	-0.201 / 0.193	0.969	no
		i_{co}	-0.017	-0.238 / 0.204	0.880	no
	AB	XCO	-0.137	-0.779 / 0.505	0.673	no
		i_{co}	0.164	-0.472 / 0.799	0.611	no
Asthma	ON	XCO	-0.138	-0.380 / 0.084	0.209	no
		i_{co}	**0.308***	0.048 / 0.568	0.021	**yes**
	AB	XCO	0.369	-0.961 / 1.698	0.584	no
		i_{co}	-0.271	-1.587 / 1.045	0.685	no

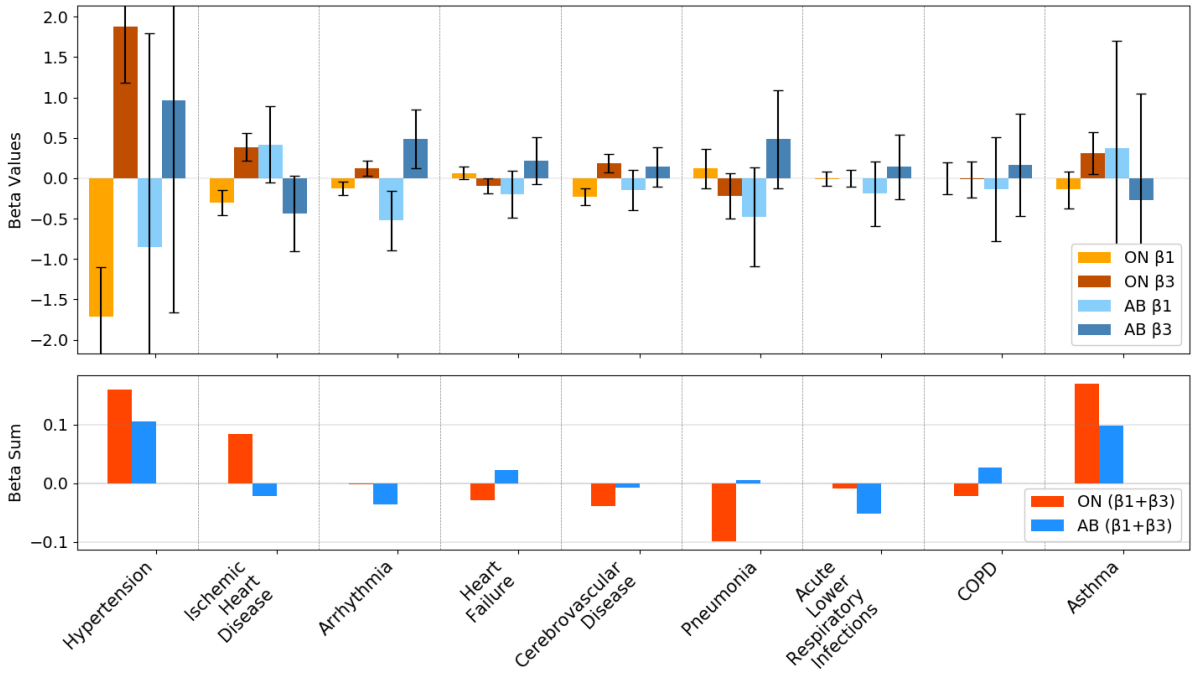

Figure 6.7: Graphical summary of DiD results from Table 6.3.

To put those numbers into context, using the approximate population of Ontario of 12.9 million in 2009 and 14.6 million in 2019, a 1 ppbv increase in XCO would correspond to 221 *fewer* hospitalizations in 2009 and 23 *more* hospitalizations in 2019. Cerebrovascular disease and hypertension in both provinces show an attenuated impact of XCO on hospitalizations, represented by a negative relationship with XCO (β_1), and a smaller in magnitude, but positive i_{co} coefficient (β_3). In this case, both confidence intervals for Alberta contain the null value, indicating that the association and interaction are not statistically significant. In contrast, the coefficients for Ontario are significant, with low p-values and confidence intervals that do not contain null values. This may suggest that with a longer dataset for the pre-2012 period, the Alberta results could be significant. In cases where the i_{co} β_3 is negative while the XCO β_1 term is positive, other underlying factors might be at play. However, for ischemic heart disease, heart failure, pneumonia, acute lower respiratory infections, COPD and asthma, the direction of the XCO β_1 term and the i_{co} β_3 term are different for Ontario and Alberta, indicating that there is not consistent evidence to support a conclusion in the scenario. To evaluate the sensitivity of the findings, the DiD was also tested with the raw XCO values (not detrended); although the β values differed, the overall directionality and significance remained generally the same.

6.3.3 Discussion

The vast majority of epidemiological studies that investigate the impacts of wildfire smoke on health use base exposures to $PM_{2.5}$, through either ground-based measurements of pollutants (Hahn et al. 2021), blended or fusion models that include ground-based measurements coupled with remote sensing data, such as aerosol optical depth or indication of smoke in the atmospheric column (Gan et al. 2017; Gan et al. 2020; Magzamen et al. 2021), chemical transport models (Maji et al., 2024), or solely remote sensing data that approximates $PM_{2.5}$ in the atmospheric column (Wettstein et al., 2018). However, CO emissions are observed to increase during smoke periods (e.g., Buchholz et al., 2022) and ambient CO levels are associated with acute health outcomes in multiple settings. In Canada, ambient CO levels in Toronto were found to contribute 4.7% (95% CI: 3.4%–6.1%) of daily, non-accidental deaths, while total suspended particles (TSP), which includes PM_{10} and $PM_{2.5}$, contributed an additional 1.0% (95% CI: 0.2–1.9%), based on changes in CO and TSP-equivalent to their average concentrations (Burnett et al., 1998). In a study of the Medicare population in the United States, Bell et al. (2009) found that ambient CO levels below the US Environmental Protection Agency (EPA) National Ambient Air Quality Standards (NAAQS) were positively and significantly associated with cardiovascular disease (CVD) hospitalizations, including ischemic heart disease, arrhythmia, heart failure, cerebrovascular diseases, and total CVD hospitalizations; these results remained robust, though attenuated with the addition of NO_2 to the models (Bell et al., 2009). A study of daily emergency room visits from 2013-2019 in Lanzhou, China shows that an increase in atmospheric CO is associated with a rise in visits for CVD (I00-I99), ischemic heart disease (I20-I25), heart rhythm disturbances (I44-I49), heart failure (I50), and cerebrovascular diseases (I60-I69) (You et al., 2023). Although these studies were linked with ambient CO, no study directly linked to CO emanating from wildfire activity.

A systematic review of 36 publications on the long-term health impacts of wildfire smoke exposure found that such studies are limited and largely focus on mental health (Gao et al., 2023). The majority of the studies assessed the cohorts for one to two years after exposure; nine of the 36 studies were based in Canada, where all but one was related to the 2016 Fort McMurray fires. The other Canadian report was a 20-year population-based cohort study that followed more than two million adults to examine the association between wildfire exposure and specific cancers related to wildfire emissions (Korsiak et al., 2022; Gao et al., 2023). Comparing health outcomes of

populations based on wildfire exposure area, defined by proximity to burned area, suggests that an increased risk of lung cancer and brain tumors is associated with long-term exposure to wildfires. Gao et al. (2024) applied a DiD analysis to cardiovascular mortality in relation to wildfire-related $PM_{2.5}$ in Brazil, between 2010 and 2018, where an observed increase in wildfires occurred in the recent years. When controlling for seasonal temperature and socio-economic status, they reported that wildfire-related $PM_{2.5}$ was statistically significant in causing mortality with a 1-year lag for all-cause cardiovascular disease (I00–I99, G45, G46), ischemic heart disease (I20–I25) and stroke (I60–I64, G45, I690–I694), but not for heart failure (I50), hypertension (I10–I13) or peripheral vascular disease (I70–I89). Use of a gas-phase marker of smoke like CO may obviate challenges in $PM_{2.5}$ as a relevant smoke exposure as long-term satellite measurements are available in remote areas, and source apportionment (e.g., background vs. smoke $PM_{2.5}$) is not required.

Unlike most wildfire smoke studies, this study found that most respiratory hospitalizations were not significantly associated with column CO in either the pre-2012 or post-2012 periods. However, pneumonia, COPD, and acute lower respiratory infections were all higher in Alberta in the post-2012 period. Given the relatively smaller time series available for Alberta, as well as the relatively lower incidence of respiratory disease in the warm-season months evaluated in this study, we interpret these findings to be suggestive of a relationship between increased column CO and these respiratory outcomes. Acute asthma events, the health outcome most consistently associated with wildfire smoke exposure, had a significant increase in the post-2012 period in Ontario, suggesting that there was a meaningful change in slope of the relation between CO and asthma. Hahn et al. (2021) report that the cardiovascular outcomes showed less significance compared to the respiratory diseases examined with the same population and wildfire events. When examining the CVD emergency room admissions within the population as a whole, Hahn et al. (2021) found that the risk went down on the day of exposure and showed an increase with a 2-3 day lag, while the odds of respiratory peaked on the first day and decreased thereafter, with the strongest effects observed for asthma. Increased morbidity from respiratory diseases due to wildfire smoke exposure is a common finding in studies, whereas correlations between cardiovascular diseases and health care utilization and wildfire smoke are less frequently reported (Henderson et al., 2011). This may be somewhat attributed to differences in exposure assessment and health data usage (Hahn et al., 2021), which would be particularly relevant to the methods applied in this work as

exposure and health metrics are aggregated on a monthly basis, while other studies have daily inputs.

The biological plausibility of the relationship between column CO and cardiovascular diseases may contribute to our current findings that are predominated by positive and significant relationships between CO and CVD outcomes in the post-2012 period compared to the pre-2012 period. Wettstein et al. (2018) found that smoke from 2015 wildfires in California were associated with a number of cardiovascular hospitalization outcomes, including myocardial infarction, ischemic heart disease, heart failure, dysrhythmia, pulmonary embolism, stroke, and transient ischemic attack (Wettstein et al. 2018). Exposure assessment was conducted using NOAA Hazard Mapping System (HMS) smoke polygons, classified as light, medium and heavy. The HMS polygons indicate if there is smoke in the atmospheric column, but does not indicate if the smoke is at the ground level. In a study spanning six wildfire seasons in Colorado, Magzamen et al. (2021) blended HMS polygon data with ground-based US EPA monitoring data for $PM_{2.5}$ to indicate if smoke in the atmospheric column was present at ground level (Magzamen et al. 2021). This study indicated that all CVD hospitalizations (as well as hospitalizations for cerebrovascular disease, heart failure, and ischemic heart disease) in single-lag model were significantly associated with a 10 $\mu g/m^3$ increase in smoke $PM_{2.5}$; in distributed lag models, smoke $PM_{2.5}$ was significantly associated with ischemic heart disease, similar to findings in the current study.

Further, the Colorado analysis demonstrated that 10 $\mu g/m^3$ increase in wildfire smoke was significantly associated with cardiac arrest mortality (Magzamen et al., 2021). A study in California indicated that exposure to wildfire smoke was significantly associated with out-of-hospital cardiovascular deaths over three seasons (Jones et al., 2020). An evaluation of the 2015 wildfire season in Calgary, Alberta, found that smoke exposure was positively and significantly associated with outpatient physician visits for congestive heart failure and ischemic heart disease (Mahsin et al. 2022), similar to findings in our study.

The scope of this analysis is limited by data availability and the aggregation thresholds of the CIHI, in frequency and duration. Alberta is in closer proximity to seasonal forest fires than Ontario, meaning the population has greater exposure to wildfire smoke and thus a greater potential for hospitalization records to reflect the change in wildfire frequency. However, Alberta hospitalization records were only available from 2010 onwards, which only provides two years in

the “before” period and can potentially constrain the DiD signal. Other provinces were not included as they did not have data available for the appropriate duration. If the data were available on a daily basis, this would allow for an analysis more similar to those in Hahn et al. (2021) and Magzamen et al. (2021). Another consideration for the significance of trends is the sample size, the entire population of Canada is comparable to the state of California (PPIC, 2024; STATS CAN, 2024). Further, utilization of health care during fire events care may vary based on several confounding factors, such as smoke density and toxicity (can depend on proximity and severity of burning fire, temperature, ecoregion, etc.), human behavior (e.g., availability of medical treatment, ability to self-treat), and local intervention measures (e.g., evacuation orders, distribution of protective equipment) (Magzamen et al., 2021).

The DiD uses the monthly average total column XCO as measured by MOPITT; as stated in Section 5.2.1.1, the TIR/NIR measurement is most sensitive to the middle troposphere. The change in seasonal cycle is observed in both the MOPITT data and the CO measurements from the TAO FTIR (as shown in Figure 5.5), which is sensitive to the lower troposphere, and it should be noted that enhancements in the surface level CO that more directly influence air quality, will vary from the column measurements. However, enhancements in the CO tropospheric column measured at TAO have been linked to episodes of degraded air quality as a result of long-range transport of wildfire plumes (Flood et al., 2025a). The overlap observed in the standard deviation of the monthly mean CO presented in Figures 5.2 and 5.3 may indicate that a longer time series is needed to better resolve the CO increase in Alberta and Ontario, which may also reflect the varying results of Table 6.3. Nonetheless, the prominence of a positive uptick in outcomes between the pre-2012 and post-2012 periods is suggestive of a shift in the relationship between health outcomes and a more intense wildfire season, as marked by enhanced atmospheric CO columns. The wide confidence intervals can be somewhat attributed to the limitations as stated, and underscore need for further research.

6.4 Conclusions

This study investigated a change in the seasonal cycle of atmospheric CO from satellite measurements in the provinces of Alberta and Ontario, in addition to ground-based monitoring in Toronto, Ontario, partitioning measurements from before and after January 1, 2012. Monthly hospital emergency room admissions for nine cardiovascular and respiratory diseases were

obtained for the health districts in Alberta (2010 to 2019) and Ontario (2004 to 2019) and analyzed with respect to the satellite-derived monthly total column CO using a difference-in-difference approach. The objective was to assess whether the hospitalization records follow a similar pattern to that observed with the atmospheric CO and to evaluate whether CO can be used as an appropriate metric for exposure.

A comparison of MOPITT XCO measurements across Canada shows areas of higher mean August values for 2012-2019 compared to 2004-2011, even without removing the overall North American downward trend of -0.57% CO per year. When assessing the detrended monthly mean XCO for Alberta and Ontario specifically, a positive shift is seen for the period from July to September, with a maximum in August. The TAO FTIR monthly mean CO total columns show a similar increase over the same time period. The standard deviations of the pre-2012 and post-2012 monthly means overlap due to year-to-year variability. Overall, the findings are consistent with the results in Buchholz et al. (2022), which showed an increase in seasonal August CO observed by MOPITT in large areas of the United States when comparing pre-2012 and post-2012, attributed to an increase of wildfires in the Pacific Northwest.

A DiD regression was applied to monthly hospital emergency room admission counts for nine cardiovascular and respiratory diagnoses to assess if the observed increase in column CO due to wildfire emissions is reflected in health diagnostics. Despite the sometimes-wide confidence intervals, several diseases show a significant change in the DiD regression when considering the interaction term between exposure and outcome. In the instances when the model shows a positive $i_{co}\ \beta_3$ interaction term, an increasingly adverse effect is observed during the more intense wildfire years (post-2012). The positive $i_{co}\ \beta_3$ coefficients indicate how many more hospitalizations per 100,000 are associated with a 1 ppbv increase in XCO after 2012 compared to before 2012 for the same month. This positive interaction is seen for hypertension (AB and ON), ischemic heart disease (ON), arrhythmia (AB and ON), heart failure (AB), cerebrovascular disease, (AB and ON), pneumonia (AB), acute lower respiratory infection (AB), COPD (AB) and asthma (ON). However, the interaction was only found to be statistically significant for hypertension (ON), ischemic heart disease (ON), arrhythmia (AB and ON), cerebrovascular disease (ON) and asthma (ON). Overall, these findings demonstrate the potential of satellite-derived CO as a metric for exposure in wildfire health analyses.

As climate change impacts the occurrence of wildfires, it is important to consider the effects of the increased emissions on human health, both locally and through long-range transport. Understanding the implications for the health care system can help build a framework for shaping policy, informed decision making, and effective risk mitigation. Establishing a connection between adverse health outcomes and satellite measurements of CO offers the potential to enhance public health advisories, leveraging the broader spatial coverage provided by satellites compared to regional ground-based monitoring methods. Studies examining the long-term and long-range health impacts of wildfires are limited, underscoring the importance of further research to expand upon the work done in this study. Further research, including broader geographical coverage, and longer-term finer-scale patient data will provide greater insight into the long-term impacts of long-range wildfire emissions on human health.

Chapter 7

7 Conclusions

7.1 Summary

This thesis demonstrates the importance of reliable long-term measurements of the atmosphere, showcasing their diverse applications to address the scientific questions and to achieve the three scientific objectives stated in Chapter 1:

(1) Maintain ongoing solar absorption FTIR measurements and trace gas retrievals at TAO, contributing to the NDACC DHF and CAMS and work towards establishing a new Canadian NDACC FTIR site at CARE.

(2) Evaluate the performance of atmospheric models by leveraging FTIR datasets from the TAO, CARE, PEARL, and four other Arctic NDACC stations, as well as other relevant in situ and satellite measurements.

(3) Investigate changes in atmospheric composition resulting from the long-range transport of wildfire emissions and assess the impact of this on local air quality and public health.

The FTIR spectrometer at the University of Toronto Atmospheric Observatory continues to make regular measurements, contributing to its long time-series of observations, dating back to 2002. Trace gas profiles and columns of 16 gases (C_2H_2, C_2H_6, CH_3OH, CH_4, CHF_2Cl, CO, H_2CO, HCl, HCN, HCOOH, HF, HNO_3, N_2O, NH_3, O_3 and OCS) are contributed to NDACC.

Project 1 (Chapter 4) addressed the question ***"How well do the SLCF model simulations in the AMAP 2021 Report represent historical measurements of CH_4, CO and O_3 from five Arctic FTIR sites, and what, if any, patterns arise in the discrepancies?"***. The evaluation of AMAP 2021 SLCF models using high-latitude NDACC FTIR sites revealed key biases and discrepancies in the modelled tropospheric columns of CH_4, CO, and O_3 in the Arctic. This contributed to the first scientific objective by utilizing NDACC FTIR measurements to examine the performance of atmospheric models. The work provides an assessment of seasonal cycles, multi-model means, and overall differences, while offering insights on where and what the models may lack. Overall, the models have a negative bias for all locations and all species examined. The mean model bias is -9.7% for CH_4 and is relatively consistent across the four years, -21% for CO with a maximum

negative bias in the spring and minimum in the summer, and -18% for O_3 with a maximum difference centered around the summer. Model assessments using historical data serve as a crucial checkpoint for both improving models and for evaluating their uncertainties for applications which simulate into the future. The Arctic plays a key role in Earth's climate system and is warming at a faster rate than the rest of the world, so predicting how changes will manifest is important for both local communities and policy building. However, constraints such as operational costs, remote locations and harsh conditions limit measurement coverage in the Arctic, therefore, evaluating models using all available metrics is highly beneficial. This project adds a new data set (column-integrated NDACC FTIR measurements) to those used in the AMAP 2021 SLCF Report, and in doing so provides an evaluation of the models in the troposphere.

Project 2 (Chapter 5) addressed the question ***"How significant were the impacts of the 2023 Canadian wildfires on the air quality and composition in Southern Ontario, and how do the GEM-MACH Firework simulations compare to ground-based and satellite measurements in the region?"***. The impact of long-range transport from the intense 2023 Canadian wildfires was investigated by integrating several applicable measurements and models. This project supported the second and third scientific objectives by performing model assessment with the CARE and TAO FTIR data and by evaluating enhancements from wildfire-related gases and the respective air quality warnings during smoke events. The work provides an appraisal of the GM-FW model, which provided operational air quality analysis for the time of the events. The comparisons to 0-10 km FTIR partial columns show the model has an overall negative bias in the troposphere across the whole summer, with a relatively overestimated response during smoke events. Assessing the profile enhancements during the three events provides information on how the model distributes the gases vertically, the shape of CO enhancements are well captured, while NH_3 has large overestimations and O_3 is variable. Although MOPITT satellite comparisons show that GM-FW has good spatial distribution during the events, surface comparisons show that the model has a general overestimation of CO, underestimation of O_3, and an overestimation of urban (Toronto) $PM_{2.5}$ and underestimation of rural (Barrie) $PM_{2.5}$. FTIR CO profiles and Mini MPLNET NRB allowed for an assessment of the approximate height of the smoke layer, for which HYSPLIT back-trajectories were run to determine the path which brought smoke to the area at the time of the events. Correlations with CO were observed for C_2H_6, CH_3OH, HCN and HCOOH, and were not present for NH_3 and O_3. Enhancement ratios were assessed for the three events, in conjunction

with back-trajectory analysis, contributes to a growing database of wildfire emission studies. This project provides a comprehensive analysis of the air composition and quality in Southern Ontario as a result of wildfire smoke transport events during the summer of 2023. Additionally, the evaluations of the GEM-MACH FireWork model provided a novel source for comparison with the operational model, which can support future air quality forecasting and model improvements.

Project 3 (Chapter 6) addressed the question ***"Has an increase in wildfires changed the CO cycle in Ontario and Alberta, Canada? Does health care utilization for respiratory and cardiovascular diseases present a change related to the CO cycle and if so, can CO be used as an exposure metric?"***. Long-term trends in CO concentrations in Ontario and Alberta were examined with respect to an increase in wildfire activity, to assess potential links between atmospheric column CO and health care utilization for respiratory and cardiovascular diseases. This evaluation of CO and public health as it relates to wildfires contributed to the third scientific objective. The work asserts that a similar increase in atmospheric CO, as reported in Buchholz et al. (2022), is observed in total column MOPITT XCO from Alberta and Ontario, and in total column CO from the TAO FTIR, when comparing 2004-2011 to 2012-2019. The use of a difference-in-difference analysis, with atmospheric CO as an exposure metric, offers a potential alternative to surface $PM_{2.5}$ in health studies, leveraging its wider availability through observations (e.g., satellite). The difference-in-difference approached allowed for controls of confounding factors, such as month and region, which may influence atmospheric CO and/or health outcomes. By analyzing long-term atmospheric CO measurements alongside health care utilization, results are suggestive of a statistically significant increase in hospitalizations for arrhythmia in Alberta and Ontario, and hypertension, ischemic heart disease, cerebrovascular disease, and asthma in Ontario. Establishing CO as a useful tracer for health impacts, in lieu of surface $PM_{2.5}$, offers the potential to provide a more comprehensive coverage for health effects associated with air pollution.

Collectively, these projects highlight the significance of the FTIR measurements made at TAO, and within NDACC, as a tool to evaluate atmospheric models, assess air composition as it relates to public health, and complement other atmospheric measurement techniques. They lay a foundation for future studies that can help improve atmospheric modelling and influence policy. These studies demonstrate the importance of long-term atmospheric measurements as they relate to a changing climate and atmospheric events, while also emphasizing the influence of long-range transport on air quality and the possible implications for human health, whether from wildfires or

the repercussions of Arctic warming. This contributes to the first scientific objective of continuing measurement acquisition and utilizing data for atmospheric studies, while underscoring the need for continued investment in long-term atmospheric monitoring and highlighting the critical role of collaborative research efforts.

7.2 Future Work

A fundamental component of this research is the utilization of the long-term database of consistent, high-quality measurements collected by the NDACC IRWG FTIR instruments. These datasets provide a valuable record of atmospheric composition that enables detailed trend analyses, model validation, and assessment of atmospheric events, such as those presented in this thesis. Following the first scientific objective, it is of the utmost importance that instrument maintenance continue, and measurements follow. Likewise, the submission of TAO retrievals to CAMS RD and the NDACC DHF should remain consistent (every 2-3 weeks and annually, respectively). A key priority in the continuation should be to update the TAO retrievals to the latest version of SFIT4, reprocess all the past spectra with this version, and update the data versions on the NDACC DHF. The IRWG has working groups for the harmonization of HCl, HF, CO, C_2H_6, HNO3, N_2O, CH_4, OCS, HCN, $ClONO_2$ (not currently retrieved with TAO), and H_2CO. When the recommended parameters are shared, the retrievals will need to be updated and applied to the complete timeseries, marked with the tag “irwg2023”, and submitted in GEOMS v3 HDF format, similar to the new O_3 retrievals (described in Section 3.3). Furthermore, there are species not currently retrieved at TAO that may be explored, such as C_2H_4 and PAN (Wizenberg, 2023). Possible improvements can be made to the TAO system by refining the currently over-modulated ILS (see Figure 2.7), placing the HBr and N_2O cells on automated carousels in the sample chamber to allow more frequent ILS measurements, and installing a laser shutter to clear zero path difference selection problems.

In recent years, substantial work has been undertaken to ensure that the CARE FTIR spectrometer is now capable of making regular measurements. The usefulness of having a complementary measurement location was shown in Project 2 and in past work such as Whaley et al. (2015). To use this dataset to its full advantage, retrievals should be initiated for all remaining species (C_2H_2, CH_4, CHF_2Cl, H_2CO, HCl, HF, HNO_3, N_2O, and OCS), and at the same time these retrievals should be undertaken with the latest SFIT4 version. Efforts should be made to continue regular measurements and retrievals as this will be required to pursue formal NDACC certification for this

instrument. As the CARE FTIR dataset grows, a comprehensive analysis of the differences between the rural (CARE) and urban (TAO) sites, and the impacts of local and long-range sources, could be carried out. Improvements which have been noted for the CARE system include streamlining data transfer, automating end-of-day quality reports, fixing precipitation sensor reporting, replacing degraded sun-tracker mirrors, and placing the HBr and N_2O cells on automated carousels in sample chamber to allow more frequent ILS measurements.

To further the model evaluations performed in Project 1 (Chapter 4), performing various sensitivity analyses would provide more information regarding the shortcomings of the models. Additionally, including a broader range of sites (such as mid-latitude) may reveal if there are latitudinal gradients in model biases. Performing the comparisons on a longer time series can help distinguish interannual variability from long-term trends, providing a clearer picture of how the models respond to changes over time.

To build on the work presented in Project 2 (Chapter 5), a reevaluation of the GEM-MACH FireWork with the latest version (not yet used operationally) could provide a checkpoint for the improvements that have been implemented by the modelling team. Additionally, comparisons could be extended to include more of the OMECP surface measurement locations, and even other provinces and territories. Another option would be to compare TAO FTIR measurements with the GM-FW model over an extended period of time to see how the model performs for other wildfire events for which TAO recorded trace gas enhancements and general background levels.

Improvements could be made to Project 3 (Chapter 6) if hospitalization data can be obtained for more regions, on a finer time resolution and for a longer time. Due to limitations in the data agreement with CIHI, data were only available for Alberta from 2010, and Ontario from 2004, less-than monthly aggregation was discouraged, and other provinces did not have data available prior to 2012. Obtaining more locations, with more years prior to 2012 and a finer time resolution (ideally daily) would allow for a more robust difference-in-difference analysis. As is, the analysis could be furthered by comparing the results with XCO and the more widely used $PM_{2.5}$ exposure metric. Combining this comparison with GEM-MACH FireWork, the difference between the tropospheric CO and surface $PM_{2.5}$ could be assessed for the duration of the analysis. Additionally, an interesting case study could be performed by comparing hospitalizations and XCO from the extreme wildfire season of 2023 with the 2004-2019 DiD results, to see how they differ.

Appendices

A. Appendix for Chapter 4

This appendix contains the supplementary figures for Chapter 4. Figures A.1-A.14 correspond to the additional figures for CH_4, Figures A.15-A.25 are for CO, and Figures A.25-A.39 are for O_3. The figures in each section are as follows: the complete time series for each site, showing all measurements and smoothed model partial columns for 2008, 2009, 2014 and 2015; the monthly mean values from the points in the previous figures for each site; and the model vs. measurement regression for all sites except Eureka (which is shown in the main text).

I. Additional CH_4 Figures

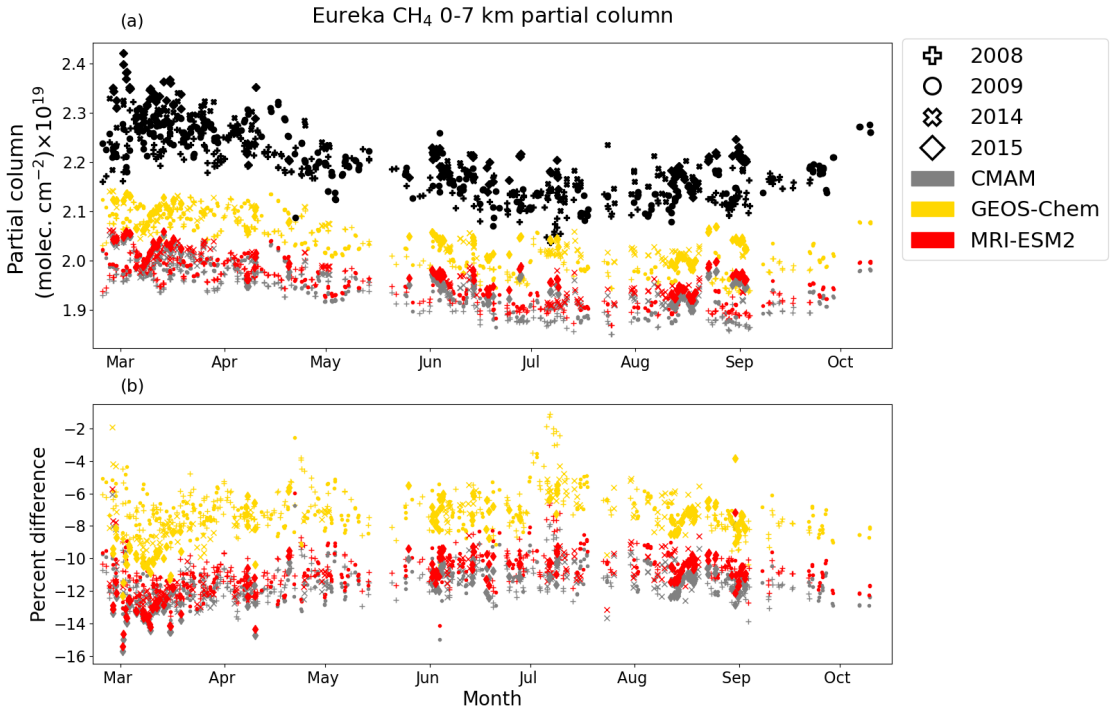

Figure A.1: (a) FTIR (black) and smoothed model (colour) 0-7 km partial columns of CH_4 by day of year, from Eureka. Model data are the nearest in time to each FTIR measurement. (b) Model-measurement percent difference (Δ_i) from Equation 3.2 by day of year. Each year is indicated by a different marker.

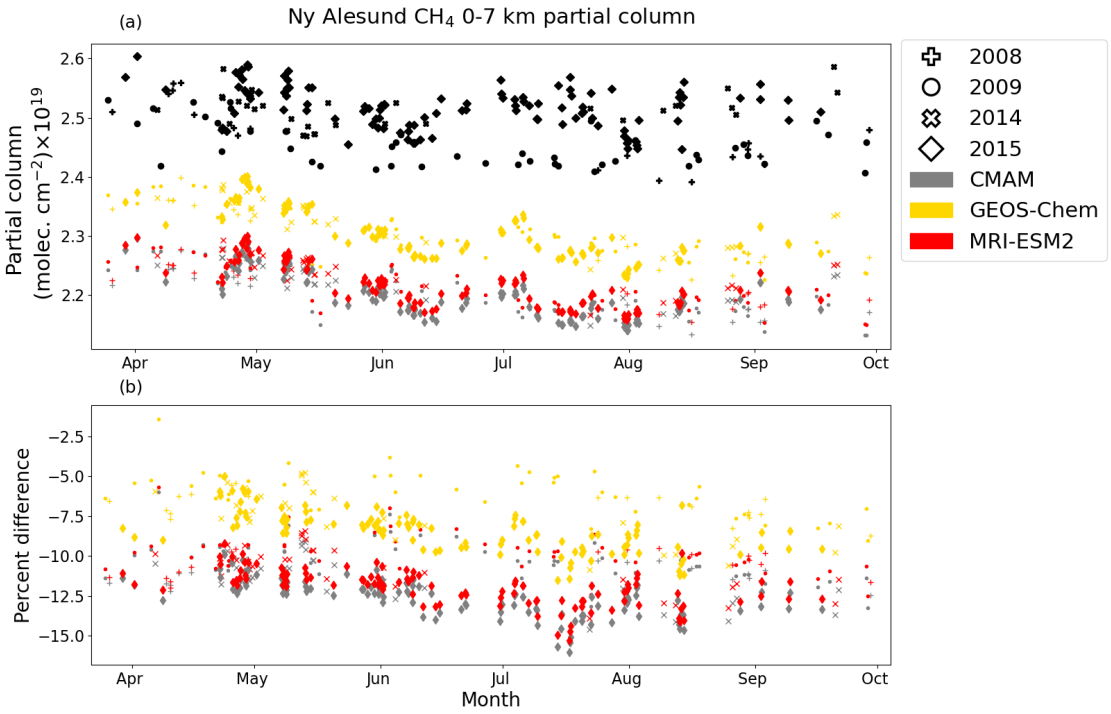

Figure A.2: Same as Figure A.1 but for Ny Ålesund.

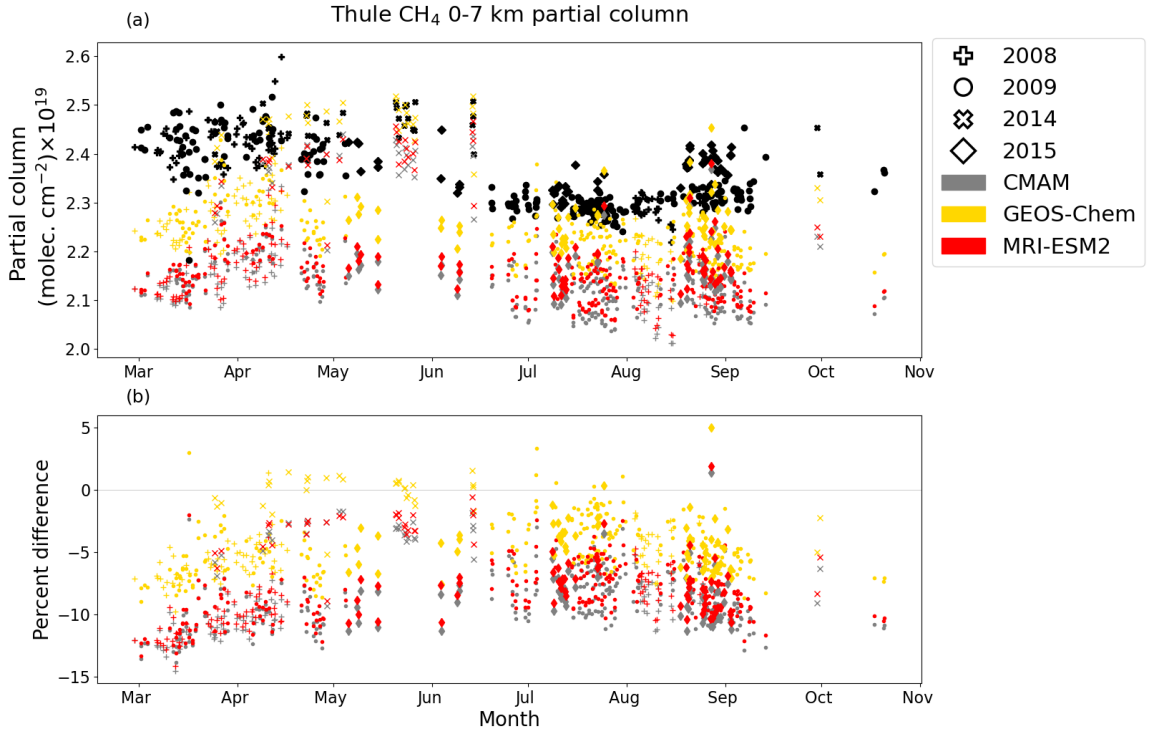

Figure A.3: Same as Figure A.1 for Thule.

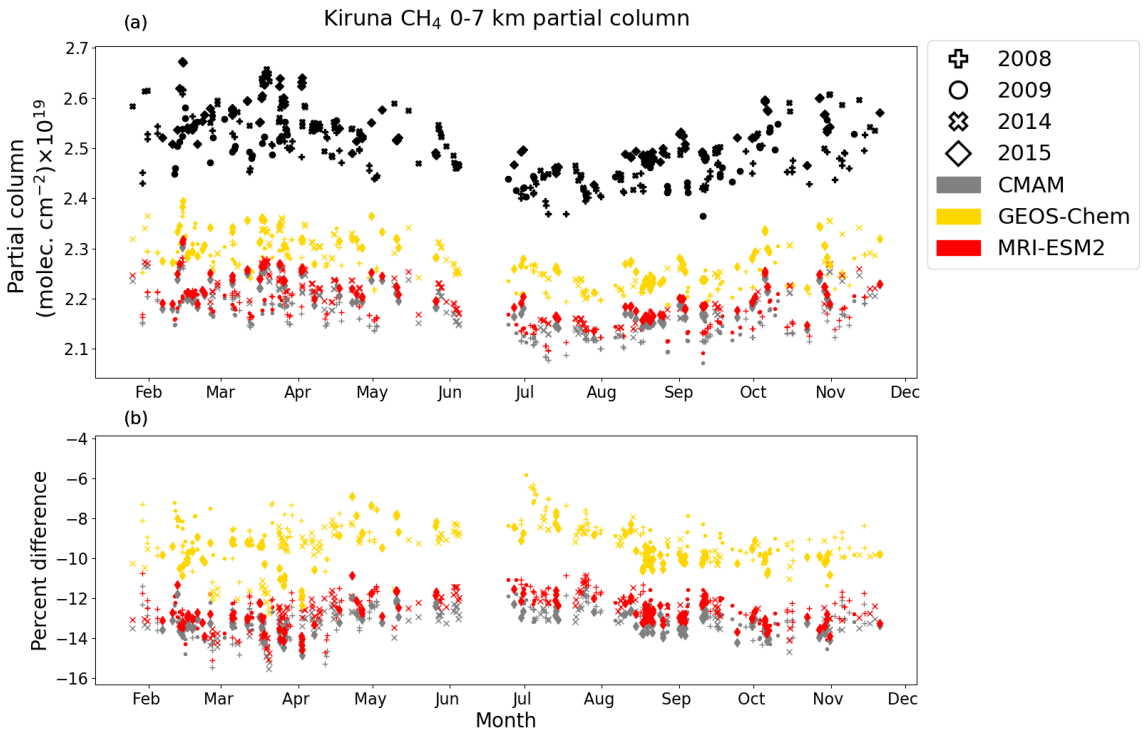

Figure A.4: Same as Figure A.1 for Kiruna

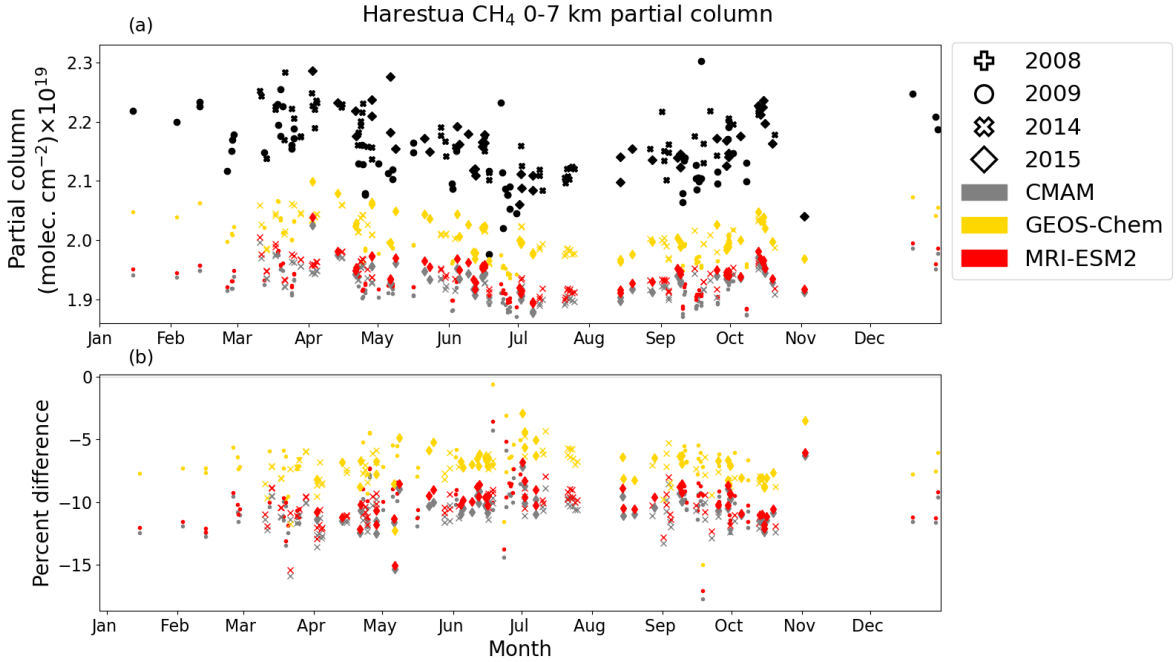

Figure A.5: Same as Figure A.1 for Kiruna.

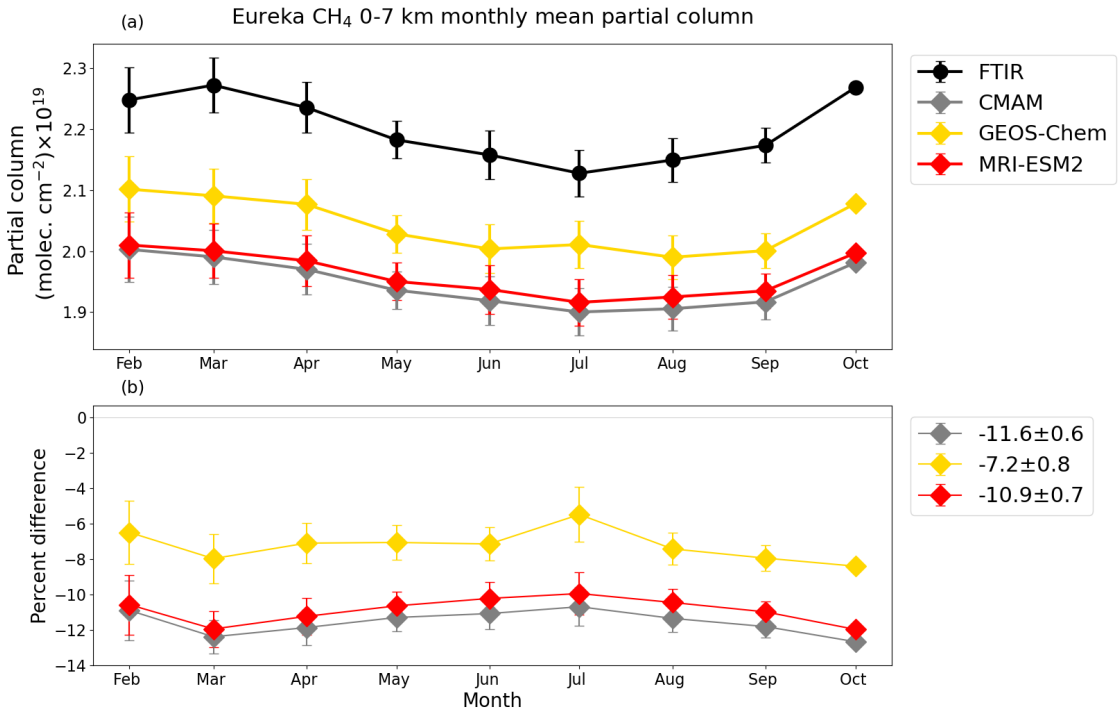

Figure A.6: (a) Monthly mean FTIR (black) and smoothed model (colour) 0-7 km partial columns CH_4 ($PC_{F,monthly,j}$ and $PC_{M,monthly,j}$, respectively), from Eureka using model data that are the nearest in time to each FTIR measurement shown in Figure A.1. Error bars represent the standard deviation of the monthly mean. (b) Model-measurement mean percent difference by month ($\Delta_{monthly,j}$). Error bars represent standard deviation of the monthly mean percent difference. The legend on panel (b) shows the overall mean percent difference (Δ_O) with the standard deviation of the overall mean percent difference.

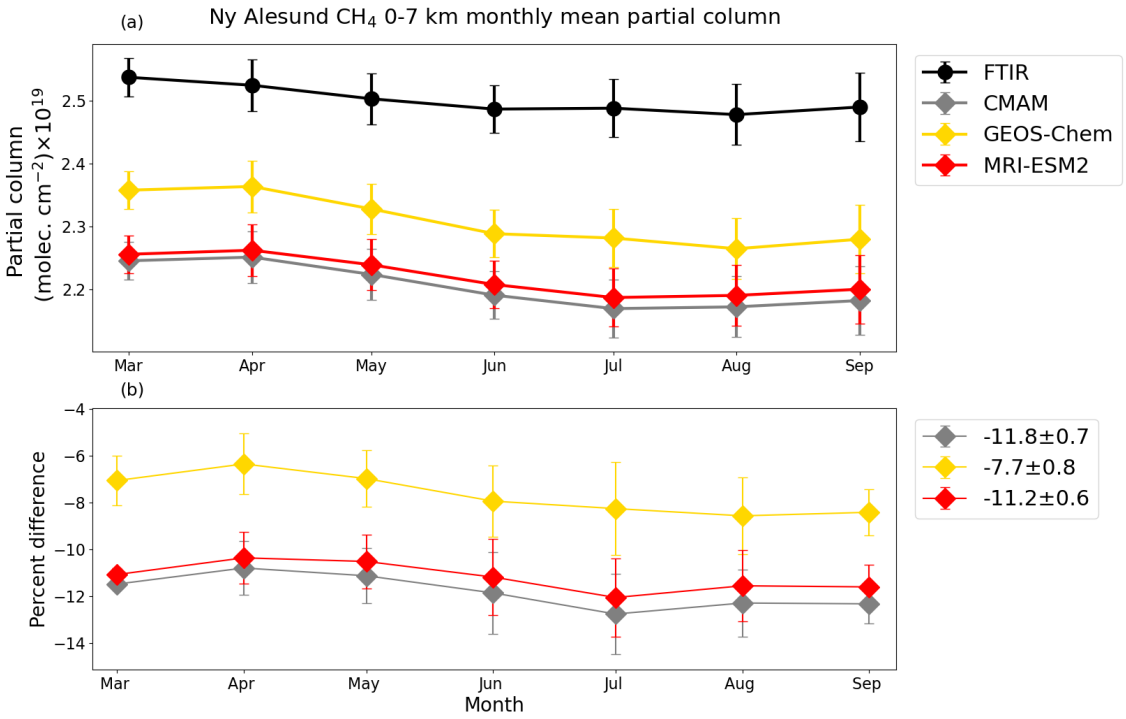

Figure A.7: Same as Figure A.6 for Ny Ålesund.

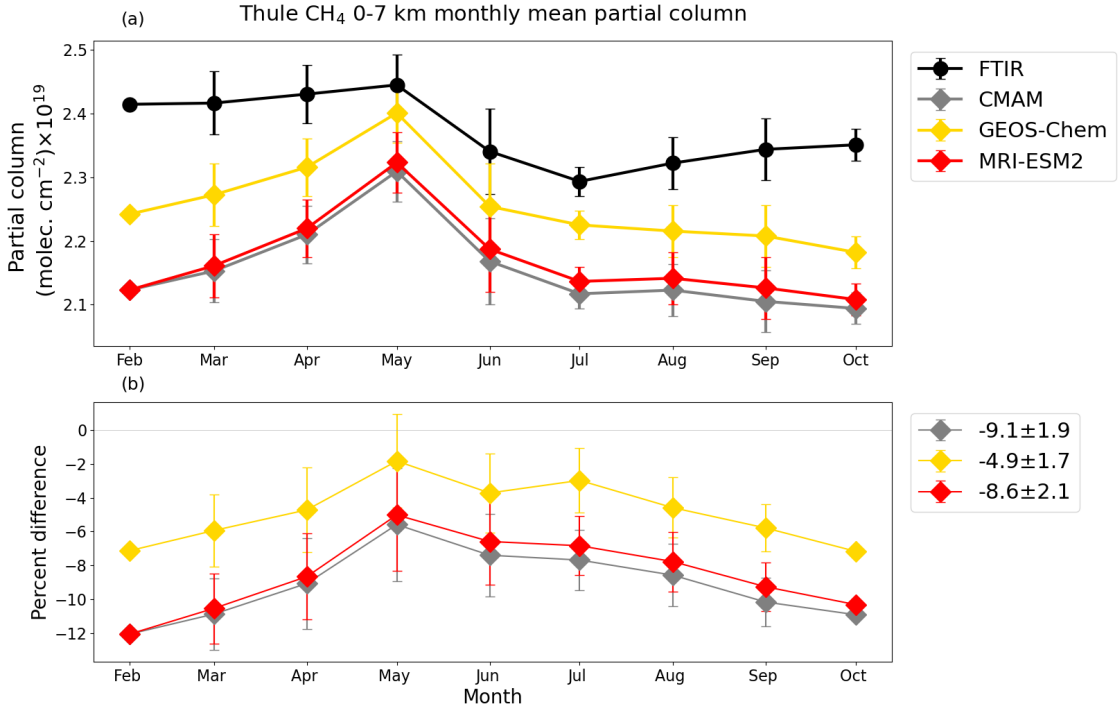

Figure A.8: Same as Figure A.6 for Thule.

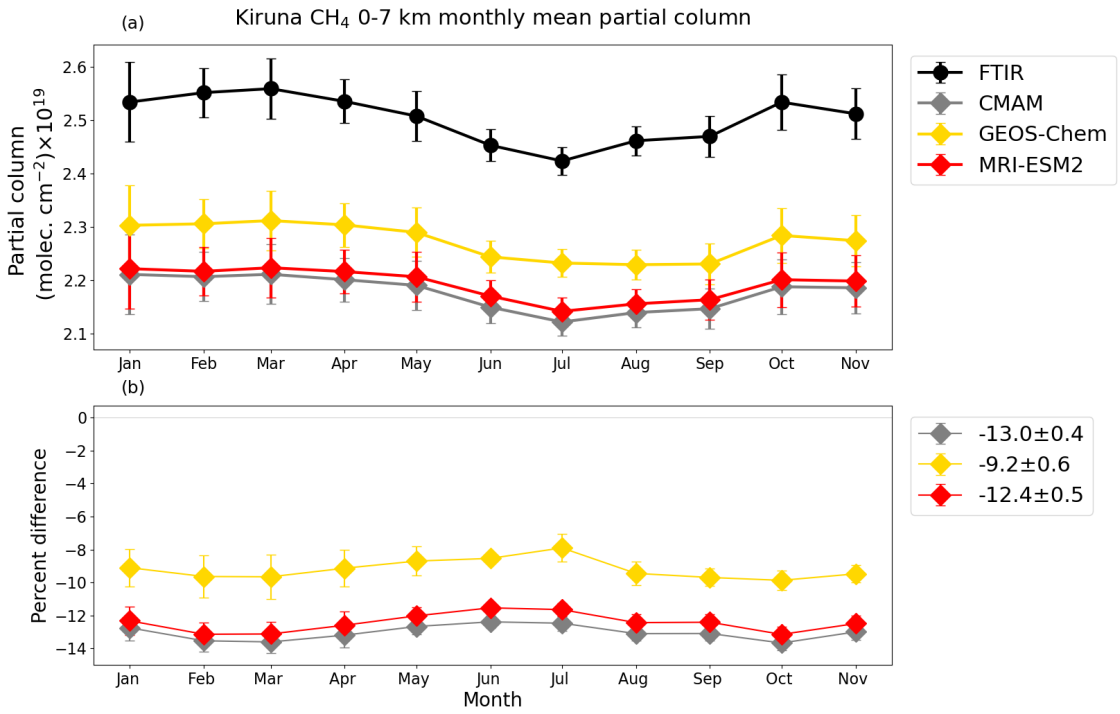

Figure A.9: Same as Figure A.6 for Kiruna.

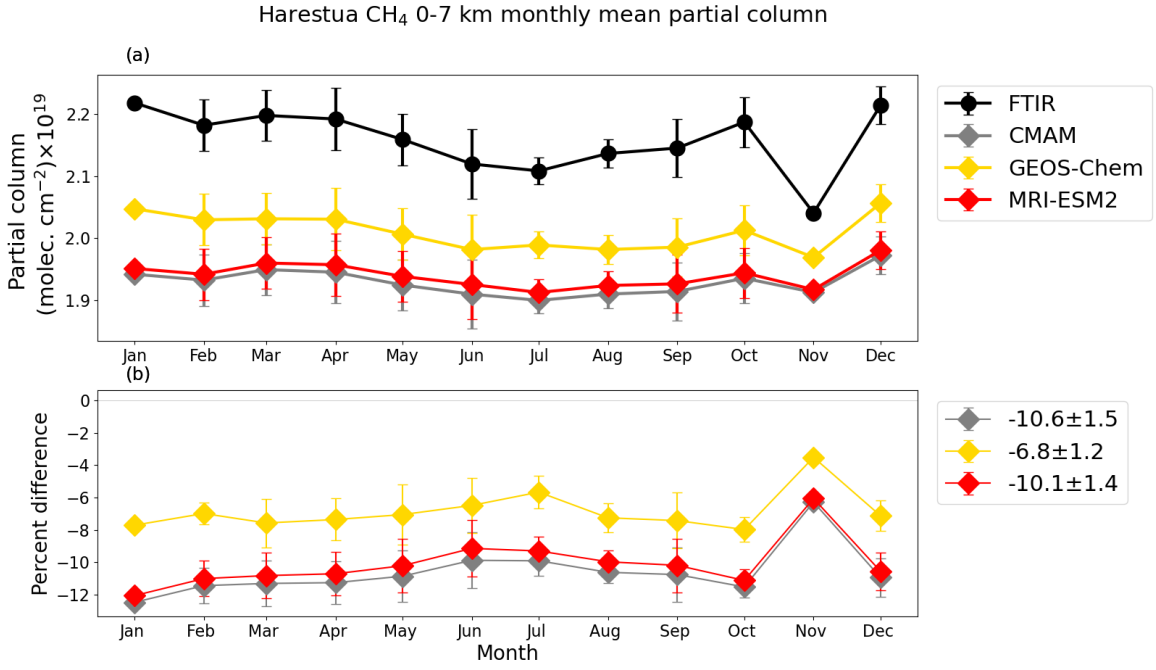

Figure A.10: Same as Figure A6 for Harestua. .

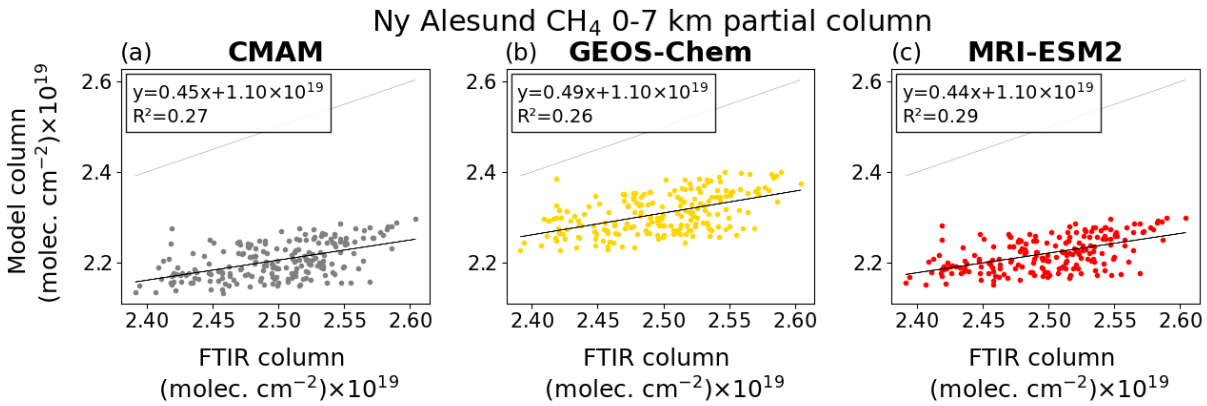

Figure A.11: Smoothed model vs. FTIR 0-7 km partial column of CH_4 for Ny Ålesund, showing all available model-FTIR corresponding data. The black line is the line of best fit, where the equation and R^2 are noted in the legend. The 1:1 line is shown in light grey.

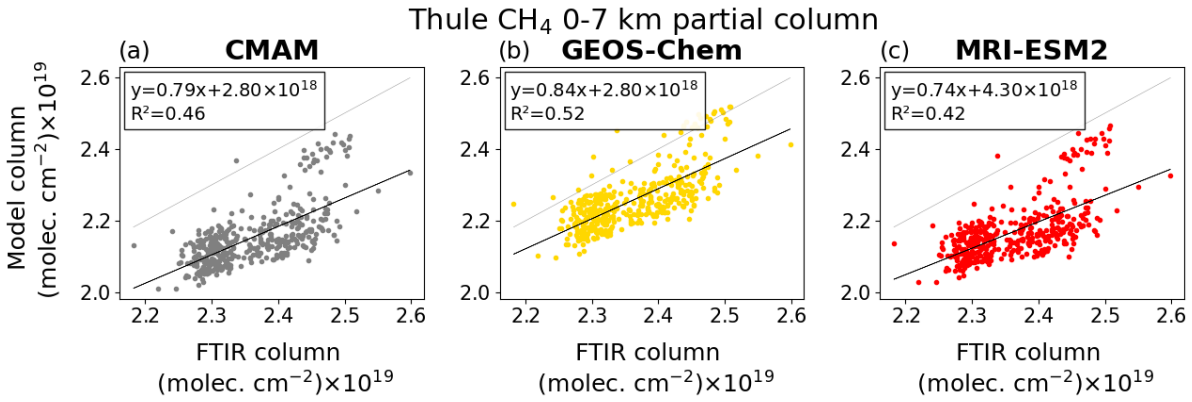

Figure A.12: Same as Figure A.11 for Thule.

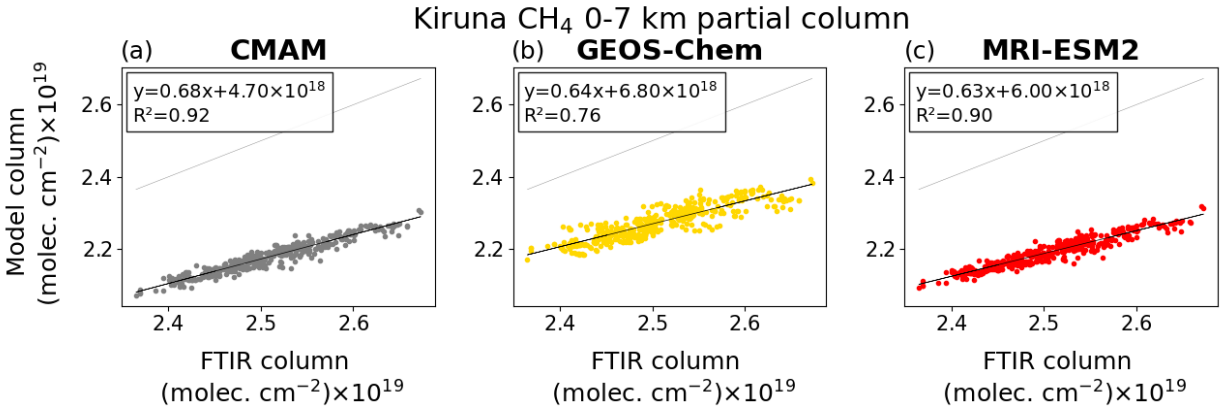

Figure A.13: Same as Figure A.11 for Kiruna.

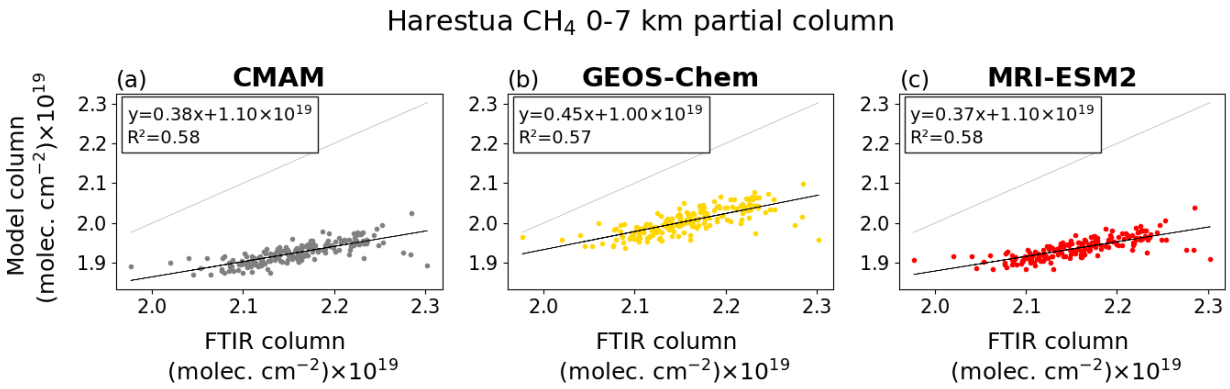

Figure A.14: Same as Figure A.11 for Harestua.

II. Additional CO Figures

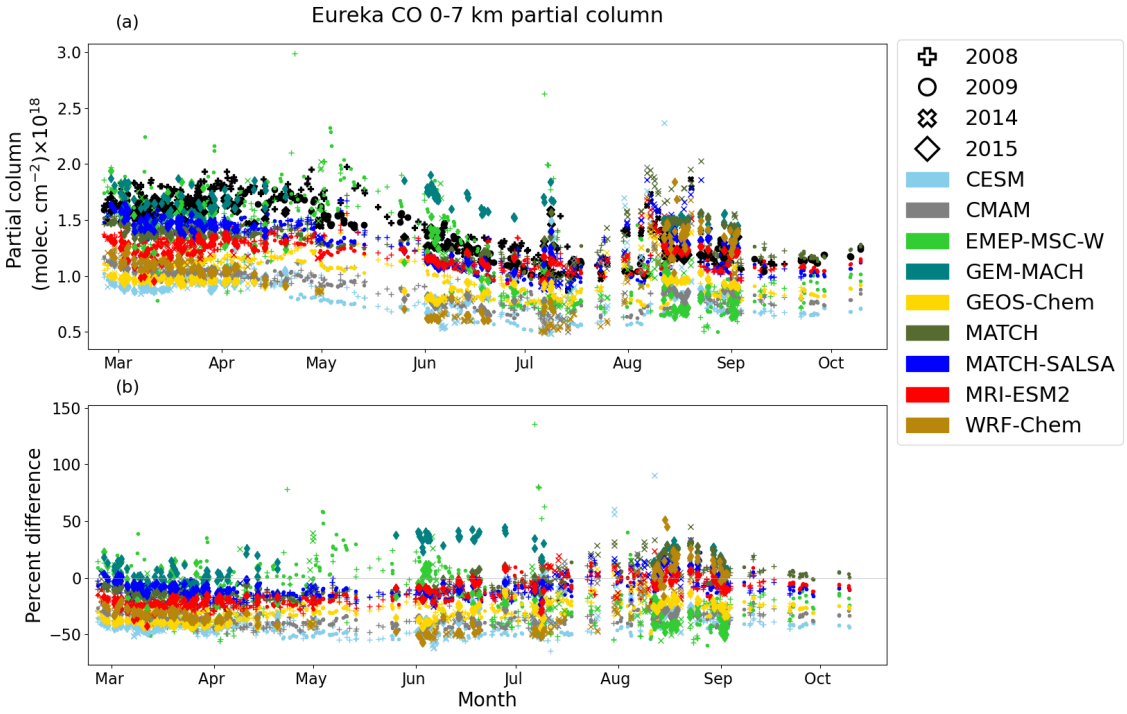

Figure A.15: (a) FTIR (black) and smoothed model (colour) 0-7 km partial columns of CO by day of year, from Eureka. Model data are the nearest in time to each FTIR measurement. (b) Model-measurement percent difference (Δ_i) from Equation 3.2 by day of year. Each year is indicated by a different marker.

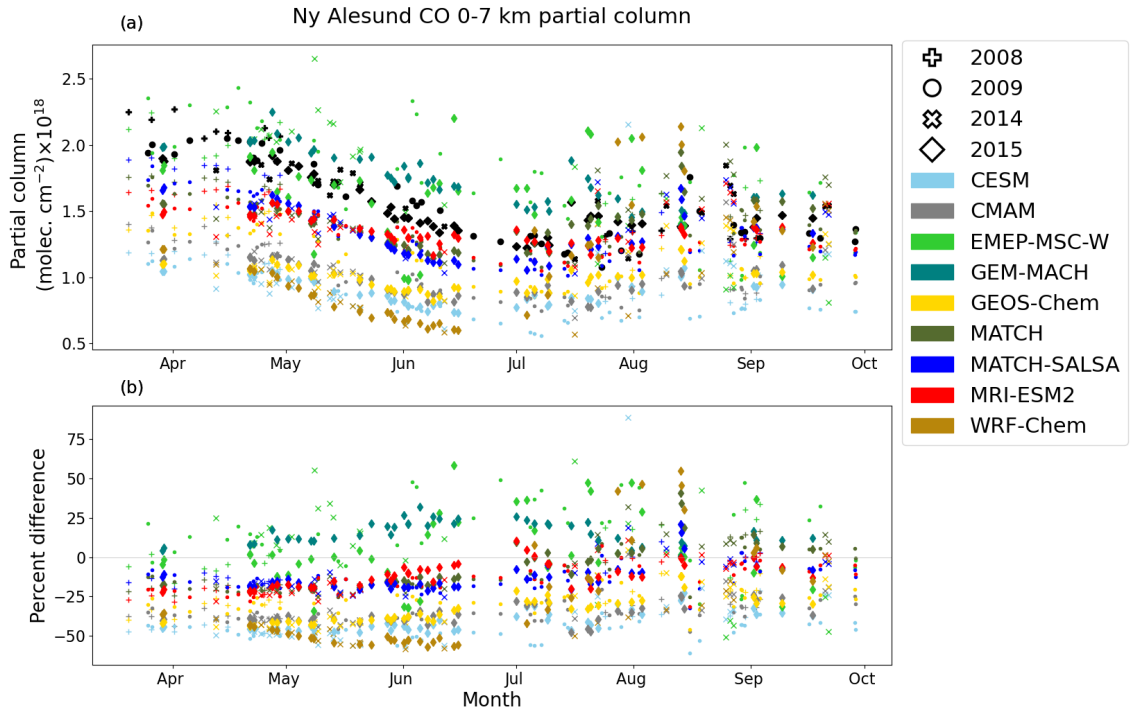

Figure A.16: Same as Figure A.15 for Ny Ålesund.

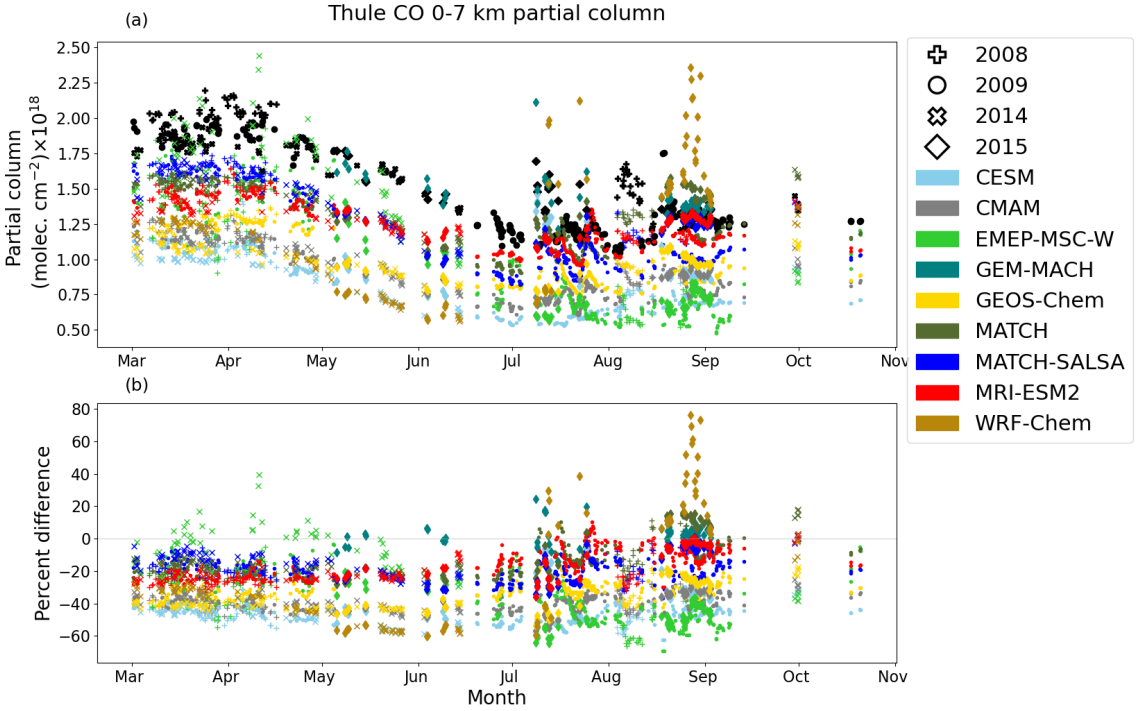

Figure A.17: Same as Figure A.15 for Thule.

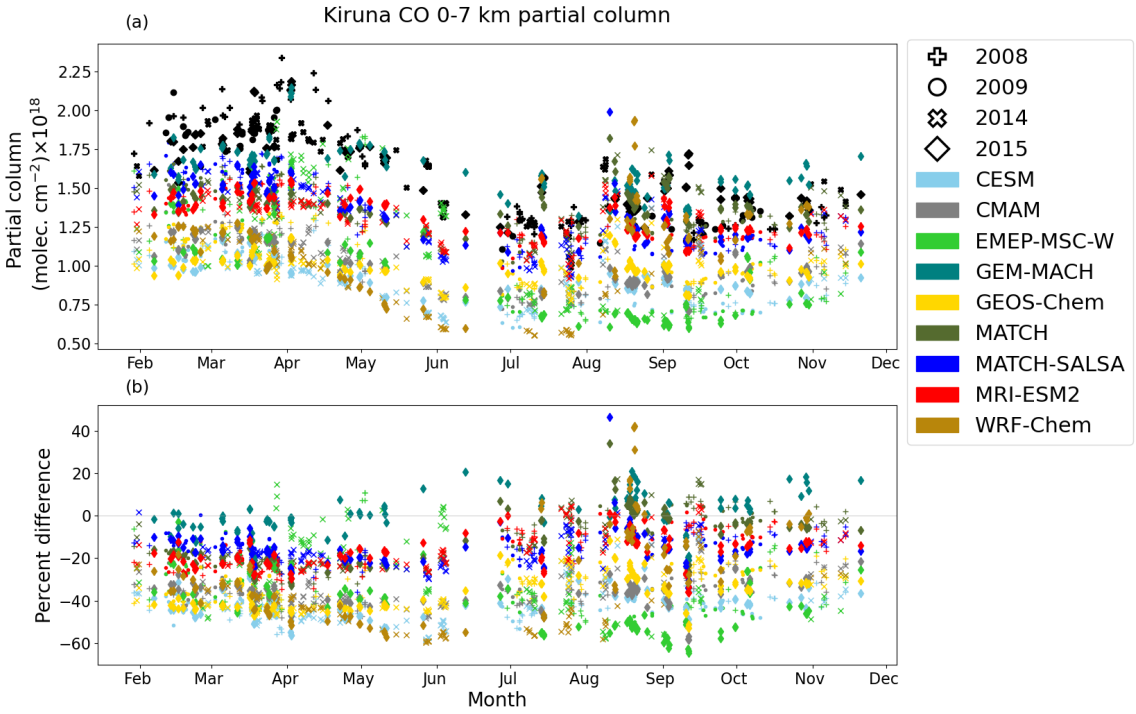

Figure A.18: Same as Figure A.15 for Kiruna.

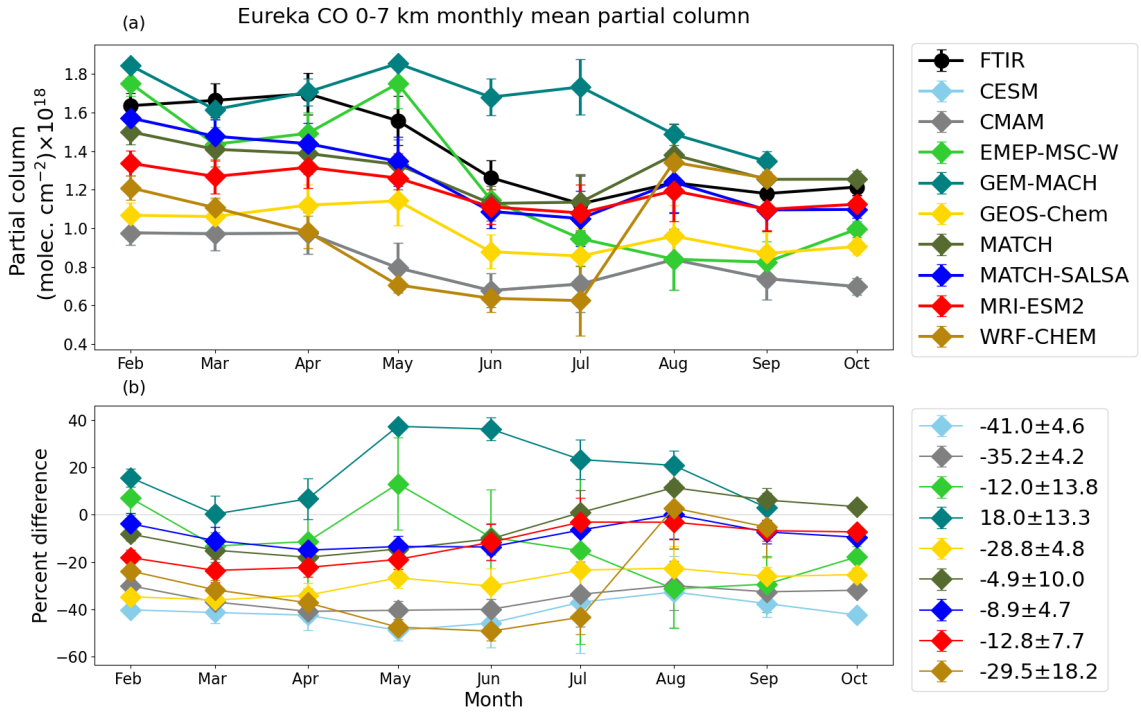

Figure A.19: (a) Monthly mean FTIR (black) and smoothed model (colour) 0-7 km partial columns of CO ($PC_{F,monthly,j}$ and $PC_{M,monthly,j}$, respectively), from Eureka using model data that are the nearest in time to each FTIR measurement shown in Figure A.15. Error bars represent the standard deviation of the monthly mean. (b) Model-measurement mean percent difference by month ($\Delta_{monthly,j}$). Error bars represent standard deviation of the monthly mean percent difference. The legend on panel (b) shows the overall mean percent difference (Δ_O) with the standard deviation of the overall mean percent difference.

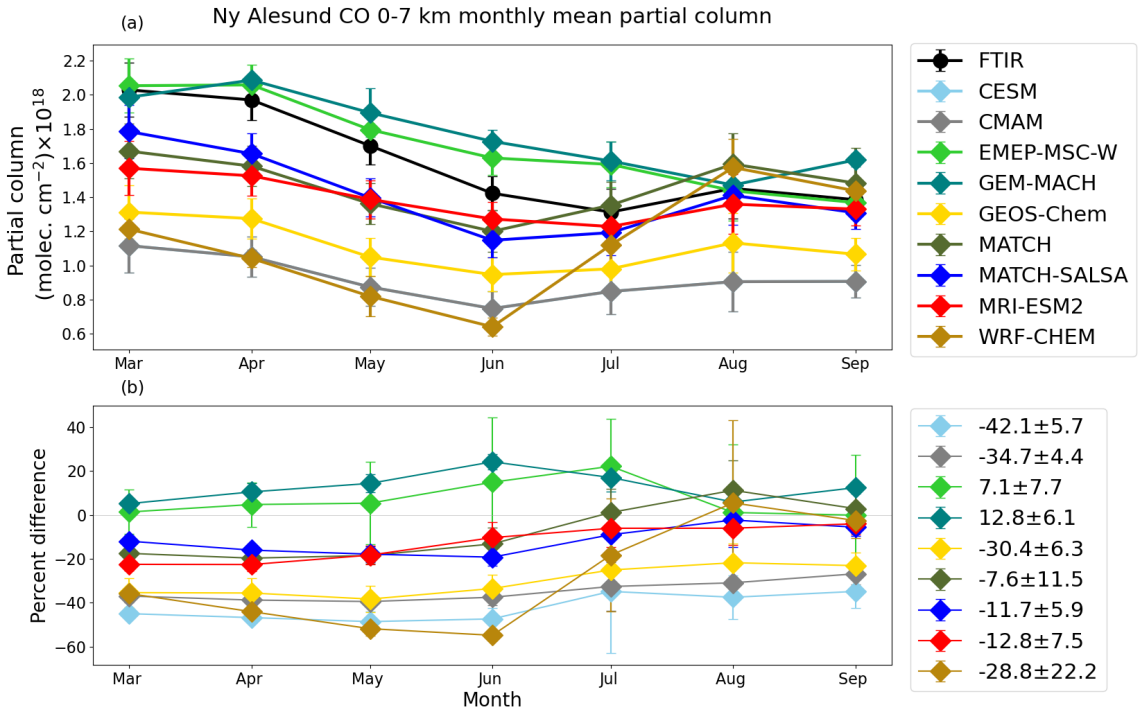

Figure A.20: Same as Figure 19 for Ny Ålesund.

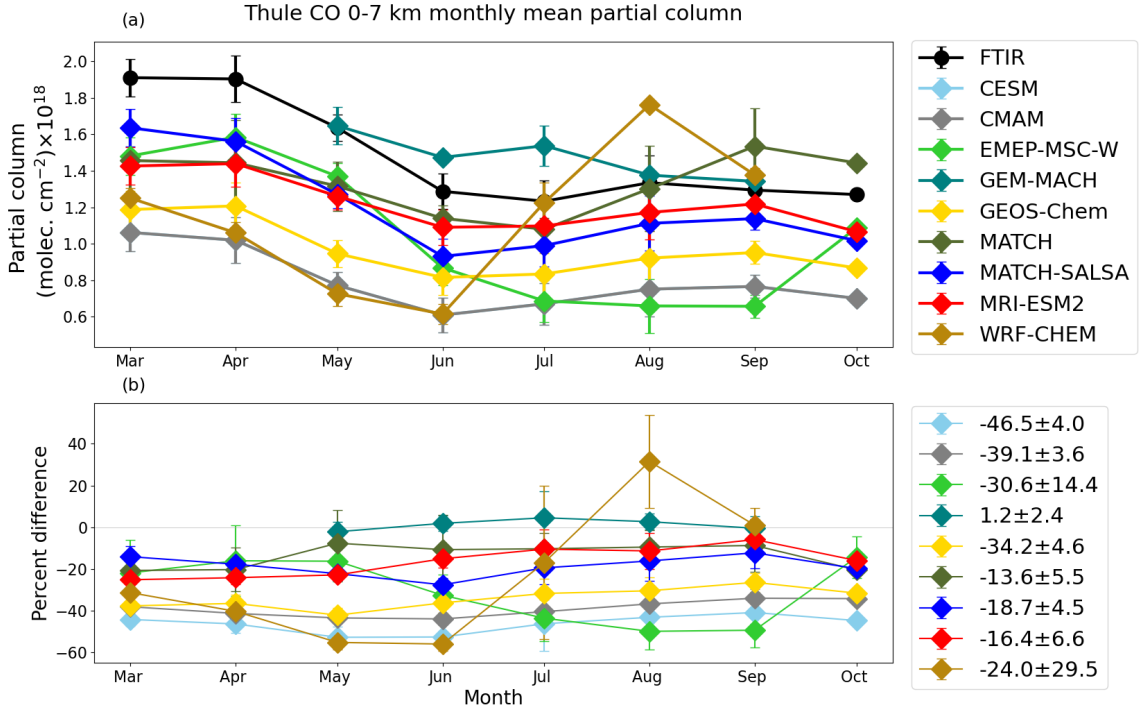

Figure A.21: Same as Figure A.19 for Thule.

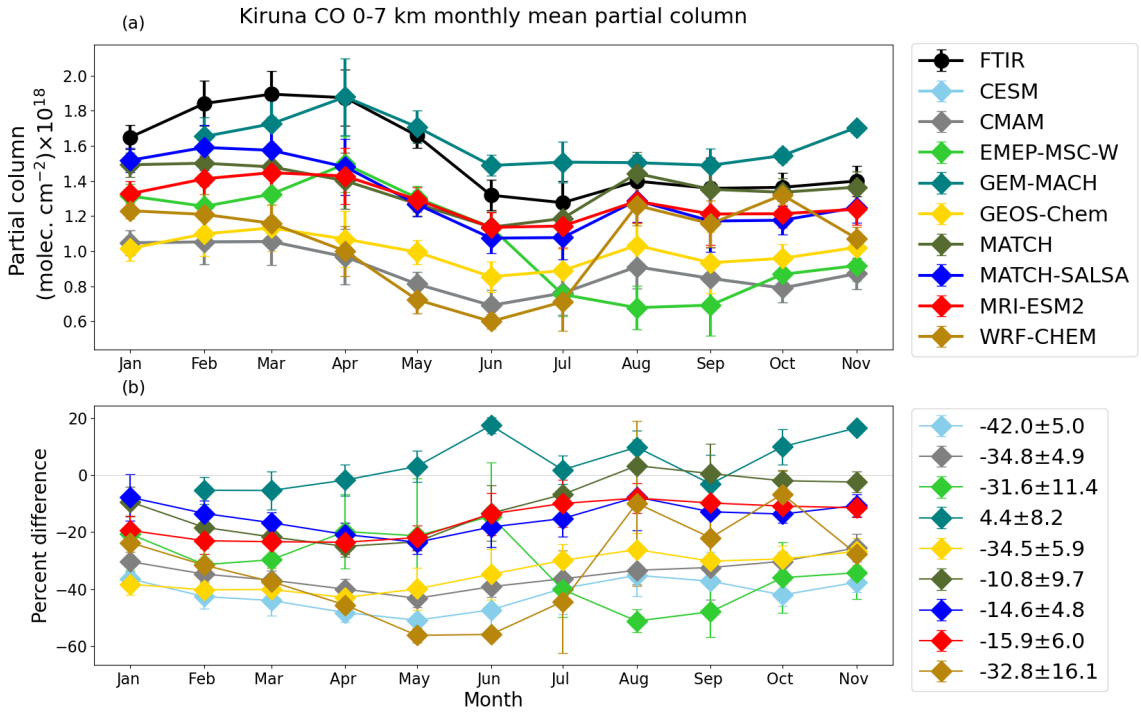

Figure A.22: Same as Figure A.19 for Kiruna.

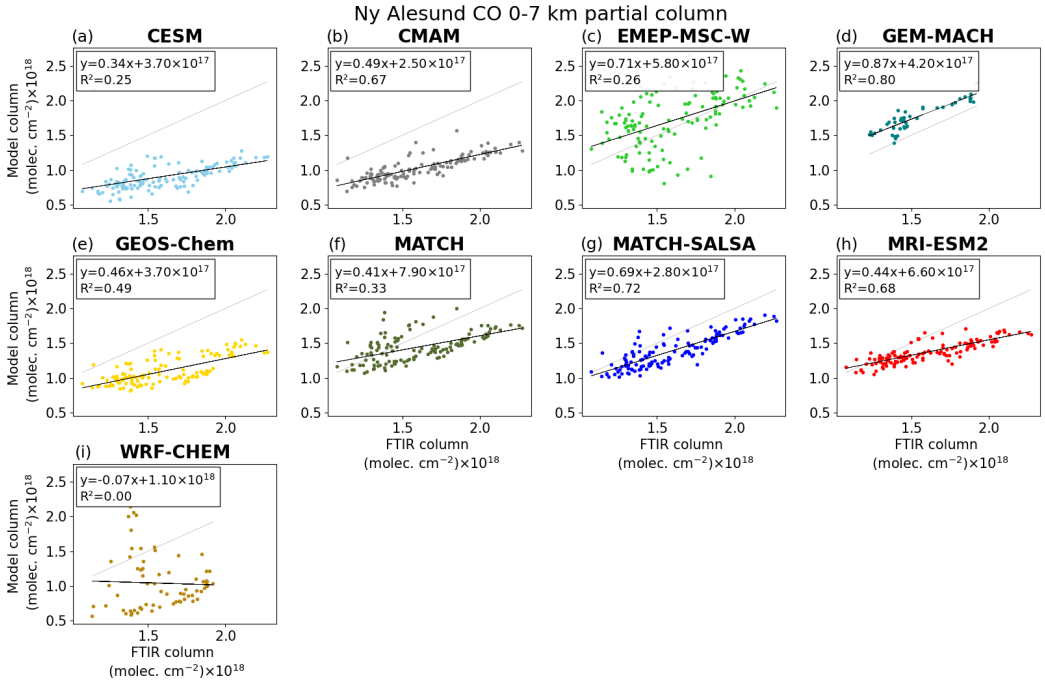

Figure A.23: Smoothed model vs. FTIR 0-7 km partial column of CO for Ny Ålesund, showing all available model-FTIR corresponding data. The black line is the line of best fit, where the equation and R^2 are noted in the legend. The 1:1 line is shown in light grey.

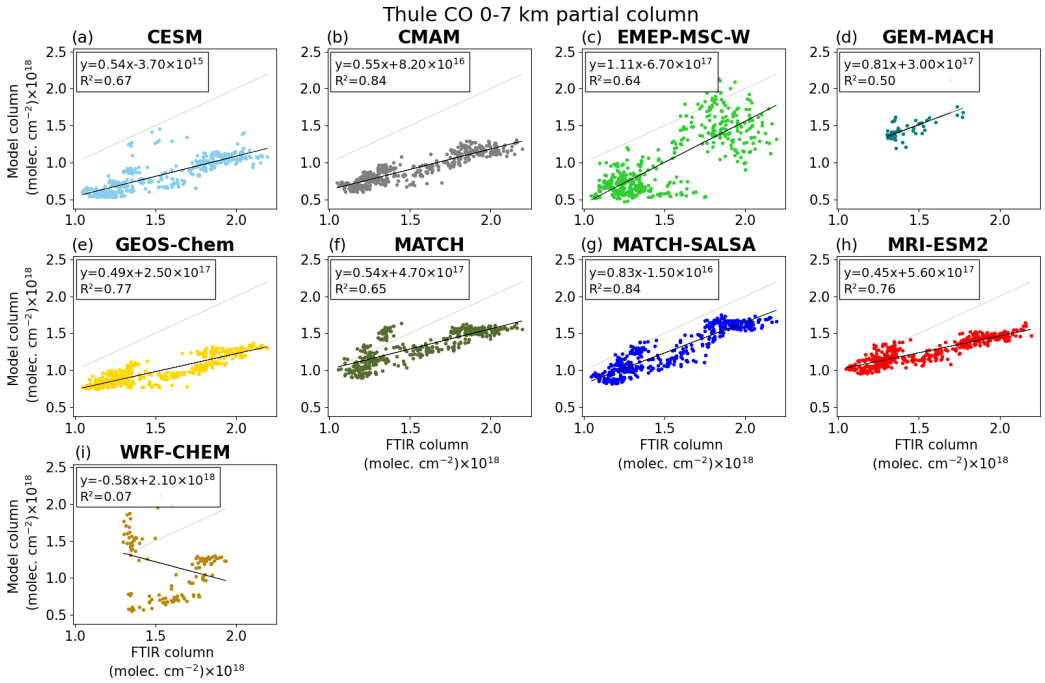

Figure A.24: Same as Figure A.23 for Thule.

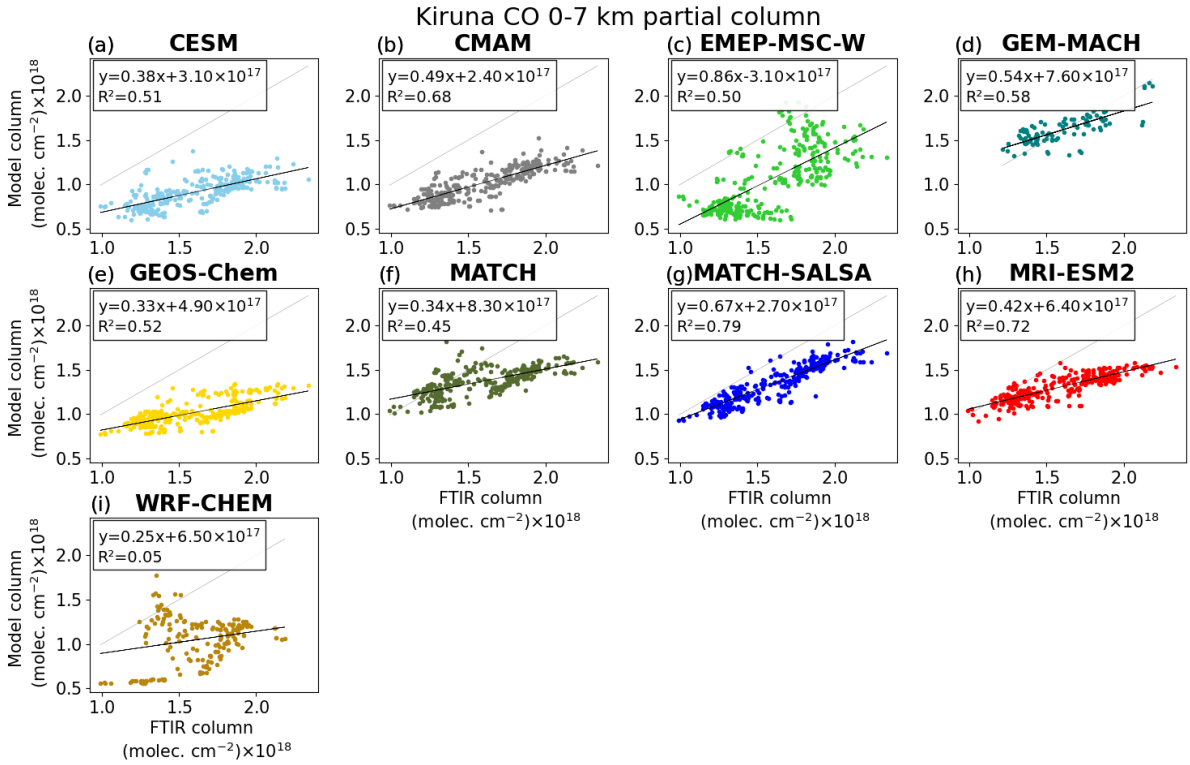

Figure A.25: Same as Figure A.23 for Kiruna.

III. Additional O_3 Figures

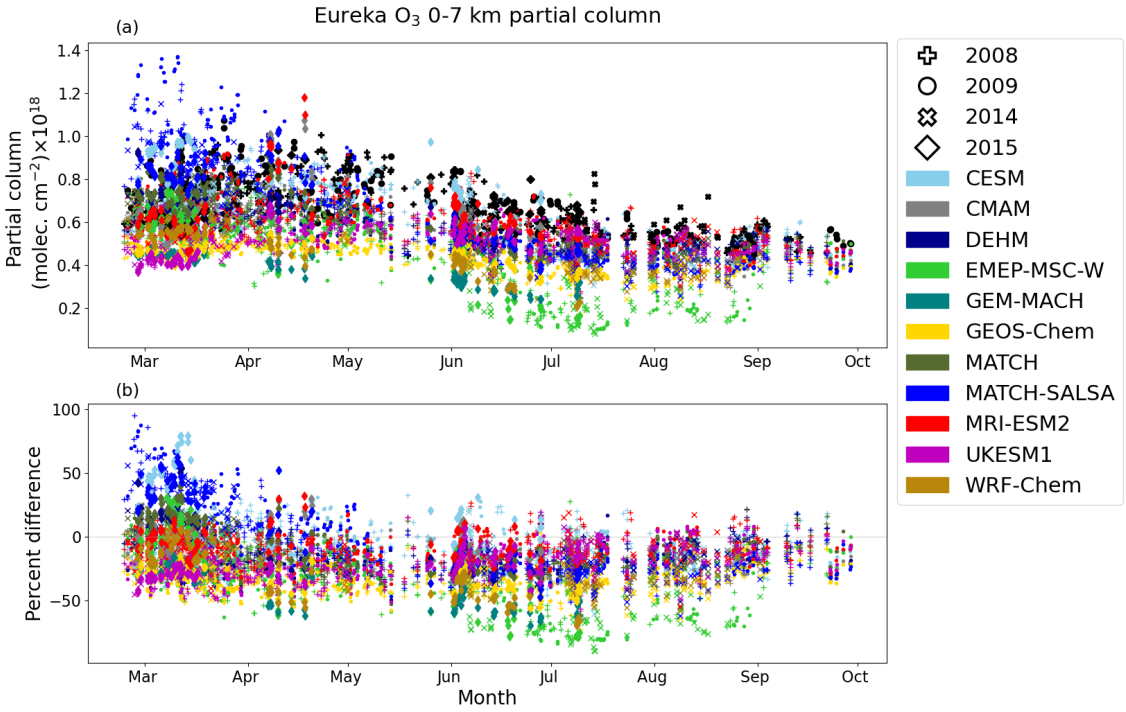

Figure A.26: (a) FTIR (black) and smoothed model (colour) 0-7 km partial columns of O_3 by day of year, from Eureka. Model data are the nearest in time to each FTIR measurement. (b) Model-measurement percent difference (Δ_i) from Equation 3.2 by day of year. Each year is indicated by a different marker.

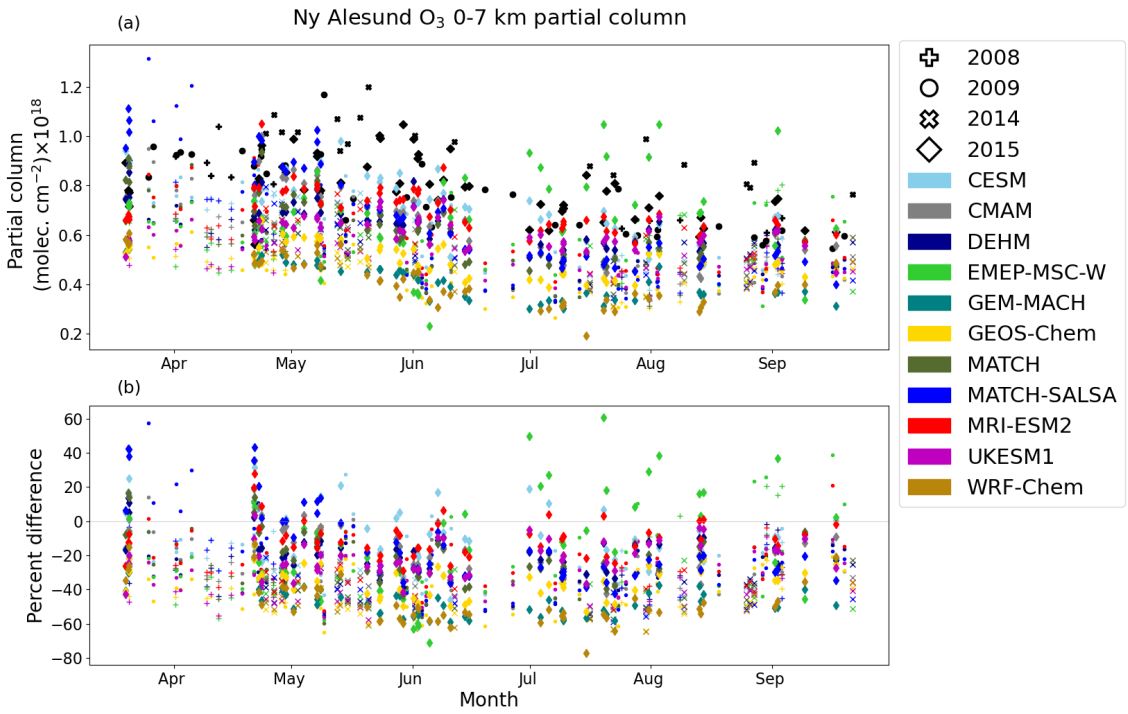

Figure A.27: Same as Figure A.26 for Ny Ålesund.

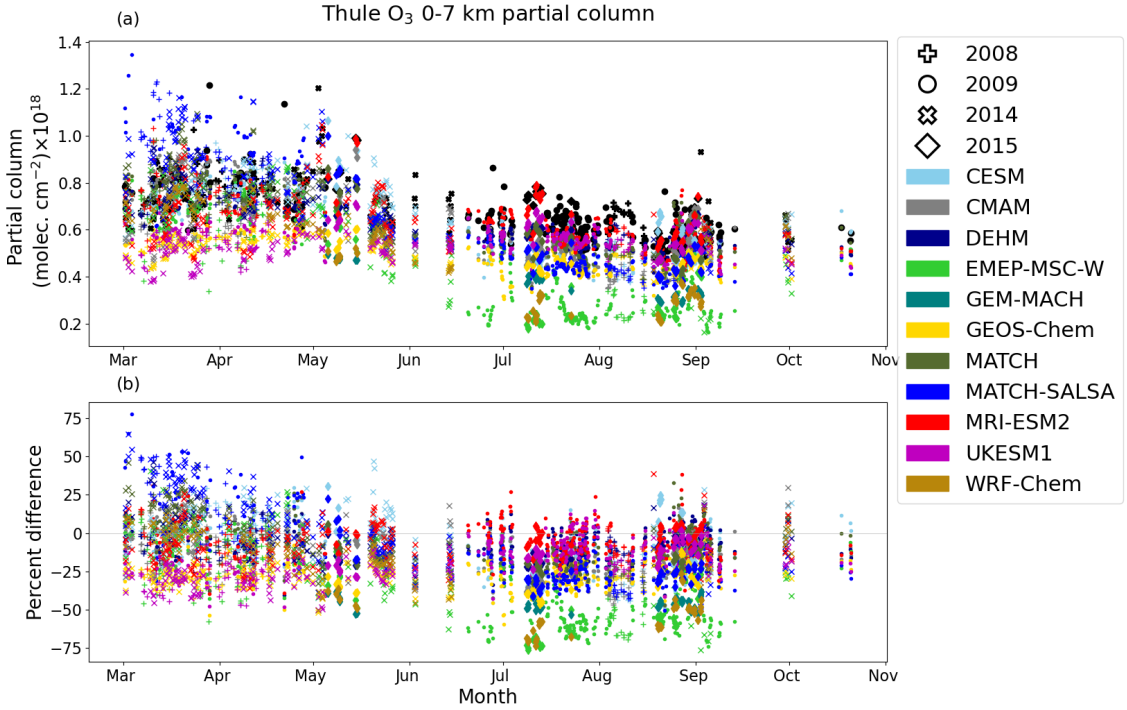

Figure A.28: Same as Figure A.26 for Thule.

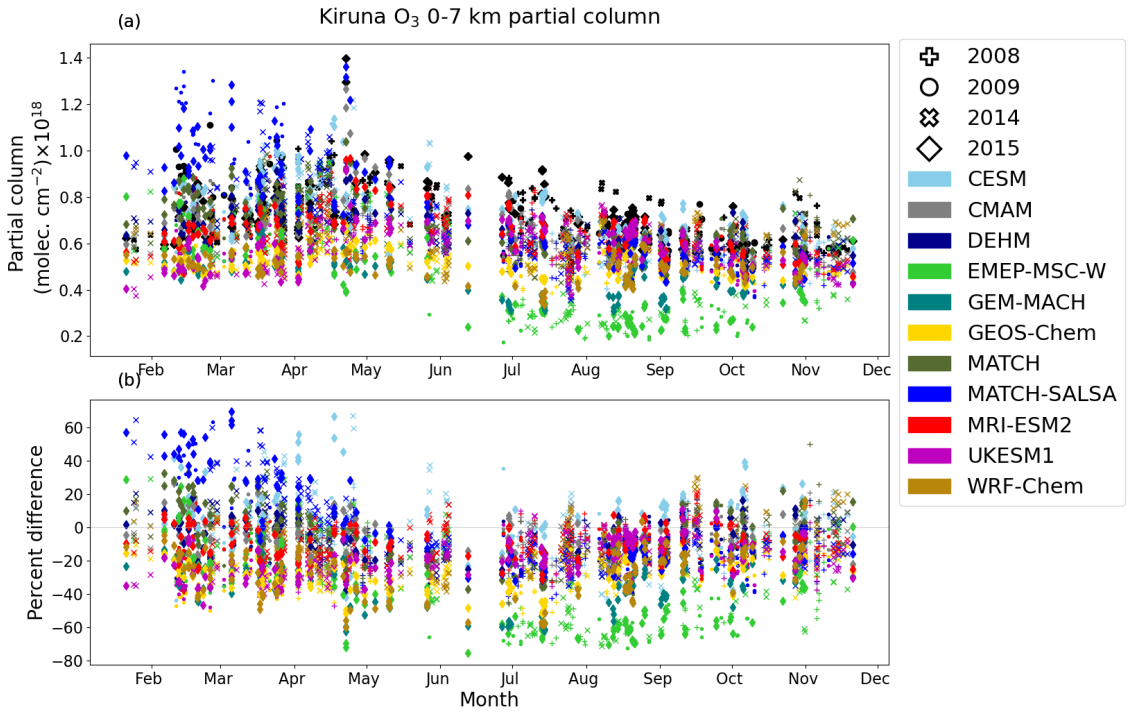

Figure A.29: Same as Figure A.26 for Kiruna.

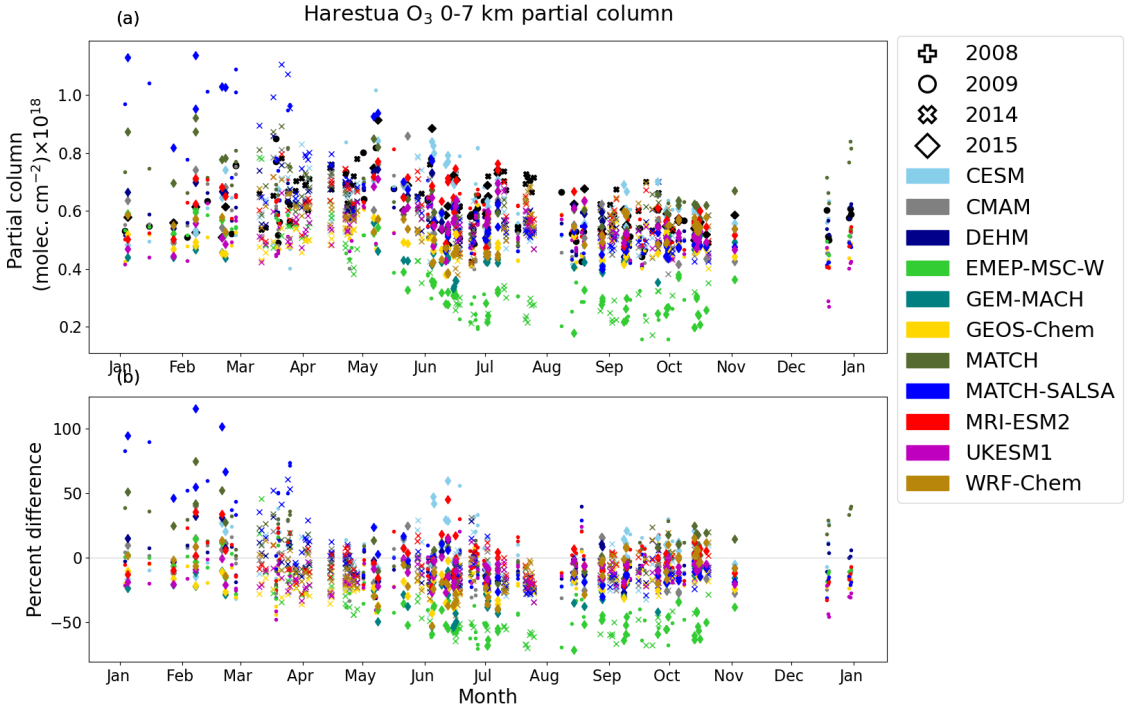

Figure A.30: Same as Figure A.26 for Harestua.

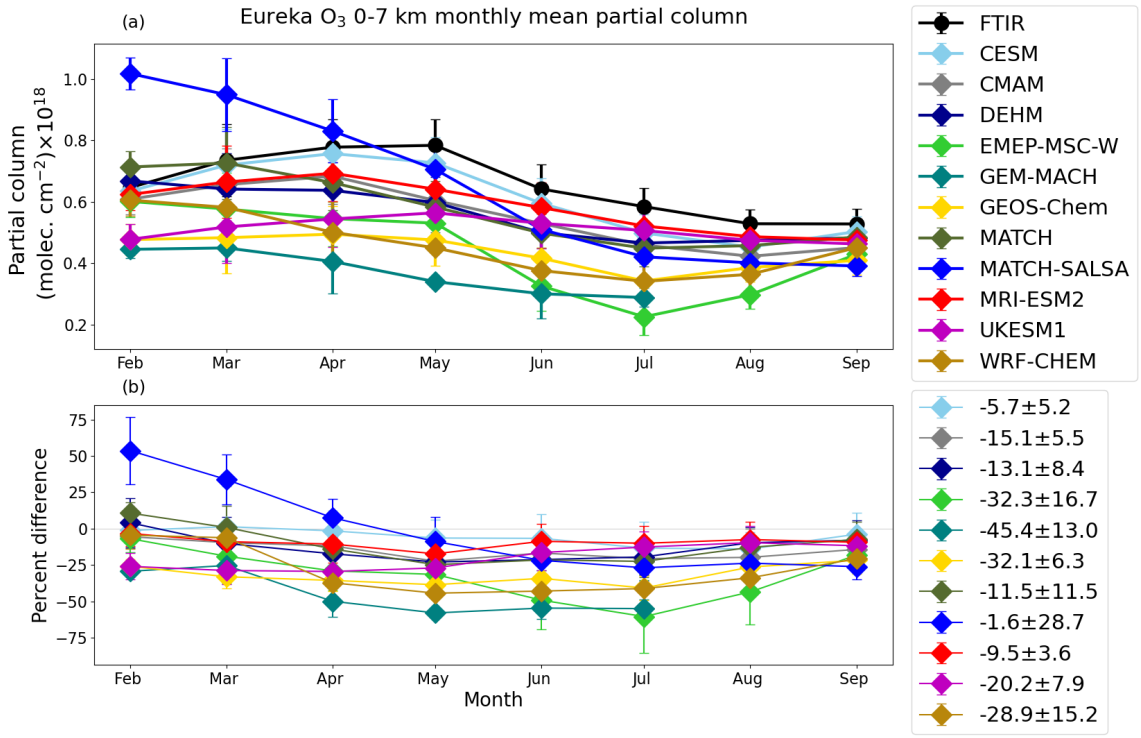

Figure A.31: (a) Monthly mean FTIR (black) and smoothed model (colour) 0-7 km partial columns of O_3 ($PC_{F,monthly,j}$ and $PC_{M,monthly,j}$, respectively), from Eureka using model data that are the nearest in time to each FTIR measurement shown in Figure A.26. Error bars represent the standard deviation of the monthly mean. (b) Model-measurement mean percent difference by month ($\Delta_{monthly,j}$). Error bars represent standard deviation of the monthly mean percent difference. The legend on panel (b) shows the overall mean percent difference (Δ_O) with the standard deviation of the overall mean percent difference.

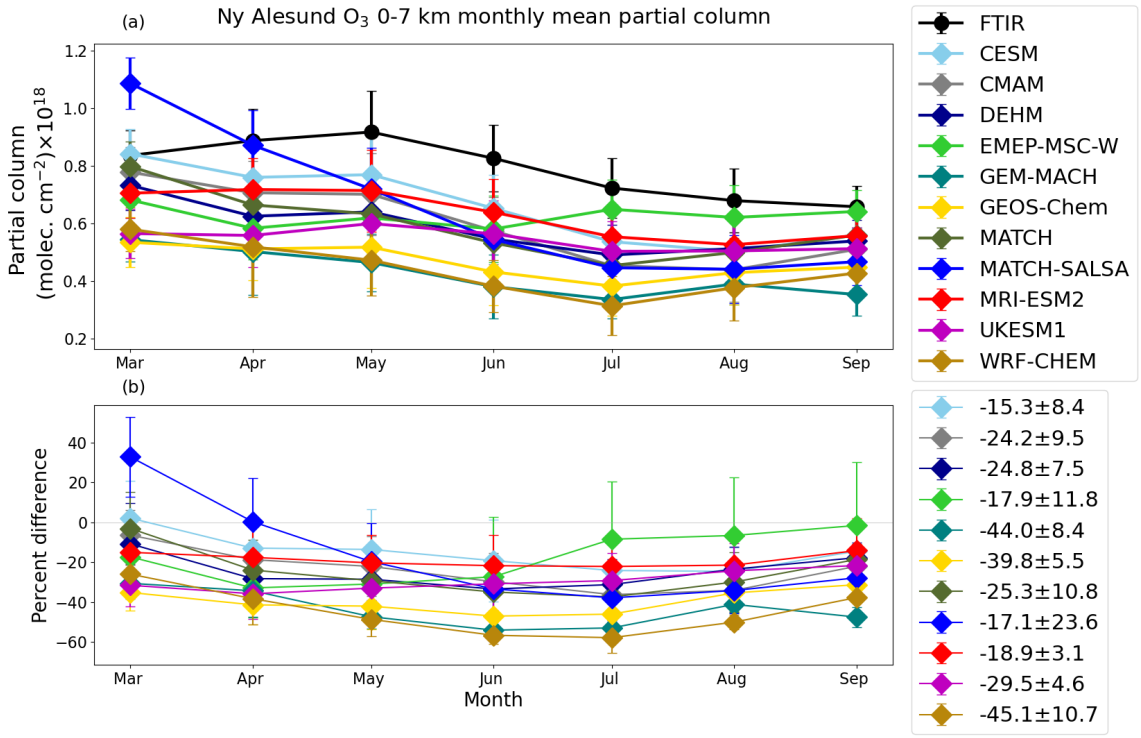

Figure A.32: Same as Figure A.31 for Ny Ålesund.

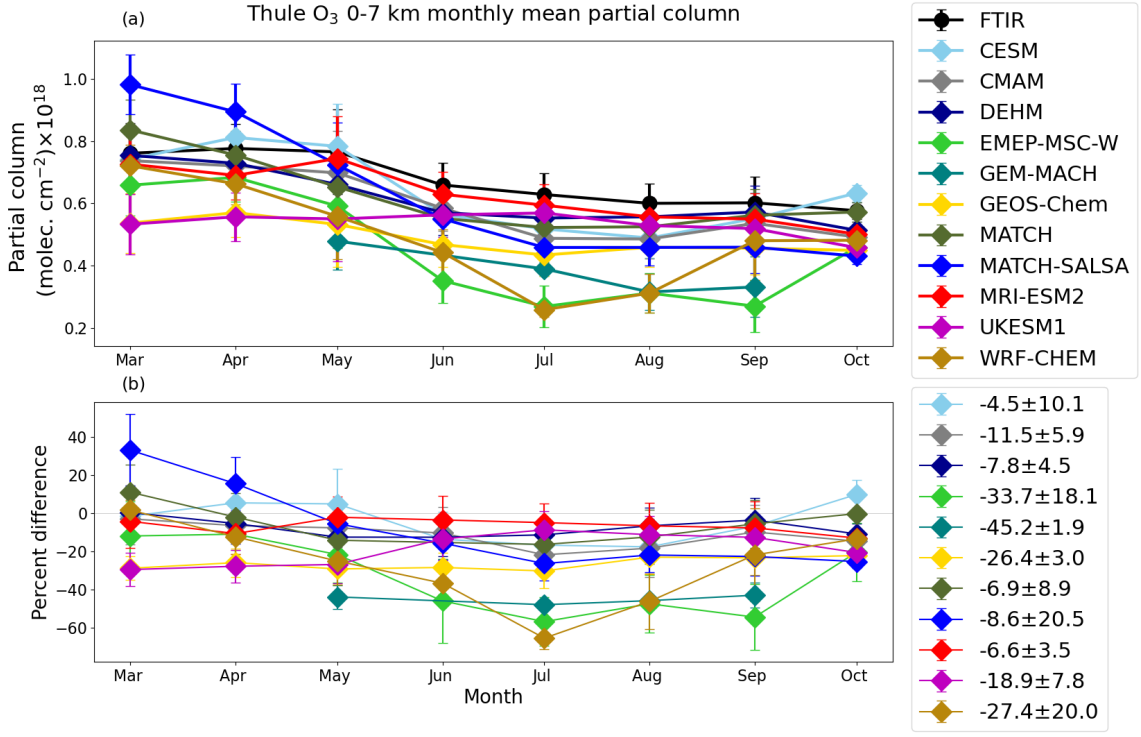

Figure A.33: Same as Figure A.31 for Thule.

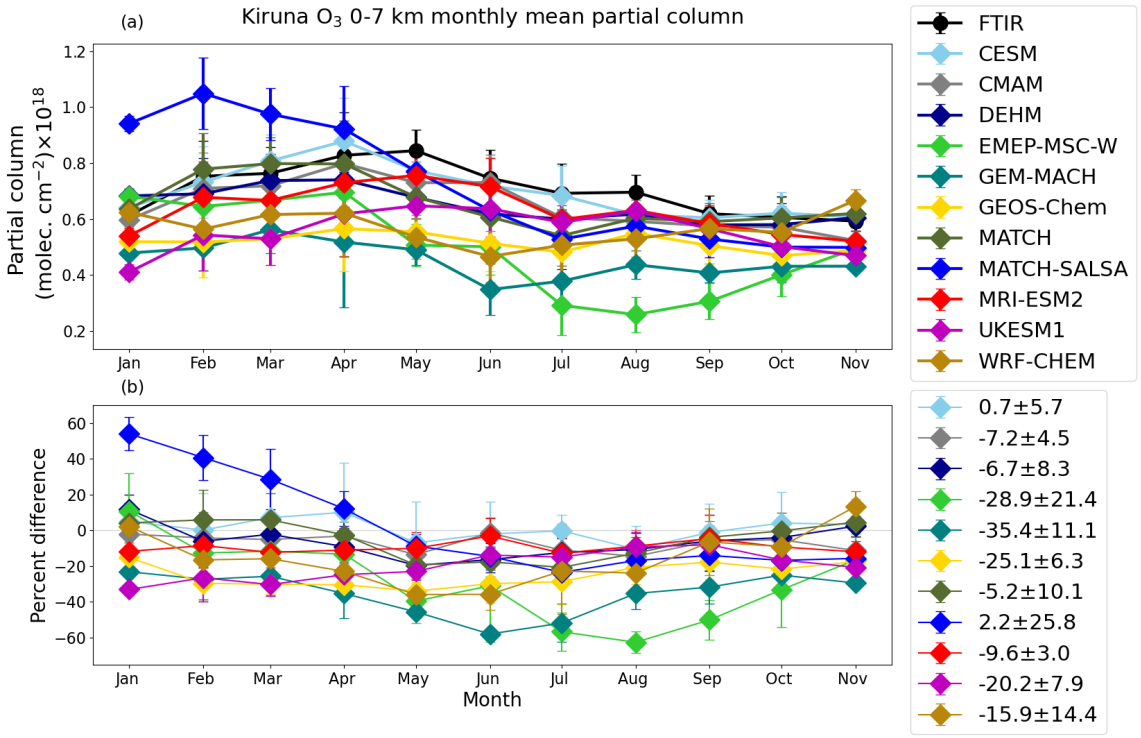

Figure A.34: Same as Figure A.31 for Kiruna.

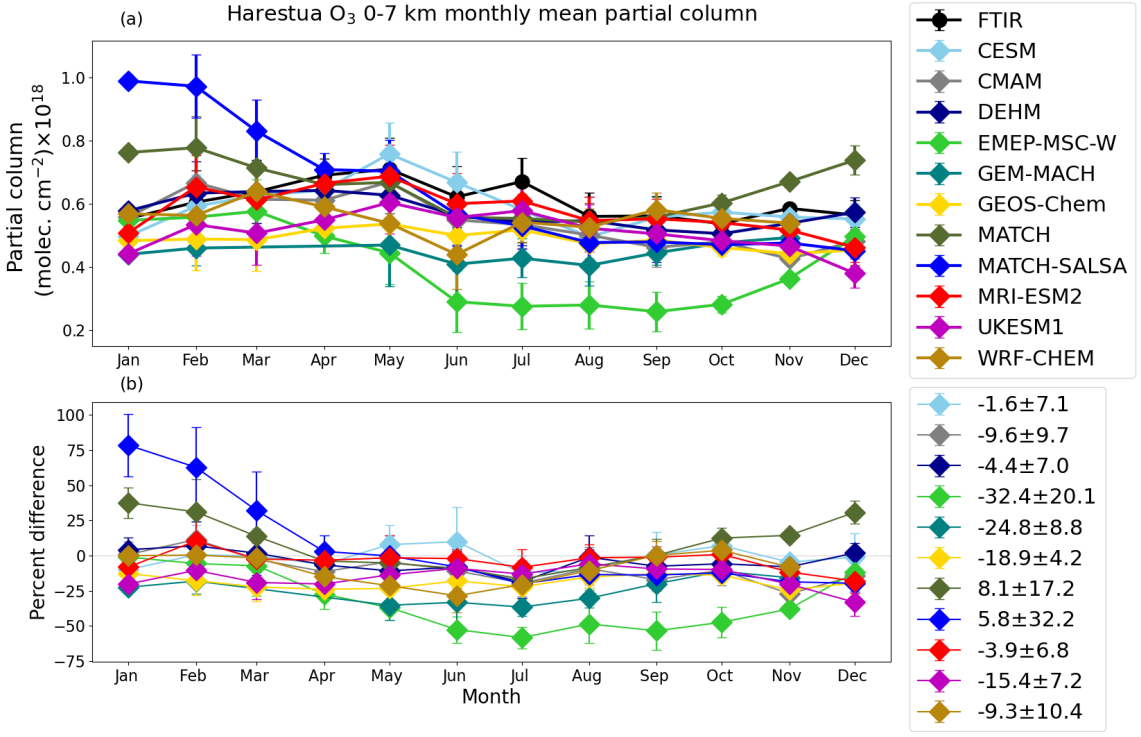

Figure A.35: Same as Figure A.31 for Harestua.

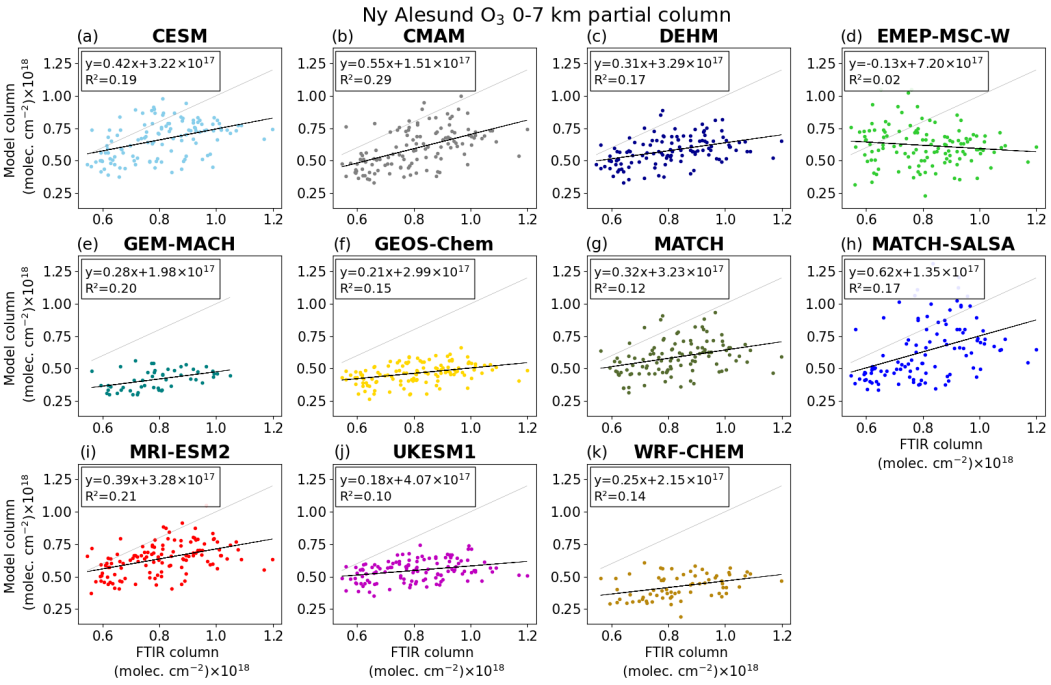

Figure A.36: Smoothed model vs. FTIR 0-7 km partial column of O_3 for Ny Ålesund, showing all available model-FTIR corresponding data. The black line is the line of best fit, where the equation and R^2 are noted in the legend. The 1:1 line is shown in light grey.

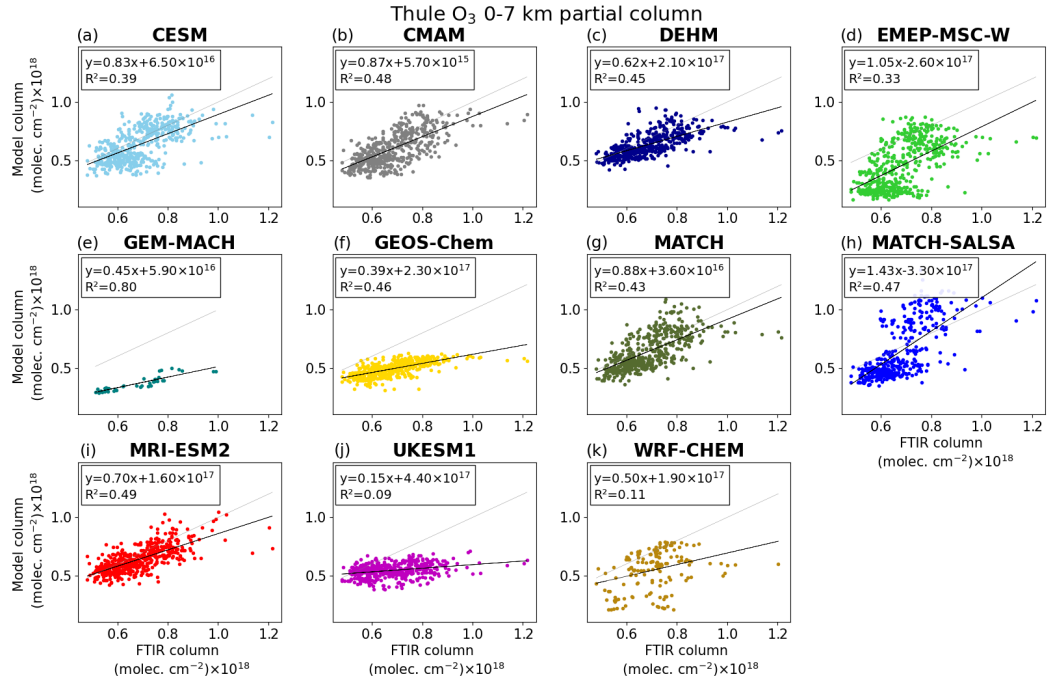

Figure A.37: Same as Figure A.36 for Thule.

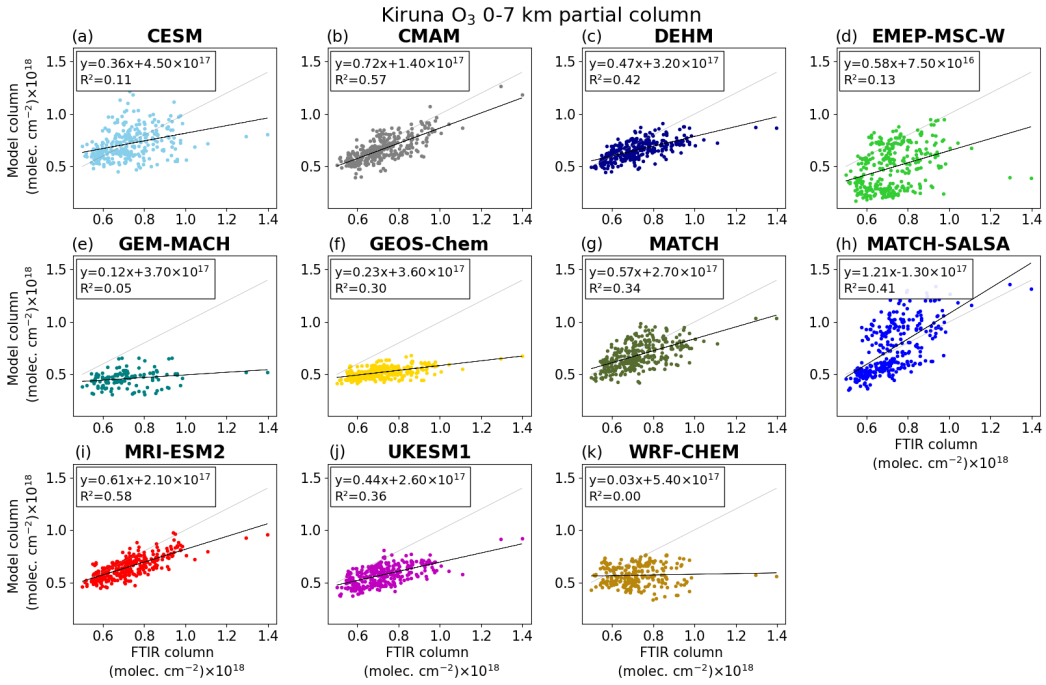

Figure A.38: Same as Figure A.36 for Kiruna.

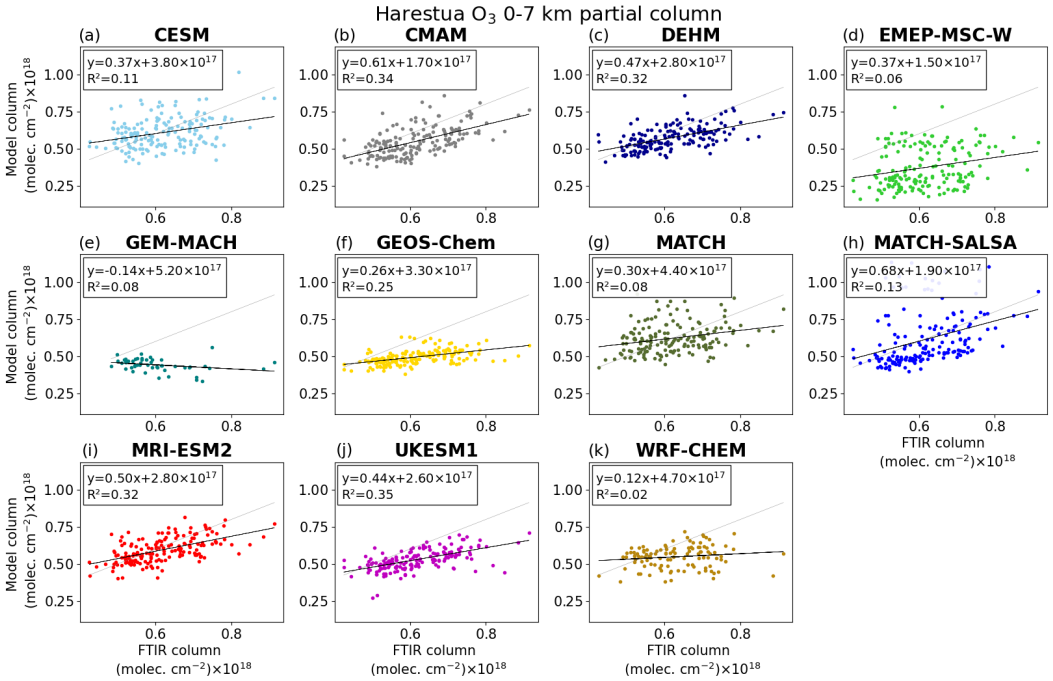

Figure A.39: Same as Figure A.36 for Harestua.

B. Appendix for Chapter 5

This appendix contains supplementary tables and figures for Chapter 5 to provide more context regarding the air quality throughout the summer of 2023. Tables B.1-B.3 provide information about the AQHI over the summer; the mean tropospheric and surface measurements of pollutants in the past, for 2023 and during the events; and comparisons of the enhancement ratios (shown in Figure B.9). Figures B.1-B.6 show the summer 2023 time series for the species for which enhancement ratios are reported. Figure B.7 shows the OMECP AQHI during the peak time of events across Ontario. Figure B.8 shows the HYSPLIT back-trajectories for CARE during the peak event times. Figure B.10 shows the summer of 2023 time series from the OMECP surface readings of CO, O_3 and $PM_{2.5}$. Figures B.11 and B.12 show measurement vs model regressions for the comparisons presented in Section 5.4.3.1 and 5.4.3.2, respectively.

Table B.1: For each defined event, AQHI readings from Downtown Toronto, indicating the maximum value reached, the number of days which reached "moderate risk" and the number of days which reached "high risk".

Event		Maximum AQHI	Number of Days with Moderate Risk	# of Days with High Risk
1	May 16 – 23, 2023	5	6	0
2	June 3 – June 9, 2023	6	5	0
3	June 17 – June 30, 2023	9	9	3

Table B.2: Mean summer (May-September) CO, O_3 and $PM_{2.5}$ values from the TAO FTIR and OMECP in situ instruments comparing the previous five years (2018-2022) and 2023. Where the difference is [100({2023 mean (total or event)/ five-year summer mean}-1)].*

Pollutant	Source	Five-year Summer Mean (2018-2022)	2023 Summer Mean	Difference	2023 Events Mean	Difference
CO	TAO FTIR (10 km partial column)	1.80 x10^{18} molec. cm^{-2}	2.28 x10^{18} molec. cm^{-2}	27% higher	2.53 x10^{18} molec. cm^{-2}	40% higher
	TOR. West OMECP (surface)	0.23 ppm	0.30 ppm	30% higher	0.32 ppm	39% higher
O_3	TAO FTIR (10 km partial column)	1.05 x10^{18} molec. cm^{-2}	1.10 x10^{18} molec. cm^{-2}	4% higher	1.22 x10^{18} molec. cm^{-2}	16% higher
	TOR. DT. OMECP (surface)	27.9 ppbv	31.4 ppbv	12% higher	30.3 ppbv	9% higher
	Barrie OMECP (surface)	25.9 ppbv	26.4 ppbv	2% higher	30.6 ppbv	18 % higher
$PM_{2.5}$	TOR. DT. OMECP (surface)	8.16 μg/m^{-3}	10.6 μg/m^{-3}	30% higher	16.5 μg/m^{-3}	202 % higher
	Barrie OMECP (surface)	6.92 μg/m^{-3}	12.0 μg/m^{-3}	73% higher	21.0 μg/m^{-3}	303% higher

Table B.3: Comparison between enhancement ratios (slope) and respective R values for the Events individually (Figure 5.6) and together (Figure B.9). Note. The box is green if the slope/R value is higher for the event compared to the combined value, yellow if it is the same, and red if it is lower.

Gas	Slope				R-value			
	Combined	Event 1	Event 2	Event 3	Combined	Event 1	Event 2	Event 3
C_2H_6	0.005	0.009	0.004	0.003	0.49	0.52	0.46	0.36
CH_3OH	0.017	0.028	0.016	0.021	0.79	0.82	0.64	0.87
HCN	0.003	0.006	0.003	0.003	0.65	0.52	0.51	0.77
HCOOH	0.013	0.030	0.012	0.013	0.67	0.86	0.66	0.87
NH_3	0.003	0.017	0.006	0.002	0.34	0.47	0.64	0.42
O_3	0.07	-0.199	-0.207	0.01	0.06	0.06	0.17	0.49

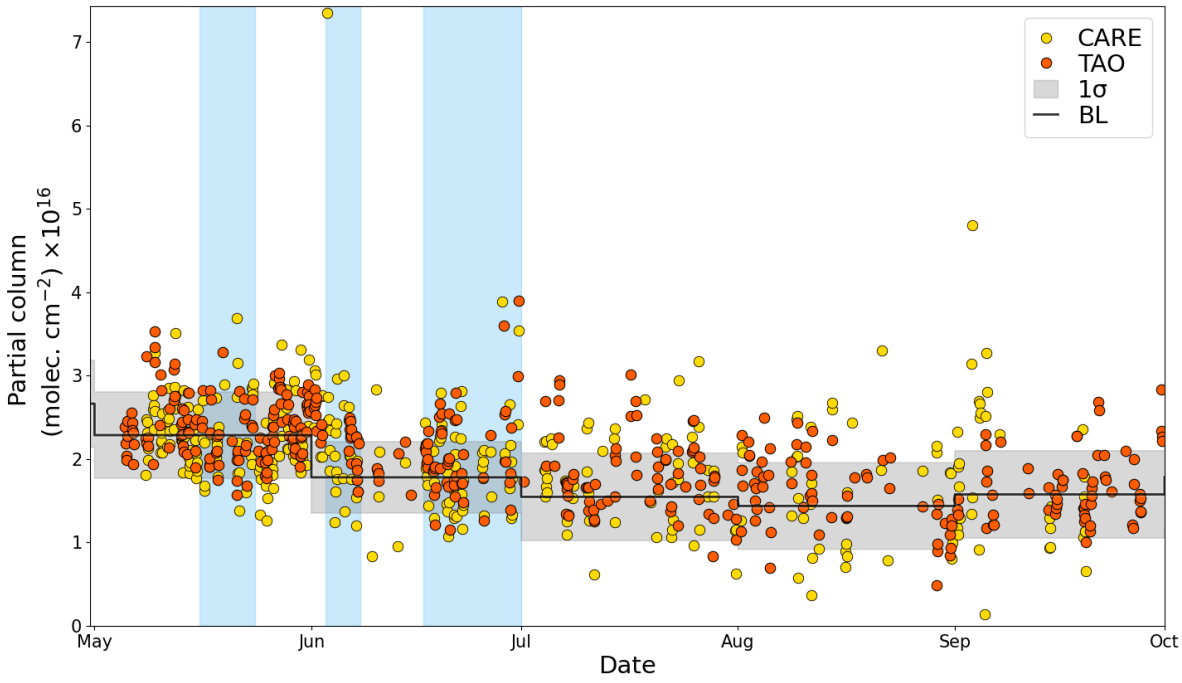

Figure B.1: 0-10 km partial column C_2H_6 from TAO (orange) and CARE (yellow) for 2023 with the TAO baseline (BL) (black line) ±1σ (grey shaded), and the time of the events marked with a blue shading.

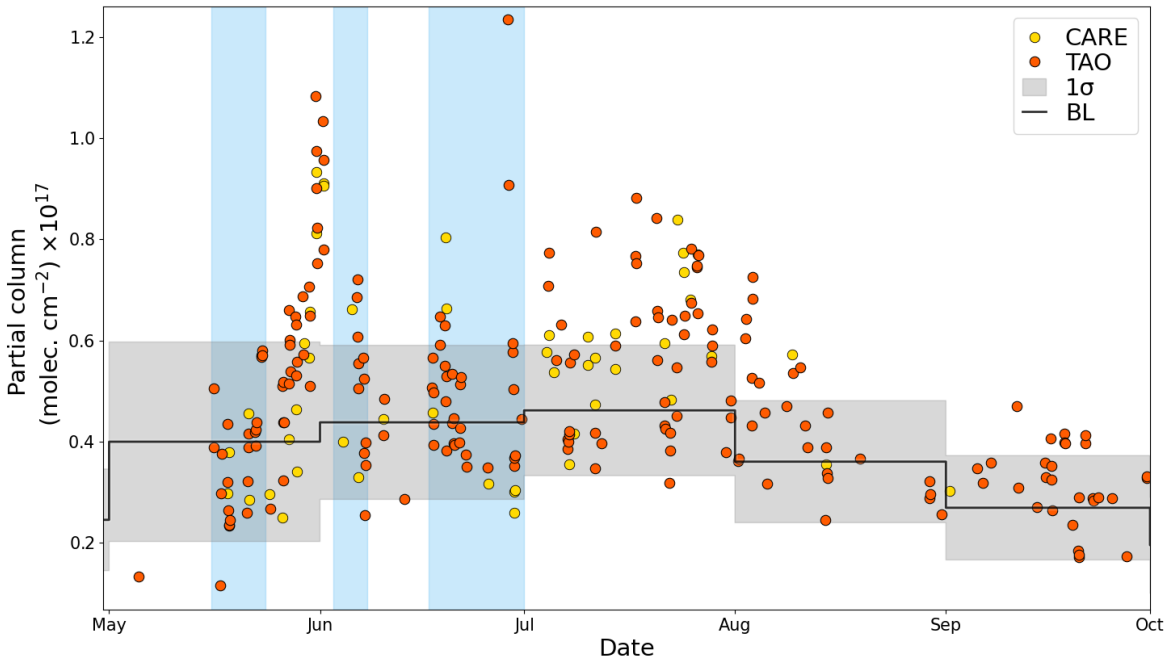

Figure B.2: Same as Figure B.1 for CH_3OH.

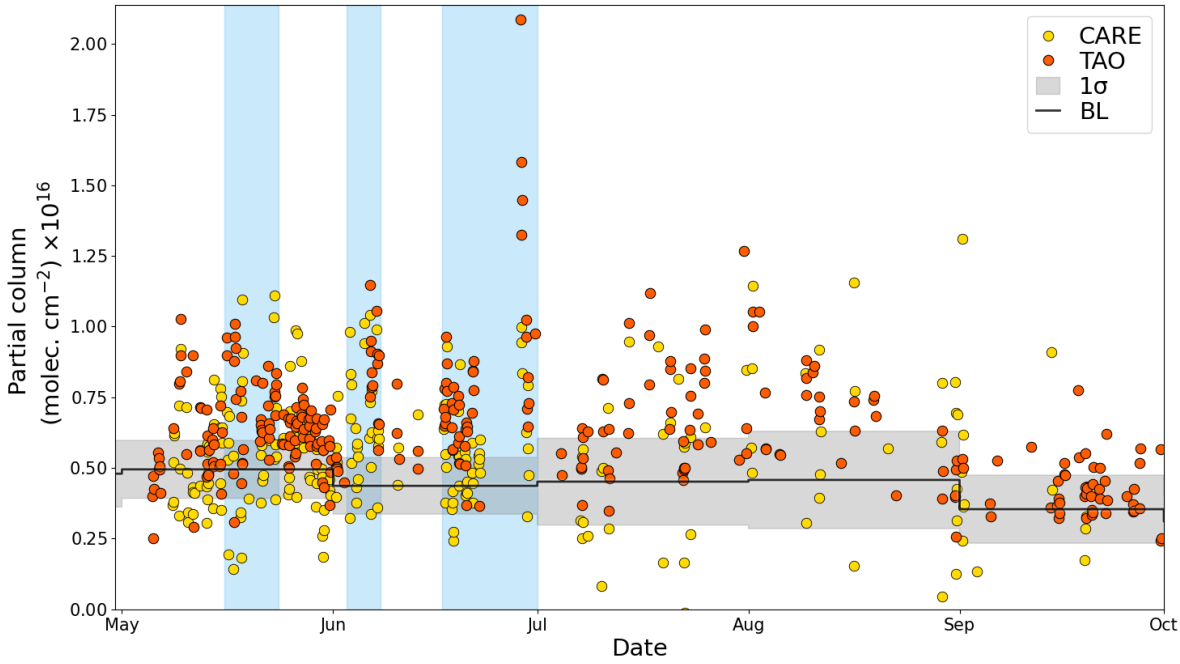

Figure B.3: Same as Figure B.1 for HCN.

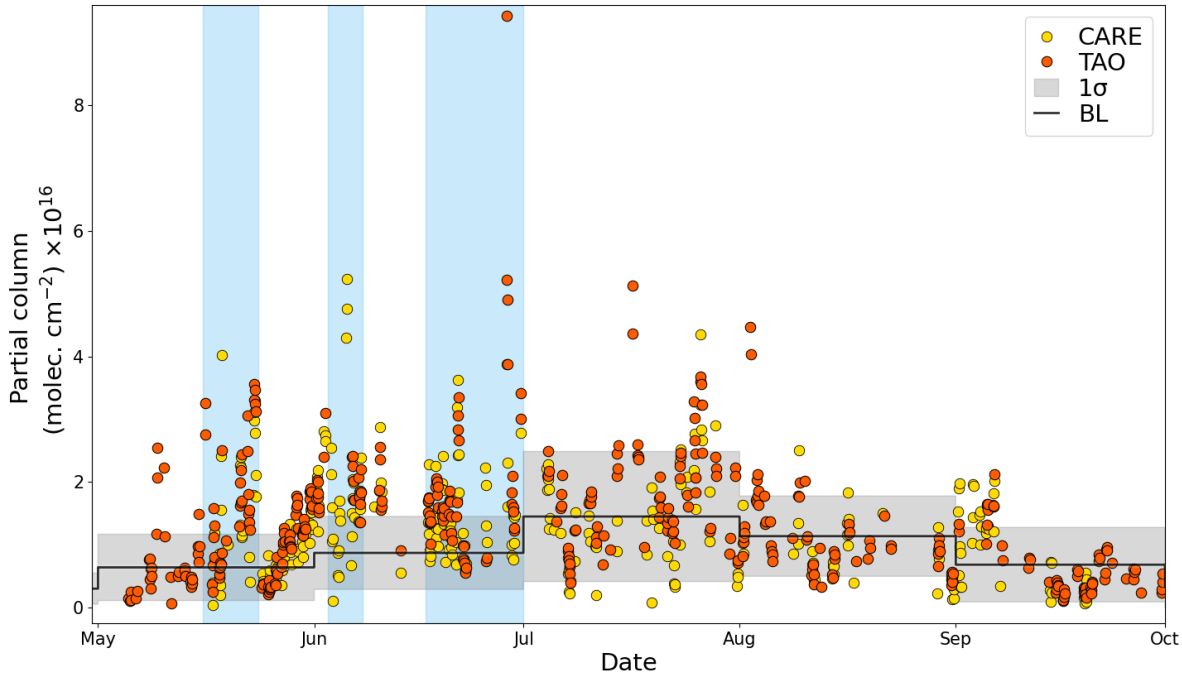

Figure B.4: Same as Figure B.1 for HCOOH.

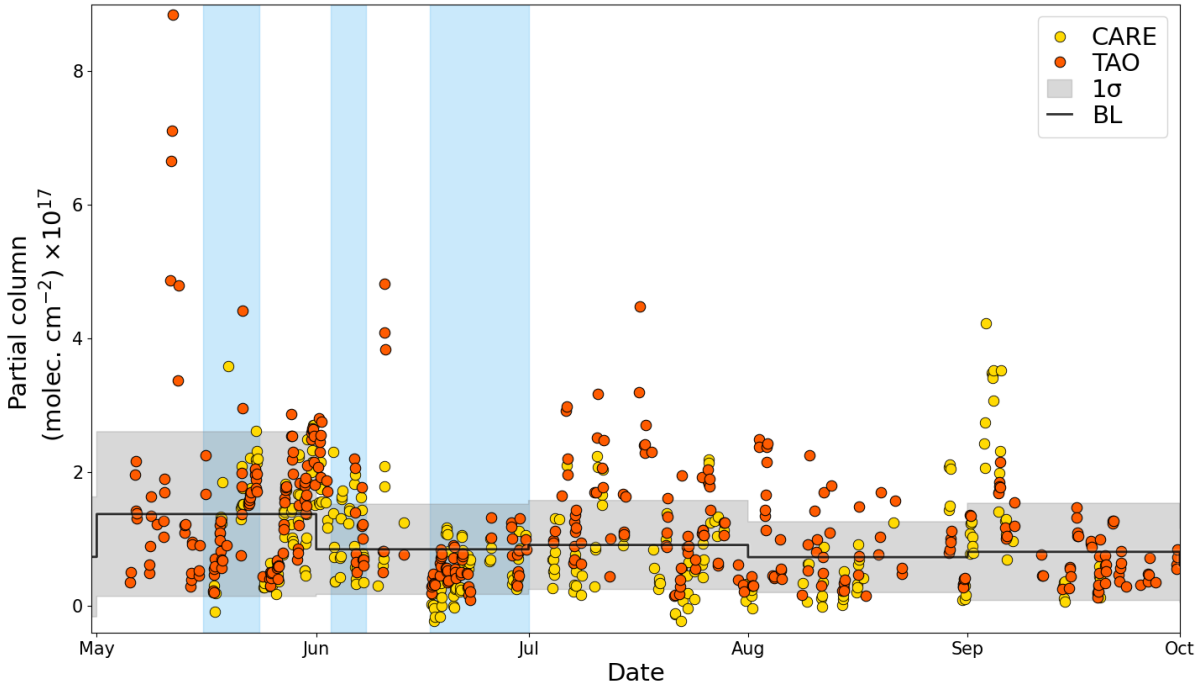

Figure B.5: Same as Figure B.1 for NH_3.

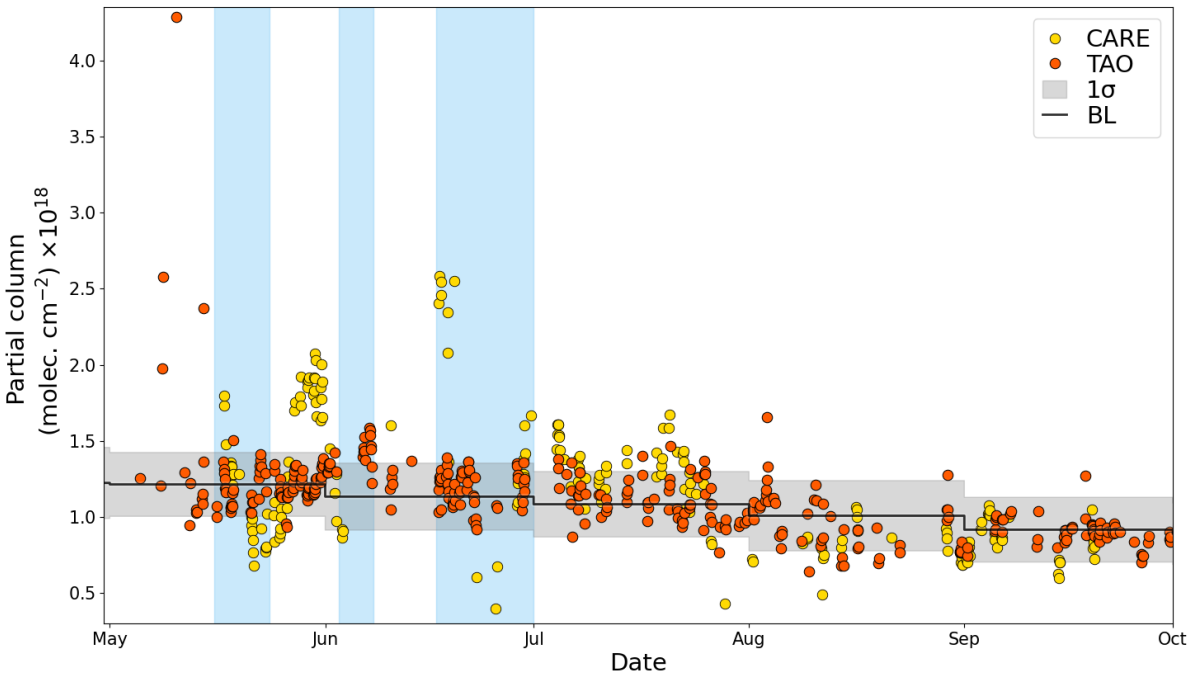

Figure B.6: Same as Figure B.1 for O_3.

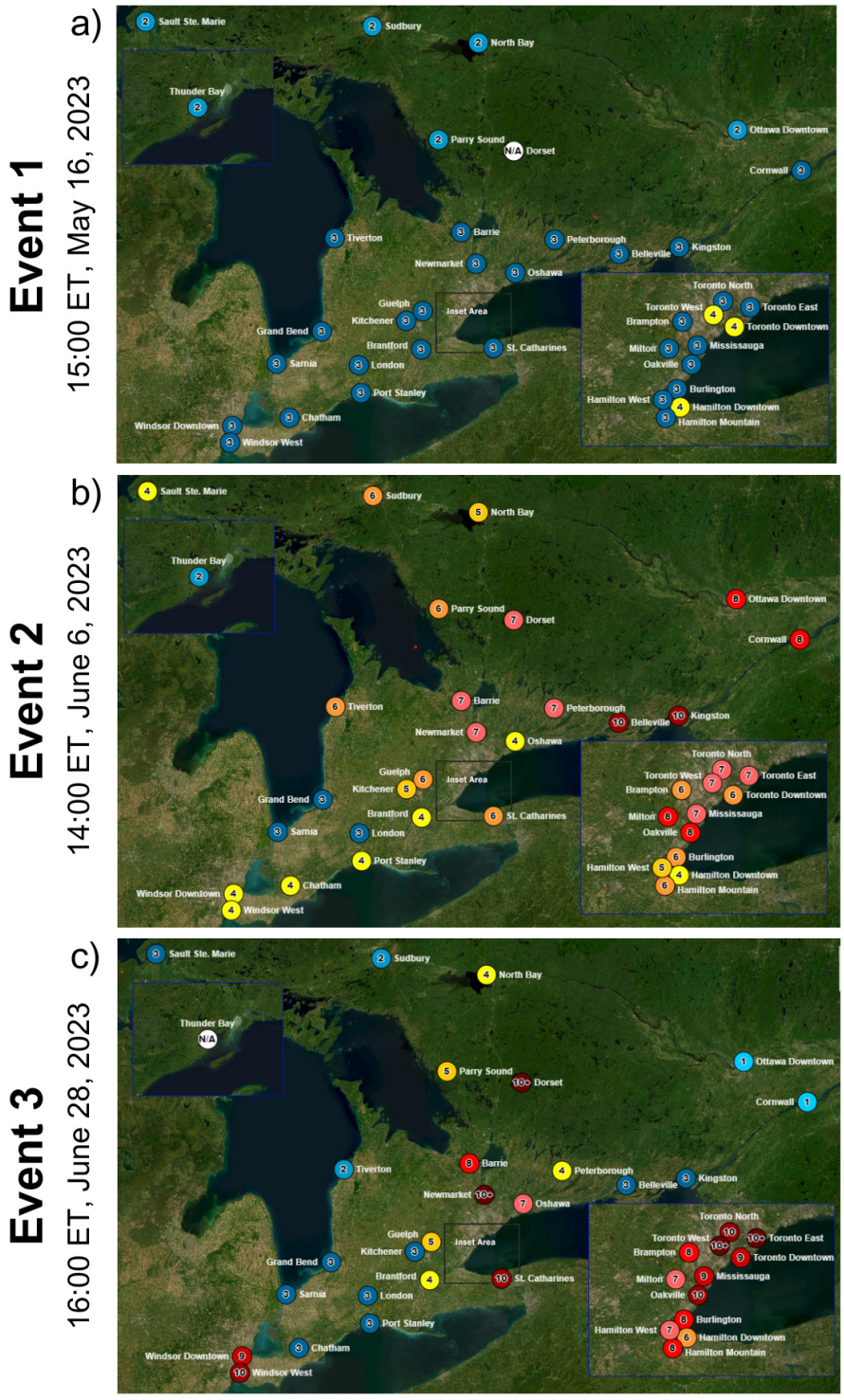

Figure B.7: OMECP AQHI readings for all Ontario stations, corresponding to the time of the HYSPLIT back-trajectory release (OMECP, 2024) for each of the three events.

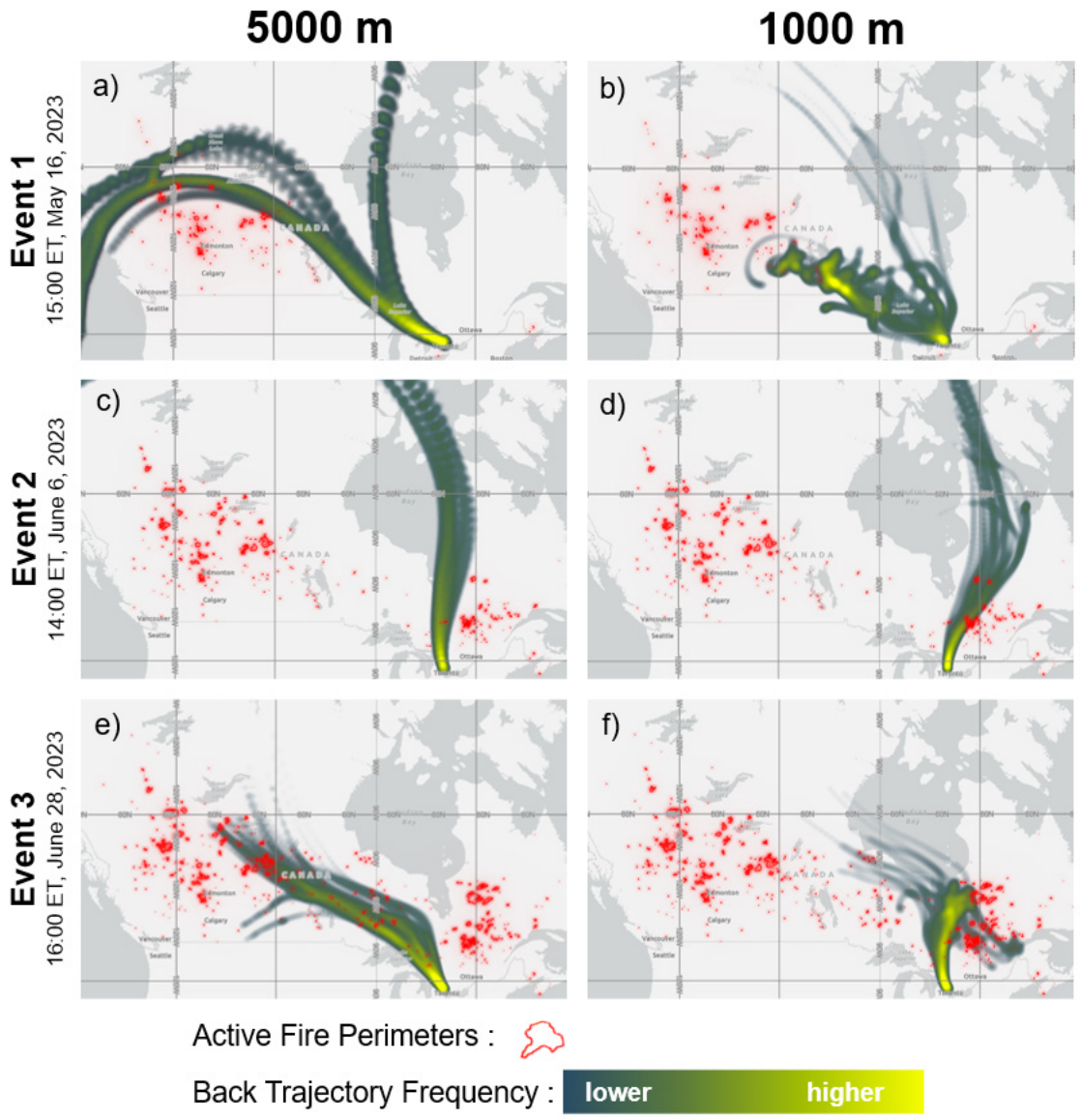

Figure B.8: HYSPLIT 72-hour ensemble back-trajectories, initiated from CARE at the times listed, from 5000 m (a, c, e) and 1000 m (b, d, f). Red polygons represent the active fires at the time (CWFIS, 2024; Esri, 2020).

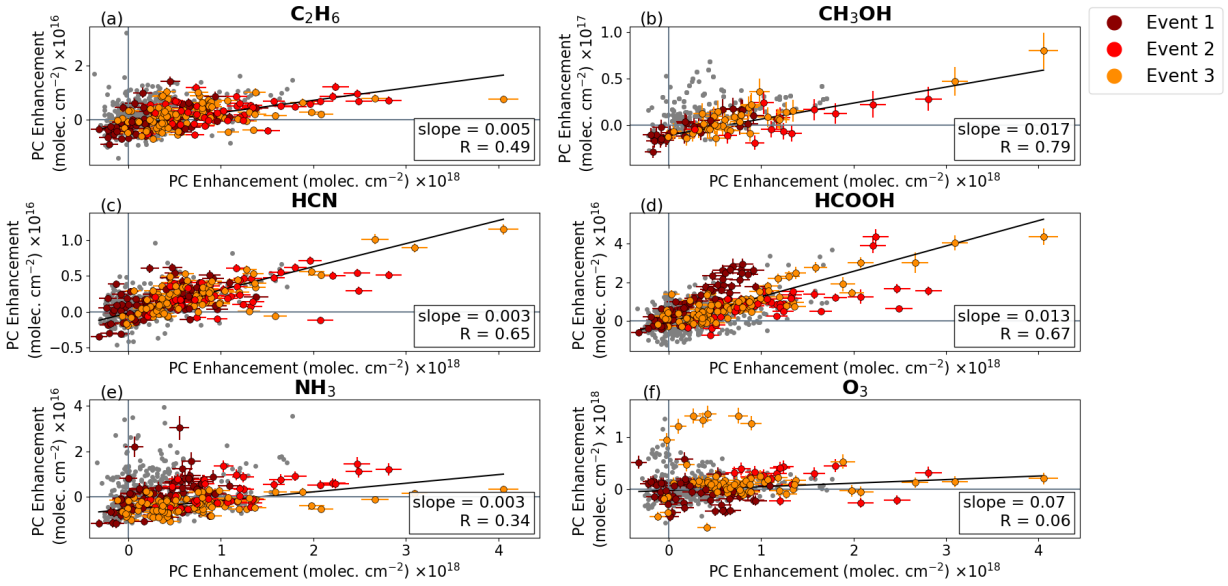

Figure B.9: 0-10 km partial column enhancement of biomass-burning-related species vs. CO (measured within ±3 hours) for TAO and CARE FTIR May - September 2023 (grey), with events marked by colour. Error-weighted slopes are shown for the combined TAO and CARE datasets with all events.

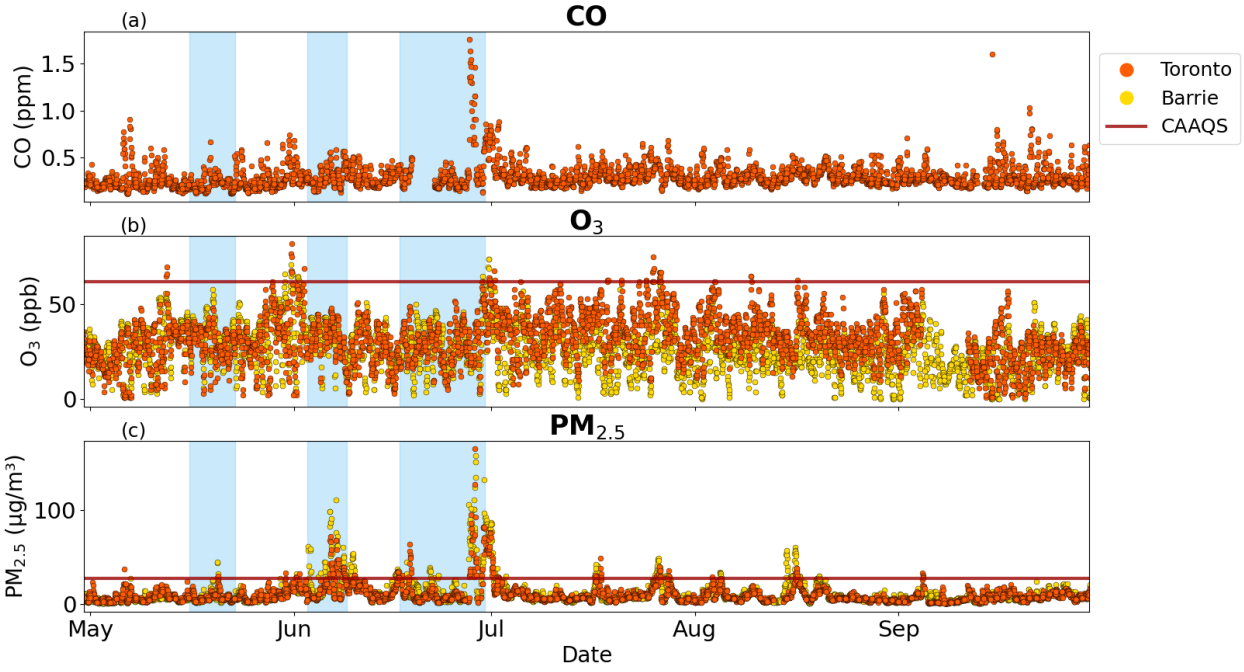

Figure B.10: OMECP surface CO, O_3, and $PM_{2.5}$ air quality readings for Toronto Downtown/West (orange) and Barrie (yellow), with the CAAQS marked in red.

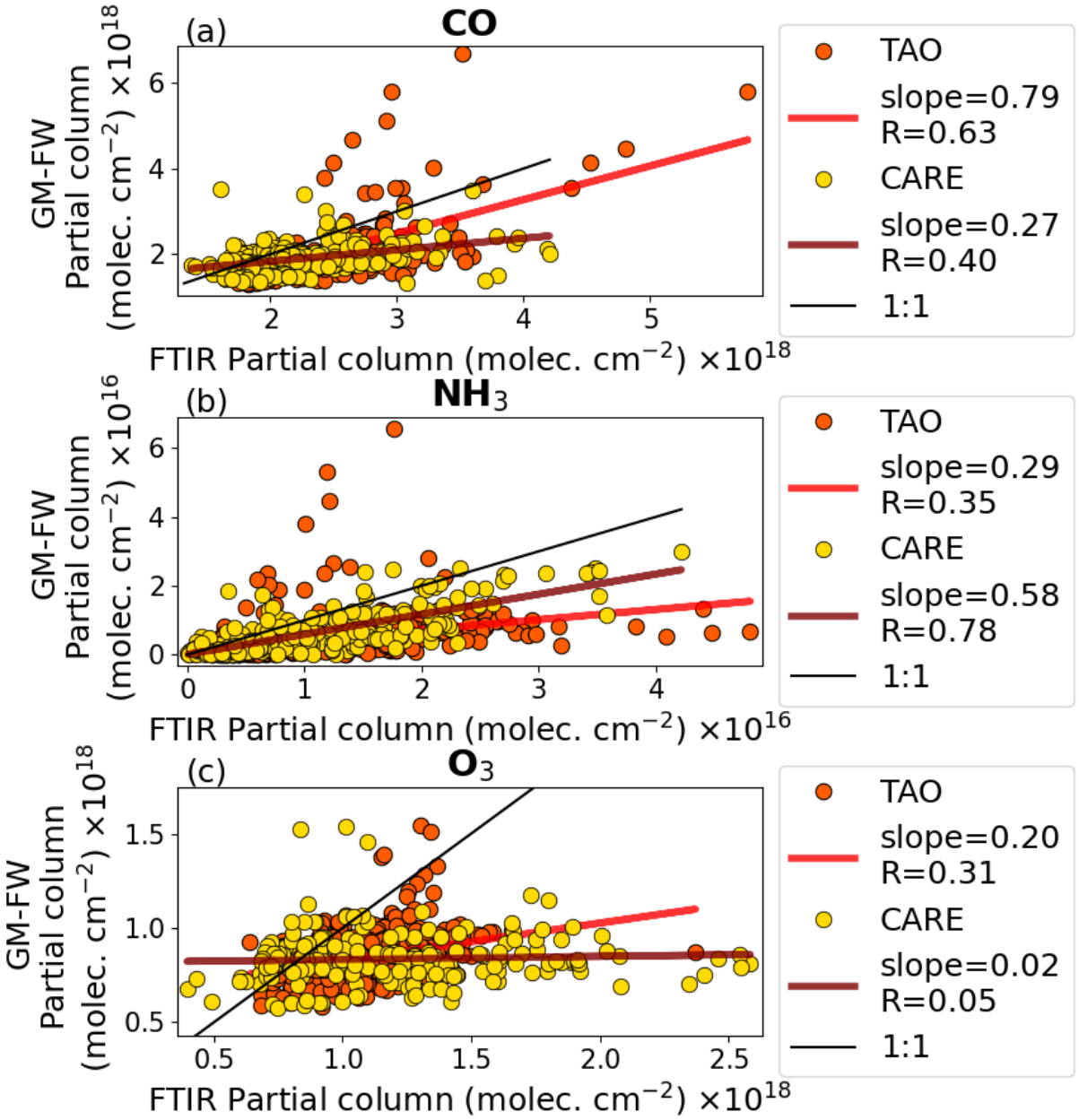

Figure B.11: (a) CO, (b) NH_3, and (c) O_3 0-10 km partial columns from GM-FW vs. FTIR at TAO (orange markers, red line) and CARE (yellow markers, maroon line), with a linear regression applied. The slope and R of each fit is given in the legend, and the black line represents 1:1.

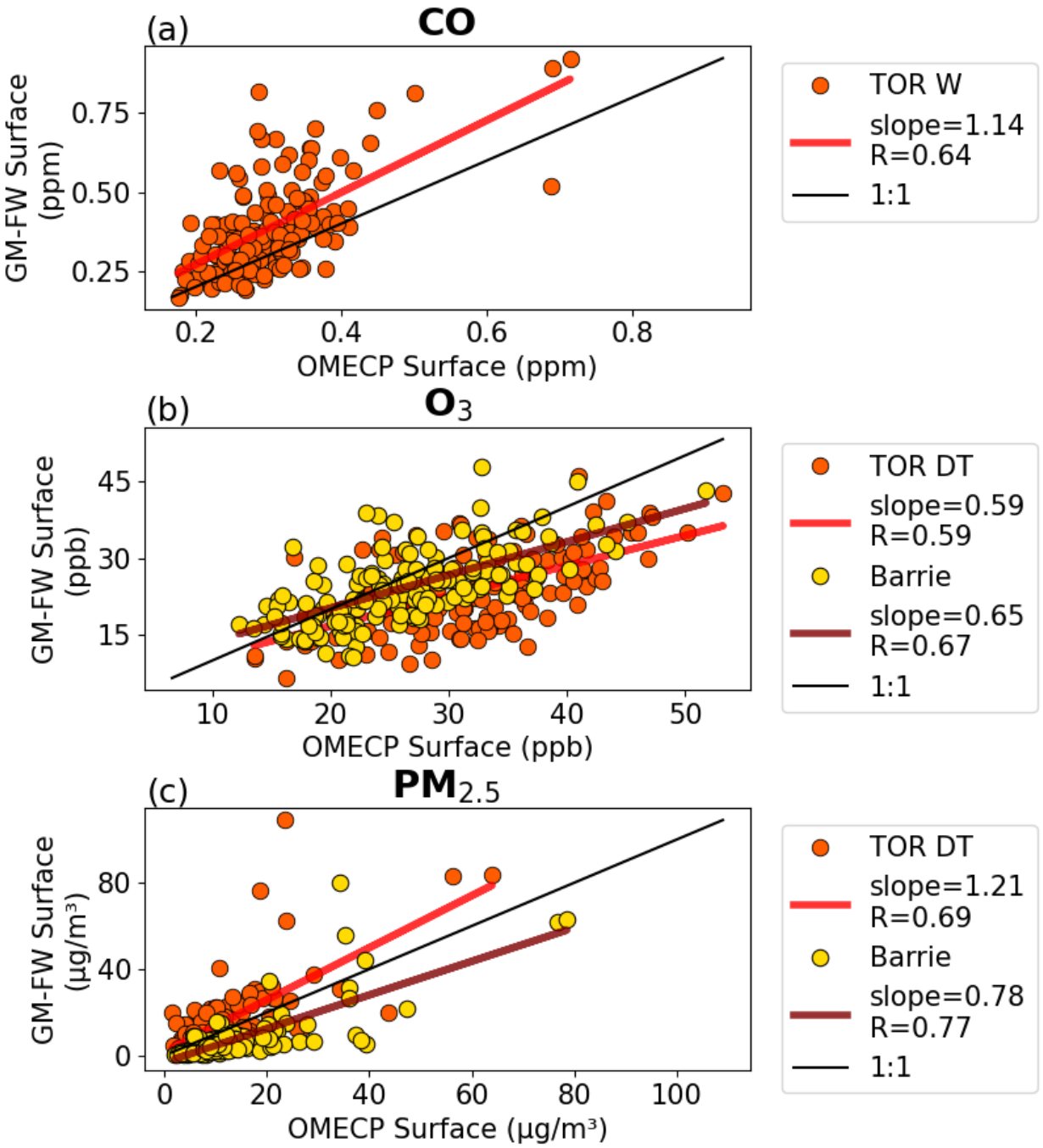

Figure B.12: (a) CO, (b) O_3 and (c) $PM_{2.5}$ daily mean surface measurements from GM-FW vs. OMECP at Toronto (orange markers, red line) and Barrie (yellow markers, maroon line), with a linear regression applied The slope and R of each fit is given in the legend and the black line represents 1:1.

C. Appendix for Chapter 6

This appendix contains additional context for the DiD analysis presented in Chapter 6. The DiD interpretation was done with the guidance of Grace Kuiper and Dr. Sheryl Magzamen from the Department of Environmental and Radiological Health Sciences, Colorado State University. The following section breaks down an example of the DiD for each variable and shows how a generalized interpretation of the numbers would follow; this text was not included in Flood et al. (2025b).

A difference-in-difference approach compares the trends between different groups; traditionally this would be a treatment and control group. Figure C.1 shows a graphical representation of a standard DiD where there are two groups before and after an intervention (CUMSPH, 2013). The difference in this application is that the x-axis would be XCO, the y-axis would be hospital admissions, and there would be one "pre intervention" group, which is the admissions prior to 2012, and one "post intervention" group, which would be the admissions post-2011.

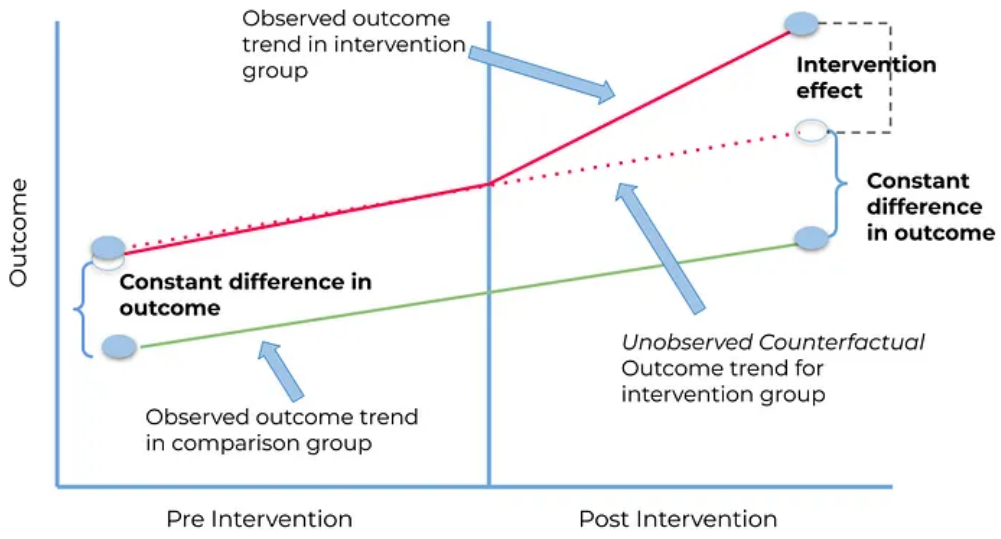

Figure C.1: Graphical example of comparison groups in a difference-in-difference approach. (CUMSPH, 2013).

The program used is the python statsmodel ols and was run individually for each disease and province (9 diseases × 2 provinces = 18 models). The program aims to predict a dependent variable (here N_{mR}) with the input of independent variables (the rest of the inputs listed) . It creates a line of best fit using an ordinary least squares function (Statsmodels, 2025).

The inputs:

- N_{mR} : a DataFrame that contains the number of hospitalizations for a disease in a particular health district in a month normalized to the is the dependent variable.
- X_{CO} : the average MOPITT XCO total column (detrended) for the respective month in the area of the health district.
- t : period that corresponds to the year of the respective data, if it is before pre-2012 it is 0, if it is 2012 and beyond it is 1.
- i_{co}: this term will be the product of $X_{CO} * t$, so either X_{CO} again or 0.
- m : this is an indicator for the month, it will be 1 for July, 2 for August, or 3 for September, depending on the respective data (N_{mR} and X_{CO}). This is not used as a number, this is used to distinguish between months as a variable.
- R: this will be a number between 1-7 for Ontario or 1-5 for Alberta, which indicates the health district that came N_{mR} from. This is not used as a number, this is used to distinguish between regions as a variable.

The outputs:

- Each coefficient describes how "one unit change" of the dependent variable will change the respective independent variable.
    - Each output has a p-value which indicates the chance of the independent variable having no impact on the dependent variable, ideally this should be less than 0.05 or 5%, and a 95% confident interval that indicates the bounds which 95% of the values are within, and to be significant will not contain a null value.
- β_0: this is the intercept of the formulated equation, it does not provide information towards the analysis of coefficients
- β_1: This is used as the exposure metric, it corresponds to the change in hospitalizations for 1 ppbv increase in XCO when the period is pre-2012 (see Equation 6.2).

- An example of an interpretation of a significant coefficient would be if $\beta_1 = -0.52$ - "Before 2012, an increase in XCO by 1ppbv is associated with a decrease in monthly hospitalizations due to arrhythmia by 0.52 per 100,000 people in Alberta."

- β_2: This is the change in hospitalization post-2012 vs pre-2012 when XCO is held constant (see Equation 6.3).

  - An example of an interpretation of a significant coefficient would be if $\beta_2 = -10.41$: "When XCO is constant, there are 10.41 fewer monthly hospitalizations per 100,000 people due to cerebrovascular disease in Ontario, after 2012 than there were before 2012."

- β_3: This is the change in hospitalization from 1ppbv increase in XCO post- vs pre-2012 (see Equation 6.4)

  - An example of an interpretation of a significant coefficient would be if $\beta_3 = 0.308$: "The effect on monthly asthma hospitalization in Ontario of a 1ppbv increase in XCO is 0.308 per 100,000 people more after 2012 versus before 2012."

- The number that is of interest to the interpretation of these results is $\beta_3 + \beta_1$; this is what is described in the analysis and dictates if there is a change in frequency of hospitalization between the two time periods. β_3 needs to be positive, and larger in magnitude than β_1 for there to be an attenuation of hospitalizations associated with an increase in XCO between the time period of before 2012 and after 2012. The instances of these are marked in Table 6.3 with a green asterisk (*) i_{co} term.

  - An example of an interpretation of a significant coefficient would be if $\beta_1 = -1.72$ and $\beta_3 = 1.8755$: "The effect on monthly hypertension hospitalization in Ontario from a 1 ppbv increase in XCO after 2012 is 0.16 more per 100,000 people, the positive outcome between $\beta_3 + \beta_1$ indicates an inverse in the relationship from before 2012 and after 2012."

- β_4: there is a value for the month August and September, these coefficients are compared to July, as the first month input. The term does not interact with other covariates so it can be interpreted independently of the others.
    - An example of an interpretation of a significant coefficient would be if $\beta_4\ [T.9] = 25.83$: "Holding health region, XCO and pre- vs post-2012 constant, September had 25.83 hospitalizations per 100,000 people per month more due to asthma than August."
- β_5: there is a value for n-1 health regions input, similar to the months, these are each compared to whatever health region was input as number 1. The term does not interact with other covariates so it can be interpreted independently of the others.
    - An example of an interpretation of a significant coefficient would be if $\beta_5\ [T.2] = -95.14$: "Holding month, XCO and pre- vs post-2012 constant, Alberta health region #2 had 95.1 hospitalizations per 100,000 people per month less due to arrhythmia than Alberta health region #1."

The following section shows an example of how the DiD model assesses the beta coefficient β_1, β_2 , and β_3. The independent variables are changed by a factor of 1, while holding the other variables constant, to assess the resulting change in hospitalizations. The grey terms correspond to the terms that are cancelled out within the calculation (following the line above it).

$$N_{mR} = \beta_0 + \beta_1 X_{CO} + \beta_2 t + \beta_3 i_{co} + \beta_4 m + \beta_5 R \tag{C.1}$$

Looking at β_1 through a change in XCO by 1 ppbv, while everything else is held constant:

$$\Delta hospitalizations = [\beta_0 + \beta_1(X_{CO} + 1) + \beta_2[0] + \beta_3(X_{CO} + 1)[0] + \beta_4 m + \beta_5 R]$$

$$- [\beta_0 + \beta_1(X_{CO}) + \beta_2[0] + \beta_3(X_{CO})[0] + \beta_4 m + \beta_5 R]$$

$$\Delta hospitalizations = [\ \beta_0 + \beta_1(X_{CO} + 1) + \beta_2[0] + \beta_3(X_{CO} + 1)[0] + \beta_4 m + \beta_5 R]$$

$$- [\beta_0 + \beta_1(X_{CO}) + \beta_2[0] + \beta_3(X_{CO})[0] + \beta_4 m + \beta_5 R]$$

$$\Delta hospitalizations = \beta_1(X_{CO} + 1) - \beta_1(X_{CO})$$

$$\Delta hospitalizations = \beta_1 \tag{C.2}$$

Looking at β_2 through a change in period before [0] or after 2012 [1], while everything else is held constant:

$$\Delta hospitalizations = [\beta_0 + \beta_1[0] + \beta_2[1] + \beta_3[0][1] + \beta_4 m + \beta_5 R]$$

$$- [\beta_0 + \beta_1[0] + \beta_2[0] + \beta_3[0][0] + \beta_4 m + \beta_5 R]$$

$$\Delta hospitalizations = [\beta_0 + \beta_1[0] + \beta_2[1] + \beta_3[0][1] + \beta_4 m + \beta_5 R]$$

$$- [\beta_0 + \beta_1[0] + \beta_2[0] + \beta_3[0][0] + \beta_4 m + \beta_5 R]$$

$$\Delta hospitalizations = \beta_2[1]$$
$$\Delta hospitalizations = \beta_2 \quad (C.3)$$

Looking at β_3 through a change in 1 ppbv XCO when the period is after, while everything else is held constant:

$$\Delta hospitalizations = [\beta_0 + \beta_1(X_{CO} + 1) + \beta_2[1] + \beta_3(X_{CO} + 1)[1] + \beta_4 m + \beta_5 R]$$

$$- [\beta_0 + \beta_1(X_{CO}) + \beta_2[1] + \beta_3(X_{CO})[1] + \beta_4 m + \beta_5 R]$$

$$\Delta hospitalizations = [\beta_0 + \beta_1(X_{CO} + 1) + \beta_2[1] + \beta_3(X_{CO} + 1)[1] + \beta_4 m + \beta_5 R]$$

$$- [\beta_0 + \beta_1(X_{CO}) + \beta_2[1] + \beta_3(X_{CO})[1] + \beta_4 m + \beta_5 R]$$

$$\Delta hospitalizations = \beta_1(X_{CO} + 1) + \beta_3(X_{CO} + 1)[1] - \beta_1(X_{CO}) - \beta_3(X_{CO})[1]$$
$$\Delta hospitalizations = \beta_1 + \beta_3 \quad (C.4)$$

References

Adams, C., McLinden, C. A., Shephard, M. W., Dickson, N., Dammers, E., Chen, J., Makar, P., Cady-Pereira, K. E., Tam, N., Kharol, S. K., Lamsal, L. N., and Krotkov, N. A. (2019). Satellite-derived emissions of carbon monoxide, ammonia, and nitrogen dioxide from the 2016 Horse River wildfire in the Fort McMurray area. Atmospheric Chemistry and Physics, 19, 2577–2599. https://doi.org/10.5194/acp-19-2577-2019

AHS - Alberta Health Services: Publications (2024). Available at: https://www.albertahealthservices.ca/scns/publications.aspx (last access: 30 August 2024).

Amann, M., Bertok, I., Borken-Kleefeld, J., Cofala, J., Heyes, C., Höglund-Isaksson, L., Klimont, Z., Nguyen, B., Posch, M., Rafaj, P., Sandler, R., Schöpp, W., Wagner, F., and Winiwarter, W. (2011). Cost-effective control of air quality and greenhouse gases in Europe: Modeling and policy applications. Environmental Modelling and Software : With Environment Data News, 26(12), 1489–1501. https://doi.org/10.1016/j.envsoft.2011.07.012

AMAP (2021). AMAP Assessment 2021: Impacts of Short-lived Climate Forcers on Arctic Climate, Air Quality, and Human Health. Arctic Monitoring and Assessment Programme (AMAP), Tromsø, Norway, viii + 324pp, https://www.amap.no/documents/doc/amap-assessment-2021-impacts-of-short-lived-climate-forcers-on-arctic-climate-air-quality-and-human-health/3614

Anderson, K., Chen, J., Englefield, P., Griffin, D., Makar, P., and Thompson, D. (2024). The Global Forest Fire Emissions Prediction System version 1.0, Geoscientific Model Development, 17, 7713–7749, https://doi.org/10.5194/gmd-17-7713-2024

Andersson, C., Langner, J., and Bergstroumm, R. (2007). Interannual variation and trends in air pollution over Europe due to climate variability during 1958-2001 simulated with a regional CTM coupled to the ERA40 reanalysis. Tellus. Series B, Chemical and Physical Meteorology, 59(1), 77–98. https://doi.org/10.1111/j.1600-0889.2006.00231.x

Ayazpour, Z., González Abad, G., Nowlan, C. R., Sun, K., Kwon, H., Chan Miller, C., Chong, H., Wang, H., Liu, X., Chance, K., O'Sullivan, E., Zhu, L., Vigouroux, C., De Smedt, I., Stremme, W., Hannigan, J. W., Notholt, J., Sun, X., Palm, M., Petri, C., Strong, K., Rohling, A.N., Mahieu, E., Smale, D., Te, Y., Morino, I., Murata, I., Nagahama, T., Kivi, R., Makarova, M., Jones, N., Sussmann, R., and Zhou, M. (2025). Aura Ozone Monitoring Instrument (OMI) Collection 4 Formaldehyde Products. Earth and Space Science (Hoboken, N.J.), 12(2). https://doi.org/10.1029/2024EA003792

Barnes, C., Boulanger, Y., Keeping, T., Gachon, P., Gillett, N., Boucher, J., Roberge, F., Kew, S.,Haas, O., Heinrich, D., Vahlberg, M., Singh, R., Elbe, M., Sivanu, S., Arrighi, J., van Aalst, M. and Krikken, F. (2023). Climate change more than doubled the likelihood of extreme fire weather conditions in eastern Canada. Scientific Reports, 1-26. https://doi.org/10.25561/105981

Batchelor, R. L., Strong, K., Lindenmaier, R., Mittermeier, R. L., Fast, H., Drummond, J. R., and Fogal, P. F. (2009). A New Bruker IFS 125HR FTIR spectrometer for the polar environment atmospheric research laboratory at Eureka, Nunavut, Canada: Measurements and comparison

with the existing Bomem DA8 Spectrometer. Journal of Atmospheric and Oceanic Technology, 26(7), 1328–1340. https://doi.org/10.1175/2009JTECHA1215.1

Bates, K. H., Jacob, D. J., Wang, S., Hornbrook, R. S., Apel, E. C., Kim, M. J., Millet, D. B., Wells, K. C., Chen, X., Brewer, J. F., Ray, E. A., Commane, R., Diskin, G. S., and Wofsy, S. C. (2021). The Global Budget of Atmospheric Methanol: New Constraints on Secondary, Oceanic, and Terrestrial Sources. Journal of Geophysical Research: Atmospheres, 126(4). e2020JD033439. https://doi.org/10.1029/2020JD033439

Bell, M. L., Peng, R. D., Dominici, F., and Samet, J. M. (2009). Emergency hospital admissions for cardiovascular diseases and ambient levels of carbon monoxide results for 126 United States urban counties, 1999-2005. Circulation. 120(11), 949–955. https://doi.org/10.1161/CIRCULATIONAHA.109.851113

Berg, T., Sekkesæter, S., Steinnes, E., Valdal, A.-K., and Wibetoe, G. (2003). Springtime depletion of mercury in the European Arctic as observed at Svalbard. Science of the Total Environment, 304(1), 43–51. https://doi.org/10.1016/S0048-9697(02)00555-7

Bernath, P. F. (2005). Spectra of atoms and molecules (2nd ed.). pp. 112–282, Oxford University Press.

Bey, I., Jacob, D. J., Yantosca, R. M., Logan, J. A., Field, B. D., Fiore, A. M., Li, Q.-B., Liu, H.-Y., Mickley, L. J., and Schultz, M. G. (2001). Global modeling of tropospheric chemistry with assimilated meteorology: Model description and evaluation. Journal of Geophysical Research, 106(D19), 23073–23095. https://doi.org/10.1029/2001JD000807

Blumenstock, T. H., Fischer, H., Friedle, A., Hase, F., and Thomas, P. (1997). Column amounts of $ClONO_2$, HCl, HNO_3, and HF from ground-based FTIR measurements made near Kiruna, Sweden, in late winter 1994. Journal of Atmospheric Chemistry, 26(3), 311–321. https://doi.org/10.1023/A:1005728713762

Blumenstock, T., Hase, F., Kramer, I., Mikuteit, S., Fischer, H., Goutail, F., and Raffalski, U. (2009). Winter to winter variability of chlorine activation and ozone loss as observed by ground-based FTIR measurements at Kiruna since winter 1993/94: 1989-2009 Remote Sensing and the Implementation of the Montreal Protocol. International Journal of Remote Sensing, 30(15–16), 4055–4064. https://doi-org.myaccess.library.utoronto.ca/10.1080/01431160902821916

Bowerman, N. H. A., Frame, D. J., Huntingford, C., Lowe, J. A., Smith, S. M., and Allen, M. R. (2013). The role of short-lived climate pollutants in meeting temperature goals. Nature Climate Change, 3(12), 1021–1024. https://doi.org/10.1038/nclimate2034

Brandt, J., Silver, J. D., Frohn, L. M., Geels, C., Gross, A., Hansen, A. B., Hansen, K. M., Hedegaard, G. B., Skjøth, C. A., Villadsen, H., Zare, A., and Christensen, J. H. (2012). An integrated model study for Europe and North America using the Danish Eulerian Hemispheric Model with focus on intercontinental transport of air pollution. Atmospheric Environment (1994), 53, 156–176. https://doi.org/10.1016/j.atmosenv.2012.01.011

Bruno, A. G., Harrison, J. J., Chipperfield, M. P., Moore, D. P., Pope, R. J., Wilson, C., Mahieu, E., and Notholt, J. (2023). Atmospheric distribution of HCN from satellite observations and 3-D model

simulations, Atmospheric Chemistry and Physics, 23, 4849–4861, https://doi.org/10.5194/acp-23-4849-2023

Buchholz, R. R., Deeter, M. N., Worden, H. M., Gille, J., Edwards, D. P., Hannigan, J. W., Jones, N. B., Paton-Walsh, C., Griffith, D. W. T., Smale, D., Robinson, J., Strong, K., Conway, S., Sussmann, R., Hase, F., Blumenstock, T., Mahieu, E., and Langerock, B. (2017). Validation of MOPITT carbon monoxide using ground-based Fourier transform infrared spectrometer data from NDACC. Atmospheric Measurement Techniques, 10, 1927–1956, https://doi.org/10.5194/amt-10-1927-2017

Buchholz, R. R., Worden, H. M., Park, M., Francis, G., Deeter, M. N., Edwards, D. P., Emmons, L. K., Gaubert, B., Gille, J., Martínez-Alonso, S., Tang, W., Kumar, R., Drummond, J. R., Clerbaux, C., George, M., Coheur, P. F., Hurtmans, D., Bowman, K. W., Luo, M., Payne, V. H., Worden, J. R., Chin, M., Levy, R. C., Warner, J., Wei, Z., and Kulawik, S. S. (2021). Air pollution trends measured from Terra: CO and AOD over industrial, fire-prone, and background regions. Remote Sensing of Environment, 256, 112275, https://doi.org/10.1016/j.rse.2020.112275

Buchholz, R.R., Park, M., Worden, H.M., Tang, W., Edwards, D.P., Gaubert, B., Deeter, M.N., Sullivan, T., Ru, M., Chin, M., Levy, R.C., Zheng, B., and Magzamen, S. (2022). New seasonal pattern of pollution emerges from changing North American wildfires. Nature Communications, 13, 2043. https://doi.org/10.1038/s41467-022-29623-8

Burnett, R. T., Cakmak, S., Raizenne, M. E., Stieb, D., Vincent, R., Krewski, D., Brook, J. R., Philips, O., and Ozkaynak, H. (1998). The Association between Ambient Carbon Monoxide Levels and Daily Mortality in Toronto, Canada. Journal of the Air and Waste Management Association, 48(8), 689–700. https://doi.org/10.1080/10473289.1998.10463718

Bush, E. and Lemmen, D.S., editors (2019): Canada's Changing Climate Report; Government of Canada, Ottawa, ON. 444 p. https://changingclimate.ca/CCCR2019/ (last access: February 2, 2023)

Byrne, B., Liu, J., Bowman, K. W., Pascolini-Campbell, M., Chatterjee, A., Pandey, S., Miyazaki, K., van der Werf, G. R., Wunch, D., Wennberg, P. O., Roehl, C. M., and Sinha, S. (2024). Carbon emissions from the 2023 Canadian wildfires. Nature, 633(8031), 835–839. https://doi.org/10.1038/s41586-024-07878-z

Campbell, J. R., D. L. Hlavka, E. J. Welton, C. J. Flynn, D. D. Turner, J. D. Spinhirne, Scott V. S., and Hwang I. H. (2002). Full-time, eye-safe cloud and aerosol lidar observation at atmospheric radiation measurement program sites: Instruments and data processing. Journal of Atmospheric and Oceanic Technology, 19, 431–442. https://doi.org/10.1175/1520-0426(2002)019<0431:FTESCA>2.0.CO;2

Card, D., and Krueger, A. B. (1993). Minimum Wages and Employment: A Case Study of the Fast Food Industry in New Jersey and Pennsylvania. National Bureau of Economic Research #4509. 1-57. https://doi.org/10.3386/w4509

CCFM (Canadian Council of Forest Ministers) (2024). Canadian Wildland Fire Prevention and Mitigation Strategy: Taking Action Together. 1-30. https://doi.org/10.4095/st000011

Chen, J., Anderson, K., Pavlovic, R., Moran, M. D., Englefield, P., Thompson, D. K., Munoz-Alpizar, R., and Landry, H. (2019). The FireWork v2.0 air quality forecast system with biomass burning emissions from the Canadian Forest Fire Emissions Prediction System v2.03. Geoscientific Model Development, 12, 3283–3310. https://doi.org/10.5194/gmd-12-3283-2019

Chen, J., and GEM-MACH development team. (2019). GEM-MACH CFFEPS rev m3848_CFFEPS (m3848_CFFEPS). Zenodo. [Software] https://doi.org/10.5281/zenodo.2579386

Christensen, J. H. (1997). The Danish eulerian hemispheric model — a three-dimensional air pollution model used for the arctic. Atmospheric Environment (1994), 31(24), 4169–4191. https://doi.org/10.1016/S1352-2310(97)00264-1

CIHI (Canadian Institute for Health Information) National Ambulatory Care Reporting System (NACRS) [metadata]. https://www.cihi.ca/en/national-ambulatory-care-reporting-system-nacrs-metadata (last access: December 12, 2024).

Connes, J. and Connes, P. (1966). Near-Infrared planetary spectra by Fourier spectroscopy. Journal of the Optical Society of America, 56(7),896–910. https://doi.org/10.1364/JOSA.56.000896

CWFIS (Canadian Wildland Fire Information System), Canadian Forest Service. (2024). Natural Resources Canada, Northern Forestry Centre, Edmonton, Alberta. [Dataset]. http://cwfis.cfs.nrcan.gc.ca (last access: August 30, 2024).

CUMSPH (Columbia University Mailman School of Public Health) (2013). Difference-in-difference estimation https://www.publichealth.columbia.edu/research/population-health-methods/difference-difference-estimation (last access: Febuary 3, 2025)

Dammers, E., Palm, M., Van Damme, M., Vigouroux, C., Smale, D., Conway, S., Toon, G. C., Jones, N., Nussbaumer, E., Warneke, T., Petri, C., Clarisse, L., Clerbaux, C., Hermans, C., Lutsch, E., Strong, K., Hannigan, J. W., Nakajima, H., Morino, I., Herrera, B., Stremme, W., Grutter, M., Schaap, M., Wichink Kruit, R. J., Notholt, J., Coheur, P.-F., and Erisman, J. W. (2016). An evaluation of IASI-NH_3 with ground-based Fourier transform infrared spectroscopy measurements, Atmospheric Chemistry and Physics, 16, 10 351–10 368, https://doi.org/10.5194/acp-16-10351-2016

Dammers, E., McLinden, C. A., Griffin, D., Shephard, M. W., Van Der Graaf, S., Lutsch, E., Schaap, M., Gainairu-Matz, Y., Fioletov, V., Van Damme, M., Whitburn, S., Clarisse, L., Cady-Pereira, K., Clerbaux, C., Coheur, P. F., and Erisman, J. W. (2019). NH_3 emissions from large point sources derived from CrIS and IASI satellite observations, Atmospheric Chemistry and Physics, 19, 12 261–12 293, https://doi.org/10.5194/acp-19-12261-2019

Danabasoglu, G., Lamarque, J. -F, Bacmeister, J., Bailey, D. A., DuVivier, A. K., Edwards, J., Emmons, L. K., Fasullo, J., Garcia, R., Gettelman, A., Hannay, C., Holland, M. M., Large, W. G., Lauritzen, P. H., Lawrence, D. M., Lenaerts, J. T. M., Lindsay, K., Lipscomb, W. H., Mills, M. J., Neale, R., Oleson,K.W., Otto-Bliesner, B., Phillips, A.S., Sacks, W., Tilmes, S., Kampenhout, L., Vertenstein, M., Bertini, A., Dennis, J., Deser, C., Fischer, C., Fox-Kemper,B., Kay, J.E., Kinnison, D., Kushner, P.J., Larson, V.E., Long, M.C., Mickelson, S., Moore, J.K., Nienhouse, E., Polvani, L., Rasch, P.J., and Strand, W. G. (2020). The Community Earth System Model

Version 2 (CESM2). Journal of Advances in Modeling Earth Systems, 12(2). e2019MS001916. https://doi.org/10.1029/2019MS001916

De Mazière, M., Thompson, A. M., Kurylo, M. J., Wild, J. D., Bernhard, G., Blumenstock, T., Braathen, G. O., Hannigan, J. W., Lambert, J.-C., Leblanc, T., McGee, T. J., Nedoluha, G., Petropavlovskikh, I., Seckmeyer, G., Simon, P. C., Steinbrecht, W., and Strahan, S. E. (2018). The Network for the Detection of Atmospheric Composition Change (NDACC): history, status and perspectives. Atmospheric Chemistry and Physics, 18, 4935–4964. https://doi.org/10.5194/acp-18-4935-2018

Deeter, M. N., S. Martínez-Alonso, D. P. Edwards, L. K. Emmons, J. C. Gille, H. M. Worden, J. V. Pittman, B. C. Daube, and S. C. Wofsy (2013). Validation of MOPITT Version 5 thermal-infrared, near-infrared, and multispectral carbon monoxide profile retrievals for 2000–2011. Journal of Geophysical Research: Atmospheres, 118, 6710–6725. https://doi.org/10.1002/jgrd.50272

Deeter, M., Francis, G., Gille, J., Mao, D., Martínez-Alonso, S., Worden, H., Ziskin, D., Drummond, J., Commane, R., Diskin, G., and McKain, K. (2022). The MOPITT Version 9 CO product: sampling enhancements and validation. Atmospheric Measurement Techniques, 15, 2325–2344, https://doi.org/10.5194/amt-15-2325-2022

Draxler, R. R., and Hess, G. D. (1998). An overview of the HYSPLIT4 modeling system for trajectories, dispersion, and deposition. Australian Meteorological Magazine, 47, 295–308. ISSN: *0004-9743*.

Draxler, R.R. (2003). Evaluation of an ensemble dispersion calculation. Journal of Applied Meteorology and Climatology, 42, 308–317. https://doi.org/10.1175/1520-0450(2003)042<0308:EOAEDC>2.0.CO;2

Draxler, R. R., and Rolph, G. D. (2007). HYSPLIT Training Seminar. https://www.arl.noaa.gov/documents/workshop/NAQC2007/HTML_Docs/index.html (last access: November 5, 2024).

Drummond, J.R., Bailak, G.V., and Mand, G. (1995). The Measurements of Pollution in the Troposphere (MOPITT) Instrument, Applications of Photonic Technology. Springer US, 197–200. https://doi.org/10.1007/978-1-4757-9247-8_38

ECCC (Environment and Climate Change Canada) (2017). Strategy on short-lived climate pollutants - 2017. ISBN: 978-0-660-08363-6 https://publications.gc.ca/collections/collection_2018/eccc/En4-299-2017-eng.pdf (last access: December 12, 2024)

ECCC (Environment and Climate Change Canada) (2024). Regional Air Quality Deterministic Prediction System (RAQDPS). https://collaboration.cmc.ec.gc.ca/cmc/CMOI/product_guide/docs/tech_notes/technote_raqdps_e.pdf (last access: November 5, 2024).

Edwards, D. P., Emmons, L. K., Hauglustaine, D. A., Chu, D. A., Gille, J. C., Kaufman, Y. J., Petron, G., Yurganov, L.N., Giglio, L., Deeter, M.N., Yudin, V., Ziskin, D.C., Warner, J., Lamarque, J.-F., Francis, G.L., Ho, S.P., Mao, D., Chen, J., Grechko, E.I., and Drummond, J. R. (2004). Observations of carbon monoxide and aerosols from the Terra satellite: Northern Hemisphere

variability. Journal of Geophysical Research: Atmospheres, 109, D24202. https://doi.org/10.1029/2004JD004727

Emmons, L. K., Walters, S., Hess, P. G., Lamarque, J. F., Pfister, G. G., Fillmore, D., Granier, C., Guenther, A., Kinnison, D., Laepple, T., Orlando, J., Tie, X., Tyndall, G., Wiedinmyer, C., Baughcum, S. L., and Kloster, S. (2010). Description and evaluation of the Model for Ozone and Related chemical Tracers, version 4 (MOZART-4). Geoscientific Model Development, 3(1), 43–67. https://doi.org/10.5194/gmd-3-43-2010

Emmons, L. K., Arnold, S. R., Monks, S. A., Huijnen, V., Tilmes, S., Law, K. S., Thomas, J. L., Raut, J. C., Bouarar, I., Turquety, S., Long, Y., Duncan, B., Steenrod, S., Strode, S., Flemming, J., Mao, J., Langner, J., Thompson, A. M., Tarasick, D., Apel, E. C., Blake, D. R., Cohen, R. C., Dibb, J., Diskin, G. S., Fried, A., Hall, S. R., Huey, L. G., Weinheimer, A. J., Wisthaler, A., Mikoviny, T., Nowak, J., Peischl, J., Roberts, J. M., Ryerson, T., Warneke, C., Helmig, D. (2015). The POLARCAT Model Intercomparison Project (POLMIP): Overview and evaluation with observations. Atmospheric Chemistry and Physics, 15(12), 6721–6744. https://doi.org/10.5194/acp-15-6721-2015

Eneroth, K., Holmén, K., Berg, T., Schmidbauer, N., and Solberg, S. (2007). Springtime depletion of tropospheric ozone, gaseous elemental mercury and non-methane hydrocarbons in the European Arctic, and its relation to atmospheric transport. Atmospheric Environment (1994), 41(38), 8511–8526. https://doi.org/10.1016/j.atmosenv.2007.07.008

Erni, S., Wang, X., Swystun, T., Taylor, S. W., Parisien, M.-A., Robinne, F.-N., Eddy, B., Oliver, J., Armitage, B., and Flannigan, M. D. (2024). Mapping wildfire hazard, vulnerability, and risk to Canadian communities. International Journal of Disaster Risk Reduction, 101, 104221. https://doi.org/10.1016/j.ijdrr.2023.104221

Esri 2020. "Topographic" [basemap]. "OpenSteetMap". January 6, 2020. https://www.arcgis.com/home/item.html?id=b834a68d7a484c5fb473d4ba90d35e71 (last access: July 4, 2024).

Esri, 2024 "Topographic" [basemap]. "Light Gray Canvas". June 21, 2024. https://www.arcgis.com/home/item.html?id=ee8678f599f64ec0a8ffbfd5c429c896 (last access: July 4, 2024).

Farquhar, G. D., Firth, P. M., Wetselaar R., and Weir, B. (1980). On the Gaseous Exchange of Ammonia between Leaves and the Environment: Determination of the Ammonia Compensation Point. Plant Physiology, 66(4), 710–714. https://doi.org/10.1104/pp.66.4.710

Fellgett, P. (1951). The multiplex advantage. PhD thesis, University of Cambridge.

Fisher, J. A., Jacob, D. J., Purdy, M. T., Kopacz, M., Le Sager, P., Carouge, C., Holmes, C. D., Yantosca, R. M., Batchelor, R. L., Strong, K., Diskin, G. S., Fuelberg, H. E., Holloway, J. S., Hyer, E. J., McMillan, W. W., Warner, J., Streets, D. G., Zhang, Q., Wang, Y., and Wu, S. (2010). Source attribution and interannual variability of Arctic pollution in spring constrained by aircraft (ARCTAS, ARCPAC) and satellite (AIRS) observations of carbon monoxide. Atmospheric Chemistry and Physics, 10(3), 977–996. https://doi.org/10.5194/acp-10-977-2010

Flood, V. A., Strong, K., Whaley, C. H., Walker, K. A., Blumenstock, T., Hannigan, J. W., Mellqvist, J., Notholt, J., Palm, M., Röhling, A. N., Arnold, S., Beagley, S., Chien, R.-Y., Christensen, J., Deushi, M., Dobricic, S., Dong, X., Fu, J. S., Gauss, M., Gong, W., Langner, J., Law, K. S., Marelle, L., Onishi, T., Oshima, N., Plummer, D. A., Pozzoli, L., Raut, J.-C., Thomas, M. A., Tsyro, S., and Turnock, S. (2024). Evaluating modelled tropospheric columns of CH_4, CO, and O_3 in the Arctic using ground-based Fourier transform infrared (FTIR) measurements. Atmospheric Chemistry and Physics, 24, 1079–1118. https://doi.org/10.5194/acp-24-1079-2024

Flood, V. A., Strong, K., Whaley, C. H., Chen, J., Wunch, D., Drummond, J. R., Colebatch, O., Gillespie, L., & Mostafavi Pak, N. (2025a). The Impact of the 2023 Canadian Forest Fires on Air Quality in Southern Ontario. Journal of Geophysical Research. Atmospheres, 130(5). https://doi.org/10.1029/2024JD042254

Flood, V.A., Strong, K., Buchholz, R.R., Kuiper, G., and Magzamen, S., (2025b). – Assessing the impact of wildfire emissions on the seasonal cycle of CO and emergency room visits in Alberta and Ontario, Canada. GeoHealth [submitted: December 24, 2024, in review]

Franco, B., Clarisse, L., Stavrakou, T., Müller, J. -F, Taraborrelli, D., Hadji-Lazaro, J., Hannigan, J. W., Hase, F., Hurtmans, D., Jones, N., Lutsch, E., Mahieu, E., Ortega, I., Schneider, M., Strong, K., Vigouroux, C., Clerbaux, C., and Coheur, P. -F. (2020). Spaceborne Measurements of Formic and Acetic Acids: A Global View of the Regional Sources. Geophysical Research Letters, 47(4). e2019GL086239. https://doi.org/10.1029/2019GL086239

Franklin, J. E., Drummond, J. R., Griffin, D., Pierce, J. R., Waugh, D. L., Palmer, P. I., Parrington, M., Lee, J. D., Lewis, A. C., Rickard, A. R., Taylor, J. W., Allan, J. D., Coe, H., Walker, K. A., Chisholm, L., Duck, T. J., Hopper, J. T., Blanchard, Y., Gibson, M. D., Curry, K. R., Sakamoto, K. M., Lesins, G., Dan, L., Kliever, J., and Saha, A. (2014). A case study of aerosol scavenging in a biomass burning plume over eastern Canada during the 2011 BORTAS field experiment. Atmospheric Chemistry and Physics, 14, 8449–8460, https://doi.org/10.5194/acp-14-8449-2014

Franklin, J. (2015). Solar Absorption Spectroscopy at the Dalhousie Atmospheric Observatory, Ph.D. thesis, Dalhousie University, Halifax, Nova Scotia, Canada, permanent link: https://dalspace.library.dal.ca//handle/10222/64642

Galle, B., Mellqvist, J., Arlander, D. W., Fløisand, I., Chipperfield, M. P., and Lee, A. M. (1999). Ground based FTIR measurements of stratospheric species from Harestua, Norway during sesame and comparison with models. Journal of Atmospheric Chemistry, 32(1), 147–164. https://doi.org/10.1023/A:1006137924562

Gan, R. W., Ford, B., Lassman, W., Pfister, G., Vaidyanathan, A., Fischer, E., Volckens, J., Pierce, J. R., and Magzamen, S. (2017). Comparison of wildfire smoke estimation methods and associations with cardiopulmonary-related hospital admissions. GeoHealth, 1(3), 122–136. https://doi.org/10.1002/2017GH000073

Gan, R. W., Liu, J., Ford, B., O'Dell, K., Vaidyanathan, A., Wilson, A., Volckens, J., Pfister, G., Fischer, E. V., Pierce, J. R., and Magzamen, S. (2020). The association between wildfire smoke exposure and asthma-specific medical care utilization in Oregon during the 2013 wildfire season.

Journal of Exposure Science and Environmental Epidemiology, 30(4), 618–628. https://doi.org/10.1038/s41370-020-0210-x

Gao, Y., Huang, W., Yu, P., Xu, R., Yang, Z., Gasevic, D., Ye, T., Guo, Y. and Li, S. (2023). Long-term impacts of non-occupational wildfire exposure on human health: A systematic review. Environmental Pollution, 320, 121041. https://doi.org/10.1016/j.envpol.2023.121041

Gao, Y., Huang, W., Yu, P., Xu, R., Gasevic, D., Yue, X., Coêlho, M. de S. Z. S., Saldiva, P. H. N., Guo, Y., and Li, S. (2024). Wildfire-related PM2.5 and cardiovascular mortality: A difference-in-differences analysis in Brazil. Environmental Pollution, 347, 123810. https://doi.org/10.1016/j.envpol.2024.123810

Gisi, M., Hase, F., Dohe, S., Blumenstock, T., Simon, A., and Keens, A. (2012). XCO_2-measurements with a tabletop FTS using solar absorption spectroscopy. Atmospheric Measurement Techniques, 5, 2969–2980. https://doi.org/10.5194/amt-5-2969-2012

Gong, W., Makar, P. A., Zhang, J., Milbrandt, J., Gravel, S., Hayden, K. L., Macdonald, A. M., and Leaitch, W. R. (2015). Modelling aerosol–cloud–meteorology interaction: A case study with a fully coupled air quality model (GEM-MACH). Atmospheric Environment, 115, 695–715. https://doi.org/10.1016/j.atmosenv.2015.05.062

Gong, W., Beagley, S. R., Cousineau, S., Sassi, M., Munoz-Alpizar, R., Ménard, S., Racine, J., Zhang, J., Chen, J., Morrison, H., Sharma, S., Huang, L., Bellavance, P., Ly, J., Izdebski, P., Lyons, L., and Holt, R. (2018). Assessing the impact of shipping emissions on air pollution in the Canadian Arctic and northern regions: Current and future modelled scenarios. Atmospheric Chemistry and Physics, 18(22), 16653–16687. https://doi.org/10.5194/acp-18-16653-2018

Gordon, I. E., Rothman, L. S., Hargreaves, R. J., Hashemi, R., Karlovets, E. V., Skinner, F. M., Conway, E. K., Hill, C., Kochanov, R. V., Tan, Y., Wcisło, P., Finenko, A. A., Nelson, K., Bernath, P. F., Birk, M., Boudon, V., Campargue, A., Chance, K. V., Coustenis, A., Drouin, B.J. Flaud, J.–M., Gamache, R.R., Hodges, J.T., Jacquemart, D., Mlawer, E.J., Nikitin, A.V., Perevalov, V.I., Rotger, M., Tennyson, J., Toon, G.C., Tran, H., Tyuterev, V.G., Adkins, E.M., Baker, A., Barbe, A., Canè, E,. Császár, A.G., Dudaryonok, A., Egorov, O., Fleisher, A.J., Fleurbaey, H., Foltynowicz, A., Furtenbacher, T., Harrison, J.J., Hartmann, J.–M., Horneman, V.–M., Huang, X., Karman, T., Karns, J., Kassi, S., Kleiner, I., Kofman, V., Kwabia–Tchana, F., Lavrentieva, N.N., Lee, T.J., Long, D.A., Lukashevskaya, A.A., Lyulin, O.M., Makhnev, V., Yu Matt, W., Massie, S.T., Melosso, M., Mikhailenko, S.N., Mondelain, D., Müller, H.S.P., Naumenko, O.V., Perrin, A., Polyansky, O.L., Raddaoui, E., Raston, P.L., Reed, Z.D., Rey, M., Richard, C., Tóbiás, R., Sadiek, I., Schwenke, D.W., Starikova, E., Sung, K., Tamassia, F., Tashkun, S.A., Vander Auwera, J., Vasilenko, I.A., Vigasin, A.A., Villanueva, G.L., Vispoel, B., Wagner, G., Yachmenev, A., Yurchenko, S. N. (2022). The HITRAN2020 molecular spectroscopic database. Journal of Quantitative Spectroscopy and Radiative Transfer, 277, 107949. https://doi.org/10.1016/j.jqsrt.2021.107949

Griffin, D., Walker, K. A., Franklin, J. E., Parrington, M., Whaley, C., Hopper, J., Drummond, J. R., Palmer, P. I., Strong, K., Duck, T. J., Abboud, I., Bernath, P. F., Clerbaux, C., Coheur, P.-F., Curry, K. R., Dan, L., Hyer, E., Kliever, J., Lesins, G., Maurice, M., Saha, A., Tereszchuk, K., and Weaver, D. (2013). Investigation of CO, C_2H_6 and aerosols in a boreal fire plume over

eastern Canada during BORTAS 2011 using ground- and satellite-based observations and model simulations, Atmospheric Chemistry and Physics, 13, 10227–10241, https://doi.org/10.5194/acp-13-10227-2013

Griffin, D., Sioris, C., Chen, J., Dickson, N., Kovachik, A., de Graaf, M., Nanda, S., Veefkind, P., Dammers, E., McLinden, C. A., Makar, P., and Akingunola, A. (2020). The 2018 fire season in North America as seen by TROPOMI: aerosol layer height intercomparisons and evaluation of model-derived plume heights, Atmospheric Measurement Techniques, 13, 1427–1445, https://doi.org/10.5194/amt-13-1427-2020

Griffiths, P. R., and De Haseth, J. A. (2007). Fourier transform infrared spectrometry (2nd ed.). pp. 1–560, Wiley-Interscience.

Hahn, M. B., Kuiper, G., O'Dell, K., Fischer, E. V., and Magzamen, S. (2021). Wildfire smoke is associated with an increased risk of cardiorespiratory emergency department visits in Alaska. GeoHealth, 5, e2020GH000349. https://doi.org/10.1029/2020GH000349

Hanes, C. C., Wang, X., Jain, P., Parisien, M. A., Little, J. M., and Flannigan, M. D. (2019). Fire-regime changes in Canada over the last half century. Canadian Journal of Forest Research, 49(3), 256–269. https://doi.org/10.1139/cjfr-2018-0293

Hannigan, J. W., Coffey, M. T., and Goldman, A. (2009). Semiautonomous FTS observation system for remote sensing of stratospheric and tropospheric gases. Journal of Atmospheric and Oceanic Technology, 26(9), 1814–1828. https://doi.org/10.1175/2009JTECHA1230.1

Hannigan, J. W., Ortega, I., Shams, S. B., Blumenstock, T., Campbell, J. E., Conway, S., Flood, V., Garcia, O., Griffith, D., Grutter, M., Hase, F., Jeseck, P., Jones, N., Mahieu, E., Makarova, M., Mazière, M., Morino, I., Murata, I., Nagahama, T., Nakijima, H., Notholt, J., Palm, M., Poberovoskii, A., Rettinger, M., Robinson, J., Rohling, A.N., Schneider, M., Servais, C., Smale, D., Stremme, W., Strong, K., Sussmann, R., Te, Y., Vigouroux, C., and Wizenberg, T. (2022). Global Atmospheric OCS Trend Analysis From 22 NDACC Stations. Journal of Geophysical Research. Atmospheres, 127(4). e2021JD035764. https://doi.org/10.1029/2021JD035764

Hase, F., Hannigan, J. W., Coffey, M. T., Goldman, A., Höpfner, M., Jones, N. B., Rinsland, C. P., and Wood, S. W. (2004). Intercomparison of retrieval codes used for the analysis of high-resolution, ground-based FTIR measurements. Journal of Quantitative Spectroscopy and Radiative Transfer, 87(1), 25–52. https://doi.org/10.1016/j.jqsrt.2003.12.008

Hase, F. (2012). Improved instrumental line shape monitoring for the ground-based, high-resolution FTIR spectrometers of the Network for the Detection of Atmospheric Composition Change. Atmospheric Measurement Techniques, 5(3), 603–610. https://doi.org/10.5194/amt-5-603-2012

Health Canada (2023). Guidance for Evaluating Human Health Effects in Impact Assessment: Air Quality. Healthy Environments and Consumer Safety Branch, Health Canada. ISBN 978-0-660-03096-8. https://publications.gc.ca/collections/collection_2024/sc-hc/H129-54-1-2023-eng.pdf (last access: November 5, 2024).

Health Canada (2024). Health Impacts of Air Pollution in Canada in 2018 – 2024 report. Government of Canada. ISBN 978-0-660-69855-7 53. https://www.canada.ca/content/dam/hc-

sc/documents/services/publications/healthy-living/health-impacts-air-pollution-2018/health-impacts-air-pollution-2018.pdf (last access: February 3, 2025).

Hedelius, J., and Wennberg, P. (2023). EM27/SUN GGG Interferogram processing suite (2020.0). CaltechDATA. https://doi.org/10.22002/25tve-4h822

Henderson, S. B., Brauer, M., MacNab, Y. C., and Kennedy, S. M. (2011). Three measures of forest fire smoke exposure and their associations with respiratory and cardiovascular health outcomes in a population-based cohort. Environmental Health Perspectives, 119(9), 1266–1271. https://doi.org/10.1289/ehp.1002288

Hicke, J.A., Lucatello, S., Mortsch, L.D., Dawson, J., Domínguez Aguilar, M., Enquist, C.A.F., Gilmore, E.A., Gutzler, D.S., Harper, S., Holsman, Jewett, E.B., Kohler, T.A., and Miller, KA. (2022). North America. In: Climate Change 2022: Impacts, Adaptation and Vulnerability. Contribution of Working Group II to the Sixth Assessment Report of the Intergovernmental Panel on Climate Change pp. 1929–2042, https://doi.org/10.1017/9781009325844.016

Hirdman, D., Sodemann, H., Eckhardt, S., Burkhart, J. F., Jefferson, A., Mefford, T., Quinn, P. K., Sharma, S., Ström, J., and Stohl, A. (2010). Source identification of short-lived air pollutants in the Arctic using statistical analysis of measurement data and particle dispersion model output. Atmospheric Chemistry and Physics, 10(2), 669–693. https://doi.org/10.5194/acp-10-669-2010

Hocking, W. K., Carey-Smith, T., Tarasick, D. W., Argall, P. S., Strong, K., Rochon, Y., Zawadzki, I., and Taylor, P. A. (2007). Detection of stratospheric ozone intrusions by windprofiler radars. Nature, 450(7167), 281–284. https://doi.org/10.1038/nature06312

Höglund-Isaksson, L., Gómez-Sanabria, A., Klimont, Z., Rafaj, P., and Schöpp, W. (2020). Technical potentials and costs for reducing global anthropogenic methane emissions in the 2050 timeframe -results from the GAINS model. Environmental Research Communications, 2(2), 25004. https://doi.org/10.1088/2515-7620/ab7457

IPCC (Intergovernmental Panel on Climate Change) (2018). Global Warming of 1.5°C: IPCC Special Report on Impacts of Global Warming of 1.5°C above Pre-Industrial Levels in Context of Strengthening Response to Climate Change, Sustainable Development, and Efforts to Eradicate Poverty. pp 1-630 https://doi.org/10.1017/9781009157940

IPCC (Intergovernmental Panel on Climate Change) (2021). Climate Change 2021: The Physical Science Basis. Contribution of Working Group I to the Sixth Assessment Report of the Intergovernmental Panel on Climate Change. pp 1-2391. https://doi.org/10.1017/9781009157896

IRWG (Infrared Working Group). (2020). Retrieval Code SFIT – SFIT Spectral Data Analysis Model. [Software] https://wiki.ucar.edu/display/sfit4/ (last access: November 5, 2024).

Jacob, D. J., Field, B. D., Li, Q., Blake, D. R., de Gouw, J., Warneke, C., Hansel, A., Wisthaler, A., Singh, H. B., and Guenther, A. (2005). Global budget of methanol: Constraints from atmospheric observations. Journal of Geophysical Research: Atmospheres, 110, D08303. https://doi.org/10.1029/2004JD005172

Jacquinot, P. and Dufour, C. (1948). Conditions optiques d'emploi des cellules photoelectriques dans les spectrographes et les interferometres. Journal Recherche CNRS, 6(91), 18.

Jaffe, D.A., and Wigder, N.L. (2012). Ozone production from wildfires: a critical review. Atmospheric Environment, 51, 1–10. https://doi.org/10.1016/j.atmosenv.2011.11.063

Jain, P., Barber, Q. E., Taylor, S. W., Whitman, E., Castellanos Acuna, D., Boulanger, Y., Chavardès, R. D., Chen, J., Englefield, P., Flannigan, M., Girardin, M. P., Hanes, C. C., Little, J., Morrison, K., Skakun, R. S., Thompson, D. K., Wang, X., & Parisien, M.-A. (2024). Drivers and Impacts of the Record-Breaking 2023 Wildfire Season in Canada. Nature Communications, 15(1), 6764–14. https://doi.org/10.1038/s41467-024-51154-7

Jolly, W.M., Cochrane, M.A., Freeborn, P.H., Holden, Z.A., Brown, T.J., Williamson, G.J., and Bowman, D.M.J.S. (2015). Climate-induced variations in global wildfire danger from 1979 to 2013. Nature Communications, 6, 7537. https://doi.org/10.1038/ncomms8537

Jones, C. G., Rappold, A. G., Vargo, J., Cascio, W. E., Kharrazi, M., McNally, B., and Hoshiko, S. (2020). Out-of-hospital cardiac arrests and wildfire-related particulate matter during 2015–2017 California wildfires. Journal of the American Heart Association, 9(8), e014125–e014125. https://doi.org/10.1161/JAHA.119.014125

Jones, M. W., Abatzoglou, J. T., Veraverbeke, S., Andela, N., Lasslop, G., Forkel, M., Smith, A. J. P., Burton, C., Betts, R. A., van der Werf, G. R., Sitch, S., Canadell, J. G., Santín, C., Kolden, C., Doerr, S. H., and Le Quéré, C. (2022). Global and regional trends and drivers of fire under climate change. Reviews of Geophysics, 60, e2020RG000726. https://doi.org/10.1029/2020RG000726

Jonsson, A. I., de Grandpré, J., Fomichev, V. I., McConnell, J. C., and Beagley, S. R. (2004). Doubled CO_2-induced cooling in the middle atmosphere: Photochemical analysis of the ozone radiative feedback. Journal of Geophysical Research: Atmospheres, 109(D24), https://doi.org/10.1029/2004JD005093

Kalnay, E., Kanamitsu, M., Kistler, R., Collins, W., Deaven, D., Gandin, L., Iredell, M., Saha, S., White, G., Woollen, J., Zhu, Y., Chelliah, M., Ebisuzaki, W., Higgins, W., Janowiak, J., Mo, K. C., Ropelewski, C., Wang, J., Leetmaa, A., Renyolds, R., Jenne, R., Joseph, D. (1996). The NCEP/NCAR 40-Year Reanalysis Project. Bulletin of the American Meteorological Society, 77(3), 437–471. https://doi.org/10.1175/1520-0477(1996)077<0437:TNYRP>2.0.CO;2

Kärnä, T., and Baptista, A. M. (2016). Evaluation of a long-term hindcast simulation for the Columbia River estuary. Ocean Modelling, 99, 1–14. https://doi.org/10.1016/j.ocemod.2015.12.007

Kawai, H., Yukimoto, S., Koshiro, T., Oshima, N., Tanaka, T., Yoshimura, H., and Nagasawa, R. (2019). Significant improvement of cloud representation in the global climate model MRI-ESM2. Geoscientific Model Development, 12(7), 2875–2897. https://doi.org/10.5194/gmd-12-2875-2019

Klimont, Z., Kupiainen, K., Heyes, C., Purohit, P., Cofala, J., Rafaj, P., Borken-Kleefeld, J., and Schöpp, W. (2017). Global anthropogenic emissions of particulate matter including black

carbon. Atmospheric Chemistry and Physics, 17(14), 8681–8723. https://doi.org/10.5194/acp-17-8681-2017

Kohlhepp, R., Ruhnke, R., Chipperfield, M. P., De Mazière, M., Notholt, J., Barthlott, S., Batchelor, R. L., Blatherwick, R. D., Blumenstock, Th., Coffey, M. T., Demoulin, P., Fast, H., Feng, W., Goldman, A., Griffith, D. W. T., Hamann, K., Hannigan, J. W., Hase, F., Jones, N. B., Kagawa, A., Kaiser, I., Kasai, Y., Kirner, O., Kouker, W., Lindenmaier, R., Mahieu, E., Mittermeier, R. L., Monge-Sanz, B., Morino, I., Murata, I., Nakajima, H., Palm, M., Paton-Walsh, C., Raffalski, U., Reddmann, Th., Rettinger, M., Rinsland, C. P., Rozanov, E., Schneider, M., Senten, C., Servais, C., Sinnhuber, B.-M., Smale, D., Strong, K., Sussmann, R., Taylor, J. R., Vanhaelewyn, G., Warneke, T., Whaley, C., Wiehle, M., and Wood, S. W. (2012). Observed and simulated time evolution of HCl, $ClONO_2$, and HF total column abundances, Atmospheric Chemistry and Physics, 12, 3527–3556. https://doi.org/10.5194/acp-12-3527-2012

Kopacz, M., Jacob, D. J., Fisher, J. A., Logan, J. A., Zhang, L., Megretskaia, I. A., Yantosca, R. M., Singh, K., Henze, D. K., Burrows, J. P., Buchwitz, M., Khlystova, I., McMillan, W. W., Gille, J. C., Edwards, D. P., Eldering, A., Thouret, V., & Nedelec, P. (2010). Global estimates of CO sources with high resolution by adjoint inversion of multiple satellite datasets (MOPITT, AIRS, SCIAMACHY, TES). Atmospheric Chemistry and Physics, 10(3), 855–876. https://doi.org/10.5194/acp-10-855-2010

Korsiak, J., Pinault, L., Christidis, T., Burnett, R. T., Abrahamowicz, M., and Weichenthal, S. (2022). Long-term exposure to wildfires and cancer incidence in Canada: a population-based observational cohort study. The Lancet Planetary Health, 6(5), e400-e409. https://doi.org/10.1016/S2542-5196(22)00067-5

Kreider, M. R., Higuera, P. E., Parks, S. A., Rice, W. L., White, N., and Larson, A. J. (2024). Fire suppression makes wildfires more severe and accentuates impacts of climate change and fuel accumulation. Nature Communications, 15(1), 2412–2412. https://doi.org/10.1038/s41467-024-46702-0

Kurylo, M. J. and Soloman, S. (1990). United States NASA Administration Upper Atmosphere Research Program and NOAA Climate and Global Change Program, Network for the Detection of Stratospheric Change: a status and implementation report. Technical report, NASA. https://ntrs.nasa.gov/api/citations/19920024855/downloads/19920024855.pdf (last access: February 3, 2025)

Law, K. S., Hjorth, J. L., Pernov, J. B., Whaley, C. H., Skov, H., Collaud Coen, M., Langner, J., Arnold, S. R., Tarasick, D., Christensen, J., Deushi, M., Effertz, P., Faluvegi, G., Gauss, M., Im, U., Oshima, N., Petropavlovskikh, I., Plummer, D., Tsigaridis, K., Tsyro, S., Solberg, S., and Turnock, S. (2023). Arctic Tropospheric Ozone Trends, Geophys. Res. Lett., 50, e2023GL103096. https://doi.org/10.1029/2023GL103096

Li, Y., Tong, D. Q., Ngan, F., Cohen, M. D., Stein, A. F., Kondragunta, S., Zhang, X., Ichoku, C., Hyer, E. J., and Kahn, R. A. (2020). Ensemble PM2.5 forecasting during the 2018 Camp fire event using the HYSPLIT transport and dispersion model. Journal of Geophysical Research: Atmospheres, 125, e2020JD032768. https://doi.org/10.1029/2020JD032768

Lindaas, J., Pollack, I. B., Calahorrano, J. J., O'Dell, K., Garofalo, L. A., Pothier, M. A., Farmer, D. K., Kreidenweis, S. M., Campos, T. L., Flocke, F., Weinheimer, A. J., Montzka, D. D., Tyndall, G. S., Palm, B. B., Peng, Q., Thornton, J. A., Permar, W., Wielgasz, C., Hu, L., Ottmar, R. D., Restaino, J. C., Hudak, A. T., Ku, I.-T., Zhou, Y., Sive, B. C., Sullivan, A., Collett, J. L., and Fischer, E. V. (2021). Empirical insights into the fate of ammonia in western U.S. wildfire smoke plumes. Journal of Geophysical Research: Atmospheres, 126, e2020JD033730. https://doi.org/10.1029/2020JD033730

Lindenmaier, R. (2012). Studies of Arctic Middle Atmosphere Chemistry using Infrared Absorption Spectroscopy, Ph.D. Thesis, .University of Toronto, Toronto, Ontario, Canada, permanent link: https://utoronto.scholaris.ca/items/7d3c2613-fc35-49ff-9f5d-2222a7005c71

Liou, K.-N. (2002). An introduction to atmospheric radiation (2nd ed.). pp 1-583. Academic Press.

Liu, X., Ma, P. L., Wang, H., Tilmes, S., Singh, B., Easter, R. C., Ghan, S. J., and Rasch, P. J. (2016). Description and evaluation of a new four-mode version of the Modal Aerosol Module (MAM4) within version 5.3 of the Community Atmosphere Model. Geoscientific Model Development, 9(2), 505–522. https://doi.org/10.5194/gmd-9-505-2016

Lobert, J. M., and Warnatz, J. (1993). Emissions from the combustion process in vegetation. Fire in the Environment, 13, 15-37.

Lolli, S., Vivone, G., Lewis, J. R., Sicard, M., Welton, E. J., Campbell, J. R., Comerón, A., Tokay, A., Giunta, A., and Pappalardo, G. (2020). Overview of the New Version 3 NASA Micro-Pulse Lidar Network (MPLNET) Automatic Precipitation Detection Algorithm. Remote Sens., 12(1). https://doi.org/10.3390/rs12010071

Lutsch, E., Dammers, E., Conway, S., and Strong K. (2016). Long-range Transport of NH_3, CO, HCN and C_2H_6 from the 2014 Canadian Wildfires. Geophysical Research Letters, 43, 8286–8297. https://doi.org/10.1002/2016GL070114

Lutsch, E., Strong, K., Jones, D. B. A., Blumenstock, T., Conway, S., Fisher, J. A., Hannigan, J. W., Hase, F., Kasai, Y., Mahieu, E., Makarova, M., Morino, I., Nagahama, T., Notholt, J., Ortega, I., Palm, M., Poberovskii, A. V., Sussmann, R., and Warneke, T. (2020). Detection and attribution of wildfire pollution in the Arctic and northern midlatitudes using a network of Fourier-Transform infrared spectrometers and GEOS-Chem. Atmospheric Chemistry and Physics, 20(21), 12813–12851. https://doi.org/10.5194/acp-20-12813-2020

Maddanu, F., and Proietti, T. (2023). Trends in atmospheric ethane. Climatic Change, 176(5), 53. https://doi.org/10.1007/s10584-023-03508-1

Magzamen, S., Gan, R. W., Liu, J., O'Dell, K., Ford, B., Berg, K., Bol, K., Wilson, A., Fischer, E.V., and Pierce, J.R. (2021). Differential cardiopulmonary health impacts of local and long-range transport of wildfire smoke. GeoHealth, 5, e2020GH000330. https://doi.org/10.1029/2020GH000330

Mahieu, E., Fischer, E. V., Franco, B., Palm, M., Wizenberg, T., Smale, D., Clarisse, L., Clerbaux, C., Coheur, P-F., Hannigan, J. W., Lutsch, E., Notholt, J., Pardo Cantos, I., Prignon, M., Servais, C., and Strong, K. (2021). First retrievals of peroxyacetyl nitrate (PAN) from ground-based FTIR

solar spectra recorded at remote sites, comparison with model and satellite data, Elementa: Science of the Anthropocene, 9, 00027, https://doi.org/10.1525/elementa.2021.00027

Mahsin, M.D., Cabaj, J., and Saini, V. (2022). Respiratory and cardiovascular condition-related physician visits associated with wildfire smoke exposure in Calgary, Canada, in 2015: a population-based study. International Journal of Epidemiology, 51(1), 166-178, https://doi.org/10.1093/ije/dyab206

Maji, K. J., Ford, B., Li, Z., Hu, Y., Hu, L., Langer, C. E., Hawkinson, C., Paladugu, S., Moraga-McHaley, S., Woods, B., Vansickle, M., Uejio, C. K., Maichak, C., Sablan, O., Magzamen, S., Pierce, J. R., and Russell, A. G. (2024). Impact of the 2022 New Mexico, US wildfires on air quality and health. Science of the Total Environment, 946, 174197. https://doi.org/10.1016/j.scitotenv.2024.174197

Makar, P. A., Gong, W., Hogrefe, C., Zhang, Y., Curci, G., Žabkar, R., Milbrandt, J., Im, U., Balzarini, A., Baró, R., Bianconi, R., Cheung, P., Forkel, R., Gravel, S., Hirtl, M., Honzak, L., Hou, A., Jiménez-Guerrero, P., Langer, M.,Moran, M., Pabla, B., Pérez, J., Pirovano, G., José, R. S., Tuccella, P., Werhahn, J., Zhang, J., and Galmarini, S. (2015a). Feedbacks between air pollution and weather, part 2: Effects on chemistry. Atmospheric Environment, 115, 499–526. https://doi.org/10.1016/j.atmosenv.2014.10.021

Makar, P. A., Gong, W., Milbrandt, J., Hogrefe, C., Zhang, Y., Curci, G., Žabkar, R., Im, U., Balzarini, A., Baró, R., Bianconi, R., Cheung, P., Forkel, R., Gravel, S., Hirtl, M., Honzak, L., Hou, A., Jiménez-Guerrero, P., Langer, M.,Moran, M., Pabla, B., Pérez, J., Pirovano, G., José, R. S., Tuccella, P., Werhahn, J., Zhang, J. and Galmarini, S. (2015b). Feedbacks between air pollution and weather, Part 1: Effects on weather. Atmospheric Environment, 115, 442–469. https://doi.org/10.1016/j.atmosenv.2014.12.003

Marelle, L., Raut, J. C., Law, K. S., Berg, L. K., Fast, J. D., Easter, R. C., Shrivastava, M., and Thomas, J. L. (2017). Improvements to the WRF-Chem 3.5.1 model for quasi-hemispheric simulations of aerosols and ozone in the Arctic. Geoscientific Model Development, 10(10), 3661–3677. https://doi.org/10.5194/gmd-10-3661-2017

Marelle, L., Raut, J. -C, Law, K. S., and Duclaux, O. (2018). Current and Future Arctic Aerosols and Ozone from Remote Emissions and Emerging Local Sources—Modeled Source Contributions and Radiative Effects. Journal of Geophysical Research. Atmospheres, 123(22), 12,942-12,963. https://doi.org/10.1029/2018JD028863

Marsh, D. R., Mills, M. J., Kinnison, D. E., Lamarque, J.-F., Calvo, N., and Polvani, L. M. (2013). Climate Change from 1850 to 2005 Simulated in CESM1 (WACCM). Journal of Climate, 26(19), 7372–7391. https://doi.org/10.1175/jcli-d-12-00558.1

Massling, A., Nielsen, I. E., Kristensen, D., Christensen, J. H., Sorensen, L. L., Jensen, B., Nguyen, Q. T., Nøjgaard, J. K., Glasius, M., and Skov, H. (2015). Atmospheric black carbon and sulfate concentrations in Northeast Greenland. Atmospheric Chemistry and Physics, 15(16), 9681–9692. https://doi.org/10.5194/acp-15-9681-2015

Matz, C. J., Egyed, M., Xi, G., Racine, J., Pavlovic, R., Rittmaster, R., Henderson, S.B. and Stieb, D. M. (2020). Health impact analysis of PM2.5 from wildfire smoke in Canada (2013–2015, 2017–

2018). Science of the Total Environment, 725, 138506. https://doi.org/10.1016/j.scitotenv.2020.138506

Mendez-Espinosa, J.F., Belalcazar, L.C., and Morales Betancourt, R. (2019). Regional air quality impact of northern South America biomass burning emissions. Atmospheric Environment, 203, 131–140. https://doi.org/10.1016/j.atmosenv.2019.01.042

Michelson, A. A. (1881). The relative motion of the Earth and of the Luminiferous Ether. American Journal of Science, s3-22(128):120–129.

Millet, D. B., Baasandorj, M., Farmer, D. K., Thornton, J. A., Baumann, K., Brophy, P., Chaliyakunnel, S., de Gouw, J. A., Graus, M., Hu, L., Koss, A., Lee, B. H., Lopez-Hilfiker, F. D., Neuman, J. A., Paulot, F., Peischl, J., Pollack, I. B., Ryerson, T. B., Warneke, C., Williams, B. J., and Xu, J. (2015). A large and ubiquitous source of atmospheric formic acid, Atmospheric Chemistry and Physics, 15, 6283–6304, https://doi.org/10.5194/acp-15-6283-2015

Monks, S. A., Arnold, S. R., Emmons, L. K., Law, K. S., Turquety, S., Duncan, B. N., Flemming, J., Huijnen, V., Tilmes, S., Langner, J., Mao, J., Long, Y., Thomas, J. L., Steenrod, S. D., Raut, J. C., Wilson, C., Chipperfield, M. P., Diskin, G. S., Weinheimer, A., Schlager, H., and Ancellet, G. (2015). Multi-model study of chemical and physical controls on transport of anthropogenic and biomass burning pollution to the Arctic. Atmospheric Chemistry and Physics, 15(6), 3575–3603. https://doi.org/10.5194/acp-15-3575-2015

Moran, M. D., Pavlovic, R., and Anselmo, D. (2018). Regional air quality deterministic prediction system (RAQDPS): update from version 019 to version 020, Environment and Climate Change Canada, https://collaboration.cmc.ec.gc.ca/cmc/CMOI/product_guide/docs/tech_notes/technote_raqdps-v20_20180918_e.pdf (last access: Febuary 2, 2023)

Mostafavi Pak, Nasrin; Gillespie, Lawson; Lu, George; Heerah, Sajjan; Hedelius, Jacob; Ars, Sebastien; Wunch, Debra, (2019). Total Column Mixing Ratios of Carbon Dioxide, Methane and Carbon Monoxide from Toronto (ta). Borealis, V2 [Dataset] https://doi.org/10.5683/SP2/RNCAWQ

Müller, J.-F., Stavrakou, T., Oomen, G.-M., Opacka, B., De Smedt, I., Guenther, A., Vigouroux, C., Langerock, B., Aquino, C. A. B., Grutter, M., Hannigan, J., Hase, F., Kivi, R., Lutsch, E., Mahieu, E., Makarova, M., Metzger, J.-M., Morino, I., Murata, I., Nagahama, T., Notholt, J., Ortega, I., Palm, M., Röhling, A., Stremme, W., Strong, K., Sussmann, R., Té, Y., and Fried, A. (2024). Bias correction of OMI HCHO columns based on FTIR and aircraft measurements and impact on top-down emission estimates. Atmospheric Chemistry and Physics, 24(4), 2207–2237. https://doi.org/10.5194/acp-24-2207-2024

NASA, MPLNET V3 Data: Toronto Downtown. (2024) [Dataset] https://mplnet.gsfc.nasa.gov/data?v=V3ands=Toronto_Downtown (last access: November 5, 2024).

NASA/LARC/SD/ASDC (2024). MOPITT CO gridded daily means (Near and Thermal Infrared Radiances) V009 [Dataset]. NASA Langley Atmospheric Science Data Center DAAC. Retrieved from https://doi.org/10.5067/TERRA/MOPITT/MOP03J.009

NDACC (Network for the Detection of Atmospheric Composition Change) Data Host Facility. NDACC Public Data Access [Dataset]. https://www-air.larc.nasa.gov/missions/ndacc/data.html (last access: November 5, 2024).

NOAA (National Oceanic and Atmospheric Administration). (2020). Arctic Report Card 2020: Surface Air Temperature, Tech. rep., National Oceanic and Atmospheric Administration (NOAA), Office of Oceanic and Atmospheric Research, Pacific Marine Environmental Laboratory (U.S.), https://doi.org/10.25923/gcw8-2z06

NOAA (National Oceanic and Atmospheric Administration). (2024). National Centers for Environmental Information, Monthly Global Climate Report for Annual 2023. Released January 2024. https://www.ncei.noaa.gov/access/monitoring/monthly-report/global/202313 (last access: Nov 5, 2024).

Notholt, J., Toon, G. C., Lehmann, R., Sen, B., and Blavier, J. -F. (1997a). Comparison of Arctic and Antarctic trace gas column abundances from ground-based Fourier transform infrared spectrometry. Journal of Geophysical Research Atmospheres, 102(D11), 12863–12869. https://doi.org/10.1029/97JD00358

Notholt, J., Toon, G., Stordal, F., Solberg, S., Schmidbauer, N., Becker, E., Meier, A., and Sen, B. (1997b). Seasonal variations of atmospheric trace gases in the high Arctic at 79°N. Journal of Geophysical Research Atmospheres, 102(D11), 12855–12861. https://doi.org/10.1029/97JD00337

Notholt, J., Toon, G. C., Rinsland, C. P., Pougatchev, N. S., Jones, N. B., Connor, B. J., Weller, R., Gautrois, M., and Schrems, O. (2000). Latitudinal variations of trace gas concentrations in the free troposphere measured by solar absorption spectroscopy during a ship cruise. Journal of Geophysical Research Atmospheres, 105(D1), 1337–1349. https://doi.org/10.1029/1999JD900940

Notholt, J., Toon, G., Jones, N., Griffith, D., and Warneke, T. (2006). Spectral line finding program for atmospheric remote sensing using full radiation transfer. Journal of Quantitative Spectroscopy and Radiative Transfer, 97(1), 112–125. https://doi.org/10.1016/j.jqsrt.2004.12.025

NRC (Natural Resources Canada and Canadian Forest Service) (2024). Is Canada's forest a carbon sink or source? Canadian Forest Service Science Policy Note ISBN 978-0-660-73902-1. pp 1-4. https://ostr-backend-prod.azurewebsites.net/server/api/core/bitstreams/d0e50a64-dd95-4a26-bfab-b58c9df7183b/content

Olivié, D., Höglund-Isaksson, L., Klimont, Z., and von Salzen, K. (2021). Boxmodel for calculation of global atmospheric methane concentration, Zenodo, https://doi.org/10.5281/zenodo.5293940

Olsen, K. S., Strong, K., Walker, K. A., Boone, C. D., Raspollini, P., Plieninger, J., Bader, W., Conway, S., Grutter, M., Hannigan, J. W., Hase, F., Jones, N., de Mazière, M., Notholt, J., Schneider, M., Smale, D., Sussmann, R., and Saitoh, N. (2017). Comparison of the GOSAT TANSO-FTS TIR CH_4 volume mixing ratio vertical profiles with those measured by ACE-FTS, ESA MIPAS, IMK-IAA MIPAS, and 16 NDACC stations. Atmospheric Measurement Techniques, 10(10), 3697–3718. https://doi.org/10.5194/amt-10-3697-2017

OMECP (Ontario Ministry of Environment, Conservation and Parks), Government of Ontario: Air Pollutant Data, [Dataset]. https://www.airqualityontario.com (last access: November 5, 2024).

Oshima, N., Yukimoto, S., Deushi, M., Koshiro, T., Kawai, H., Tanaka, T. Y., and Yoshida, K. (2020). Global and Arctic effective radiative forcing of anthropogenic gases and aerosols in MRI-ESM2.0. Progress in Earth and Planetary Science, 7(1), 1–21. https://doi.org/10.1186/s40645-020-00348-w

Parisien, M. A., Barber, Q. E., Hirsch, K. G., Stockdale, C. A., Erni, S., Wang, X., Arseneault, D., and Parks, S. A. (2020). Fire deficit increases wildfire risk for many communities in the Canadian boreal forest. Nature Communications, 11, 2121. https://doi.org/10.1038/s41467-020-15961-y

Paton-Walsh, C., Jones, N. B., Wilson, S. R., Haverd, V., Meier, A., Griffith, D. W. T., and Rinsland, C. P. (2005). Measurements of trace gas emissions from Australian forest fires and correlations with coincident measurements of aerosol optical depth. Journal of Geophysical Research: Atmospheres, 110, 24305. https://doi.org/10.1029/2005JD006202

Paulot, F., Wunch, D., Crounse, J. D., Toon, G. C., Millet, D. B., DeCarlo, P. F., Vigouroux, C., Deutscher, N. M., González Abad, G., Notholt, J., Warneke, T., Hannigan, J. W., Warneke, C., de Gouw, J. A., Dunlea, E. J., De Mazière, M., Griffith, D. W. T., Bernath, P., Jimenez, J. L., and Wennberg, P. O.(2011). Importance of secondary sources in the atmospheric budgets of formic and acetic acids. Atmospheric Chemistry and Physics, 11(5), 1989–2013. https://doi.org/10.5194/acp-11-1989-2011

Pavlovic, R., Chen, J., Anderson, K., Moran, M. D., Beaulieu, P.- A., Davignon, D., and Cousineau, S. (2016). The FireWork Air Quality Forecast System with Near-Real-Time Biomass Burning Emissions: Recent Developments and Evaluation of Performance for the 2015 North American Wildfire Season. Journal of the Air & Waste Management Association, 66, 819–841. https://doi.org/10.1080/10962247.2016.1158214

Perkins, W. D. (1986). Fourier transform-infrared spectroscopy: Part l. Instrumentation. Journal of Chemical Education, 63(1), A5. https://doi.org/10.1021/ed063pA5

PHO - Public Health Ontario: Data and Analysis – Snapshots (2024). Available at: https://www.publichealthontario.ca/en/Data-and-Analysis/Commonly-Used-Products/Snapshots (last access: August 30, 2024).

Pope, R. J., Kerridge, B. J., Siddans,R., Latter, B. G., Chipperfield, M.P., Arnold, S. R., Ventress, L. J., Pimlott, M. A., Graham, A. M., Knappett, D. S., and Rigby, R. (2021). Large enhancements in Southern Hemisphere satellite-observed trace gases due to the 2019/2020 Australian wildfires. Journal of Geophysical Research: Atmospheres, 126, e2021JD034892. https://doi.org/10.1029/2021JD034892

Pougatchev, N. S., Connor, B. J., and Rinsland, C. P. (1995). Infrared measurements of the ozone vertical distribution above Kitt Peak. Journal of Geophysical Research, 100(D8), 16689–16697. https://doi.org/10.1029/95JD01296

PPIC - Public Policy Institute of California : California's Population. Available at: https://www.ppic.org/publication/californias-population/ (last access: August 30, 2024).

Prather, M. J., Holmes, C. D., and Hsu, J. (2012). Reactive greenhouse gas scenarios: Systematic exploration of uncertainties and the role of atmospheric chemistry. Geophysical Research Letters, 39(9). L09803. https://doi.org/10.1029/2012GL051440

Rantanen, M., Karpechko, A. Y., Lipponen, A., Nordling, K., Hyvärinen, O., Ruosteenoja, K., Vihma, T., and Laaksonen, A. (2022). The Arctic has warmed nearly four times faster than the globe since 1979. Communications Earth and Environment, 3(1), 1–10. https://doi.org/10.1038/s43247-022-00498-3

Rap, A., Richards, N. A. D., Forster, P. M., Monks, S. A., Arnold, S. R., and Chipperfield, M. P. (2015). Satellite constraint on the tropospheric ozone radiative effect. Geophysical Research Letters, 42(12), 5074–5081. https://doi.org/10.1002/2015GL064037

Ravishankara, A., Daniel, J., and Portmann, R. (2009). Nitrous oxide (N_2O): The dominant ozone-depleting substance emitted in the 21st century, Science, 326 123–125, https://doi.org/10.1126/science.1176985

Robertson, L., Langner, J., and Engardt, M. (1999). An Eulerian limited-area atmospheric transport model. Journal of Applied Meteorology and Climatology, 38(2), 190. https://doi.org/10.1175/1520-0450(1999)038<0190:AELAAT>2.0.CO;2

Rodgers, C. D. (2000). Inverse Methods for Atmospheric Sounding: Theory and Practice. World Scientific (Vol. 2), 13–100. https://doi.org/10.1142/3171

Rodgers, C. D., and Connor, B. J. (2003). Intercomparison of remote sounding instruments. Journal of Geophysical Research. D. Atmospheres, 108(D3), 4116. https://doi.org/10.1029/2002JD002299

Rolph, G., Stein, A., and Stunder, B. (2017). Real-Time Environmental Applications and Display System: READY. Environ. Modell. Software, 95, 210–228. https://doi.org/10.1016/j.envsoft.2017.06.025

Rothman, L. S., Gordon, I. E., Barbe, A., Benner, D. C., Bernath, P. F., Birk, M., Boudon, V., Brown, L. R., Campargue, A., Champion, J.-P., Chance, K., Coudert, L. H., Dana, V., Devi, V. M., Fally, S., Flaud, J.-M., Gamache, R. R., Goldman, A., Jacquemart, D., Kleiner, I., Lacome, N., Lafferty, W., Mandin, J.-Y., Massie, S., Mikhailenko, S., Miller, C., Moazzen-Ahmadi, N., Naumenko, O., Nikitin, A., Orphal, J., Perevalov, V., Perrin, A., Predoi-Cross, A., Rinsland, C., Rotger, M., Simeckova, M., Smith, M., Sung, K., Tashkun, S., Tennyson, J., Toth, R., Vandaele, A., and Vander Auwera, J. (2009). The HITRAN 2008 molecular spectroscopic database. Journal of Quantitative Spectroscopy and Radiative Transfer, 110(9), 533–572. https://doi.org/10.1016/j.jqsrt.2009.02.013

Rothman, L. S., Gordon, I. E., Babikov, Y., Barbe, A., Chris Benner, D., Bernath, P. F., Birk, M., Bizzocchi, L., Boudon, V., Brown, L. R., Campargue, A., Chance, K., Cohen, E. A., Coudert, L. H., Devi, V. M., Drouin, B. J., Fayt, A., Flaud, J.-M., Gamache, R. R., Gamache, R., Harrison, J., Hartmann, J.-M., Hill, C., Hodges, J., Jacquemart, D., Jolly, A., Lamouroux, J., Le Roy, R., Li, G., Long, D., Lyulin, O., Mackie, C., Massie, S., Mikhailenko, S., Muller, H., Naumenko, O., Nikitin, A., Orphal, J., Perevalov, V., Perrin, A., Polovtseva, E., Richard, C., Smith, M., Starikova, E., Sung, K., Tashkun, S., Tennyson, J., Toon, G., Tyuterev, V., and Wagner, G.

(2013). The HITRAN2012 molecular spectroscopic database. Journal of Quantitative Spectroscopy and Radiative Transfer, 130, 4–50. https://doi.org/10.1016/j.jqsrt.2013.07.002

Saunois, M., Stavert, A. R., Poulter, B., Bousquet, P., Canadell, J. G., Jackson, R. B., Raymond, P. A., Dlugokencky, E. J., Houweling, S., Patra, P. K., Ciais, P., Arora, V. K., Bastviken, D., Bergamaschi, P., Blake, D. R., Brailsford, G., Bruhwiler, L., Carlson, K. M., Carrol, M., Castaldi, S., Chandra, N., Crevoisier, C., Crill, P. M., Covey, K., Curry, C. L., Etiope, G., Frankenberg, C., Gedney, N., Hegglin, M. I., Höglund-Isaksson, L., Hugelius, G., Ishizawa, M., Ito, A., Janssens-Maenhout, G., Jensen, K. M., Joos, F., Kleinen, T., Krummel, P. B., Langenfelds, R. L., Laruelle, G. G., Liu, L., Machida, T., Maksyutov, S., McDonald, K. C., McNorton, J., Miller, P. A., Melton, J. R., Morino, I., Müller, J., Murguia-Flores, F., Naik, V., Niwa, Y., Noce, S., O'Doherty, S., Parker, R. J., Peng, C., Peng, S., Peters, G. P., Prigent, C., Prinn, R., Ramonet, M., Regnier, P., Riley, W. J., Rosentreter, J. A., Segers, A., Simpson, I. J., Shi, H., Smith, S. J., Steele, L. P., Thornton, B. F., Tian, H., Tohjima, Y., Tubiello, F. N., Tsuruta, A., Viovy, N., Voulgarakis, A., Weber, T. S., van Weele, M., van der Werf, G. R., Weiss, R. F., Worthy, D., Wunch, D., Yin, Y., Yoshida, Y., Zhang, W., Zhang, Z., Zhao, Y., Zheng, B., Zhu, Q., Zhu, Q., and Zhuang, Q. (2020). The Global Methane Budget 2000–2017, Earth System Science Data, 12, 1561–1623. https://doi.org/10.5194/essd-12-1561-2020

Schneider, S. R., Lee, K., Santos, G., and Abbatt, J. P. (2021). Air quality data approach for defining wildfire influence: Impacts on PM2.5, NO_2, CO, and O_3 in Western Canadian cities. Environmental Science & Technology Journal, 55(20), 13709-13717. https://doi.org/10.1021/acs.est.1c04042

Scinocca, J. F., McFarlane, N. A., Lazare, M., Li, J., and Plummer, D. (2008). Technical note: The CCCma third generation AGCM and its extension into the middle atmosphere. Atmospheric Chemistry and Physics, 8(23), 7055–7074. https://doi.org/10.5194/acp-8-7055-2008

Selimovic, V., Yokelson, R. J., McMeeking, G. R., and Coefield, S. (2019). In situ measurements of trace gases, PM, and aerosol optical properties during the 2017 NW US wildfire smoke event. Atmospheric Chemistry and Physics, 19, 3905–3926. https://doi.org/10.5194/acp-19-3905-2019

Sellar, A. A., Jones, C. G., Mulcahy, J. P., Tang, Y., Yool, A., Wiltshire, A., O'Connor, F. M., Stringer, M., Hill, R., Palmieri, J., Woodward, S., Mora, L., Kuhlbrodt, T., Rumbold, S. T., Kelley, D. I., Ellis, R., Johnson, C. E., Walton, J., Abraham, N. L., Andrews, M. B., Andrews, T., Archibald, A. T., Berthou, S., Burke, E., Blockley, E., Carslaw, K., Dalvi, M., Edwards, J., Folberth, G. A., Gedney, N., Griffiths, P. T., Harper, A. B., Hendry, M. A., Hewitt, A. J., Johnson, B., Jones, A., Jones, C. D., Keeble, J., Liddicoat, S., Morgenstern, O., Parker, R. J., Predoi, V., Robertson, E., Siahaan, A., Smith, R. S., Swaminathan, R., Woodhouse, M. T., Zeng, G., and Zerroukat, M. (2019). UKESM1: Description and Evaluation of the U.K. Earth System Model. Journal of Advances in Modeling Earth Systems, 11(12), 4513–4558. https://doi.org/10.1029/2019MS001739

Sha, M. K., Langerock, B., Blavier, J.-F. L., Blumenstock, T., Borsdorff, T., Buschmann, M., Dehn, A., De Mazière, M., Deutscher, N. M., Feist, D. G., García, O. E., Griffith, D. W. T., Grutter, M., Hannigan, J. W., Hase, F., Heikkinen, P., Hermans, C., Iraci, L. T., Jeseck, P., Jones, N., Kivi, R., Kumps, N., Landgraf, J., Lorente, A., Mahieu, E., Makarova, M. V., Mellqvist, J., Metzger, J.-M., Morino, I., Nagahama, T., Notholt, J., Ohyama, H., Ortega, I., Palm, M., Petri, C., Pollard,

D. F., Rettinger, M., Robinson, J., Roche, S., Roehl, C. M., Röhling, A. N., Rousogenous, C., Schneider, M., Shiomi, K., Smale, D., Stremme, W., Strong, K., Sussmann, R., Té, Y., Uchino, O., Velazco, V. A., Vigouroux, C., Vrekoussis, M., Wang, P., Warneke, T., Wizenberg, T., Wunch, D., Yamanouchi, S., Yang, Y., and Zhou, M. (2021). Validation of methane and carbon monoxide from Sentinel-5 Precursor using TCCON and NDACC-IRWG stations. Atmospheric Measurement Techniques, 14(9), 6249–6304. https://doi.org/10.5194/amt-14-6249-2021

Simpson, D., Benedictow, A., Berge, H., Bergström, R., Emberson, L. D., Fagerli, H., Flechard, C. R., Hayman, G. D., Gauss, M., Jonson, J. E., Jenkin, M. E., Nyíri, A., Richter, C., Semeena, V. S., Tsyro, S., Tuovinen, J.-P., Valdebenito, Á., and Wind, P. (2012). The EMEP MSC-W chemical transport model – technical description. Atmospheric Chemistry and Physics, 12(16), 7825–7865. https://doi.org/10.5194/acp-12-7825-2012

Simpson, D., Bergström, R., Tsyro, S., and Wind, P. (2019). Updates to the EMEP MSC-W model, 2018–2019, in: Transboundary particulate matter, photo-oxidants, acidifying and eutrophying components, Emep status report 1/2019, The Norwegian Meteorological Institute, Oslo, Norway, https://emep.int/publ/reports/2019/EMEP_Status_Report_1_2019.pdf (last access: February 2, 2023)

Skov, H., Brooks, S. B., Goodsite, M. E., Lindberg, S. E., Meyers, T. P., Landis, M. S., Larsen, M. R. B., Jensen, B., McConville, G., and Christensen, J. (2006). Fluxes of reactive gaseous mercury measured with a newly developed method using relaxed eddy accumulation. Atmospheric Environment (1994), 40(28), 5452–5463. https://doi.org/10.1016/j.atmosenv.2006.04.061

Solberg, S., Schmidbauer, N., Semb, A., Stordal, F., and Hov, Ø. (1996). Boundary-layer ozone depletion as seen in the Norwegian Arctic in spring. Journal of Atmospheric Chemistry, 23(3), 301–332. https://doi.org/10.1007/BF00055158

STATS CAN (Statistics Canada) (2018a). Health Regions: Boundaries and Correspondence with Census Geography (82-402-X). Produced by the Statistical Geomatics Centre for Health Statistics Division. Available at: https://www150.statcan.gc.ca/n1/pub/82-402-x/2018001/maps-cartes/rm-cr11-eng.htm Reproduced and distributed on an "as is" basis with the permission of Statistics Canada. (last access: December 23, 2024).

STATS CAN (Statistics Canada) (2018b). Health Regions: Boundaries and Correspondence with Census Geography (82-402-X). Produced by the Statistical Geomatics Centre for Health Statistics Division. Available at: https://www150.statcan.gc.ca/n1/pub/82-402-x/2018001/maps-cartes/rm-cr08-eng.htm Reproduced and distributed on an "as is" basis with the permission of Statistics Canada. (last access: December 23, 2024).

STATS CAN (Statistics Canada) (2023). Census Profile. 2021 Census of Population. Statistics Canada Catalogue number 98-316-X2021001. Released November 15, 2023. https://www12.statcan.gc.ca/census-recensement/2021/dp-pd/prof/index.cfm?Lang=E (last access: November 5, 2024).

STATS CAN (Statistics Canada) (2024). Canada's population clock (real-time model). Available at: https://www150.statcan.gc.ca/n1/pub/71-607-x/71-607-x2018005-eng.htm (last access: August 30, 2024).

Statsmodels (2025). Ordinary Least Squares https://doi.org/10.5281/zenodo.593847

Stein, A. F., Rolph, G. D., Draxler, R. R., Stunder, B., and Ruminski, M. (2009). Verification of the NOAA smoke forecasting system: Model sensitivity to the injection height. Weather and Forecasting. 24(2), 379–394. https://doi.org/10.1175/2008WAF2222166.1

Stein, A. F., Draxler, R. R., Rolph, G. D., Stunder, B. J. B., Cohen, M. D., and Ngan, F. (2015). NOAA's HYSPLIT Atmospheric Transport and Dispersion Modeling System. Bull. Amer. Meteor. Soc., 96, 2059–2077. https://doi.org/10.1175/BAMS-D-14-00110.1

Steinbrecht, W., Kubistin, D., Plass-Dülmer, C., Davies, J., Tarasick, D. W., Gathen, P. v. d., Deckelmann, H., Jepsen, N., Kivi, R., Lyall, N., Palm, M., Notholt, J., Kois, B., Oelsner, P., Allaart, M., Piters, A., Gill, M., Van Malderen, R., Delcloo, A. W., Sussmann, R., Mahieu, E., Servais, C., Romanens, G., Stübi,R., Ancellet, G., Godin-Beekmann, S., Yamanouchi, S., Strong, K., Johnson, B., Cullis, P., Petropavlovskikh, I., Hannigan, J. W., Hernandez, J.-L., Diaz Rodriguez, A., Nakano, T., Chouza, F., Leblanc, T., Torres, C., Garcia, O., Röhling, A. N., Schneider, M., Blumenstock, T., Tully, M., Paton-Walsh, C., Jones, N., Querel, R., Strahan, S., Stauffer, R. M., Thompson, A. M., Inness, A., Engelen, R., Chang, K.-L., and Cooper, O. R. (2021). COVID-19 Crisis Reduces Free Tropospheric Ozone Across the Northern Hemisphere, Geophysical Research Letters, 48, e2020GL091987, https://doi.org/10.1029/2020GL091987

Stohl, A., Aamaas, B., Amann, M., Baker, L. H., Bellouin, N., Berntsen, T. K., Boucher, O., Cherian, R., Collins, W., Daskalakis, N., Dusinska, M., Eckhardt, S., Fuglestvedt, J. S., Harju, M., Heyes, C., Hodnebrog, Hao, J., Im, U., Kanakidou, M., Klimont, Z., Kupiainen, K., Law, K. S., Lund, M. T., Maas, R., MacIntosh, C. R., Myhre, G., Myriokefalitakis, S., Olivié, D., Quaas, J., Quennehen, B., Raut, J.-C., Rumbold, S. T., Samset, B. H., Schulz, M., Seland, Ø., Shine, K. P., Skeie, R. B., Wang, S., Yttri, K. E., and Zhu, T. (2015). Evaluating the climate and air quality impacts of short-lived pollutants. Atmospheric Chemistry and Physics, 15(18), 10529–10566. https://doi.org/10.5194/acp-15-10529-2015

Strong, K., Wolff, M. A., Kerzenmacher, T. E., Walker, K. A., Bernath, P. F., Blumenstock, T., Boone, C., Catoire, V., Coffey, M., De Mazière, M., Demoulin, P., Duchatelet, P., Dupuy, E., Hannigan, J., Höpfner, M., Glatthor, N., Griffith, D. W. T., Jin, J. J., Jones, N., Jucks, K., Kuellmann, H., Kuttippurath, J., Lambert, A., Mahieu, E., McConnell, J. C., Mellqvist, J., Mikuteit, S., Murtagh, D. P., Notholt, J., Piccolo, C., Raspollini, P., Ridolfi, M., Robert, C., Schneider, M., Schrems, O., Semeniuk, K., Senten, C., Stiller, G. P., Strandberg, A., Taylor, J., Tétard, C., Toohey, M., Urban, J., Warneke, T., and Wood, S. (2008). Validation of ACE-FTS N_2O measurements, Atmospheric Chemistry and Physics, 8, 4759– 4786, https://doi.org/10.5194/acp-8-4759-2008

Sussmann, R., Forster, F., Rettinger, M., and Jones, N. (2011). Strategy for high-accuracy-and-precision retrieval of atmospheric methane from the mid-infrared FTIR network. Atmospheric Measurement Techniques, 4(9), 1943–1964. https://doi.org/10.5194/amt-4-1943-2011

Szopa, S., Naik, V., Adhikary, B., Artaxo, P., Berntsen, T., Collins, W.D., Fuzzi, S., Gallardo, L., Kiendler-Scharr, A., Klimont, Z., Liao, H., Unger, N., and Zanis, P. (2021). Short-Lived Climate Forcers. In Climate Change 2021: The Physical Science Basis. Contribution of Working Group I to the Sixth Assessment Report of the Intergovernmental Panel on Climate Change, pp. 817–922, https://doi.org/10.1017/9781009157896.008

Taylor, J. R. (2008). Assessment of trace gas observations from the Toronto Atmospheric Observatory, Ph.D. thesis, University of Toronto, Toronto, Ontario, Canada, permanent link: https://librarysearch.library.utoronto.ca/permalink/01UTORONTO_INST/fedca1/cdi_proquest_journals_304368879

Teledyne Advanced Pollution Instrumentation. (2016). Model T640 PM Mass Monitor User Manual. CA, USA. https://www.teledyne-api.com/prod/Downloads/08354C%20T640%20USER%20MANUAL.pdf (last access: November 5, 2024).

Thermo Fisher Scientific. (2013). Model 5030 Synchronized Hybrid Ambient Real-time Particulate Monitor Instruction Manual. MA, USA. https://tools.thermofisher.com/content/sfs/manuals/EPM-manual-Model%205030%20SHARP.pdf (last access: November 5, 2024).

Thermo Fisher Scientific. (2017a). Model 48i Gas Filter Correlation CO Analyzer Instruction Manual. MA, USA. https://assets.thermofisher.com/TFS-Assets/LSG/manuals/48i_101891-00_10Aug2017.pdf (last access: November 5, 2024).

Thermo Fisher Scientific. (2017b). Model 49i UV Photometric O_3 Analyzer Instruction Manual. MA, USA. https://assets.thermofisher.com/TFS-Assets/EPM/manuals/EPM-manual-Model%2049i.pdf (last access: November 5, 2024).

Tomsche, L., Piel, F., Mikoviny, T., Nielsen, C. J., Guo, H., Campuzano-Jost, P., Nault, B. A., Schueneman, M. K., Jimenez, J. L., Halliday, H., Diskin, G., DiGangi, J. P., Nowak, J. B., Wiggins, E. B., Gargulinski, E., Soja, A. J., and Wisthaler, A. (2023). Measurement report: Emission factors of NH_3 and NH_x for wildfires and agricultural fires in the United States, Atmospheric Chemistry and Physics, 23, 2331–2343. https://doi.org/10.5194/acp-23-2331-2023

Toon, G. C. (2015). Atmospheric Line List for the 2014 TCCON Data Release. https://data.caltech.edu/records/248 (last access: February 20, 2025).

Toon, G. C. (2022). Atmospheric Voigt Line List for the TCCON 2020 Data Release. https://data.caltech.edu/records/8972 (last access: February 20, 2025).

Toronto Public Health. (2014). Path to Healthier Air: Toronto Air Pollution Burden of Illness Update. Technical Report https://www.toronto.ca/wp-content/uploads/2017/11/9190-tph-Air-Pollution-Burden-of-Illness-2014.pdf (last access: February 3, 2025)

USFS (United States Forest Service) Ensemble - Wildland Fire Air Quality Tools. https://portal.airfire.org/ (last access: November 5, 2024).

Van Damme, M., Clarisse, L., Whitburn, S., Hadji-Lazaro, J., Hurtmans, D., Clerbaux, C., and Coheur, P.-F. (2018). Industrial and agricultural ammonia point sources exposed. Nature, 564(7734), 99–103. https://doi.org/10.1038/s41586-018-0747-1

Van Der Werf, G. R., Randerson, J. T., Giglio, L., Van Leeuwen, T. T., Chen, Y., Rogers, B. M., Mu, M., Van Marle, M. J. E., Morton, D. C., Collatz, G. J., Yokelson, R. J., and Kasibhatla, P. S.

(2017). Global fire emissions estimates during 1997-2016. Earth System Science Data, 9(2), 697–720. https://doi.org/10.5194/essd-9-697-2017

Van Malderen, R., Thompson, A. M., Kollonige, D. E., Stauffer, R. M., Smit, H. G. J., Maillard Barras, E., Vigouroux, C., Petropavlovskikh, I., Leblanc, T., Thouret, V., Wolff, P., Effertz, P., Tarasick, D. W., Poyraz, D., Ancellet, G., De Backer, M.-R., Evan, S., Flood, V., Frey, M. M., Hannigan, J. W., Hernandez, J. L., Iarlori, M., Johnson, B. J., Jones, N., Kivi, R., Mahieu, E., McConville, G., Müller, K., Nagahama, T., Notholt, J., Piters, A., Prats, N., Querel, R., Smale, D., Steinbrecht, W., Strong, K., and Sussmann, R. (2025a). Global Ground-based Tropospheric Ozone Measurements: Reference Data and Individual Site Trends (2000–2022) from the TOAR-II/HEGIFTOM Project, Atmospheric Chemistry and Physics [preprint], https://doi.org/10.5194/egusphere-2024-3736

Van Malderen, R., Zang, Z., Chang, K.-L., Björklund, R., Cooper, O. R., Liu, J., Maillard Barras, E., Vigouroux, C., Petropavlovskikh, I., Leblanc, T., Thouret, V., Wolff, P., Effertz, P., Gaudel, A., Tarasick, D. W., Smit, H. G. J., Thompson, A. M., Stauffer, R. M., Kollonige, D. E., Poyraz, D., Ancellet, G., De Backer, M.-R., Frey, M. M., Hannigan, J. W., Hernandez, J. L., Johnson, B. J., Jones, N., Kivi, R., Mahieu, E., Morino, I., McConville, G., Müller, K., Murata, I., Notholt, J., Piters, A., Prignon, M., Querel, R., Rizi, V., Smale, D., Steinbrecht, W., Strong, K., and Sussmann, R. (2025b). Ground-based Tropospheric Ozone Measurements: Regional tropospheric ozone column trends from the TOAR-II/ HEGIFTOM homogenized datasets, Atmospheric Chemistry and Physics [preprint], https://doi.org/10.5194/egusphere-2024-3745

Van Wagner, C. E. (1987). Development and structure of the Canadian forest fire weather index system. Forestry Technical Report, pp 1-35. https://cfs.nrcan.gc.ca/publications?id=19927 (last access: November 5, 2024).

Viatte, C., Strong, K., Paton-Walsh, C., Mendonca, J., O'Neill, N. T., and Drummond, J. R. (2013). Measurements of CO, HCN, and C_2H_6 total columns in smoke plumes transported from the 2010 Russian boreal forest fires to the Canadian high Arctic. Atmosphere-Ocean, 51(5), 522–531. https://doi.org/10.1080/07055900.2013.823373

Viatte, C., Strong, K., Hannigan, J., Nussbaumer, E., Emmons, L. K., Conway, S., Paton-Walsh, C., Hartley, J., Benmergui, J., and Lin, J. (2015). Identifying fire plumes in the Arctic with tropospheric FTIR measurements and transport models. Atmospheric Chemistry and Physics, 15(5), 2227–2246. https://doi.org/10.5194/acp-15-2227-2015

Viatte, C., Abeed, R., Yamanouchi, S., Porter, W. C., Safieddine, S., Van Damme, M., Clarisse, L., Herrera, B., Grutter, M., Coheur, P.-F., Strong, K., and Clerbaux, C. (2022). NH_3 spatiotemporal variability over Paris, Mexico City, and Toronto, and its link to PM2.5 during pollution events, Atmospheric Chemistry and Physics, 22, 12907–12922, https://doi.org/10.5194/acp-22-12907-2022

Vigouroux, C., Hendrick, F., Stavrakou, T., Dils, B., De Smedt, I., Hermans, C., Merlaud, A., Scolas, F., Senten, C., Vanhaelewyn, G., Fally, S., Carleer, M., Metzger, J. M., Müller, J. F., Van Roozendael, M., and De Maziére, M. (2009). Ground-based FTIR and MAX-DOAS observations of formaldehyde at Réunion Island and comparisons with satellite and model data.

Atmospheric Chemistry and Physics, 9(24), 9523–9544. https://doi.org/10.5194/acp-9-9523-2009

Vigouroux, C., Bauer Aquino, C. A., Bauwens, M., Becker, C., Blumenstock, T., De Mazière, M., García, O., Grutter, M., Guarin, C., Hannigan, J., Hase, F., Jones, N., Kivi, R., Koshelev, D., Langerock, B., Lutsch, E., Makarova, M., Metzger, J.-M., Müller, J.-F., Notholt, J., Ortega, I., Palm, M., Paton-Walsh, C., Poberovskii, A., Rettinger, M., Robinson, J., Smale, D., Stavrakou, T., Stremme, W., Strong, K., Sussmann, R., Té, Y., and Toon, G. (2018). NDACC harmonized formaldehyde time series from 21 FTIR stations covering a wide range of column abundances, Atmospheric Measurement Techniques, 11, 5049–5073. https://doi.org/10.5194/amt-11-5049-2018

Vigouroux, C., Langerock, B., Bauer Aquino, C. A., Blumenstock, T., Cheng, Z., De Mazière, M., De Smedt, I., Grutter, M., Hannigan, J. W., Jones, N., Kivi, R., Loyola, D., Lutsch, E., Mahieu, E., Makarova, M., Metzger, J.-M., Morino, I., Murata, I., Nagahama, T., Notholt, J., Ortega, I., Palm, M., Pinardi, G., Röhling, A., Smale, D., Stremme, W., Strong, K., Sussmann, R., Té, Y., van Roozendael, M., Wang, P., and Winkler, H. (2020). TROPOMI–Sentinel-5 Precursor formaldehyde validation using an extensive network of ground-based Fourier-transform infrared stations, Atmospheric Measurement Techniques, 13, 3751–3767, https://doi.org/10.5194/amt-13-3751-2020

Walker, T. W., Jones, D. B. A., Parrington, M., Henze, D. K., Murray, L. T., Bottenheim, J. W., Anlauf, K., Worden, J. R., Bowman, K. W., Shim, C., Singh, K., Kopacz, M., Tarasick, D. W., Davies, J., von der Gathen, P., Thompson, A. M., & Carouge, C. C. (2012). Impacts of midlatitude precursor emissions and local photochemistry on ozone abundances in the Arctic. Journal of Geophysical Research Atmospheres, 117, D01305. https://doi.org/10.1029/2011JD016370

Wentworth, G. R., Aklilu, Y.-A., Landis, M. S., and Hsu, Y.-M. (2018). Impacts of a large boreal wildfire on ground level atmospheric concentrations of PAHs, VOCs and ozone. Atmospheric Environment, 178, 19–30. https://doi.org/10.1016/j.atmosenv.2018.01.013

Wespes, C., Emmons, L., Edwards, D. P., Hannigan, J., Hurtmans, D., Saunois, M., Coheur, P. F., Clerbaux, C., Coffey, M. T., Batchelor, R. L., Lindenmaier, R., Strong, K., Weinheimer, A. J., Nowak, J. B., Ryerson, T. B., Crounse, J. D., and Wennberg, P. O. (2012). Analysis of ozone and nitric acid in spring and summer Arctic pollution using aircraft, ground-based, satellite observations and MOZART-4 model: Source attribution and partitioning. Atmospheric Chemistry and Physics, 12(1), 237–259. https://doi.org/10.5194/acp-12-237-2012

Wettstein, Z. S., Hoshiko, S., Fahimi, J., Harrison, R. J., Cascio, W. E., and Rappold, A. G. (2018). Cardiovascular and cerebrovascular emergency department visits associated with wildfire smoke exposure in California in 2015. Journal of the American Heart Association, 7(8). e007492. https://www.ahajournals.org/doi/10.1161/JAHA.117.007492

Whaley, C., Strong, K., Adams, C., Bourassa, A. E., Daffer, W. H., Degenstein, D. A., Fast, H., Fogal, P. F., Manney, G. L., Mittermeier, R. L., Pavlovic, B., and Wiacek, A. (2013). Using FTIR measurements of stratospheric composition to identify midlatitude polar vortex intrusions over Toronto. Journal of Geophysical Research. Atmospheres, 118(22), 12,766-12,783. https://doi.org/10.1002/2013JD020577

Whaley, C. (2014). Improvements to our Understanding of Toronto-Area Atmospheric Composition, Ph.D. thesis, University of Toronto, Toronto, Ontario, Canada, permanent link: https://librarysearch.library.utoronto.ca/permalink/01UTORONTO_INST/fedca1/cdi_proquest_journals_1674733813

Whaley, C. H., Makar, P. A., Shephard, M. W., Zhang, L., Zhang, J., Zheng, Q., Akingunola, A., Wentworth, G. R., Murphy, J. G., Kharol, S. K., and Cady-Pereira, K. E. (2018). Contributions of natural and anthropogenic sources to ambient ammonia in the Athabasca Oil Sands and northwestern Canada. Atmospheric Chemistry and Physics, 18, 2011–2034. https://doi.org/10.5194/acp-18-2011-2018

Whaley, C. H., Mahmood, R., Salzen, K. von, Winter, B., Eckhardt, S., Arnold, S., Beagley, S., Becagli, S., Chien, R.-Y., Christensen, J., Damani, S. M., Dong, X., Eleftheriadis, K., Evangeliou, N., Faluvegi, G. S., Flanner, M., Fu, J. S., Gauss, M., Giardi, F., Gong, W., Hjorth, J. L., Huang, L., Im, U., Kanaya, Y., Krishnan, S., Klimont, Z., Kühn, T., Langner, J., Law, K. S., Marelle, L., Massling, A., Olivié, D., Onishi, T., Oshima, N., Peng, Y., Plummer, D. A., Popovicheva, O., Pozzoli, L., Raut, J.-C., Sand, M., Saunders, L. N., Schmale, J., Sharma, S., Skeie, R. B., Skov, H., Taketani, F., Thomas, M. A., Traversi, R., Tsigaridis, K., Tsyro, S., Turnock, S., Vitale, V., Walker, K. A., Wang, M., Watson-Parris, D., Weiss-Gibbons, T. (2022). Model Evaluation of Short-Lived Climate Forcers for the Arctic Monitoring and Assessment Programme: A Multi-Species, Multi-Model Study. Atmospheric Chemistry and Physics, 22(9), 5775–5828. https://doi.org/10.5194/acp-22-5775-2022

Whaley, C., Law, K., Hjorth, J. L., Skov, H., Arnold, S., Langner, J., Pernov, J. B., Chien, R.-Y., Christensen, J., Dong, X., Faluvegi, G., Flanner, M., Fu, J., Gauss, M., Im, U., Marelle, L., Onishi, T., Oshima, N., Plummer, D., Pozzoli, L., Raut, J.-C., Skeie, R., Thomas, M., Tsigaridis, K., Tsyro, S., Turnock, S., von Salzen, K., Tarasick, D., and Worthy, D. (2023). Arctic tropospheric ozone: assessment of current knowledge and model performance., Atmospheric Chemistry and Physics, 23(1), 637–661. https://doi.org/10.5194/acp-23-637-2023

Whitman, E., Parks, S. A., Holsinger, L. M., and Parisien, M. A. (2022). Climate-induced fire regime amplification in Alberta, Canada. Environmental Research Letters, 17(5), 055003. https://doi.org/10.1088/1748-9326/ac60d6

WHO (World Health Organization) (2015). Reducing global health risks through mitigation of short-lived climate pollutants. Scoping report for policy-makers. ISBN 978 92 4 156508 0. pp 1-148. https://iris.who.int/bitstream/handle/10665/189524/9789241565080_eng.pdf?sequence=1

WHO (World Health Organization) (2021). global air quality guidelines. Particulate matter (PM2.5 and PM10), ozone, nitrogen dioxide, sulfur dioxide and carbon monoxide. ISBN 9789240034228. pp 1-300. https://iris.who.int/bitstream/handle/10665/345329/9789240034228-eng.pdf?sequence=1

Wiacek, A. (2006). First Trace Gas Measurements Using Fourier Transform Infrared Solar Absorption Spectroscopy at the University of Toronto Atmospheric Observatory, Ph.D. thesis, University of Toronto, Toronto, Ontario, Canada, permanent link: https://librarysearch.library.utoronto.ca/permalink/01UTORONTO_INST/14bjeso/alma991106405283106196

Wiacek, A., Taylor, J. R., Strong, K., Saari, R., Kerzenmacher, T. E., Jones, N. B., and Griffith, D. W. T. (2007). Ground-based solar absorption FTIR spectroscopy: Characterization of retrievals and first results from a novel optical design instrument at a new NDACC complementary station. Journal of Atmospheric and Oceanic Technology, 24(3), 432–448. https://doi.org/10.1175/JTECH1962.1

Williams, K. D., Copsey, D., Blockley, E. W., Bodas-Salcedo, A., Calvert, D., Comer, R., Davis, P., Graham, T., Hewitt, H. T., Hill, R., Hyder, P., Ineson, S., Johns, T. C., Keen, A. B., Lee, R. W., Megann, A., Milton, S. F., Rae, J. G. L., Roberts, M. J., Scaife, A. A., Schiemann, R., Storkey, D., Thorpe, L., Watterson, I. G., Walters, D. N., West, A., Wood, R. A., Woollings, T., and Xavier, P. K. (2018). The Met Office Global Coupled Model 3.0 and 3.1 (GC3.0 and GC3.1) Configurations. Journal of Advances in Modeling Earth Systems, 10(2), 357–380. https://doi.org/10.1002/2017MS001115

Wizenberg, T., Strong, K., Jones, D. B.A., Lutsch, E., Mahieu, E., Franco, B., and Clarisse, L. (2023). Exceptional wildfire enhancements of PAN, C_2H_4, CH_3OH, and HCOOH over the Canadian high Arctic during August 2017. Journal of Geophysical Research: Atmospheres, 128(10), e2022JD038052. https://doi.org/10.1029/2022JD038052

Wizenberg, T. T. (2024). Improving Our Understanding of Arctic Tropospheric Pollution Through Measurements and Models, Ph.D. thesis, University of Toronto, Toronto, Ontario, Canada, permanent link: https://librarysearch.library.utoronto.ca/permalink/01UTORONTO_INST/fedca1/cdi_proquest_journals_3034099903

Wizenberg, T., Strong, K., Jones, D. B. A., Hannigan, J. W., Ortega, I., & Mahieu, E. (2024). Measured and Modeled Trends of Seven Tropospheric Pollutants in the High Arctic From 1999 to 2022. Journal of Geophysical Research. Atmospheres, 129(12). https://doi.org/10.1029/2023JD040544

Wolff, M., Kerzenmacher, T., Strong, K., Walker, K. A., Toohey, M., Dupuy, E., Bernath, P., Boone, C. D., Brohede, S., Catoire, V., von Clarmann, T., Coffey, M., Daffer, W. H., De Mazière, M., Duchatelet, P., Glatthor, N., Griffith, D. W. T., Hannigan, J., Hase, F., Höpfner, M., Huret, N., Jones, N., Jucks, K., Kagawa, A., Kasai, Y., Kramer, I., Küllmann, H., Kuttippurath, J., Mahieu, E., Manney, G., McElroy, C. T., McLinden, C., Mébarki, Y., Mikuteit, S., Murtagh, D., Piccolo, C., Raspollini, P., Ridolfi, M., Ruhnke, R., Santee, M., Senten, C., Smale, D., Tétard, C., Urban, J., and Wood, S. W. (2008). Validation of HNO3, ClONO2, and N2O5 from the Atmospheric Chemistry Experiment Fourier Transform Spectrometer (ACE-FTS). Atmospheric Chemistry and Physics, 8(13), 3529–3562. https://doi.org/10.5194/acp-8-3529-2008

Wunch, D., Toon, G. C., Wennberg, P. O., Wofsy, S. C., Stephens, B. B., Fischer, M. L., Uchino, O., Abshire, J. B., Bernath, P., Biraud, S. C., Blavier, J.-F. L., Boone, C., Bowman, K. P., Browell, E. V., Campos, T., Connor, B. J., Daube, B. C., Deutscher, N. M., Diao, M., Elkins, J.W., Gerbig, C., Gottlieb, E., Griffith, D.W.T., Hurst, D.F., Jimenez, R., Keppel-Aleks, G., Kort, E.A., Macatangay, R., Machida, T., Matsueda, H., Moore, F., Morino, I., Park, S., Robinson, J., Roehl, C.M., Sawa, Y., Sherlock, V., Sweeney, C., Tanaka, T., and Zondlo, M. A. (2010). Calibration of the Total Carbon Column Observing Network using aircraft profile data. *Atmospheric Measurement Techniques*, *3*(5), 1351–1362. https://doi.org/10.5194/amt-3-1351-2010

Xiao, Y., Logan, J. A., Jacob, D. J., Hudman, R. C., Yantosca, R., and Blake, D. R. (2008). Global budget of ethane and regional constraints on U.S. sources. Journal of Geophysical Research: Atmospheres, 113, D21306. https://doi.org/10.1029/2007JD009415

Yamanouchi, S., Strong, K., Lutsch, E., and Jones, D. B. A. (2020). Detection of HCOOH, CH_3OH, CO, HCN, and C_2H_6 in wildfire plumes transported over Toronto using ground-based FTIR measurements from 2002–2018. Journal of Geophysical Research: Atmospheres, 125, e2019JD031924. https://doi.org/10.1029/2019JD031924

Yamanouchi, S., Strong, K., Colebatch, O., Conway, S., Jones, D. B. A., Lutsch, E., and Roche, S. (2021a). Atmospheric trace gas trends obtained from FTIR column measurements in Toronto, Canada from 2002-2019. Environmental Research Communications, 3(5), 51002. https://doi.org/10.1088/2515-7620/abfa65

Yamanouchi, S., Viatte, C., Strong, K., Lutsch, E., Jones, D. B. A., Clerbaux, C., Van Damme, M., Clarisse, L., and Coheur, P.-F. (2021b). Multiscale observations of NH_3 around Toronto, Canada, Atmospheric Measurement Techniques, 14, 905–921, https://doi.org/10.5194/amt-14-905-2021

Yamanouchi, S. (2021c). Long-Term Analysis of Toronto-Area Atmospheric Composition, Ph.D. thesis, University of Toronto, Toronto, Ontario, Canada, permanent link: https://librarysearch.library.utoronto.ca/permalink/01UTORONTO_INST/fedca1/cdi_proquest_journals_2557243130

Yamanouchi, S., Conway, S., Strong, K., Colebatch, O., Lutsch, E., Roche, S., Taylor, J., Whaley, C. H., and Wiacek, A. (2023). Network for the Detection of Atmospheric Composition Change (NDACC) Fourier transform infrared (FTIR) trace gas measurements at the University of Toronto Atmospheric Observatory from 2002 to 2020. Earth System Science Data, 15, 3387–3418. https://doi.org/10.5194/essd-15-3387-2023

York, D., Evensen, N. M., Martínez, M. L., and De Basabe Delgado, J. (2004). Unified equations for the slope, intercept, and standard errors of the best straight line, American Journal of Physics72(3), 367–375. https://doi.org/10.1119/1.1632486

You, J., Liu, Y., Dong, J., Wang, J., and Bao, H. (2023). Ambient carbon monoxide and the risk of cardiovascular disease emergency room visits: a time-series study in Lanzhou, China. Environ. Environmental Geochemistry and Health, 45(11), 7621–7636. https://doi.org/10.1007/s10653-023-01653-1

Yukimoto, S., Kawai, H., Koshiro, T., Oshima, N., Yoshida, K., Urakawa, S., Tsujino, H., Deushi, M., Tanaka, T., Hosaka, M., Yabu, S., Yoshimura, H., Shindo, E., Mizuta, R., Obata, A., Adachi, Y., and Ishii, M (2019). The Meteorological Research Institute Earth System Model Version 2.0, MRI-ESM2.0: Description and Basic Evaluation of the Physical Component. Journal of the Meteorological Society of Japan, 97(5), 931–965. https://doi.org/10.2151/jmsj.2019-051

Zahran, S., Magzamen, S., Breunig, I.M., Mielke, H.W. (2014). Maternal exposure to neighborhood soil Pb and eclampsia risk in New Orleans, Louisiana (USA): evidence from a natural experiment in flooding. Environmental Research 133, 274–281. https://doi.org/10.1016/j.envres.2014.06.007

Zhang, S., Solomon, S., Boone, C. D., and Taha, G. (2024). Investigating the vertical extent of the 2023 summer Canadian wildfire impacts with satellite observations, Atmospheric Chemistry and Physics, 24, 11727–11736, https://doi.org/10.5194/acp-24-11727-2024

Zhao, X., Strong, K., Adams, C., Schofield, R., Yang, X., Richter, A., Friess, U., Blechschmidt, A. -M, and Koo, J. -H. (2016). A case study of a transported bromine explosion event in the Canadian high arctic. Journal of Geophysical Research, 121(1), 457–477. https://doi.org/10.1002/2015JD023711

Zhou, M., Langerock, B., Wells, K. C., Millet, D. B., Vigouroux, C., Sha, M. K., Hermans, C., Metzger, J. M., Kivi, R., Heikkinen, P., Smale, D., Pollard, D. F., Jones, N., Deutscher, N. M., Blumenstock, T., Schneider, M., Palm, M., Notholt, J., Hannigan, J. W., and De Mazière, M. (2019). An intercomparison of total column-averaged nitrous oxide between ground-based FTIR TCCON and NDACC measurements at seven sites and comparisons with the GEOS-Chem model. Atmospheric Measurement Techniques, 12(2), 1393–1408. https://doi.org/10.5194/amt-12-1393-2019

Zhou, M., Langerock, B., Vigouroux, C., Smale, D., Toon, G., Polyakov, A., Hannigan, J. W., Mellqvist, J., Robinson, J., Notholt, J., Strong, K., Mahieu, E., Palm, M., Prignon, M., Jones, N., García, O., Morino, I., Murata, I., Ortega, I., Nagahama, T., Wizenberg, T., Flood, V., Walker, K., and De Mazière, M. (2024). Recent Decreases in the Growth Rate of Atmospheric HCFC-22 Column Derived From the Ground-Based FTIR Harmonized Retrievals at 16 NDACC Sites. Geophysical Research Letters, 51(22), e2024GL112470. https://doi.org/10.1029/2024GL112470